

## Sammendrag (Norwegian)

Denne masteravhandlingen er en del av en 2 års mastergrad i strukturkemi ved NTNU. Utgangspunktet var syntese og karakterisering av krystallinske og mikroporøse aluminiumsfosfater (AlPO) med AFN topologi (tilhørende blant annet  $\text{AlPO}_4\text{-14}$ ), som var vinklet mot inkorporering av kobber og silisium ved hydrotermisk syntese. Inkorporeringen var rettet mot forbedring av materialet til å kunne redusere  $\text{NO}_x$  gasser (kobber), og konvertere metanol til olefiner (silisium). De publiserte syntesemetodene for dette materialet ble imidlertid vist å være lite reproduerbare, spesielt utmerket i det faktum at flere faser ble dannet under syntesene ( $\text{AlPO}_4\text{-14A}$  og  $\text{AlPO}_4\text{-15}$ ). For å prøve å løse problemet med flerfaseprodukter ble ulike synteseparametere og deres effekt utforsket, men endring av disse viste seg å gi andre faser enn ønsket. Da mengden isopropylamin (templat) i en syntese gel ble økt til den gav en pH over 7, ble produktet fasen  $\text{AlPO}_4\text{-14A}$ . Dette gav opphav til en videre syntese studie rettet mot å syntetisere faserne materialer av typen AlPO og SAPO i basisk miljø. Denne metoden ble bl.a. brukt til å syntetisere en tidligere antatt termisk ustabil SAPO,  $\text{SAPO}_4\text{-43}$ , ved bruk av to ulike templat. Forutsetningen for termisk stabilitet ble vist til å være avhengig av type templat brukt i syntesen av materialet, i tillegg til oppvarmingsmetode. Dette åpner for videre studier av denne SAPOen, noe som tidligere har vært umulig.

# Acknowledgements

First of all I would like to thank my supervisor Morten Bjørgen for setting high standards and thereby ensuring that quality always comes before quantity (“Er det faserent?”). I would also like to thank my co-supervisor Karina Mathisen for introducing me to the sometimes frustrating art (“D e jo rein bingo”) of synthesizing AlPOs, MeAPOs, and SAPOs, and for convincing me that studying inorganic structure chemistry was the right choice.

Many thanks goes to my fellow students Andrey Volynkin, Ragnhild Skorpa, and Tove-Nanny Edvardsen. It has been a pleasure working with all of you and I hope we stay in touch.

I would like to thank family and friends for putting up with my almost addictive behavior towards the work with this thesis.

I would also like to thank the following:

- Wilhelm Dall and Julian Tolchard for help with the X-ray diffraction instruments and the electron microscope.
- Gunnar Svare and Roger Aarvik for fixing broken equipment, ordering chemicals, and much more.
- Syverin Lierhagen for running the ICP-MS analyses.
- Sema Akyalcin and Saepurahman for help with running the FT-IR experiments.
- David G. Nicholson for words of wisdom and funny comments.
- The Research Council of Norway for financial support to run the XAS experiments at ESRF in Grenoble France.

This thesis could not have been written without the help of all these wonderful people, and all their efforts are greatly appreciated.

# Contents

<b>1</b>	<b>Introduction</b>	<b>1</b>
1.1	Background . . . . .	1
1.1.1	The Zeolites . . . . .	1
1.1.2	The aluminophosphates (AlPOs) . . . . .	2
1.1.3	Characterization of Zeolites and Zeotypes . . . . .	4
1.1.4	Zeolites as heterogeneous catalysts . . . . .	5
1.2	Zeotypes with the AFN topology . . . . .	9
1.2.1	Classification and previous work . . . . .	9
1.3	Scope of this thesis work . . . . .	10
<b>2</b>	<b>Theory</b>	<b>11</b>
2.1	Powder X-ray Diffraction (PXRD) . . . . .	11
2.1.1	Introduction . . . . .	11
2.1.2	Theory . . . . .	11
2.1.3	Applications for this thesis . . . . .	15
2.2	Inductively Coupled Plasma - Mass Spectrometry (ICP-MS) . . . . .	16
2.2.1	Introduction . . . . .	16
2.2.2	Sample preparation . . . . .	16
2.2.3	Plasma generation . . . . .	16
2.2.4	Double-focusing magnetic sector mass spectrometer . . . . .	17
2.2.5	Applications for this thesis . . . . .	17
2.3	Scanning Electron Microscopy (SEM) . . . . .	18
2.3.1	Introduction . . . . .	18
2.3.2	Instrumentation . . . . .	18
2.3.3	Theory . . . . .	19
2.3.4	Applications for this thesis . . . . .	20
2.4	Thermogravimetric Analysis (TGA) and Differential Scanning Calorimetry . . . . .	21
2.4.1	Introduction . . . . .	21
2.4.2	Instrumentation . . . . .	21
2.4.3	Theory . . . . .	21
2.4.4	Applications for this thesis . . . . .	24
2.5	Surface Area Measurement (BET theory) . . . . .	25
2.5.1	Introduction . . . . .	25
2.5.2	Theory . . . . .	25
2.5.3	Application for this thesis . . . . .	27
2.6	X-ray Absorption Spectroscopy (XAS) . . . . .	28
2.6.1	Introduction . . . . .	28
2.6.2	Synchrotron radiation . . . . .	28

---

2.6.3	Theory . . . . .	28
2.6.4	Applications for this thesis . . . . .	29
2.7	Fourier Transform - Infrared (FT-IR) spectroscopy . . . . .	30
2.7.1	Introduction . . . . .	30
2.7.2	The Michelson interferometer and the Fourier Transform . . . . .	30
2.7.3	Theory . . . . .	30
2.7.4	The gross selection rule . . . . .	31
2.7.5	Applications for this thesis . . . . .	33
2.8	Gas Chromatography - Mass spectrometry (GC-MS) . . . . .	34
2.8.1	Introduction . . . . .	34
2.8.2	Gas chromatography . . . . .	34
2.8.3	Flame Ionization Detector (FID) . . . . .	34
2.8.4	Gas Chromatography - Mass Spectrometry (GC-MS) . . . . .	34
2.8.5	Applications for this thesis . . . . .	35
<b>3</b>	<b>Experimental</b>	<b>37</b>
3.1	Synthesis procedures . . . . .	37
3.1.1	First generation (F) compositions . . . . .	37
3.1.2	Various preparations for AlPOs and SAPOs in alkaline mixtures discovered in this thesis work . . . . .	39
3.2	Calcination procedures . . . . .	40
3.3	Improvised stirred autoclaves . . . . .	41
3.4	Equipment used in the thesis work . . . . .	42
3.4.1	PXRD . . . . .	42
3.4.2	SEM . . . . .	42
3.4.3	TGA . . . . .	42
3.4.4	BET . . . . .	42
3.4.5	ICP-MS . . . . .	42
3.4.6	XAS . . . . .	42
3.4.7	FT-IR . . . . .	43
3.4.8	GC-MS . . . . .	43
<b>4</b>	<b>Results and Discussion</b>	<b>45</b>
4.1	PXRD . . . . .	45
4.1.1	ipaAlPO <sub>4</sub> -14F . . . . .	45
4.1.2	A pseudo <i>in-situ</i> PXRD study of the calcination of ipaAlPO <sub>4</sub> -14F . . . . .	48
4.1.3	tbaAlPO <sub>4</sub> -14F . . . . .	49
4.1.4	ipaCuAPO <sub>4</sub> -14F . . . . .	51
4.1.5	tbaSAPO <sub>4</sub> -14F . . . . .	59
4.1.6	Attempts at synthesizing phase-pure AlPO <sub>4</sub> -14 . . . . .	62
4.1.7	ipaAlPO <sub>4</sub> -14A . . . . .	76
4.1.8	ipaSAPO <sub>4</sub> -43 . . . . .	83
4.1.9	dpaAlPO <sub>4</sub> -11 and dpaSAPO <sub>4</sub> -43 . . . . .	87
4.1.10	Augelite and pipSAPO <sub>4</sub> -20 . . . . .	93
4.1.11	tbaAlPO <sub>4</sub> -15 and tbaSAPO <sub>4</sub> -20 . . . . .	95
4.1.12	dipaAlPO <sub>4</sub> -11 and dipaSAPO <sub>4</sub> -34 . . . . .	97
4.1.13	Unidentified phase . . . . .	99
4.1.14	teaAlPO <sub>4</sub> -5 and teaSAPO <sub>4</sub> -18 . . . . .	100

---

---

4.1.15	dpaipaSAPO <sub>4</sub> -43 . . . . .	103
4.1.16	as-synthesized and calcined . . . . .	103
4.2	ICP-MS . . . . .	105
4.2.1	First generation molecular sieves . . . . .	105
4.2.2	Various other compositions . . . . .	105
4.3	SEM . . . . .	108
4.3.1	ipaAlPO <sub>4</sub> -14F . . . . .	108
4.3.2	ipaCuAPO <sub>4</sub> -14F . . . . .	110
4.3.3	ipaAlPO <sub>4</sub> -14A . . . . .	112
4.3.4	ipaSAPO <sub>4</sub> -43 . . . . .	113
4.3.5	dpaSAPO <sub>4</sub> -43 . . . . .	114
4.3.6	Augelite and pipSAPO <sub>4</sub> -20 . . . . .	116
4.3.7	dipaSAPO <sub>4</sub> -34 . . . . .	117
4.3.8	teaSAPO <sub>4</sub> -18 . . . . .	117
4.3.9	Unidentified phase . . . . .	118
4.3.10	dpaipaSAPO <sub>4</sub> -43 . . . . .	118
4.4	TGA and DSC . . . . .	120
4.4.1	ipaAlPO <sub>4</sub> -14F . . . . .	120
4.4.2	ipaCuAPO <sub>4</sub> -14F . . . . .	122
4.4.3	tbaAlPO <sub>4</sub> -14F . . . . .	125
4.4.4	tbaSAPO <sub>4</sub> -14F . . . . .	127
4.5	BET surface area . . . . .	132
4.5.1	First generation molecular sieves . . . . .	132
4.6	XAS . . . . .	135
4.6.1	ipa0.01CuAPO <sub>4</sub> -14F and ipa0.03CuAPO <sub>4</sub> -14F . . . . .	135
4.7	FT-IR . . . . .	140
4.7.1	SAPO <sub>4</sub> -14F . . . . .	141
4.7.2	AlPO <sub>4</sub> -14A . . . . .	142
4.7.3	SAPO <sub>4</sub> -18 . . . . .	144
4.8	Catalysis . . . . .	146
4.8.1	Methanol to Olefins (MTO) reaction . . . . .	146
<b>5</b>	<b>Conclusions</b>	<b>151</b>
<b>6</b>	<b>Future work</b>	<b>153</b>
	<b>References</b>	<b>155</b>
<b>A</b>	<b>Additional data</b>	<b>164</b>
A.1	Results from ICP-MS analyses . . . . .	164
A.2	BET isotherm data . . . . .	165
<b>B</b>	<b>Resources</b>	<b>166</b>
B.1	Conversions . . . . .	166
B.1.1	Conversion from phosphoric acid to phosphorous pentoxide . . . . .	166
B.1.2	Conversion from aluminum isopropoxide to alumina . . . . .	166
B.2	Crystallographic Information Files (CIF) . . . . .	167
B.2.1	AlPO <sub>4</sub> -14A . . . . .	167
B.2.2	AlPO <sub>4</sub> -15 . . . . .	168

---

---

B.3	Calculations . . . . .	169
B.3.1	Calculation of theoretical % mass loss for TGA analysis . . . . .	169
B.3.2	Calculation of carrier gas flow . . . . .	170

---



# Chapter 1

## Introduction

### 1.1 Background

#### 1.1.1 The Zeolites

##### Discovery and structure

Zeolites are a class of crystalline aluminosilicates recognized by Axel Fredrik Cronstedt in 1756<sup>1</sup>. The name “Zeolite” comes from Greek meaning boiling stones, and was given to this class of materials based on the ability to visibly lose water upon heating. Their structures are composed of tetrahedral  $[\text{SiO}_4]^{4-}$  and  $[\text{AlO}_4]^{5-}$  building units, linked together in an alternating fashion by the corner-sharing of oxygen atoms<sup>2</sup>. It is common to illustrate corner-sharing oxygen atoms as lines, and aluminum or silicon (often called T-atoms) atoms as junctions. An example of this is shown in figure 1.1.

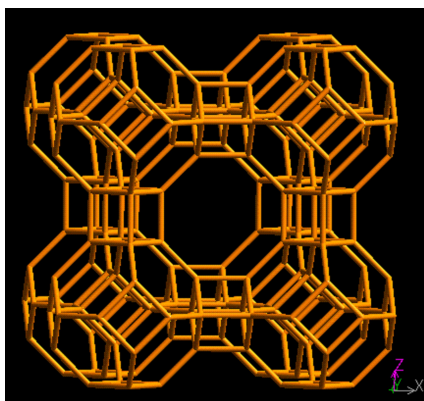


**Figure 1.1:** An illustration<sup>3</sup> of zeolite A. Corner-sharing oxygen atoms are represented by lines, and the  $[\text{SiO}_4]^{4-}$  and  $[\text{AlO}_4]^{5-}$  tetrahedra are represented by the junctions.

The Zeolites were long regarded as a curiosity and the only commercial application was as jewelry until the work by Richard M. Barrer in 1938. His early work<sup>4</sup> on chabazite and analcite

is by many regarded as the birth of the zeolite science<sup>1</sup>. The IZA<sup>3</sup> (International Zeolite Association) structure commission has been given the authority from IUPAC (International Union of Pure and Applied Chemistry) to assign a three capital letter framework type code (FTC) to each unique zeolite structure/topology (e.g. CHA, LTA, FAU). These structure codes are flexible in terms of Zeolite composition as long as the overall crystal structure is unchanged.

## Synthetic Zeolites

Naturally occurring Zeolites were originally found in small cavities in rocks of volcanic origin<sup>1</sup>. Synthetic Zeolites can be obtained from amorphous precursor gels containing water, silica, and alumina in the presence of a cation source<sup>5</sup>. The (usually) alkaline gels are placed in sealed autoclaves and heated to above ambient temperatures. The temperature and corresponding autogenous pressure causes the amorphous Si-O and Al-O fragments to connect and form the Zeolite crystal lattice. During crystallization some of the cations and water molecules get trapped inside the finished Zeolite.

### 1.1.2 The aluminophosphates (AIPOs)

#### Discovery, structure, and characteristics

The crystalline aluminophosphates (AIPOs) were discovered as a new class of materials in 1982 by Wilson et al.<sup>6</sup>. The AIPOs are similar to the Zeolites in that their structures are comprised of alternating  $[\text{PO}_4]^{3-}$  and  $[\text{AlO}_4]^{5-}$  tetrahedra<sup>7</sup> (see figure 1.2). The fact that they are not comprised of alternating  $[\text{SiO}_4]^{4-}$  and  $[\text{AlO}_4]^{5-}$  tetrahedra makes them better described as Zeotypes<sup>8</sup>. The general nomenclature for these materials is  $\text{AIPO}_4-n$ , where  $n$  is an integer denoting a particular structure (e.g.  $\text{AIPO}_4-5$ ,  $\text{AIPO}_4-12$ ,  $\text{AIPO}_4-14$ ). Some of the AIPOs have structures identical to Zeolites, while other are unique. The AIPOs are also given FTCs since these codes allow for compositional variation.

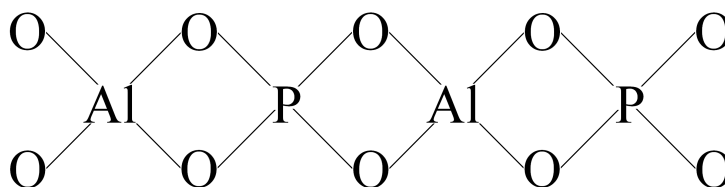


**Figure 1.2:** An illustration of alternating  $[\text{PO}_4]^{3-}$  and  $[\text{AlO}_4]^{5-}$  tetrahedra in AIPOs.

#### The silicoaluminophosphates (SAPOs)

The silicoaluminophosphates were discovered in 1984 by Lok et al.<sup>9</sup>. These materials are also composed of alternating  $[\text{PO}_4]^{3-}$  and  $[\text{AlO}_4]^{5-}$  tetrahedra, but ideally some of the  $[\text{PO}_4]^{3-}$  tetrahedra

have been replaced by  $[\text{SiO}_4]^{4-}$  tetrahedra. The ideal case introduces local anionic lattice points that can be balanced by suitable cations. An illustration of this is shown in figure 1.3. The general nomenclature for SAPOs is  $\text{SAPO}_{4-n}$ , and the structures are identical to the parent  $\text{AlPO}_{4-n}$  material.

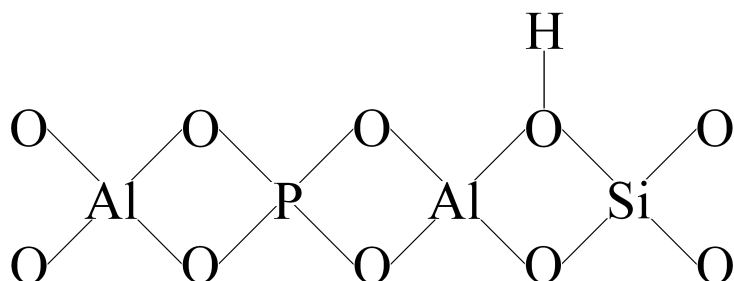


**Figure 1.3:** An illustration of incorporated tetravalent silicone (replacing pentavalent phosphorous) in a SAPO. Also shown is the charge balancing proton.

### Metal aluminophosphates (MeAPOs) and metal silicoaluminophosphates (MeAPSOs)

In 1986, Stephen T. Wilson and Edith M. Flanigen<sup>10</sup> introduced yet another modification of the AlPOs, namely the metal aluminophosphates (MeAPOs). As with the SAPOs, these materials were modified to contain other elements in addition to aluminum and phosphorous, this time also composed of magnesium ( $\text{MAPO}_{4-n}$ ), zinc ( $\text{ZnAPO}_{4-n}$ ), manganese ( $\text{MnAPO}_{4-n}$ ), and cobalt ( $\text{CoAPO}_{4-n}$ ). An illustration of a MeAPO is shown in figure 1.4. A fusion of the SAPOs and MeAPOs also exists in the MeAPSOs/MeSAPOs, materials in which both a metal and silicon has been incorporated in the AlPO framework.

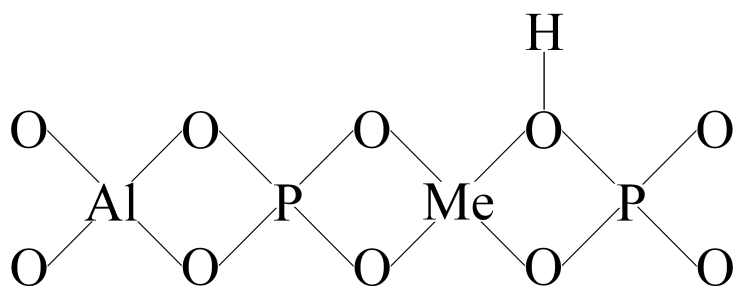


**Figure 1.4:** Illustration of incorporated divalent transition metal (Me) (replacing trivalent aluminum). In this representation the oxidation state of the transition metal also creates a local anionic lattice point balanced by a proton.

### AlPO, MeAPO, and SAPO Syntheses

The AlPOs can be synthesized by the hydrothermal crystallization of aluminophosphate gels at elevated temperatures, usually under mildly acidic ( $\text{pH} = 3.5$ ) conditions<sup>6</sup>. Common sources of constituent atoms (Al, O, and P) to be incorporated are phosphoric acid ( $\text{H}_3\text{PO}_4$ ), pseudo-boehmite ( $\text{AlOOH}$ ), and aluminum isopropoxide ( $\text{Al}(\text{OCH}(\text{CH}_3)_2)_3$ ). Also added is an organic

amine or ammonium salt which acts as a structure directing agent (SDA or template). The presence of this template is of crucial importance for crystallization of the material, and in its absence only dense phases such as tridymite and berlinite form<sup>6</sup>. In the case of SAPOs, MeAPOs, and MeAPSOs, sources for other elements in addition to aluminum and phosphorous are added, such as colloidal or fumed silica (SAPOs), transition metal oxides or acetate salts (MeAPOs), or mixtures of both (MeAPSOs)<sup>9,10</sup>. The different sources of elements are mixed sequentially, usually in the order: water, acid, aluminum source, and template. The composition of the gel is usually stated as a molar oxide ratio: R:Al<sub>2</sub>O<sub>3</sub>:MeO:P<sub>2</sub>O<sub>5</sub>:SiO<sub>2</sub>:H<sub>2</sub>O (R = template, Me = metal), with the relative number of moles varying from one preparation to the next. The aluminophosphate gels are sealed in autoclaves and heated at temperatures usually ranging from 100 to 200°C, for times varying from hours to weeks. Recovery of the materials (in the form of powders) are usually done by either filtration or centrifugation, followed by drying in an oven at around 100°C.

### **Calcination**

Though the crystallization mechanism for AlPOs is not fully understood<sup>11</sup>, the finished products usually contain the trapped or clathrated template within its pores<sup>7</sup>. Removal of the template molecules is usually achieved by heating (or “calcining”) the materials to temperatures where the organic amines become mobile and diffuse out of the crystal lattice<sup>6</sup>.

### **1.1.3 Characterization of Zeolites and Zeotypes**

Several characterization methods have been successfully applied to describe zeolites and zeotypes. Some of these are routine methods such as Powder X-ray Diffraction (PXRD), Scanning Electron Microscopy (SEM), Thermal gravimetric analysis (TGA), and Surface area measurement (BET theory), while others are more advanced such as X-ray Absorption Spectroscopy (XAS) (for studying MeAPOs), and Fourier Transform - Infrared Spectroscopy (FT-IR).

PXRD is usually the characterization method applied directly after a product has been obtained from a given synthesis procedure. The method provides an easy way of identifying a polycrystalline product, as well as qualitatively assessing its purity. SEM can be employed to study the product at the micro- and (sometimes) nanoscale, giving insight to crystallite morphology and qualitative size distribution. TGA enables the scientist to determine if complete removal of the templates used in the syntheses has taken place, and to determine the step-wise behavior of this removal. Surface area measurements are frequently performed on the materials to ensure that their characteristically high surface areas are available for chemical reactions to take place. When the basic methods have been employed, advanced characterization methods (XAS, FT-IR) can be used to study the material during a catalytic process.

---

### 1.1.4 Zeolites as heterogeneous catalysts

#### The definition of a catalyst

One can imagine the hypothetical compounds A and B reacting and forming the products C and D. The reaction can be described by the following equation:



where the small letters symbolize their stoichiometric coefficients. Figure 1.5 illustrates that the pathway from reactants A and B involves an initial increase in Gibbs energy prior to forming the products C and D. This additional energy is referred<sup>12</sup> to as the activation energy,  $E_A$ . The rate at which C and D is formed is dependent on the size of  $E_A$ . A catalyst can be defined as a substance that lowers the  $E_A$  of the reaction, without itself being consumed<sup>13</sup>. The catalyst does this by introducing new pathways (intermediates) with lower activation energies than the pathway in the absence of a catalyst. The end result is increased reaction rates, meaning that the products C and D are formed in a shorter time than in the absence of a catalyst.

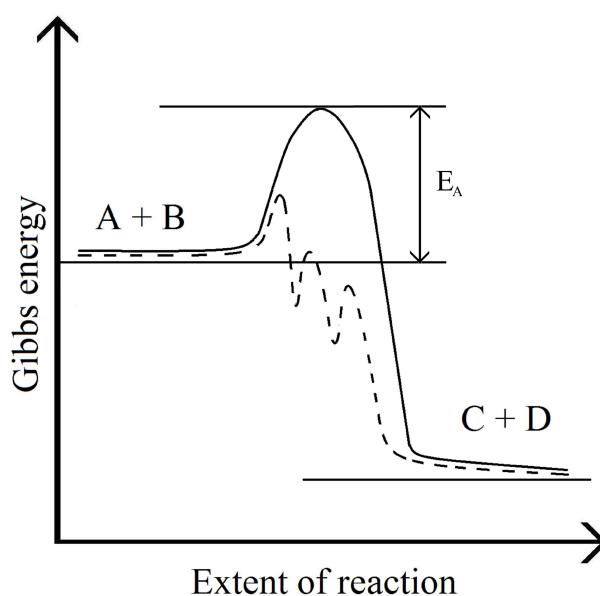


**Figure 1.5:** An illustration of the Gibbs free energy as a function of the extent of reaction for catalyzed and uncatalyzed reactions. Reacting species A and B require an activation energy,  $E_A$ , to be converted to the products C and D. In the presence of a catalyst (dotted line), the products are formed by consecutive intermediates with lower  $E_A$  than the uncatalyzed reaction.

#### Heterogeneous catalysis

Heterogeneous catalysis is the case where the catalyst is in a different phase (solid, liquid, gas) than the reagents. In the case where the catalyst and reagents are in the same phase it is called homogeneous catalysis<sup>14</sup>. Zeolites and Zeotypes (solids) are examples of heterogeneous catalysts in that they convert reagents in the gas phase.

### Active sites

It is usually not the entire surface of a catalyst that is active or available for a reaction to occur. A reaction usually occurs at some parts of the catalyst that is more active than others<sup>15</sup>. In SAPOs, some of the  $[\text{PO}_4]^{3-}$  tetrahedra are replaced with  $[\text{SiO}_4]^{4-}$  tetrahedra causing a local negative charge in the lattice. After calcination, these negative charges are balanced by protons as shown in figure 1.3, creating bridged hydroxyls. The definition of Zeolites ensures that they also possess such sites, as shown in figure 1.6. In Zeolites, these sites can be obtained by ion exchange with ammonium and subsequent calcination<sup>16</sup>. The presence of bridging hydroxyls is what gives the SAPOs and Zeolites acidity, and it is the quality of such sites that can make them active catalysts.

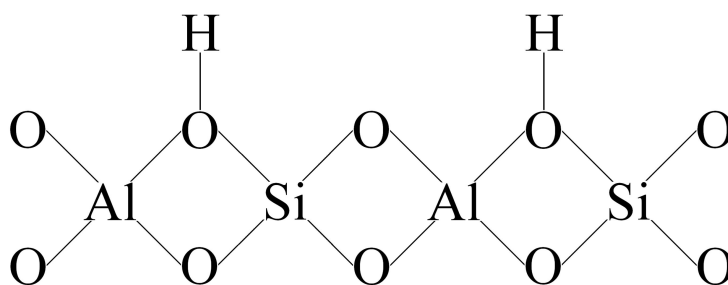


**Figure 1.6:** An illustration of the active sites in Zeolites caused by alternating  $[\text{SiO}_4]^{4-}$  and  $[\text{AlO}_4]^{5-}$  tetrahedra. The Al-OH-Si linkages constitute the Brønsted acid sites.

### Zeolites and Zeotypes as “Molecular sieves”

Ordinary molecular diffusion in gases occurs as a result of concentration differences<sup>17</sup>. The diffusion process tries to balance these differences, resulting in a gas flux. Diffusion of gas molecules into and out of Zeolites and Zeotypes are directly affected by the size of their pores. For large pores ( $d > 100 \text{ nm}$ ,  $d = \text{diameter}$ ) Bulk diffusion dominates, and molecules collide more with each other than with the pore walls. For intermediate pores ( $2 \text{ nm} < d < 100 \text{ nm}$ ) the molecules collide more with the pore walls than with each other, and this is referred to as Knudsen diffusion. In the case of microporous Zeolites and Zeotypes ( $d < 2 \text{ nm}$ ), the pores are so small that even the configuration of molecules entering and exiting plays a role in the diffusion process<sup>18</sup>. A result of this is that molecules can be “sieved” based on their shape, size and corresponding diffusivity, earning the Zeolites and Zeotypes their categorization as “Molecular sieves”<sup>18</sup>.

### Shape-selective catalysis

The selectivity of a catalyst can be defined as its ability to yield a high proportion of the desired product with minimum amount of side products<sup>19</sup>. The molecular sieving ability of Zeolites and Zeotypes also gives them rather unique selectivities. An example illustrating this is the

butanol dehydration in CaA, where *n*-butanol can enter the pores and dehydrate, whereas *i*-butanol cannot<sup>20</sup>. In this case the catalyst is said to be *reactant selective*. In the alkylation of toluene to xylene over H-ZSM-5, only the *para*-xylene isomer exits the catalyst, while the *o*-xylene and *m*-xylene isomers do not. In this case the *para*-xylene isomer is obtained because it has much greater diffusivity, and the catalyst is said to be *product selective*<sup>21</sup>. The well defined pores of the Zeolites and Zeotypes can also be shaped in such a way that only one type of intermediate has enough room to fit, and bulkier intermediates are prevented from forming. This leads to the production of a product dependent on the transition state intermediate with the suitable geometry. In this case the catalyst is *restricted transition state selective*<sup>21</sup>. The three different types are illustrated in figure 1.7.

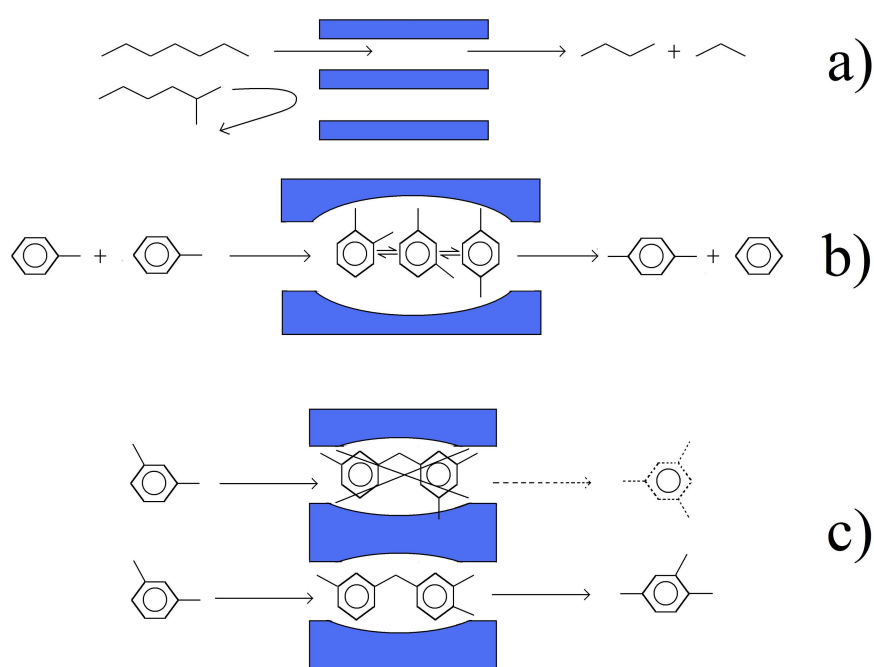


**Figure 1.7:** An illustration of the different types of selectivities that are characteristic for the microporous Zeolites and Zeotypes: a) some reactants are excluded from entering the pores: reactant selectivity; b) some products are prevented from exiting the pores: product selectivity; c) some transition state intermediates are prevented from forming: restricted transition state selectivity.

### The methanol-to-olefins (MTO) process

The world's need for the olefins ethylene and propylene is apparent in the everyday appliances ranging from soda bottles, plastic bags, buckets, containers, and so much more<sup>22</sup>. It is almost impossible in our modern society not to run into the acronyms HDPE and LDPE, signifying respectively high- and low density polyethylene. Polyethylene and polypropylene belong to a class of materials known as polymers, and are composed respectively of the monomers ethylene and propylene. The methanol to olefins, or simply MTO, process provides a catalytic route from syngas (a mixture of  $H_2$  and  $CO$ ) to these olefins.

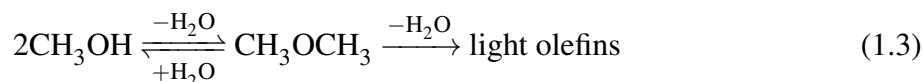
The starting point in the MTO process is of course methanol, which itself can be produced from syngas using a ZnO-Cr<sub>2</sub>O<sub>3</sub> catalyst<sup>23</sup>:



The methanol produced may be converted to hydrocarbons (MTH) by the use of Zeolites and Zeotypes. The process can be simplified into three steps<sup>24</sup>:

1. The reversible dehydration of methanol to form dimethyl ether
2. The conversion of dimethyl ether to light olefins
3. The conversion of light olefins to heavier olefins, naphthenes, n-paraffins, or aromatics

The MTO process aims at terminating the process after step 2, effectively achieving only lighter olefins (ethylene, propylene, butylene). This is best achieved by utilizing SAPO<sub>4</sub>-34, a Zeotype with CHA topology. Its well defined pores (see figure 1.8) act as catalytic reactors allowing methanol molecules to diffuse in and interact with the catalyst's acid sites. A "hydrocarbon-pool" mechanism has been proposed for the MTO process by S.Kolboe and I.M. Dahl<sup>25,26</sup>, in which methanol forms reactive intermediates shown to be polymethylbenzenes (polyMBs)<sup>27</sup>. The polyMBs and the acid sites of SAPO<sub>4</sub>-34 interact with methanol molecules and effectively splits of olefins which diffuse out of the catalyst as products. However, the small size of the pore openings prohibit the larger hydrocarbon intermediates from escaping<sup>24</sup>:



In other words, the process exploits the *product selectivity* of the SAPO<sub>4</sub>-34 catalyst<sup>28</sup>.

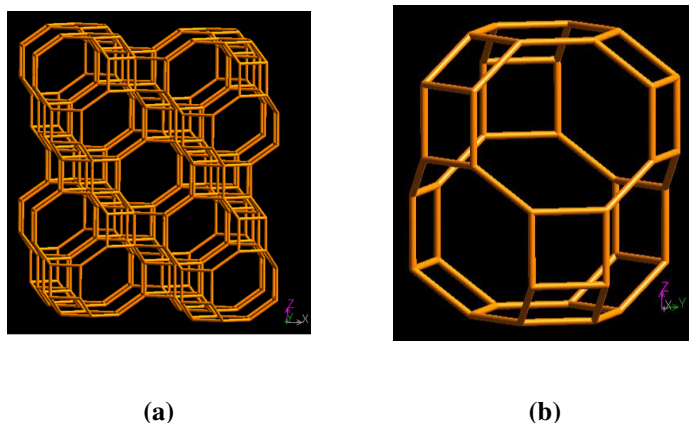


**Figure 1.8:** Images illustrating parts of the chabazite structure<sup>3</sup> of SAPO<sub>4</sub>-34: a) viewed along (010); b) cage viewed normal to (001)

## 1.2 Zeotypes with the AFN topology

### 1.2.1 Classification and previous work

AlPO<sub>4</sub>-14 was one of the first AlPOs discovered in 1982 by Wilson et al., and was synthesized using both isopropylamine and tert-butylamine as template<sup>6</sup>. It has the chemical formula [Al<sub>8</sub>P<sub>8</sub>O<sub>32</sub>]-AFN and received the IZA FTC: AFN in 1998<sup>3</sup>. Zeotypes with the AFN topology refers to structural equivalents of AlPO<sub>4</sub>-14 that differs in chemical composition. Parts of the AFN topology is shown in figure 1.9. It can be described as chains of open double cubes, with each cube missing one vertex. It has a three dimensional network of channels formed by 4-, 6-, and 8-ring pores. Its unit cell is triclinic ( $a = 9.704 \text{ \AA}$ ,  $b = 9.736 \text{ \AA}$ ,  $c = 10.202 \text{ \AA}$ ,  $\alpha = 77.81^\circ$ ,  $\beta = 77.50^\circ$ ,  $\gamma = 87.69^\circ$ )<sup>29</sup>.

The original preparations for AlPO<sub>4</sub>-14 also crystallized small amounts of AlPO<sub>4</sub>-14A and AlPO<sub>4</sub>-15, sieves that have received little characterization<sup>30</sup>. Broach et al.<sup>29</sup> performed Rietveld refinement of the crystal structure of the calcined dehydrated material in 1999. Both metal substituted (CrAPO<sub>4</sub>-14) and metal and silicon (CoSAPO<sub>4</sub>-14) substituted AlPO<sub>4</sub>-14 have been reported by Helliwell et al.<sup>31</sup> and Rajić et al.<sup>32</sup>. The CrAPO<sub>4</sub>-14 was obtained as a single-crystal, while the CoSAPO<sub>4</sub>-14 was observed as a competing phase with CoSAPO<sub>4</sub>-34. Parise et al.<sup>33</sup> synthesized single-crystals of GaPO<sub>4</sub>-14 in 1986 as part of a two-phase product.

Zibrowius et al.<sup>34</sup> have demonstrated that piperidine can crystallize AlPO<sub>4</sub>-14 and have also revealed using NMR that the as-synthesized material has both tetrahedrally and octahedrally coordinated Al. The calcined product was shown to reduce the coordination of Al to four, with the transformation caused by removal of the organic template and water residing in the pores of the as-synthesized material. Yang et al.<sup>35</sup> have shown that calcined hydrated AlPO<sub>4</sub>-14 is distinctly different than calcined dehydrated AlPO<sub>4</sub>-14.

Girnus et al.<sup>36</sup> have claimed the impossibility of crystallizing SAPO<sub>4</sub>-14 using piperidine as template. The conclusion was made after observing the crystallization of SAPO<sub>4</sub>-34 in AlPO<sub>4</sub>-14 gels containing silicon.

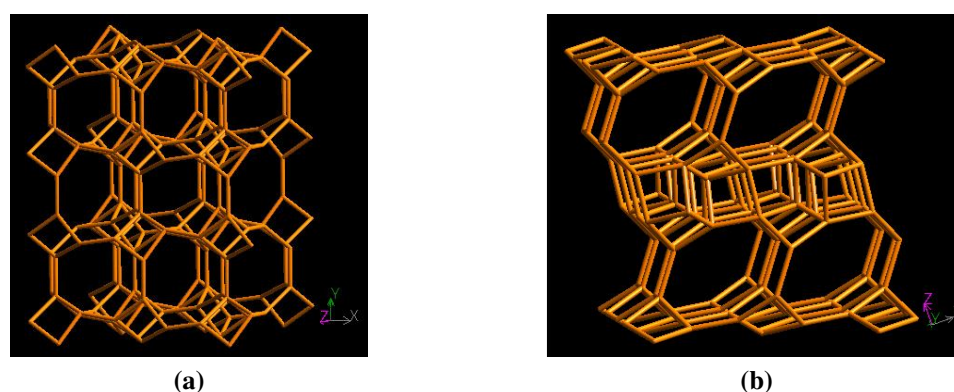


**Figure 1.9:** Images illustrating parts of the AFN topology<sup>3</sup>: a) viewed normal to (001); b) viewed along (010).

### 1.3 Scope of this thesis work

The initial scope of this work was to investigate the catalytic applicability of aluminophosphate zeotypes with the AFN topology. This involved research into the incorporation of copper (CuAPO<sub>4</sub>-14) and silicon (SAPO<sub>4</sub>-14) into such materials to make them catalytically active. The materials were to be tested for activity in the following two processes:

1. The selective catalytic reduction of NO<sub>x</sub> (CuAPO<sub>4</sub>-14)
2. The conversion of methanol-to-olefins (MTO) (SAPO<sub>4</sub>-14)

However, during the thesis work it was discovered that synthesizing phase-pure AlPO<sub>4</sub>-14 proved difficult, and the products contained the impurities AlPO<sub>4</sub>-14A and AlPO<sub>4</sub>-15. Several synthesis parameters were varied to see if phase-pure AlPO<sub>4</sub>-14 was obtainable. However, all the variations resulted in the crystallization of undesired phases.

One of the parameters tested was the template content of the synthesis gel. It was discovered that crystallizing an AlPO<sub>4</sub>-14 gel with a pH of 10 yielded phase-pure AlPO<sub>4</sub>-14A. When adding silicon to the same high pH gel it was discovered that SAPO<sub>4</sub>-43 could be crystallized. This eventually led to the study of synthesizing AlPOs and SAPOs in alkaline mixtures.

---

# Chapter 2

## Theory

### 2.1 Powder X-ray Diffraction (PXRD)

#### 2.1.1 Introduction

An identification method is necessary to determine if the desired product is obtained from a given synthesis procedure. X-ray diffraction exploits the fact that crystalline materials are built from a repeating unit, the unit cell, which by translation reproduces their entire topology. The result of a synthesis may result in single-crystals or a polycrystalline sample (powder). In the case of single-crystals, single-crystal X-ray diffraction is used to obtain atomic positions and enables structural determination of the material synthesized. In the case of a powder, Powder X-ray Diffraction is used for identification of the material (in advanced cases structural refinement). Most AIPOs (and compositional variants) are synthesized in powder form. Interactions between X-ray beams and matter can be detected and converted to a diffraction pattern characteristic for the material studied. If the reflections obtained only belong to one topology the material studied is said to be phase-pure. If other reflections are present, the material is a blend of several crystalline materials. Powder X-ray diffraction can therefore be used as a fingerprint method to identify polycrystalline materials and evaluate the synthesis procedures.

#### 2.1.2 Theory

##### The unit cell and its parameters

Figure 2.1 shows a generalized picture of the unit cell and its parameters. The unit cell's three dimensional representation is defined by its lattice parameters: the length parameters ( $a$ ,  $b$  and  $c$ ) along Cartesian axes ( $x$ ,  $y$  and  $z$  respectively) and angle parameters ( $\alpha$ ,  $\beta$  and  $\gamma$ ). By convention, the angle between  $a$  and  $b$  is  $\gamma$ , between  $a$  and  $c$  is  $\beta$ , and between  $b$  and  $c$  is  $\alpha$ .<sup>37</sup> The following seven crystal systems can be generated by varying these lattice parameters<sup>37</sup>: monoclinic, triclinic, rhombohedral, orthorhombic, tetragonal, hexagonal, and cubic.

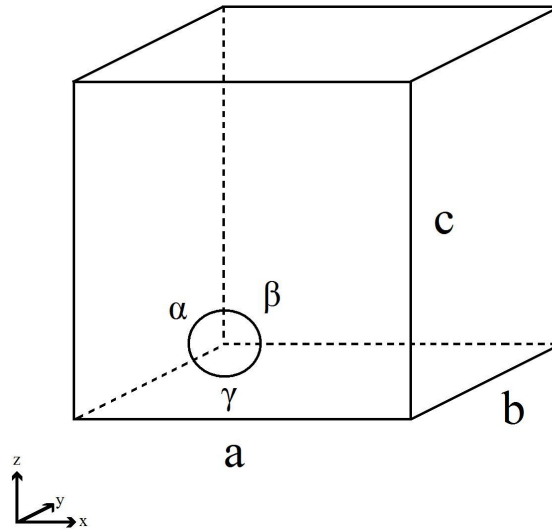


**Figure 2.1:** The general unit cell and its parameters.

### Crystal planes and the Miller index

Lattice points (e.g atoms) in crystal structures have specific coordinates within a unit cell. Because of translational symmetry, lines (two-dimensional systems) or planes (three-dimensional systems) linking these lattice points arise within the crystals. All the crystal lines/planes are members of a set of equally spaced parallel lines/planes, and all lattice points must lie on one of these<sup>38</sup>. The crystal lines/planes cut through the length parameters  $a$ ,  $b$ , and  $c$  at specific lengths measured from the origin of the Cartesian axes. The inverse of these lengths are defined as the Miller indices;  $h$ ,  $k$ , and  $l$ , and are usually shown as  $(h, k, l)$ . The Miller indices are integers; positive, negative, or zero<sup>39</sup>.

### X-ray diffraction

X-rays hitting a solid material will scatter<sup>40</sup>. Beams of X-rays hitting a crystalline material have wavelengths in the range of interatomic distances (of the order of Ångström (Å) =  $10^{-10}$  m) in the materials investigated. Figure 2.2 shows an illustration of two beams hitting atoms in the crystal lattice. The beam hitting point  $B$  must travel an extra distance  $AB + BC$ , resulting in the expression<sup>41</sup>:

$$\text{path difference} = AB + BC = 2d_{hkl} \sin \theta \quad (2.1)$$

where  $\theta$  is the glancing angle and  $d_{hkl}$  is the spacing between two  $(h,k,l)$  planes. If the path length for a glancing angle is an integer number of wavelengths, the two waves are in phase and constructive interference occurs. This leads to the relationship between glancing angle and wavelength (the condition for allowed reflections) known as Bragg's law<sup>40</sup>:

$$n\lambda = 2d_{hkl} \sin \theta \quad (2.2)$$

Different values of the integer  $n$  corresponds to different order reflections;  $n = 1$  is a first order reflection,  $n = 2$  is a second order reflection, and so on. From measured  $\theta$  (or more commonly  $2\theta$ ) values, one can, with the knowledge of the incident wavelength (determined by the X-ray generator, usually with Cu  $K_{\alpha}$  radiation), calculate the d-spacings. These spacings between two lines/planes in turn relate to the different unit cells with their lattice parameters, as well as the corresponding miller indices.

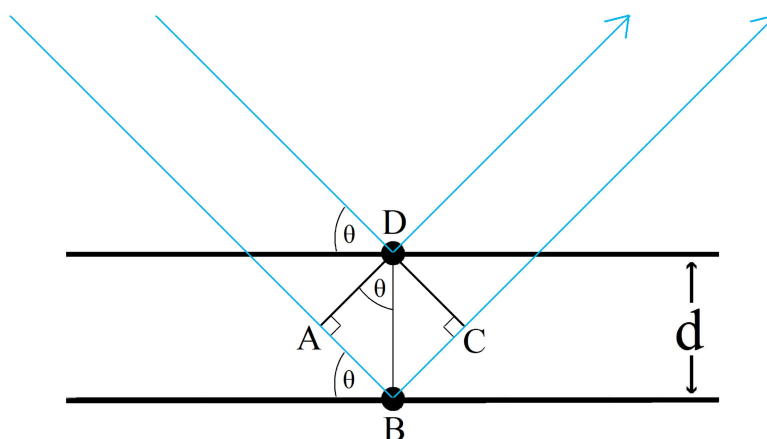


**Figure 2.2:** Incoming X-ray beams hitting different points on a lattice resulting in the diffraction of these.

### Powder X-ray Diffraction (PXRD)

A polycrystalline powder sample is a collection of an enormous amount of small crystallites all randomly coordinated in space<sup>42</sup>. This randomness ensures that the X-ray beam is diffracted in all directions allowed by equation 2.2. The result is the diffraction cones shown in figure 2.3<sup>43</sup>.

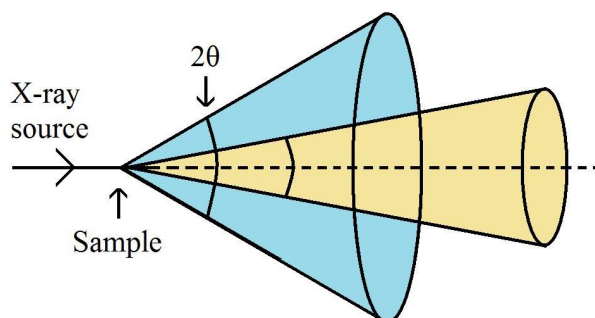


**Figure 2.3:** Diffraction cones arising from all reflections allowed by equation 2.2.

### Experimental setup for PXRD

The goal in powder X-ray diffraction is to obtain the  $2\theta$  values for the various diffraction cones, and the corresponding photon counts (intensity). A typical powder diffractometer has the X-ray source and detector moving around the sample along the circumference of a circle, as shown in figure 2.4. This cuts through the cones at the diffraction maxima and the result is a plot of intensity as a function of diffraction angle ( $2\theta$ ). The positions of the cones are dependent on properties such as cell parameters, crystal system, and X-ray wavelength. The intensity depends on the type of atoms present and their position<sup>42</sup>.

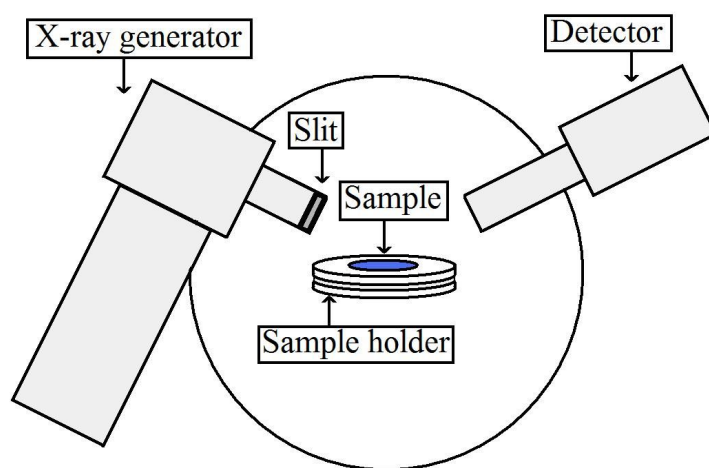


**Figure 2.4:** Schematic representation of a PXRD experiment. The displayed setup is with Bragg-Brentano geometry.

### The identification of materials

When a diffraction pattern is obtained for a sample synthesized in the laboratory, it can be identified by comparing the pattern with patterns of known materials. This can be done using a database (by the Joint Committee of Powder Diffraction Standards (JCPDS)) that suggests matches based on compiled data sets from inorganic, organometallic, and organic compounds<sup>44</sup>. Another method one can use (if one aims to synthesize a specific material from a published procedure) is to compare the experimental pattern with those found in publications. If single-crystal structure determination of the material (or compositional variants) have been published, it is possible to simulate a diffraction pattern for comparison.

An example of the second method is shown in figure 2.5, where the diffraction patterns of two synthesized samples are compared to a published pattern. In this case, sample 1 has the same number of peaks (and the correct positions) and is determined to be phase-pure. Sample 2 has some extra peaks and is not considered phase-pure, but a mixture of phases. If on the other hand a sample is missing peaks, this may be an indication that only part of the desired material has been obtained<sup>42</sup>. It is also possible, using more advanced analysis such as Rietveld refinement, to determine how much of each material is present (sample 2 in figure 2.5).

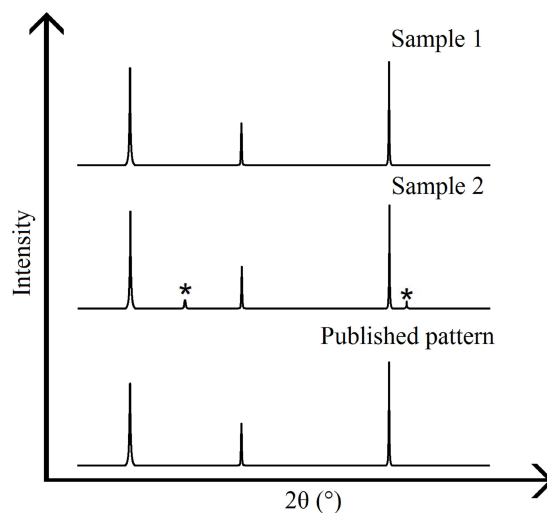


**Figure 2.5:** An illustration of a comparison of experimental and published diffraction patterns. The \* indicates peaks from an impurity.

### 2.1.3 Applications for this thesis

PXRD was used for phase identification of obtained products. Phase-purity was determined by comparison of sample patterns with patterns from publications or simulated patterns from single-crystal studies.

## 2.2 Inductively Coupled Plasma - Mass Spectrometry (ICP-MS)

### 2.2.1 Introduction

MeAPOs and SAPOs often display a range of properties not present in the neutral AlPOs. Inductively coupled plasma mass spectrometry, ICP-MS, is an analytical method for determining trace amounts of substances in known or unknown samples. The ICP-MS is able to detect substances in amounts as low as ppt (parts per trillion) and quantitative amounts at the ppm (parts per million) range<sup>45</sup>. The quantitative amounts of Me or Si found with ICP-MS can be correlated with material characteristics observed with other characterization methods.

### 2.2.2 Sample preparation

The samples to be analyzed by ICP-MS need to be liquid or liquefied by convenient methods. AlPOs are solids and must therefore be dissolved by the use of either *aqua regia*, or Hydrofluoric acid (HF). The dissolved species, which cannot exceed a concentration of 0.1%<sup>46</sup> are then fed into a pneumatic nebulizer and converted to a fine aerosol.

### 2.2.3 Plasma generation

The instrument's torch creates the inductively coupled plasma used to ionize the sample before mass analysis. A schematic representation of an ICP torch is shown in figure 2.6. The main part of the ICP torch consists of three tubes: the outer tube, the middle tube, and the sample injector<sup>46</sup>. The outer tubes' function is to house the two smaller tubes, and thus determines the size of the torch. The middle tubes' function is to introduce a void between it and the outer tube, in which the ICP gas (argon) can be introduced. The smallest tube, the sample injector, is used to introduce the sample aerosol into the plasma beam.

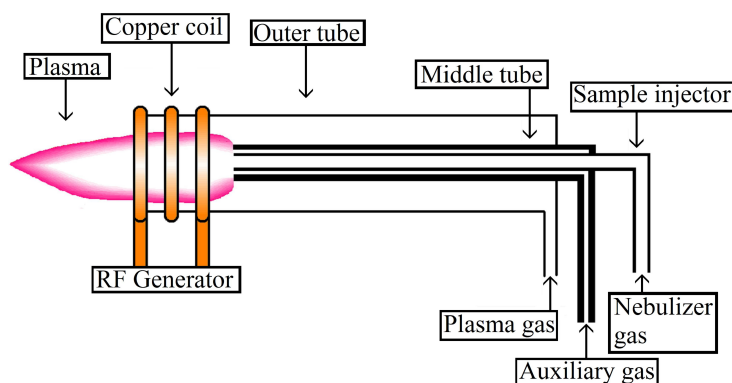
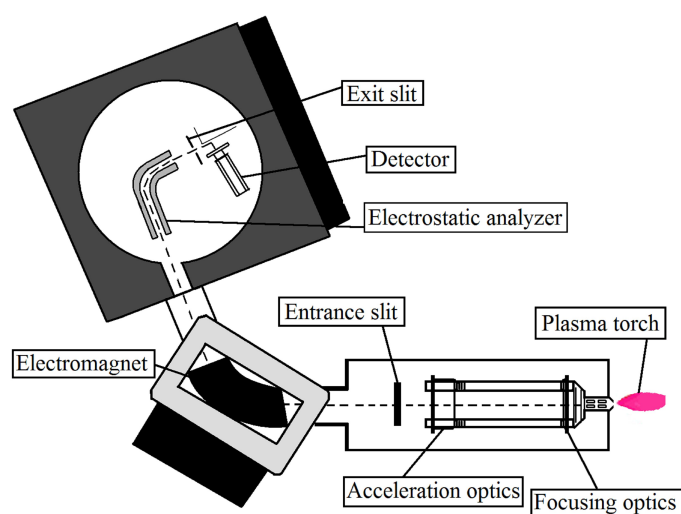


Figure 2.6: An Illustration showing the different parts of an ICP torch.

At the end of the tubes a RF (Radio Frequency) copper coil is mounted, supplying AC (Alternating current) and creating an intense induced magnetic field around the coil. To create the plasma the argon gas is introduced spirally into the void between the outer and middle tube, and a high-voltage spark is supplied to ionize some of the argon atoms<sup>47</sup>. The free electrons then get accelerated by the magnetic field and causes a chain reaction leading to ionization of more argon atoms. The result is an inductively coupled plasma consisting of argon atoms, argon ions, and electrons.

## 2.2.4 Double-focusing magnetic sector mass spectrometer

A schematic view of a double focusing magnetic sector MS is shown in figure 2.7. After the sample has been ionized in the ICP, the ions pass through entrance slits to an optics region where they are accelerated to a few kV<sup>48</sup>. From there, the ions are focused by an electromagnet that is dispersive with respect into both ion energy and ion mass (first focusing). Further down the ion path an electrostatic analyzer (ESA), which is only ion energy dispersive, focuses the ion energies to the exits slits and the detector (double focusing). By changing the electric field in the opposite direction of the magnetic field, the mass of interest is effectively “stopped” for analysis<sup>48</sup>.



**Figure 2.7:** A schematic illustration of a reverse Nier-Johnson double-focusing magnetic sector mass spectrometer.

## 2.2.5 Applications for this thesis

ICP-MS was used for determining the moles present of relevant elements (e.g. Si, Al, P, Cu) in synthesized samples.

## 2.3 Scanning Electron Microscopy (SEM)

### 2.3.1 Introduction

A scanning electron microscope, or SEM, can be used to investigate the surface of polycrystalline powders, more specifically the size and shape of the composite crystallites. SEM also gives some insight to the quality of the sample (i.e. if the crystallites are uniform, twinned, defected, etc).

### 2.3.2 Instrumentation

A schematic illustration of the main components in a SEM is shown in figure 2.8. An electron gun (tungsten or lanthanum hexaboride filaments<sup>49</sup>) mounted at the top of the SEM is used to accelerate electrons toward the sample through focusing lenses. This is done by the use of a potential difference of several kV<sup>50</sup>. The lenses focus the cloud of electrons and guides them downward to a set of scanning coils.

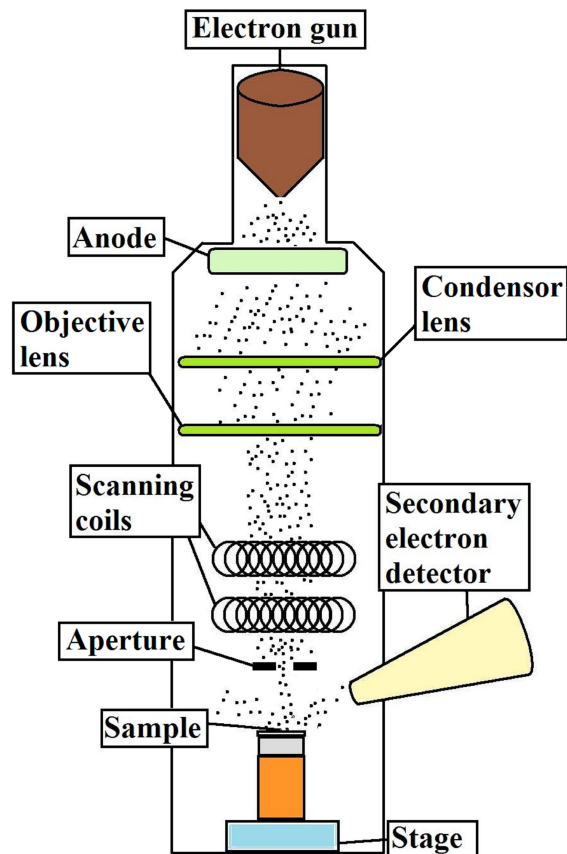


**Figure 2.8:** A schematic illustration of the main components in a SEM. The colors are for illustrative purposes and the black dots represent electrons.

By applying an adjustable current through the coils the focused electrons are manipulated to move/scan across the sample. An aperture is used to control the number of electrons that reach the sample, as well as position of the electron beam. A SEM also has a series of coils

surrounding the electron beam referred to as stigmator (not illustrated), which is used to correct for astigmatism<sup>51</sup>.

### 2.3.3 Theory

#### Electron-sample interactions

When the beam of electrons interacts with the sample several signals can be generated. The various signals that arise are: secondary electrons, backscattered electrons, X-rays, auger electrons, and visible light<sup>52</sup> (illustrated in figure 2.9). Out of these, the secondary electrons are of highest interest. There is also an induced current and phonons arising from electrons that do not participate in generating the aforementioned signals.

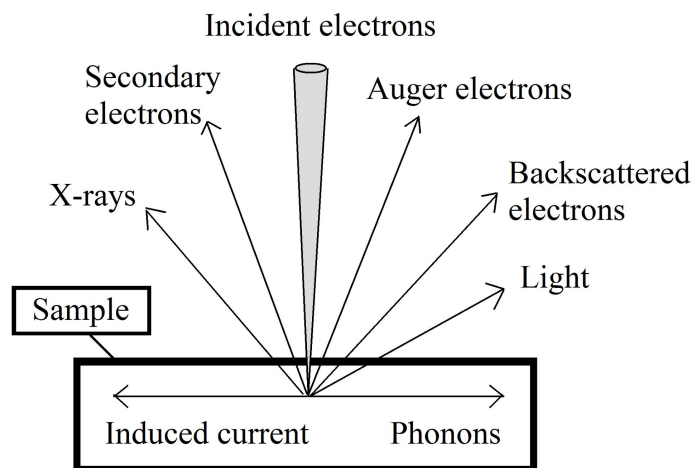


**Figure 2.9:** An illustration of the various signals generated in a SEM from electron-sample interactions.

#### Secondary electrons (SE)

The scattering of electrons by the sample can be either elastic or inelastic<sup>53</sup>. In the case of inelastic scattering, a variety of interactions between the incident electrons and the atoms and electrons of the sample occur. This interaction is accompanied by the transfer of a significant amount of energy to the sample, and causes an ionization of its corresponding atoms. The electrons leaving the sample's atoms during this ionization is referred to as secondary electrons (SE), and can be defined as electrons having energies less than 50 eV<sup>53</sup>. As a result of the low energies of the SE, these electrons provide surface topographical information since they can only escape from a region within a few nanometers of the material's surface<sup>54</sup>.

#### Image formation

The SEM image is the result of acquisition of the signals produced when the primary beam of electrons interact with the sample. The standard SE detector is the Everhart-Thornley<sup>55</sup>

detector, where a scintillator converts the electron signal into photons that are transferred via a light pipe, for then to be transferred back to an electric signal using a photomultiplier tube (PMT)<sup>55</sup>. Electron dense regions (sample) will appear as bright spots on the computer screen, areas of low electron density will appear darker.

### Magnification

The scanning electron microscope is a mapping device, meaning it generates a grid or matrix across the sample for which the electron beam moves across<sup>56</sup>. As a sample is irradiated with a beam of electrons, the radiations from the components of the sample is recorded and used to modulate a second beam of electrons scanned synchronously with the first beam across a computer display. If the area covered by the beam on the sample is  $S \times S$ , and the area covered by the beam on the computer display  $C \times C$ , then the magnification,  $M$ , is defined as<sup>56</sup>:

$$M = C/S \quad (2.3)$$

This is illustrated in figure 2.10.

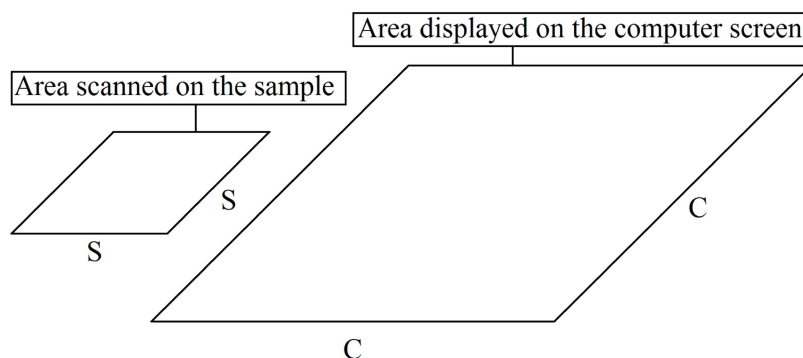


**Figure 2.10:** An illustration of the areas scanned on the sample and the area displayed on the computer display.

### Stigmatism

Lens defects and contaminants on the instruments aperture can cause a variation in the profile of the cross-section of the electron beam. This imperfection is referred to as astigmatism<sup>51</sup>. A SEM instrument with astigmatism correction will have a circular probe spot, and the beam cross section will be focused to the smallest point.

#### 2.3.4 Applications for this thesis

SEM was used to determine the size (or qualitative range of sizes) and shape of crystallites in synthesized samples. It was also used to study the effects of calcination on the individual crystallites.

## 2.4 Thermogravimetric Analysis (TGA) and Differential Scanning Calorimetry

### 2.4.1 Introduction

After a microporous solid is synthesized and identified, the template needs to be removed by heating the material to high temperatures. This process can be studied by thermogravimetry to ensure that all the template molecules are removed. By also applying calorimetry during the calcination, the energy changes in the sample can also be studied.

### 2.4.2 Instrumentation

A schematic illustration of a simultaneous TGA/DSC experimental setup is shown in figure 2.11. A sample ( $\approx 20$  mg) is placed in one of two crucibles (sample holders/containers) with the other one containing a refer

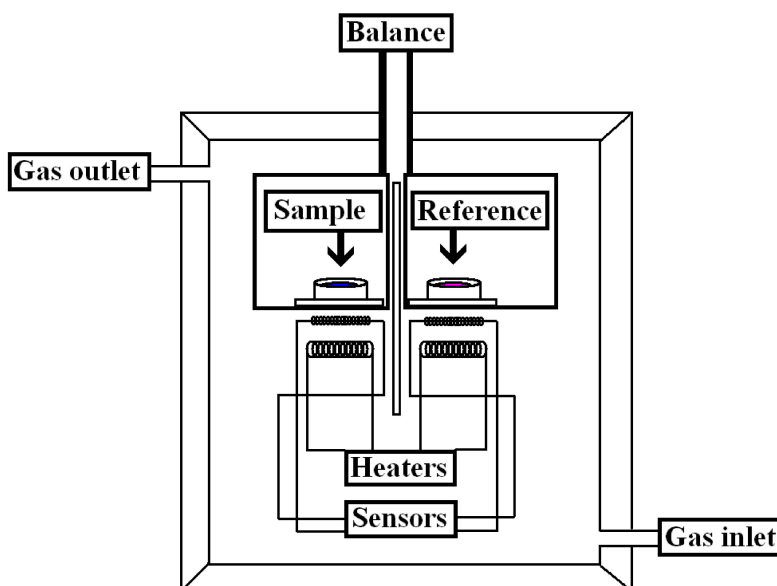


**Figure 2.11:** A schematic illustration of a simultaneous TGA/DSC experimental setup.

### 2.4.3 Theory

#### Thermal Gravimetry (TG)

When a sample is heated and thermal events occur, the instrument's balance may record a mass loss (in %) relative to the original mass of the sample. The result is a TG curve which is a plot of mass lost as a function of temperature or time<sup>57</sup>. An illustration of a TG curve is shown in figure 2.12. Based on the characteristics of the thermal event the TG curve changes accordingly.

In the event that no mass is lost the TG curve will “flatline”. A few examples of mass loss events are shown in figure 2.13.

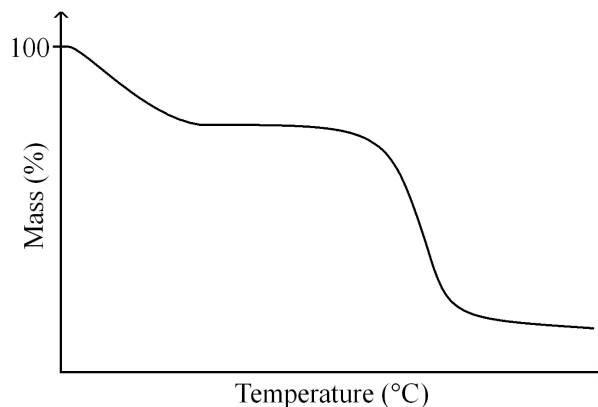


**Figure 2.12:** An illustration of a TG curve

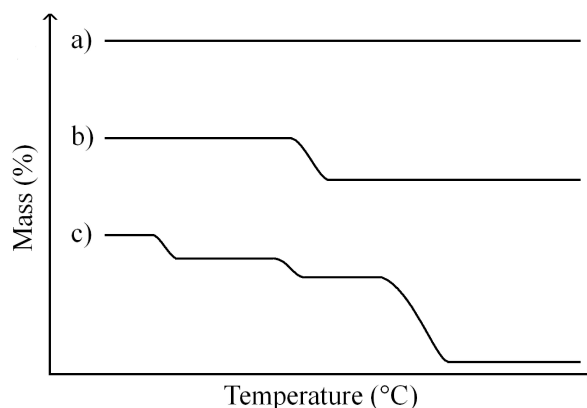


**Figure 2.13:** An illustration of the mass responses in a sample: a) no mass lost (flatline); b) a single mass lost; c) several masses lost.

### Differential Scanning Calorimetry (DSC)

By simultaneously measuring the energy difference between the sample and a reference, one can observe if the thermal events are endothermic (positive  $\Delta H$ ) or exothermic (negative  $\Delta H$ ). This helps in determining whether a decomposition- (endothermic) or combustion/oxidation (exothermic) takes place<sup>58</sup>. A DSC curve is a plot of specific effect (mW/mg) as a function of either temperature or time. An energy difference will show up on a DSC curve as either a valley (endothermic) or a hill (exothermic) (depending on the convention used). This is illustrated in figure 2.14. If one integrates a feature on the DSC curve with respect to time, the result is energy in joule, J ( $W = J/s$ ,  $W \cdot s = J$ ).

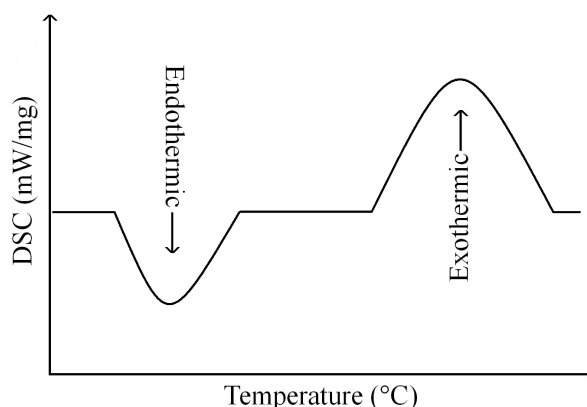


**Figure 2.14:** An illustration of a DSC curve showing the characteristics of an endothermic and exothermic thermal event.

### Thermal events during the calcination of AlPOs, MeAPOs, and SAPOs

During the synthesis of microporous Zeotypes the template used becomes trapped in the pores of the materials. The occluded template may be chemisorbed on acid sites (SAPOs and MeAPOs), physisorbed on the materials surfaces, or trapped in the materials channels or cavities<sup>59</sup>. This template needs to be removed to enable full utilization of the catalyst. To do this, samples are heated to temperatures which cause the organic molecules to become unstable and diffuse out of the crystal lattice.

**Dehydration** The first stage in calcination of such materials is usually dehydration<sup>60,61</sup>, which occurs in the temperature interval 25 to 150°C. This endothermic stage usually involves the removal of surface physisorbed water and template molecules.

**Decomposition/Removal of organic template** Decomposition of the organic amine usually occurs at higher temperatures than the dehydration cycle, and the temperature at which this occurs depends greatly on the template used in the synthesis of the material. It can involve the removal of the template in a single step, which is characteristic for AlPOs<sup>60,61,62</sup>. The presence of transition metals or silicon generally leads to the template being removed in two successive steps, the first one often encompassing a larger mass loss than the second<sup>63,62</sup>. This of course depends on their incorporation mechanisms, and only mechanisms involving the generation of an anionic lattice will exhibit such behavior. The consensus regarding this phenomenon is that the second step involves removal of template molecules balancing negatively charged lattice points<sup>61</sup>. Generalized TG curves for AlPOs and MeAPOs/SAPOs is illustrated in figure 2.15.

The endothermic decomposition itself is generally attributed a *Hofman* elimination reaction, where the organic amine (or ammonium salt) is broken down to olefins, ammonia, and water<sup>64,65,66</sup>.

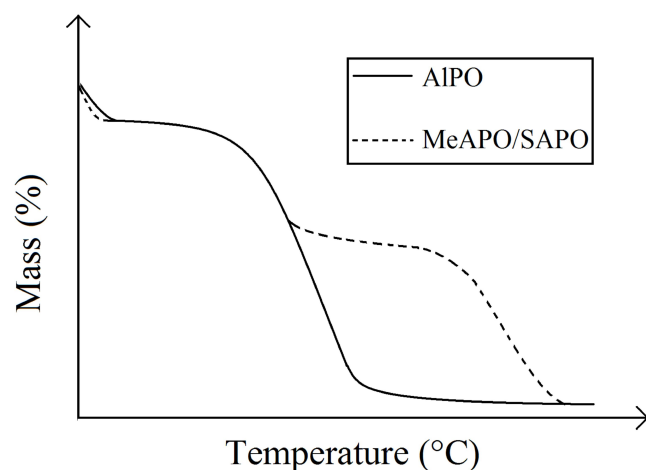


**Figure 2.15:** An illustration of generalized TG curves for AIPOs and MeAPOs/SAPOs.

### Determining if the template has been removed

Crystallographic files for AIPOs usually come with unit cell compositions. By calculating the percentage of organic template present in the unit cell one can obtain an estimate for mass loss involved in template removal<sup>60</sup>. This enables an evaluation of whether or not the template has been removed for a given calcination procedure.

### 2.4.4 Applications for this thesis

Simultaneous TGA/DSC experiments were used to study the template removal from the pores of various synthesized materials.

## 2.5 Surface Area Measurement (BET theory)

### 2.5.1 Introduction

A high surface area (measured in units of  $\text{m}^2/\text{g}$ ) for catalyst materials (such as MeAPOs and SAPOs) is an important characteristic, because it enables larger quantities of molecules to interact with active sites on the surface of the catalysts. A high surface area also enables the active sites to spread over a wider area, avoiding unwanted interactions between neighboring sites.

### 2.5.2 Theory

#### Porous materials and Surface area

A material need not be dense, but can have areas in which constituent atoms are packed less tightly, or areas where large groups of atoms are systematically absent (cavities). In such cases, one can refer to the material as having pores, or being porous. A pore is a cavity that is deeper than it is wide<sup>67</sup>. The size of such pores are categorized as being either micropores ( $d \text{ nm} < 2 \text{ nm}$ ,  $d = \text{diameter of pore}$ ), mesopores ( $2 < d < 50 \text{ nm}$ ), or macropores ( $d > 50 \text{ nm}$ )<sup>68</sup>.

Surface area is a measure of the exposed area of a particle (or particles) of a specific geometry. The specific surface area is the exposed surface area per gram of material. For cubic particles the surface area can be defined as<sup>69</sup>:

$$A = \frac{6}{\rho l} \quad (2.4)$$

where  $\rho$  is the density ( $\text{g}/\text{cm}^3$ ) and  $l$  is the length of the cube's edges. If a particle is of porous nature (i.e. has pores) it has a larger surface area than a similar sized particle that is non-porous. It is possible to distinguish between two types of surface area: internal and external<sup>70</sup>. Internal surface area is the area exposed due to pores (the area of pore walls), external surface area is the exposed area outside these pores.

#### Isotherms

An isotherm is the relationship between the amount of gas adsorbed and the pressure (or relative pressure) at a constant temperature<sup>71</sup>. There exists several such isotherms, a few examples being: Langmuir, Temkin, Freundlich, and the BET isotherm<sup>72</sup>. A graphical representation of the shapes of such isotherms (amount of gas adsorbed as a function of pressure) can be categorized into five (I to V) different types<sup>69</sup>. An illustration of the different types of isotherms is shown in figure 2.16. Isotherms IV and V exhibit a splitting of the curve representing the isotherm which is then combined at higher relative pressures. The lower of these two curves represent the adsorption of gas, the higher one represent the desorption of gas. Such a feature is referred to as a hysteresis loop and is a characteristic feature of mesopores<sup>73</sup>.

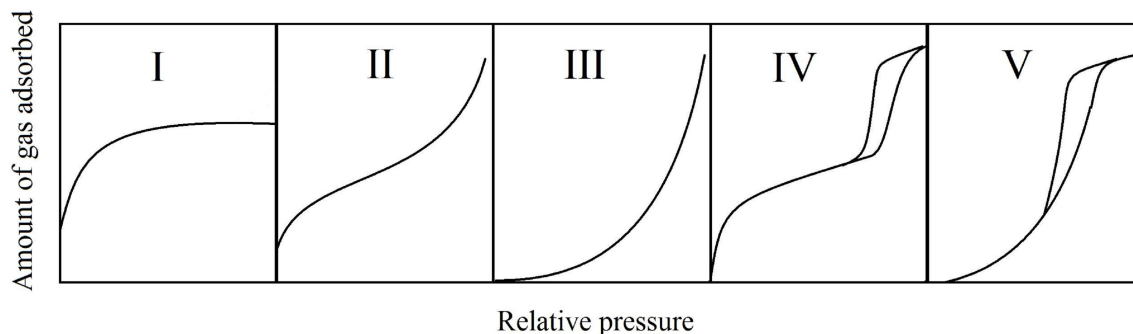


**Figure 2.16:** A schematic illustration of the five (I-V) different types of isotherms, represented here as plots of volume (of gas) adsorbed as a function of (gas) pressure of the adsorbing gas. The five different types of isotherms are numbered using roman numerals.

**The Langmuir isotherm** The Langmuir isotherm is a type I isotherm that describes the reversible process of adsorbing a single gas molecule on an active site on the surface of a catalyst<sup>74</sup>:



where  $A$  is a monoatomic gas molecule,  $*$  is an active site, and  $A^*$  is  $A$  adsorbed on the active site  $*$ . By defining  $A^*$  as the fraction of occupied sites (i.e. the coverage) and substituting it with the Greek letter  $\theta$ , it can be shown that the expression for the Langmuir isotherm is<sup>74</sup>:

$$\theta = \frac{KP_A}{1 + KP_A} \quad (2.6)$$

where  $K = k_1/k_{-1}$  and  $P_A$  is the partial pressure of  $A$ .

**The BET isotherm** In the BET theory (named by its inventors Brunauer, Emmet, and Teller) the surface area is treated as a matrix, with the adsorbed species occupying discrete positions. It is suggested that interaction between adsorbents only occur in the vertical direction, neglecting interaction between adsorbates in the horizontal direction (statistical-mechanical approach)<sup>75</sup> as illustrated in figure 2.17. The BET theory has its origin in the Langmuir isotherm, but instead of a unimolecular adsorption it is expanded to account for an infinite amount of adsorption layers<sup>76</sup>. The BET equation for an infinite amount of adsorption layers is as follows<sup>77</sup>:

$$\frac{p}{v(p_0 - p)} = \frac{1}{v_m c} + \frac{c - 1}{v_m c} \frac{p}{p_0} \quad (2.7)$$

where  $v$  is the total volume of gas adsorbed,  $v_m$  is the volume of gas required to form a complete unimolecular adsorption layer,  $c \approx e^{E_1 - E_L/RT}$ ,  $p$  is the pressure, and  $p_0$  is the saturation gas pressure. A plot of  $p/v(p_0 - p)$  vs.  $p/p_0$  gives a straight line with slope  $(c - 1)/v_m c$  and intercept  $1/v_m c$ . This enables the determination of  $v_m$  and  $c$  from the resulting system of linear equations. From the values of  $v_m$ , one can then calculate the total and specific surface area<sup>78</sup>:

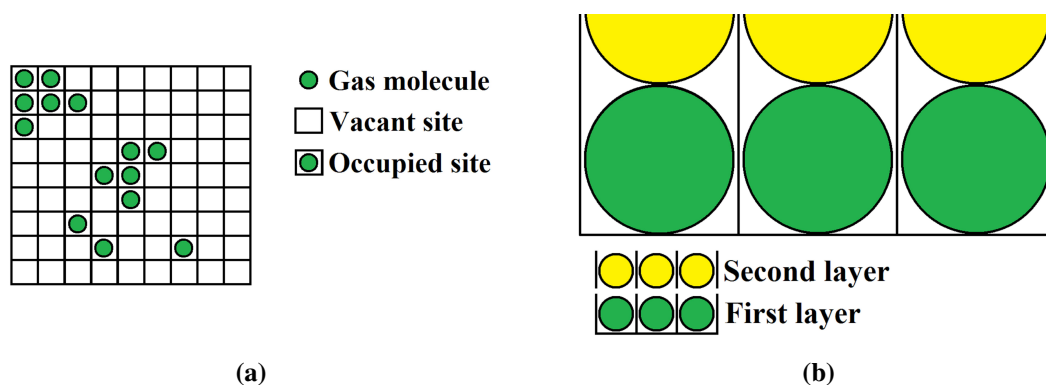


**Figure 2.17:** An illustration of the concept that active sites on the surface of a catalyst treated as a matrix: (a) the matrix of active sites; (b): a cross-section view showing the concept of vertical but not horizontal interaction between successive adsorbed layers of gas molecules (illustrated by the fact that the spheres are not touching horizontally neighboring spheres).

$$S_{BET,total} = \frac{v_m N s}{V} S_{BET} = \frac{S_{total}}{a} \quad (2.8)$$

where  $N$  is Avogadro's number,  $V$  is the molar volume of adsorbent gas,  $a$  is the molar weight of adsorbed species, and  $s$  is the adsorption cross section.

### 2.5.3 Application for this thesis

Surface measurement using BET theory was used for determining the BET surface area of various calcined samples.

## 2.6 X-ray Absorption Spectroscopy (XAS)

### 2.6.1 Introduction

X-ray Absorption Spectroscopy (XAS) can be used for probing the chemical environment of transition metals in MeAPOs. One of the advantages with XAS is that no long range order is required<sup>79</sup>, enabling the study of transition metal sites (local ordering) that can be independent of the crystal structure of the MeAPO that is being investigated.

### 2.6.2 Synchrotron radiation

Synchrotron radiation is non-thermal electromagnetic radiation which is generated by charged particles in a magnetic field<sup>80</sup>. The polarizing radiation is characterized by high brilliance and intensity, having frequencies ranging from infrared to hard X-rays<sup>81</sup>. It is generated in particle accelerators and storage rings for use with various characterization methods. The process involves accelerating electrons to nearly relativistic speeds and subjecting them to magnetic fields.

### 2.6.3 Theory

#### The XAS spectrum

In XAS spectroscopy incident X-rays from a synchrotron storage ring bombards a sample and the resulting transmitted or fluorescent intensity is measured. The absorption coefficient ( $\mu$ ) for a sample of thickness  $x$  for fluorescence mode can be expressed mathematically as<sup>82</sup>:

$$\mu_f x = \frac{I_f}{I_0} \quad (2.9)$$

where  $I_0$  is the incident intensity of the X-rays, and  $I_f$  is the intensity of the fluorescent flux. A schematic view of an XAS spectrum is shown in figure 2.18. The figure shows a plot of the absorption coefficient vs. the electron energy (in electron Volts, eV). There exists a discontinuity in the absorption coefficient arising when the energy of the incident photons equal the binding energy of electrons in the 1s orbital of the hypothetical element. Energies half-way up this continuity is referred to as the element's K-edge<sup>82</sup>.

**The X-ray Absorption Near-edge Structure (XANES)** The X-ray Absorption Near Edge Structure (XANES) region reaches from approximately 8 eV to around 40 eV after the edge<sup>82</sup>, and provides information about the elements valence state, its coordination number, and site symmetry. This information is obtained by comparing the sample to known model compounds containing the same elements as the sample one wants to investigate<sup>83</sup>.

---

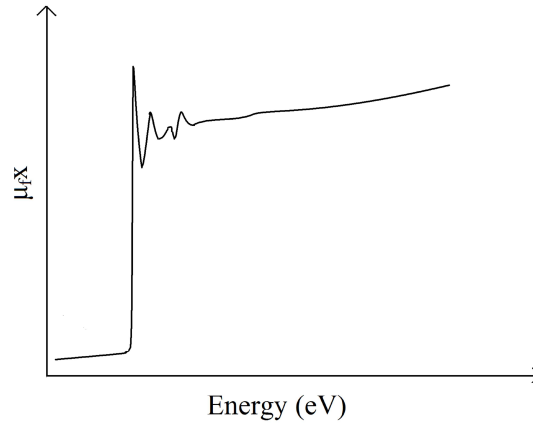


**Figure 2.18:** An illustration of an XAS spectrum showing a hypothetical element's K-edge.

**Extended X-ray Absorption Fine structure (EXAFS)** The Extended X-ray Absorption Fine Structure, or EXAFS, is the oscillating appearance of the absorption coefficient reaching from a few eV to a 1000 eV past the K-edge of the XAS spectrum in figure 2.18. This “fine structure” can be described mathematically by the  $k$ -weighted EXAFS equation<sup>82</sup>:

$$k^n \chi(k) = k^{n-1} \sum_j N_j / r_j^2 F_j(k) S_i(k) \exp(-2\sigma_j^2 k^2) \exp[-2r_j / \Lambda(k)] \sin[2kr_j + \phi_{ij}(k)] \quad (2.10)$$

where important symbols are:  $N_j$  - number of neighbors of type  $j$  (multiplicity),  $r_j$  - nearest neighbor distance between central atom ( $i$ ) and backscatterers in  $j$ th shell,  $2\sigma_j^2$  - Debye-Waller factor accounting for thermal and static disorder,  $S_i$  - amplitude reduction factor (AFAC),  $n$  - degree of weighting. The complicated nature of this equation makes analytical solutions impossible to obtain, but can be solved using *ab-initio* calculations.

#### 2.6.4 Applications for this thesis

XAS was used to investigate the oxidation state and the local chemical environment in two MeAPO samples.

## 2.7 Fourier Transform - Infrared (FT-IR) spectroscopy

### 2.7.1 Introduction

The world of molecules is a world of motion. Atoms on lattice positions in AlPOs, MeAPOs, and SAPOs, as well as molecules adsorbed in the channels and on their surfaces exhibit vibrational motion. FT-IR spectroscopy can be used to study these vibrations, and provides valuable information about microporous systems.

### 2.7.2 The Michelson interferometer and the Fourier Transform

A schematic representation of a Michelson interferometer is shown in figure 2.19. An incident beam with intensity  $I_0$  is split by a semitransparent mirror into two components with intensity  $I_1 = I_2 = I_0/2$  (idealized case). One component of the beam travels to a fixed mirror (Mirror 2 in figure 2.19), the other travels to a movable mirror (Mirror 1 in figure 2.19). The components then travel back to the semitransparent mirror and recombine into a new beam. The Michelson interferometer's function is to obtain the power density as a function of path length, which is called an interference pattern<sup>84</sup>. One then applies a mathematical operation known as a Fourier Transform to obtain the intensity as a function of wavenumber, which is the FT-IR spectrum.

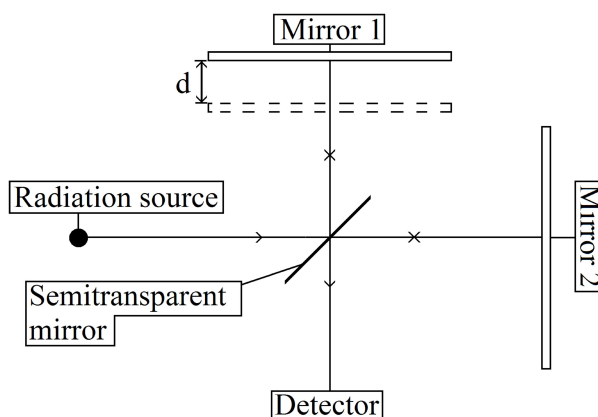


**Figure 2.19:** A schematic representation of a Michelson interferometer.

### 2.7.3 Theory

#### Infrared radiation

Electromagnetic radiation is radiation composed of an electric part and a magnetic part<sup>85</sup>. The electromagnetic spectrum is a continuum but has been divided into sections according to the wavelength and frequency of the radiation. These properties are related by the expression<sup>86</sup>:

$$c = \lambda f \quad (2.11)$$

where  $c$  is the speed of light ( $\approx 3 \times 10^8$  m/s), and  $\lambda$  and  $f$  is respectively the wavelength and frequency of the radiation. When working with IR spectroscopy it is common to report spectra as functions of wavenumber,  $\tilde{\nu}$ , in units of reciprocal centimeters ( $\text{cm}^{-1}$ ):

$$\tilde{\nu} = \frac{1}{\lambda} = \frac{f}{c} \quad (2.12)$$

Spectra from 4000 to 400  $\text{cm}^{-1}$  is referred to as the mid-infrared region<sup>87</sup>.

### Normal modes of vibration

Molecules can be modeled as masses joined by bonds with spring-like properties<sup>88</sup>. The masses can undergo several types of movement, namely: translational, rotational, and vibrational. Movement of these types are referred to as a molecule's degrees of freedom; there are  $3N$  degrees of freedom for a molecule of  $N$  atoms. A linear molecule has  $3N-5$  vibrational degrees of freedom, a non-linear molecule has  $3N-6$  vibrational degrees of freedom<sup>89</sup>.

#### 2.7.4 The gross selection rule

The gross selection rule for vibrational transitions is that the transition must invoke a change in the molecule's electric dipole moment<sup>90</sup>. Thus, homonuclear diatomic molecules that have no net electric dipole moment show no vibrational spectra. Heteronuclear diatomic molecules, however, has a net electric dipole moment that varies with extension of the molecular bond, and thus show vibrational spectra. An illustration of a homonuclear and a heteronuclear diatomic molecule is given in figure 2.20.

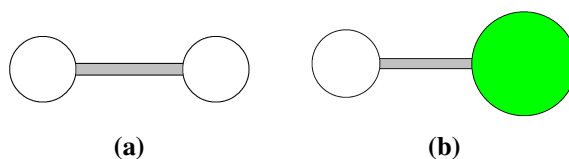


**Figure 2.20:** An illustration of: a)  $\text{H}_2$  - A homonuclear diatomic molecule; b)  $\text{HCl}$  - A heteronuclear diatomic molecule. The spheres represent the atoms (hydrogen atoms are white, the chlorine atom is green), the gray lines between them represent the molecular bonds.

### The energy of vibrational transitions

IR spectra are a result of transitions between quantized vibrational states<sup>91</sup>. Each normal mode involves a displacement of the atoms from their equilibrium positions. The variation of the potential energy as a function of displacement is best described using the Morse-type potential function illustrated in figure 2.21. The energy levels for a diatomic molecule are given by the

equation<sup>90</sup>:

$$V_{iv} = hv_i \left( v_i + \frac{1}{2} \right) + hv_i x_i \left( v_i + \frac{1}{2} \right)^2 \quad (2.13)$$

where  $h$  is Planck's constant,  $v_i$  is the fundamental frequency (encompassing force constants and reduced masses),  $v_i$  is the vibrational quantum number (can take the values: 0,1,2,...), and  $x_i$  is the anharmonicity constant. The anharmonicity constant only becomes significant for large  $v_i$  and the zero point energy is  $(v_i = 0) 1/2hv_0$ .

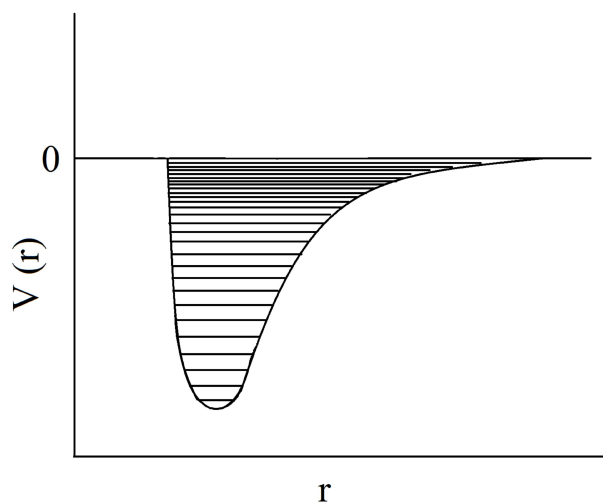


**Figure 2.21:** An illustration of the potential energy of a diatomic molecule as a function of atomic displacement during a vibration (anharmonic oscillator).

### Overtones, and combination bands

A result of the anharmonicity of molecular vibrations is that transitions involving multiples and sums of the fundamental frequency are infrared active<sup>90</sup>:

$$\Delta v_i = \pm 1, \pm 2, \dots \quad (2.14)$$

and

$$\Delta v_i = 1; \Delta v_j = 1 \quad (2.15)$$

Equation 2.14 represents overtones and equation 2.15 represents combination bands.

### Degeneracy

Linear B-A-B molecules have four normal modes, two bending and three stretching modes<sup>89</sup>. Figure 2.22 illustrates the three normal modes of the linear B-A-B molecule CO<sub>2</sub>. The symmetric stretching involves simultaneous movement of the two oxygen atoms and does not involve a change in the molecule's dipole moment (IR inactive). The other stretching mode, as well as the two bending modes, cause a change in the dipole moment and IR interactions occur.

The two bending modes have the same frequency and is said to be degenerate. Thus, only two absorptions are observed in the spectrum of CO<sub>2</sub>.

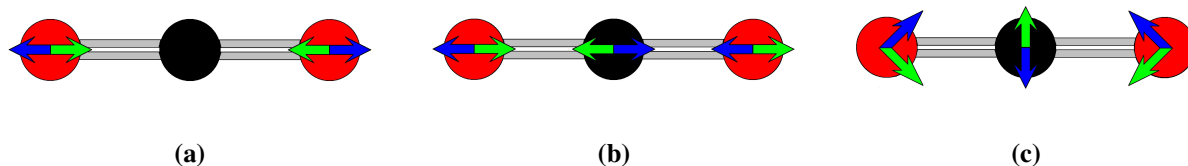


**Figure 2.22:** An illustration of the normal modes of CO<sub>2</sub>: a) symmetric stretching; b) asymmetric stretching; c) symmetric bending: one of the two bending modes (in the other one the molecules bend out of the paper plane). Red spheres represent oxygen atoms, black spheres represent carbon atoms. The color coded arrows indicate motion; arrows with the same color indicate synchronous movement.

### IR spectra of Zeolites and Zeotypes

**Silicon incorporation in SAPOs** FT-IR provides an easy way of evaluating the local siting of Si in the framework of SAPOs. Incorporation of Si can be narrowed down to three substitution mechanisms<sup>92</sup>: i) Si substitution for Al; ii) Si substitution for P; iii) simultaneous substitution of two Si for one Al and one P. The resulting framework site charges resulting from these three possible incorporation mechanisms are respectively, +1 (cationic), -1 (anionic), and 0 (neutral). To retain a neutral lattice site in case i) and ii), charge balancing ions are required. In the case of a cationic lattice, OH<sup>-</sup> act as charge balancers, giving rise to Si-OH (or silanol) groups. In the case of an anionic lattice, an H<sup>+</sup> ion balances the charge which results in an Si-OH-Al linkage. The presence of such charge balancing species affects the infrared spectrum of SAPOs, and each group can be identified by distinctive absorptions occurring at characteristic frequencies. The Si-OH group is characterized by a stretching vibration occurring near 3747 and 3700 cm<sup>-1</sup>, and is attributed to internal and external Si defects<sup>59,93,94,95,96</sup>. Absorptions near 3600 cm<sup>-1</sup> are attributed the stretching vibration of bridging hydroxyls, Si-OH-Al linkages, that constitute the Brönsted acid sites<sup>59,95,97,98,99</sup>. Additional absorptions are observed due to P-OH and Al-OH stretching vibrations arising from end-groups and defect sites involving P and Al. The P-OH absorptions are normally observed<sup>59,96,95,97</sup> near 3670 cm<sup>-1</sup>, and the Al-OH absorptions are observed<sup>94,93,95</sup> in the range 3800 to 3760 cm<sup>-1</sup>.

### 2.7.5 Applications for this thesis

FT-IR was used to confirm Si substitution for P in the framework of synthesized materials.

## 2.8 Gas Chromatography - Mass spectrometry (GC-MS)

### 2.8.1 Introduction

GC-MS provides an effective means of analyzing the products from a catalytic process. By applying GC-MS to the effluents exiting the reactor, one can qualitatively and quantitatively (with a bit more processing) assess the catalyst's performance.

### 2.8.2 Gas chromatography

Chromatography is the physical process of separation in which the components are distributed between two phases, one of which is stationary while the other moves in a definite direction<sup>100</sup>. In gas chromatography the mixture to be analyzed is diluted by a gas (the mobile phase) and introduced into a column filled with a liquid or polymer (the stationary phase)<sup>101</sup>. The flow of the mobile phase causes the mixture to move through the stationary phase in a chromatographic column, and the components partition between the two phases. The time needed for the components to move through the column depends on their individual distribution between the mobile phase and the stationary phase. Components that have a higher distribution in the gas phase will move more quickly through the column and vice versa. Therefore, as the mixture is moved through the column, its individual components can be separated on the basis of the time needed for them to exit the column. More specifically, components are separated on the basis of their retention times: the time elapsed from injection of the sample component to the recording of the peak maximum<sup>102</sup>.

### 2.8.3 Flame Ionization Detector (FID)

A common detector used in GC is the flame ionization detector (FID)<sup>103</sup>. The column effluent is introduced into a stream of hydrogen and led to a flame where the molecules are ionized. The ions and electrons are then accelerated by a potential difference between the flame and a surrounding cylindrical electrode. The resulting flow of current is monitored and amplified. Linking the detector response with the retention times yields the chromatogram: A plot of abundance (or detector response, or amount) vs. retention times, and each peak ideally corresponds to one eluted fraction of the mixture (see figure 2.23).

### 2.8.4 Gas Chromatography - Mass Spectrometry (GC-MS)

Even though the GC readily separates the components of a mixture, identifying these components is not so straightforward<sup>104</sup>. This is where combining a GC and a mass spectrometer (MS) becomes handy, and this coupling of analytical techniques enables identification of the individual components on the basis of their mass spectra. Instead of interpreting the mass spectrum

---

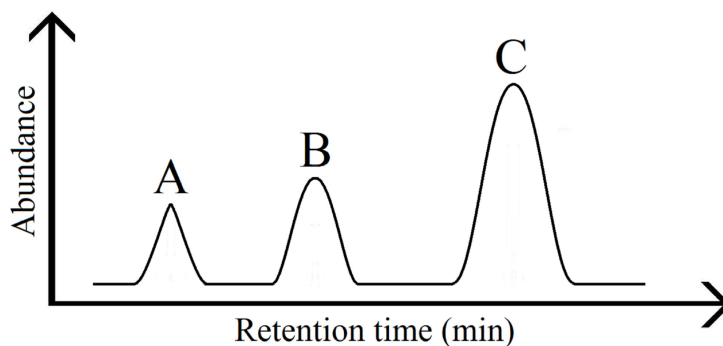


**Figure 2.23:** An illustration of a chromatogram showing the retention times and abundances for a mixture's components A, B, and C.

of a mixture, the GS is first used to separate the individual components, then MS is sequentially applied to the individual components. In this way, one obtains mass spectra for all the components, making possible the identification of these<sup>105</sup>.

### 2.8.5 Applications for this thesis

GC-MS was used to analyze reactor effluents during the catalytic testing of AlPOs and SAPOs, and to qualitatively assess a catalyst's performance based on these results.



# Chapter 3

## Experimental

### 3.1 Synthesis procedures

*All products made by the following preparations were obtained by crystallization under static conditions (i.e. by using autoclaves without stirring).*

#### 3.1.1 First generation (F) compositions

##### **ipaAlPO<sub>4</sub>-14F**

The isopropylamine template version of AlPO<sub>4</sub>-14F (ipaAlPO<sub>4</sub>-14F) was synthesized by a preparation given in U.S. patent 4,310,440 by Wilson et al.<sup>6</sup>(Example 40):

A mixture of 9.22 grams of orthophosphoric acid (85 wt% H<sub>3</sub>PO<sub>4</sub>, 15 wt% H<sub>2</sub>O, Merck Eurolab AS), 23.71 grams of distilled water, and 5.68 grams of Catapal B alumina (71.9 wt% Al<sub>2</sub>O<sub>3</sub>, 28.1 wt% H<sub>2</sub>O, boehmite, SASOL North America Inc.) was stirred until homogeneous. Then 2.38 grams of isopropylamine (99 wt% C<sub>3</sub>H<sub>9</sub>N, 1wt% H<sub>2</sub>O, Aldrich) was added and the mixture was again stirred to homogeneous. The resulting molar oxide ratio of the gel was: 1.00R:Al<sub>2</sub>O<sub>3</sub>:P<sub>2</sub>O<sub>5</sub>:40.00H<sub>2</sub>O (R = isopropylamine). A method for rewriting moles of H<sub>3</sub>PO<sub>4</sub> to moles of P<sub>2</sub>O<sub>5</sub> and H<sub>2</sub>O is given in Appendix B.1.1. The gel was transferred to a 45 mL Teflon lined pressure vessel, placed in an oven preheated to 200°C, and left for 24 h. The product was recovered by centrifugation and dried in an oven at 110°C for 12h.

##### **tbaAlPO<sub>4</sub>-14F**

The tert-butylamine template version of AlPO<sub>4</sub>-14F (tbaAlPO<sub>4</sub>-14) was synthesized by another preparation given in U.S. patent 4,310,440 by Wilson et al.<sup>6</sup>(Example 39):

A mixture of 11.53 grams of orthophosphoric acid (85 wt% H<sub>3</sub>PO<sub>4</sub>, 15 wt% H<sub>2</sub>O, Merck

Eurolab AS), 19.66 grams of distilled water, and 7.09 grams of Catapal B alumina (71.9 wt%  $\text{Al}_2\text{O}_3$ , 28.1 wt%  $\text{H}_2\text{O}$ , SASOL North America Inc.) was stirred until homogeneous. Then 3.73 grams of tert-butylamine (98 wt%  $\text{C}_4\text{H}_{11}\text{N}$ , 2wt%  $\text{H}_2\text{O}$ , Aldrich) and 9.88 grams of water was added and the mixture was again stirred to homogeneous. The resulting molar oxide ratio of the gel was: 1.00R:  $\text{Al}_2\text{O}_3$ : $\text{P}_2\text{O}_5$ :40.00 $\text{H}_2\text{O}$  (R = tert-butylamine). The gel was transferred to a 45 mL Teflon lined pressure vessel, placed in an oven preheated to 150°C, and left for 96 h. The product was recovered by centrifugation and dried in an oven at 110°C for 12h.

### ipaCuAPO<sub>4</sub>-14F

CuAPO-14F was synthesized by crystallization of  $\text{AlPO}_4$ -14F gels containing copper acetate ( $\approx 100$  wt%  $\text{Cu}(\text{OAc})_2 \cdot \text{H}_2\text{O}$ , Merck's reagenzien), and having the molar oxide ratios given in table 3.1 (R = isopropylamine). The reactants were added in the following order: water, phosphoric acid, copper acetate, alumina, and isopropylamine.

**Table 3.1:** Synthesis parameters for all ipaCuAPO<sub>4</sub>-14F compositions (Cryst. = Crystallization).

Sample	R	$\text{Al}_2\text{O}_3$	$\text{Cu}(\text{OAc})_2$	$\text{P}_2\text{O}_5$	$\text{H}_2\text{O}$	Cryst. Time (days)	T (°C)
ipa0.01CuAPO <sub>4</sub> -14F	1	0.99	0.02	1	40	1	150
ipa0.03CuAPO <sub>4</sub> -14F	1	0.97	0.06	1	40	3	150
ipa0.08CuAPO <sub>4</sub> -14F	1	0.92	0.16	1	40	8	150

### tbaSAPO<sub>4</sub>-14F

tbaSAPO<sub>4</sub>-14F was synthesized by hydrothermal treatment of  $\text{AlPO}_4$ -14F gels containing silica (40 wt%  $\text{SiO}_2$ , 60 wt%  $\text{H}_2\text{O}$ , Aldrich), and having the molar oxide ratios given in table 3.2 (R = tert-butylamine). The reactants were added in the following order: water, phosphoric acid, alumina, tert-butylamine, and silica.

**Table 3.2:** Synthesis parameters for all tbaSAPO<sub>4</sub>-14F compositions. \*50 mg of tbaAlPO<sub>4</sub>-14F was added to the synthesis gel (Cryst. = Crystallization).

Sample	R	$\text{Al}_2\text{O}_3$	$\text{P}_2\text{O}_5$	$\text{SiO}_2$	$\text{H}_2\text{O}$	Cryst. Time (days)	T (°C)
tba0.06SAPO-14F	1	1	0.94	0.12	40	6	200
tba0.08SAPO-14F*	1	1	0.92	0.16	40	1	200
tba0.20SAPO-14F*	1	1	0.80	0.40	40	1	200

### 3.1.2 Various preparations for AlPOs and SAPOs in alkaline mixtures discovered in this thesis work

In the following preparations the sources for elements are as follows: (Al) Catapal B alumina (71.8 wt%  $\text{Al}_2\text{O}_3$ , 28.2 wt%  $\text{H}_2\text{O}$ , Sasol North America), (P) orthophosphoric acid (85 wt%  $\text{H}_3\text{PO}_4$ , 25 wt%  $\text{H}_2\text{O}$ , Merck Eurolab AS), (Si) Ludox AS-40 (40 wt%  $\text{SiO}_2$ , 60 wt%  $\text{H}_2\text{O}$ , Aldrich), and templates of 98 and 99 wt% purity. The gels were placed in Teflon lined autoclaves and crystallized according to the parameters stated.

#### ipaAlPO<sub>4</sub>-14A

The phase ipaAlPO<sub>4</sub>-14A was synthesized by crystallizing a gel with molar oxide ratio: 4.36R:Al<sub>2</sub>O<sub>3</sub>:P<sub>2</sub>O<sub>5</sub>:40H<sub>2</sub>O for 24 h at 200°C. The reactants were added in the following order: water, alumina, phosphoric acid, and isopropylamine. The initial pH of the synthesis gel was 10, and changed to 11 upon crystallization.

#### ipaSAPO<sub>4</sub>-43

The phase ipaSAPO<sub>4</sub>-43 was synthesized by crystallizing a gel with molar oxide ratio: 4.36R:0.80Al<sub>2</sub>O<sub>3</sub>:P<sub>2</sub>O<sub>5</sub>:0.40SiO<sub>2</sub>:40H<sub>2</sub>O for 24 h at 200°C. The reactants were added in the following order: water, alumina, silica, phosphoric acid, and isopropylamine. The initial pH of the synthesis gel was 9, and changed to 11 upon crystallization.

#### AlPOs and SAPOs synthesized using only two molar oxide ratios

During the thesis work it was found that gels with the following two molar oxide ratios:

- xR:Al<sub>2</sub>O<sub>3</sub>:P<sub>2</sub>O<sub>5</sub>:40H<sub>2</sub>O (Preparation 1)
- xR:0.80Al<sub>2</sub>O<sub>3</sub>:P<sub>2</sub>O<sub>5</sub>:0.40SiO<sub>2</sub>:40H<sub>2</sub>O (Preparation 2)

crystallized at 200°C for y h, were found to work with other templates than isopropylamine. Table 3.3 summarizes the synthesis parameters and products obtained.

#### dpaipaSAPO<sub>4</sub>-43

A dual template approach was used to synthesize a SAPO<sub>4</sub>-43 sample comprising crystallites with maximum size 10 μm. The sample was obtained from a mixture with molar oxide ratio: 3R1:0.2R2:0.80Al<sub>2</sub>O<sub>3</sub>:P<sub>2</sub>O<sub>5</sub>:0.40SiO<sub>2</sub>:40H<sub>2</sub>O (R1 = di-n-propylamine, R2 = isopropylamine), crystallized at 200°C for 24 h. The reactants were added in the following order: water, alumina, phosphoric acid, di-n-propylamine, and isopropylamine. The initial pH of the synthesis gel was 10, and did not change during crystallization.

**Table 3.3:** Synthesis parameters for AlPOs and SAPOs made with preparation 1 and 2. \*100 mg of ipaAlPO<sub>4</sub>-14A was added to the synthesis gel.

Template	Preparation	x	y (h)	Product
Piperidine	1	2.92	72	Augelite
Piperidine	2	3	72	SAPO <sub>4</sub> -20
di-n-propylamine	1	4.36	72	AlPO <sub>4</sub> -11
di-n-propylamine	2	4.36	72	SAPO <sub>4</sub> -43
diisopropylamine	1	4-36	72	AlPO <sub>4</sub> -11
diisopropylamine	2	4.36	24	SAPO <sub>4</sub> -34
triethylamine*	1	10	24	AlPO <sub>4</sub> -5
triethylamine	2	10	48	SAPO <sub>4</sub> -18
methylamine	1	4.36	24	Unidentified phase

## 3.2 Calcination procedures

Several different calcination procedures were employed in the thesis work due to the different nature of the samples synthesized.

The first procedure was adapted from work done on CuAPO<sub>4</sub>-5 by Mathisen et al.<sup>106</sup>, and consisted of heating the as-synthesized materials from 25 to 550°C at a rate of 1°C/min. The samples were then kept at this temperature for approximately 17 hours before being cooled down to room temperature. This procedure was used for all CuAPO<sub>4</sub>-14F samples, but was also modified in terms of not letting the samples cool down after heating.

It was discovered that due to rehydration of the crystal lattice upon cooling the calcined samples, diffraction patterns were inconsistent with those presented by Wilson et al.<sup>6</sup> (as shown by the PXRD results in chapter 4). The second procedure had its origin due to several reports<sup>107,29,35,108,6</sup> of AlPO<sub>4</sub>-14 being calcined at 600°C for 2 to 3 h, without any mention of what heating rate had been used. The article on water-framework interactions by Yang et al.<sup>35</sup> showed how the diffraction pattern for calcined rehydrated AlPO<sub>4</sub>-14 differed from that of the calcined dehydrated material. Based on this, and the lack of reported heating rates, a preheated oven procedure was developed. This procedure consisted of preheating the oven to 600°C and then placing room-tempered as-synthesized materials in the oven for a period of 3 h. The samples were then removed at elevated temperatures to minimize rehydration. The preheated oven procedure was hard to reconstruct using a TGA/DSC instrument, but the validity of the method was reflected in the increased surface area (measured by BET) of samples compared to those using the method of Mathisen et al.<sup>106</sup>

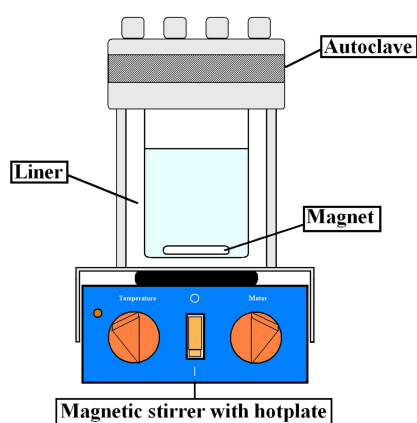
As shown by TGA/DSC experiments, the SAPO<sub>4</sub>-14F (see Results and Discussion in chapter 4) samples exhibited thermal behavior beyond 550°C (up to 1000°C), and a third calcination procedure was therefore developed. This procedure consisted of heating the as-synthesized materials to 1000°C at a rate of 5°C/min, and then dwelling for 3 h. The samples were exposed to

the high temperatures to ensure that all thermal events (or the ones occur

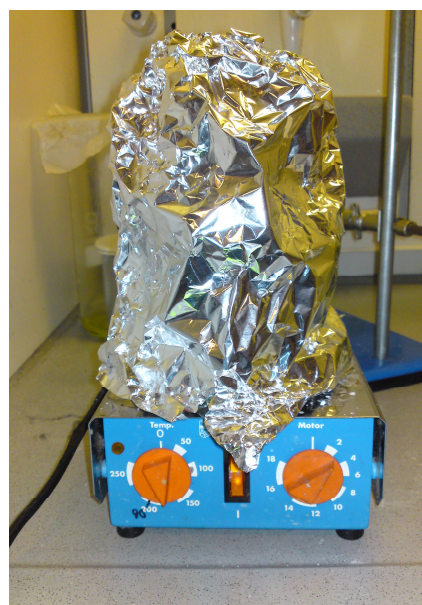
The  $\text{pipAlPO}_4\text{-14F}$  sample was calcined using the TGA program presented by Zibrowius et al.<sup>34</sup> It consisted of heating the material to  $800^\circ\text{C}$  at a rate of  $5^\circ\text{C}/\text{min}$ . Since no isothermal step was reported for the TGA experiment, the sample was kept at  $800^\circ\text{C}$  for 10 h.

### 3.3 Improvised stirred autoclaves

Since factory built stirred autoclaves were not available at the lab, and the effect of stirring during crystallization was deemed an important aspect of investigation, improvised stirring was achieved by utilizing magnetic stirrers with hotplates. To stir the contents of the autoclave during crystallization, a magnet of appropriate size and shape was placed inside the Teflon liner. The autoclaves were then filled with the reaction mixture, and placed on the magnetic stirrer device. The core temperature of the autoclaves were measured, and was found to be stable within  $\pm 1^\circ\text{C}/10\text{min}$ , with the temperature overshooting more than undershooting. An illustration of the magnetic stirrer and autoclave is given in figure 3.1a. An image taken of the actual experiment is given in figure 3.1b (the autoclave has been insulated with aluminum foil to reduce radiant heat loss).



(a)



(b)

**Figure 3.1:** Improvised stirred autoclaves: (a) an illustration made in Microsoft paint; (b) an image of an actual experiment using the improvised stirred autoclave.

## **3.4 Equipment used in the thesis work**

### **3.4.1 PXRD**

The PXRD patterns were obtained on a Bruker AXS D8 FOCUS diffractometer with a Bragg-Brentano geometry using Cu  $K_{\alpha}$  radiation. The scan-range was from 5 to 50 degrees  $2\theta$ , the step-size was  $0.02^{\circ}$ , and a 0.2 mm manual slit size was selected (unless otherwise noted).

### **3.4.2 SEM**

The SEM images was obtained on a Hitachi S-3400N Scanning electron microscope, with a electron voltage ranging from 2-15 kV and a working distance ranging from 5-20 mm. Prior to analysis, samples were either dispersed on metal stubs using ethanol, or adhered on metal stubs using carbon tape.

### **3.4.3 TGA**

The TGA/DSC curves were obtained on a Netzsch STA-449C TG/DSC instrument. The parameter file was set to ramp from 25-550°C, and then isothermal heating for 12 h. The ramp rate was set at  $2^{\circ}\text{C}/\text{min}$  and the gas flow was set to 80mL/min air with 20 mL/min Argon as protective gas.

### **3.4.4 BET**

The surface area data was obtained on a Tristar 3000 instrument with isotherms recorded from on samples cooled to  $-196^{\circ}\text{C}$  with liquid  $\text{N}_2$ . All samples were degassed at  $250^{\circ}\text{C}$  and 100 mTorr for 24 h prior to analysis.

### **3.4.5 ICP-MS**

The elemental analysis were performed on the HR-ICP-MS instrument Element 2. Prior to analysis the samples (14 mg) were dissolved in a mixture of HCl and  $\text{HNO}_3$  in a volumetric ratio of 3:1 (aqua regia).

### **3.4.6 XAS**

The XAS spectra were obtained in fluorescence mode at beam line BM01 at the European Synchrotron Radiation Facility (ESRF) in Grenoble France. The K-edge of copper containing samples were studied from 8920 to 9750 eV.

---

### **3.4.7 FT-IR**

The FT-IR spectra was obtained in a commercially available in-situ cell mounted in a Vertex 80 FT-IR instrument, in the range 4000-400  $\text{cm}^{-1}$  and a resolution of 4  $\text{cm}^{-1}$ . Samples were pressed into self-supporting wafers, mounted in the cell, and dehydrated prior to scans.

### **3.4.8 GC-MS**

Reactor effluents were analyzed on-line using a 7890A GC system in conjunction with a 5975C MSD, both from Agilent Technologies.

---



# Chapter 4

## Results and Discussion

### 4.1 PXRD

#### 4.1.1 ipaAlPO<sub>4</sub>-14F

##### as-synthesized

AlPO<sub>4</sub>-14 was first tried synthesized using a preparation by Wilson et al.<sup>6</sup> found in U.S. patent 4,310,440. The preparation involved crystallizing an aluminophosphate gel with molar oxide ratio: 1R:Al<sub>2</sub>O<sub>3</sub>:P<sub>2</sub>O<sub>5</sub>:40H<sub>2</sub>O (R = isopropylamine) at 200°C for 24 h. The pH of the gel was 3.5 and changed to 10 upon crystallization (mother liquor). The preparation was used early in the thesis work, before realizing its flaw that leads to the co-crystallization of AlPO<sub>4</sub>-14A and AlPO<sub>4</sub>-15. The flaw was pointed out by J.J. Pluth and J.V. Smith<sup>30</sup> in an article concerned with elucidating the structure of AlPO<sub>4</sub>-14A. All samples obtained using the flawed preparation by Wilson et al.<sup>6</sup> (including modifications of this) are labeled with an F (“First generation” or “Flawed”), to indicate that several phases are present. All as-synthesized samples in this thesis are labeled with an acronym representing the template used. Figure 4.1 shows the diffraction pattern obtained for ipaAlPO<sub>4</sub>-14F. The 2θ values for the peaks were compared to tabulated values supplied by Wilson et al.<sup>6</sup> for tbaAlPO<sub>4</sub>-14F (sample synthesized using tert-butylamine, tba, as template). The 2θ values showed great consistency and the sample was determined to be phase-pure. Due to the flaw in the preparation leading to unwanted by-products, a new preparation has been proposed by Broach et al.<sup>29</sup>. The pattern for ipaAlPO<sub>4</sub>-14F is also in agreement with the refined pattern represented by these authors for ipaAlPO<sub>4</sub>-14, indicating that the impurity phases are not visible in the patterns of as-synthesized samples.

##### calcined partially-hydrated and dehydrated

The ipaAlPO<sub>4</sub>-14F sample was first calcined using a modification of a procedure proposed by Mathisen et al.<sup>106</sup> for CuAPO<sub>4</sub>-5. This procedure consisted of heating the sample in a high temperature oven from 25°C to 550°C at a rate of 1°C/min, and then dwelling (isothermal)

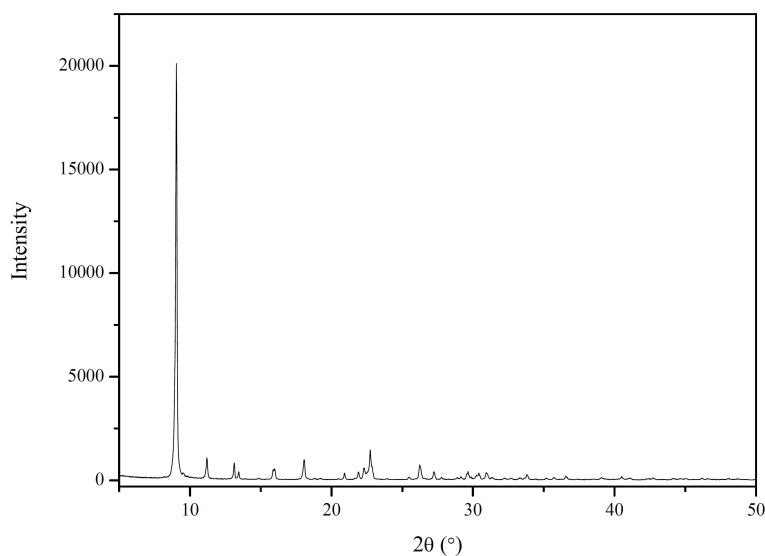


**Figure 4.1:** PXRD pattern for a sample of as-synthesized ipaAlPO<sub>4</sub>-14F.

for 999 min. The sample was then allowed to cool down to room temperature before being analyzed by PXRD. The resulting diffraction pattern for the sample obtained after employing this calcination method is shown in figure 4.2 a). The template acronym has been removed to indicate that the material is free of template. The choice of calcination method was based on the fact that after the successful synthesis of AlPO<sub>4</sub>-14, copper incorporated samples were to be synthesized and subsequently calcined using the same procedure. synthesis of AlPO<sub>4</sub>-14, copper incorporated samples were to be synthesized and subsequently calcined using the same procedure.

The diffraction pattern for calcined AlPO<sub>4</sub>-14F showed inconsistencies with the tabulated  $2\theta$  values presented by Wilson et al.<sup>6</sup> for the calcined material. Figure 4.2 a) shows broad diffraction peaks and a remarkable drop in intensity from the as-synthesized sample. Experimentation with different calcination procedures was done to obtain samples with diffraction patterns more in agreement with the tabulated values. The majority of published calcination procedures found for AlPO<sub>4</sub>-14 states that the material was calcined at 600°C for periods ranging from 2 to 3 h, but mentions nothing about what heating rate was used<sup>107,29,35,108,6</sup>. Yang et al.<sup>35</sup> have published an article regarding water-framework interactions in calcined hydrated AlPO<sub>4</sub>-14. They supplied a diffraction pattern for the calcined hydrated material that was distinctly different from a calcined dehydrated one. This led to the mindset of not allowing the samples to cool down before storing them, believing this to prevent them from rehydrating. Combining this with the short calcination times published by other authors, led to the development of a preheated oven procedure. This procedure consisted of preheating the oven to 600°C, placing the materials in the oven, and removing them after 3 h. 4.2.

Figure 4.2 b) shows the diffraction pattern for a sample of AlPO<sub>4</sub>-14F after calcination in a preheated oven at 600°C for 3 hours. The sample was not allowed to cool down before being

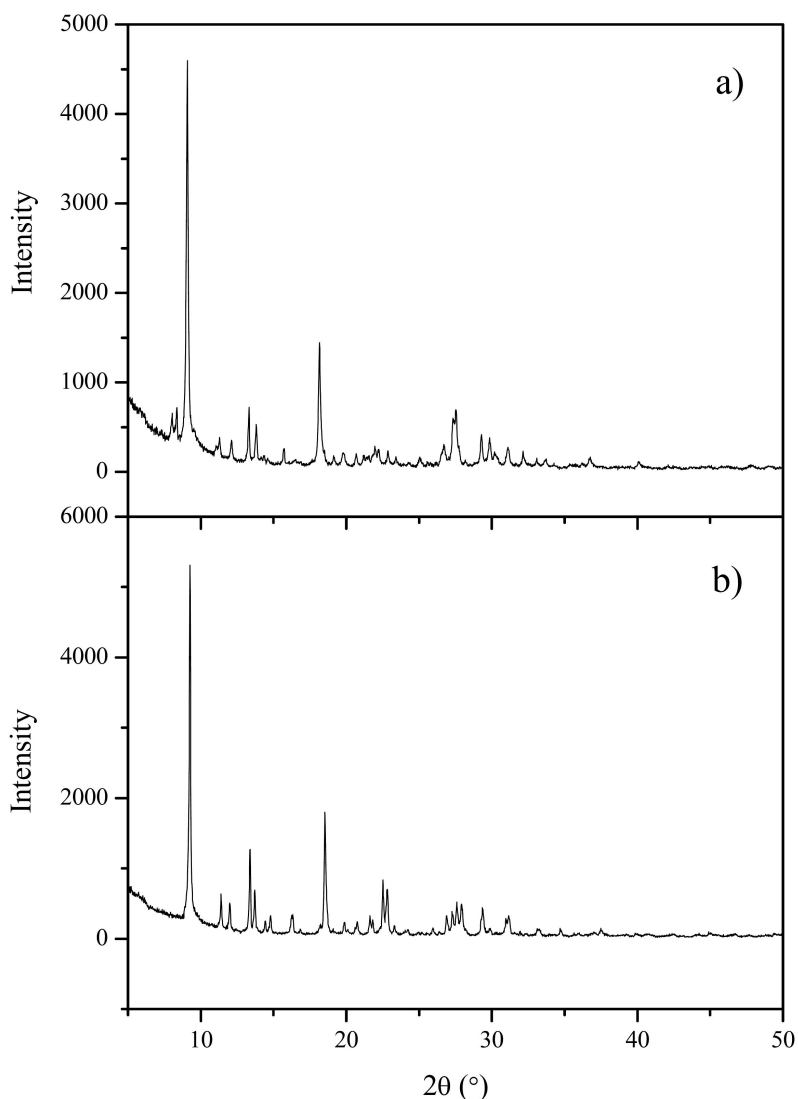


**Figure 4.2:** PXR D pattern for a sample for: a) calcined partially-hydrated AlPO<sub>4</sub>-14F; b) calcined dehydrated AlPO<sub>4</sub>-14F.

stored, and so is treated as being dehydrated. Some hydration of the sample may have occurred during preparation for PXR D, but seems negligible compared to partially-hydrated samples. The pattern of calcined dehydrated AlPO<sub>4</sub>-14F was deemed phase-pure with respect to the 2θ values presented by Wilson et al.<sup>6</sup> It is possible that the procedure by Mathisen et al.<sup>106</sup> would have yielded a similar result had the samples not been allowed to cool down before analysis.

The pattern was not, however, in agreement with the refined pattern for calcined dehydrated AlPO<sub>4</sub>-14 presented by Broach et al.<sup>29</sup>. Extra peaks were observed, and an effort was made to identify these. The peaks for calcined AlPO<sub>4</sub>-14A was assigned based on the diffraction pattern obtained for a sample in this work (see section 4.1.7). The remainder of peaks were assigned to AlPO<sub>4</sub>-15, though this material has been shown to transition to tridymite during calcination if synthesized with hexamethylenetetraamine.

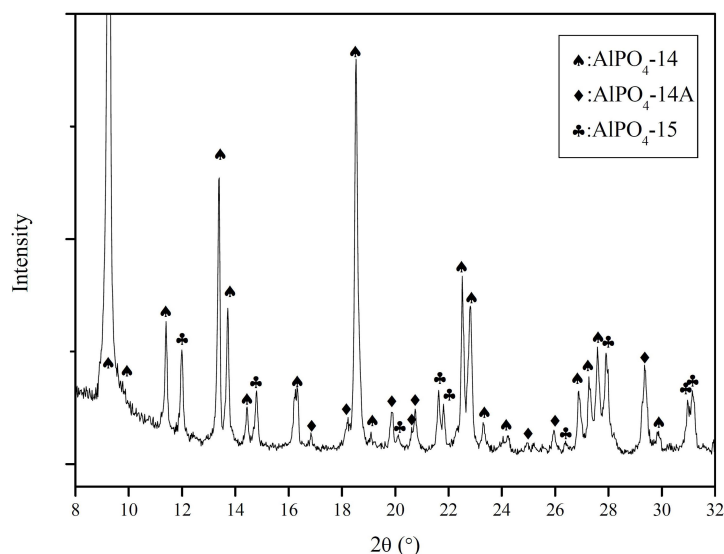


**Figure 4.3:** PXRD pattern for calcined dehydrated  $\text{AlPO}_4\text{-14F}$  with the peaks (and an early shoulder) assigned to the materials  $\text{AlPO}_4\text{-14}$ ,  $\text{AlPO}_4\text{-14A}$ , and  $\text{AlPO}_4\text{-15}$ .

### calcined hydrated

In the work done by Yang et al.<sup>35</sup> a calcined sample of  $\text{AlPO}_4\text{-14}$  was hydrated by leaving it in moist air. The same treatment was tested for a sample of  $\text{AlPO}_4\text{-14F}$ , which was left in a porcelain cup surrounded by moist air for 72 h. The resulting diffraction pattern obtained for the sample is shown in figure 4.4. Since previous samples that were calcined and allowed to cool to  $25^\circ\text{C}$  was designated as calcined partially-hydrated, the sample allowed to hydrate for 72 h was designated calcined hydrated. The diffraction pattern is distinctly different from patterns obtained for both calcined dehydrated and partially-dehydrated  $\text{AlPO}_4\text{-14F}$  samples. The most characteristic features are the improved signal to noise ratio (the same parameter file is used for all samples unless otherwise noted), and the dominant appearance of a high-intensity peak at approximately  $8^\circ$ . The same low  $2\theta$  peak is present in the diffraction pattern for calcined hydrated  $\text{AlPO}_4\text{-14}$  reported by Yang et al, but with peaks of higher  $2\theta$  value suffering from broadening. It is difficult to make a direct comparison due to the different nature of their sample and the one obtained in this work, but it seems that their material probably could have been hydrated even more. A calcined fully hydrated  $\text{AlPO}_4\text{-14}$  may have sharp enough peaks for further structural studies.

### 4.1.2 A pseudo *in-situ* PXRD study of the calcination of ipa $\text{AlPO}_4\text{-14F}$

To further investigate the calcination of ipa $\text{AlPO}_4\text{-14F}$ , a slightly unusual calcination procedure was used. This procedure encompassed heating several ceramic cups containing enough sample for PXRD analysis from 25 to  $500^\circ\text{C}$  at a rate of  $2^\circ\text{C}/\text{min}$ . The samples were then removed at discrete temperatures and stored. Since PXRD was performed on several samples (and not a

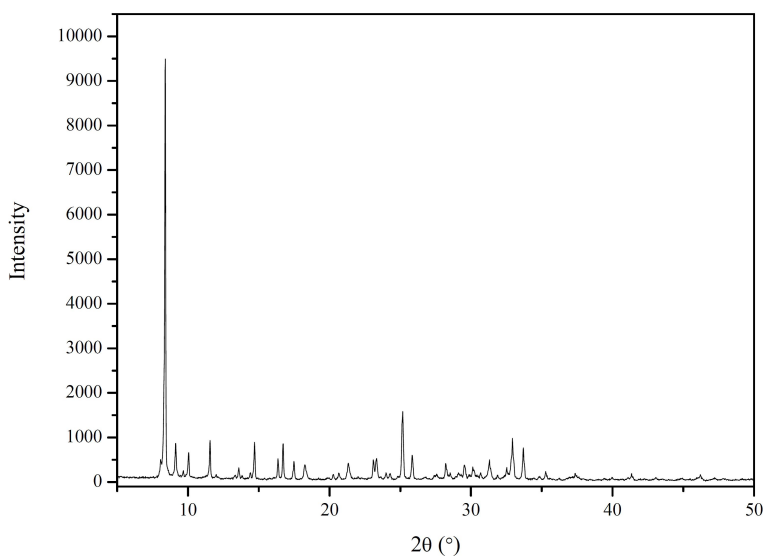


**Figure 4.4:** PXRD pattern for a sample of calcined hydrated  $\text{AlPO}_4\text{-14F}$ .

single sample), the experiment was called pseudo *in-situ* PXRD. The result of this experiment is the diffraction patterns for ipa $\text{AlPO}_4\text{-14F}$  at discrete temperatures, and the corresponding changes in the observed peaks as a result of the template removal (shown in figure 4.5). The sample suffers an initial intensity loss in the interval  $300^\circ\text{C}$  to  $350^\circ\text{C}$ , but the number and positions of the peaks are unchanged. The structural changes do not occur until reaching the interval  $400^\circ\text{C}$  to  $450^\circ\text{C}$ , upon which additional peaks appear. The intensity is also further reduced in this interval. This is a likely point for some type of reaction to occur with the organic template molecules residing in the material's pores. This temperature region might also affect the crystallites themselves, since the impurities start to become visible. The change is not likely the result of a phase transition since the impurities form during the crystallization<sup>30</sup>. Although the experiment is most likely quite different from the *in-situ* experiments performed in either factory built or rebuilds of factory XRD instruments, the experiment shows the abrupt change in the appearance of the pattern as a result of calcination.

### 4.1.3 tba $\text{AlPO}_4\text{-14F}$

#### as-synthesized

$\text{AlPO}_4\text{-14}$  was also tried synthesized using tert-butylamine as template. Figure 4.6 shows the diffraction pattern obtained for a sample of as-synthesized tba $\text{AlPO}_4\text{-14F}$ . The sample was made by another preparation given by Wilson et al.<sup>6</sup> from a gel with molar oxide ratio:  $1\text{R}:\text{Al}_2\text{O}_3:\text{P}_2\text{O}_5:40\text{H}_2\text{O}$  (R = tert-butylamine). The gel had a pH of 3.5 and was crystallized for 96 h at  $150^\circ\text{C}$ . The mother liquor after crystallization had a pH of 10.

The pattern was inconsistent with the tabulated values supplied in the aforementioned patent, and the impurity is marked on the diffraction pattern by an \*. The impurity was found to be

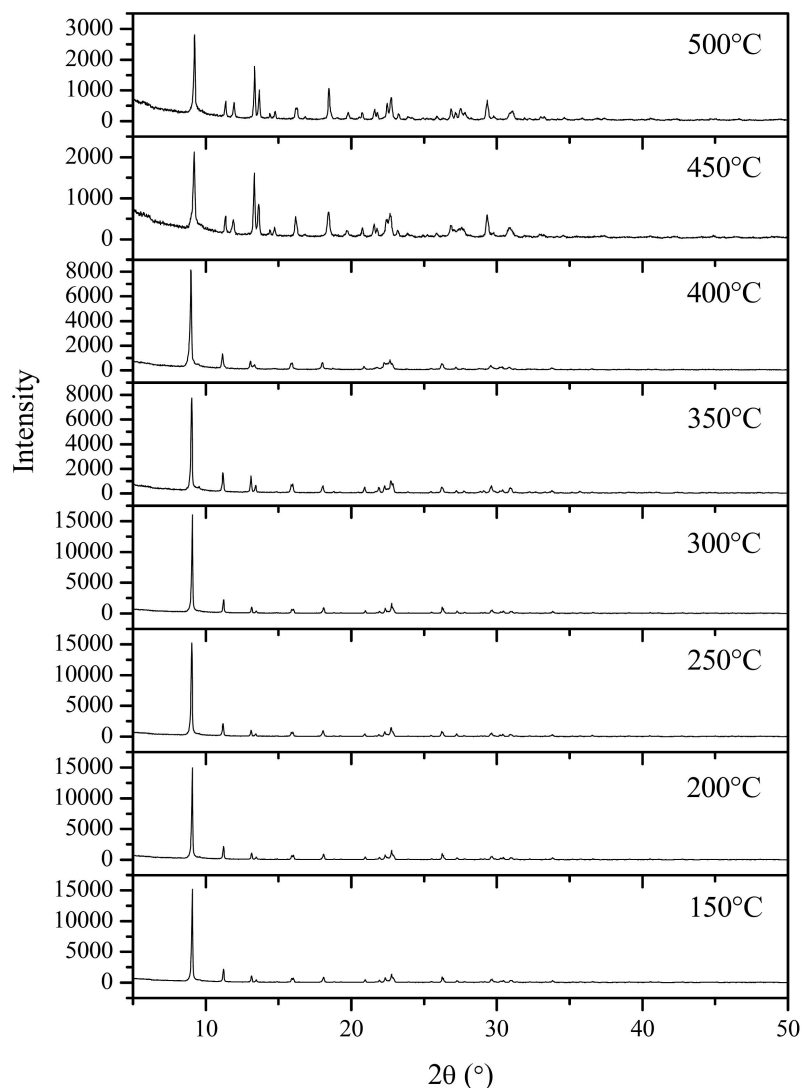


**Figure 4.5:** PXRD patterns for samples of ipaAlPO<sub>4</sub>-14F at different temperatures during the calcination process - an experiment called pseudo *in-situ* PXRD.

the result of contaminated tert-butylamine used in the synthesis. The sample for tbaAlPO<sub>4</sub>-14 using pure tert-butylamine is shown in figure 4.7. This pattern is consistent with the refined pattern for as-synthesized AlPO<sub>4</sub>-14 by Broach et al.<sup>29</sup>, as was the case for ipaAlPO<sub>4</sub>-14F. As was observed for ipaAlPO<sub>4</sub>-14F, the impurities are not visible in the as-synthesized material.

### calcined dehydrated

Figure 4.8 shows the diffraction pattern for calcined dehydrated tbaAlPO<sub>4</sub>-14F. The patterns for calcined samples using the isopropylamine and tert-butylamine templates are identical, indicating that the same phases crystallize. This makes the template acronym somewhat redundant for calcined samples. This is also an indication that isopropylamine and tert-butylamine have

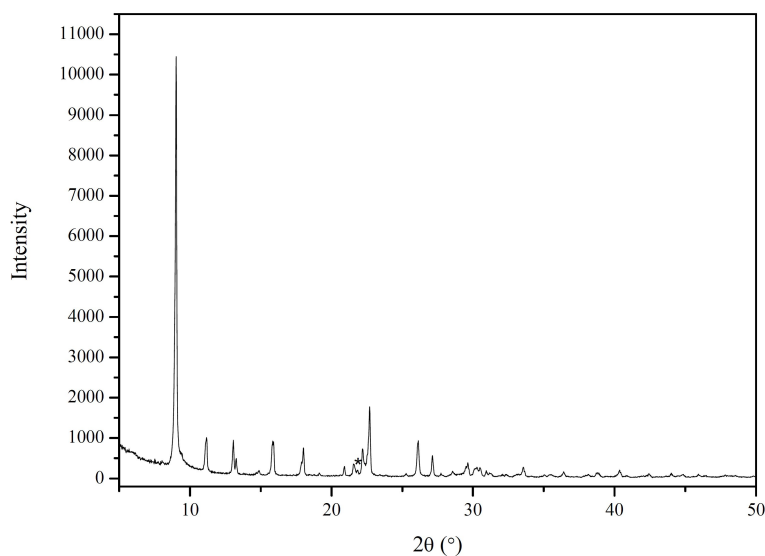


**Figure 4.6:** PXRD pattern for tbaAlPO<sub>4</sub>-14F. The \* indicates an impurity caused by a contaminated template.

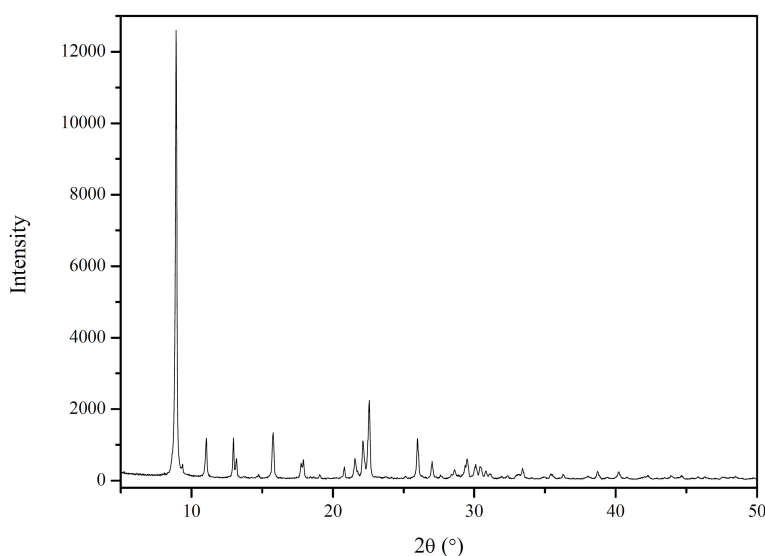


**Figure 4.7:** PXRD pattern for as-synthesized tbaAlPO<sub>4</sub>-14F.

similar roles as templates, and that the small structural differences between them has little effect on the crystallization of AlPO<sub>4</sub>-14F (see scheme 4.1).

#### 4.1.4 ipaCuAPO<sub>4</sub>-14F

##### as-synthesized

The incorporation of metals in Zeotypes with the AFN topology has previously been reported for the transition metals cobalt<sup>32</sup> (CoAPO<sub>4</sub>-14), chromium<sup>31</sup> (CrAPO<sub>4</sub>-14), and manganese (MAPO<sub>4</sub>-14), as well as for the alkaline earth metal magnesium<sup>10</sup> (MAPO<sub>4</sub>-14).

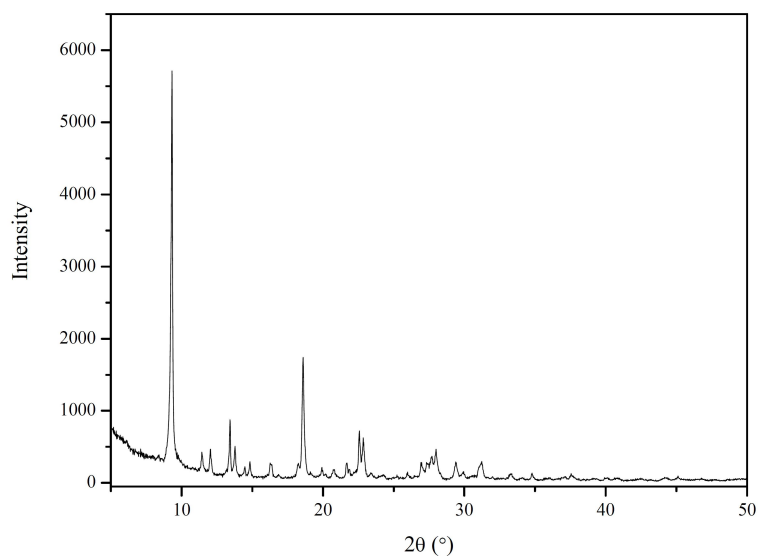
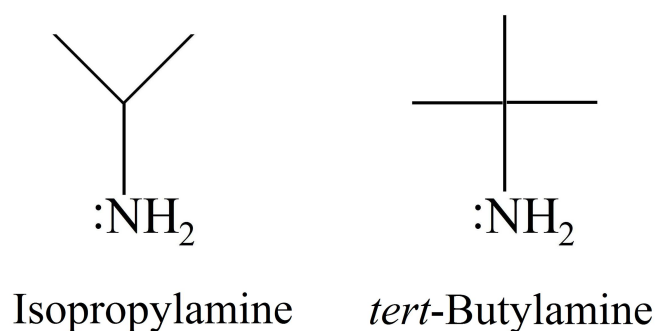


**Figure 4.8:** PXRD pattern for calcined dehydrated  $\text{AlPO}_4\text{-14F}$ . The sample was calcined in a preheated oven at  $600^\circ\text{C}$  for 3 h.



**Scheme 4.1**

There has so far not been reported any cases of  $\text{CuAPO}_4\text{-14}$ . The general approach to synthesizing these  $\text{MeAPO}_4\text{-14}$  compositions seems to be the addition of the metal (in oxide or hydrated acetate salt form) to the synthesis gel. In addition, a reduction in crystallization temperature ( $125$  to  $195^\circ\text{C}$ ) and rather lengthy crystallization times are common (from 24 h to weeks).

Muñoz et al.<sup>109</sup> were the first to prove incorporation of copper in the AFI topology ( $\text{CuAPO}_4\text{-5}$ ). The choice for copper source was  $\text{CuO}$ , the crystallization temperature and time was  $150^\circ\text{C}$  and 24 h. The authors suggested that copper substituted for phosphorous in the framework, deviating from the general understanding that metals replace aluminum<sup>110</sup>. Mathisen et al.<sup>106</sup> showed, using a modified method of Muñoz et al.<sup>109</sup>, that both copper(II) oxide and copper acetate can be used to incorporate the transition metal.

$\text{CuAPO}_4\text{-14F}$  was synthesized by replacing equimolar amounts of Al with Cu in the molar oxide ratio of the synthesis gel of  $\text{AlPO}_4\text{-14F}$ . Copper acetate was selected as transition metal source since it has been previously shown<sup>111,112</sup> to improve the catalytic activity for  $\text{CuAPO}_4\text{-5}$

in the selective catalytic reduction (SCR) of NO<sub>x</sub>. The template of choice was isopropylamine. Table 4.1 summarizes the synthesis parameters for all CuAPO<sub>4</sub>-14F compositions. The diffraction patterns for all ipaCuAPO<sub>4</sub>-14F compositions are shown in figure 4.9.

**Table 4.1:** Gel composition and crystallization parameters for all CuAPO<sub>4</sub>-14F compositions (Cryst. = Crystallization).

Sample	R	Al <sub>2</sub> O <sub>3</sub>	Cu(OAc) <sub>2</sub>	P <sub>2</sub> O <sub>5</sub>	H <sub>2</sub> O	Cryst. Time (days)	T (°C)
ipa0.01CuAPO <sub>4</sub> -14F	1	0.99	0.02	1	40	1	150
ipa0.03CuAPO <sub>4</sub> -14F	1	0.97	0.06	1	40	3	150
ipa0.08CuAPO <sub>4</sub> -14F	1	0.92	0.16	1	40	8	150

The diffraction patterns are consistent with the refined patterns for AlPO<sub>4</sub>-14 presented by Broach et al., indicating that no other phases form in the presence of copper. During sample recovery from the autoclaves it was observed that they exhibited various nuances of turquoise color. The color intensity of the samples increased with copper content in the gel. This is consistent with an octahedral environment for hydrated Cu(II) ions<sup>109,106,111</sup>.

An evaluation of copper and silicon incorporation in Zeotypes with AFI (AlPO<sub>4</sub>-5) and AEL (AlPO<sub>4</sub>-11) topologies have previously been reported by Arild Moen and David G. Nicholson<sup>113</sup>. Their work highlighted a problem with divalent copper incorporation due to its reduction and subsequent disproportionation. The authors attributed this to the organic amine (template) acting as a reducing agent at high temperatures (190°C). Lower temperatures was also shown to be a problem due to the complexing nature of the amine and copper. These factors thus prevented the incorporation of copper in AFI and AEL topologies.

The complexing nature reported does not seem to hinder the crystallization of CuAPO<sub>4</sub>-14F. The results reported for the AFI and AEL topologies were based on work with secondary (di-n-propylamine) and tertiary (triethylamine) amines, and seems not to apply for the primary amine isopropylamine. As can be inferred from the work on successfully incorporated copper CuAPO<sub>4</sub>-5, quaternary ammonium ions are also unaffected by this phenomena<sup>111,109,106</sup>.

When increasing amounts of copper in the synthesis gels were tested, the crystallization times were also increased. Not allowing the materials the extra crystallization time resulted in an additional dark blue powder with a “sugar like consistency”. The diffraction patterns of such samples showed characteristic peaks of both AlPO<sub>4</sub>-14 and a tridymite phase, and was attributed to an intermediate stage of the CuAPO<sub>4</sub>-14F crystallization process. The presence of tridymite in the products obtained after insufficient crystallization times could be a result of copper retarding the crystallization process. It perhaps introduces an alternate mechanism for building the AlPO<sub>4</sub>-14F lattice.

The presence of copper in the impurities AlPO<sub>4</sub>-14A and AlPO<sub>4</sub>-15 can not be ruled out. The presence of AlPO<sub>4</sub>-14 and tridymite could be an indication that, in the presence of copper, this topology crystallizes faster than the other two. If copper is incorporated in the impurities, it

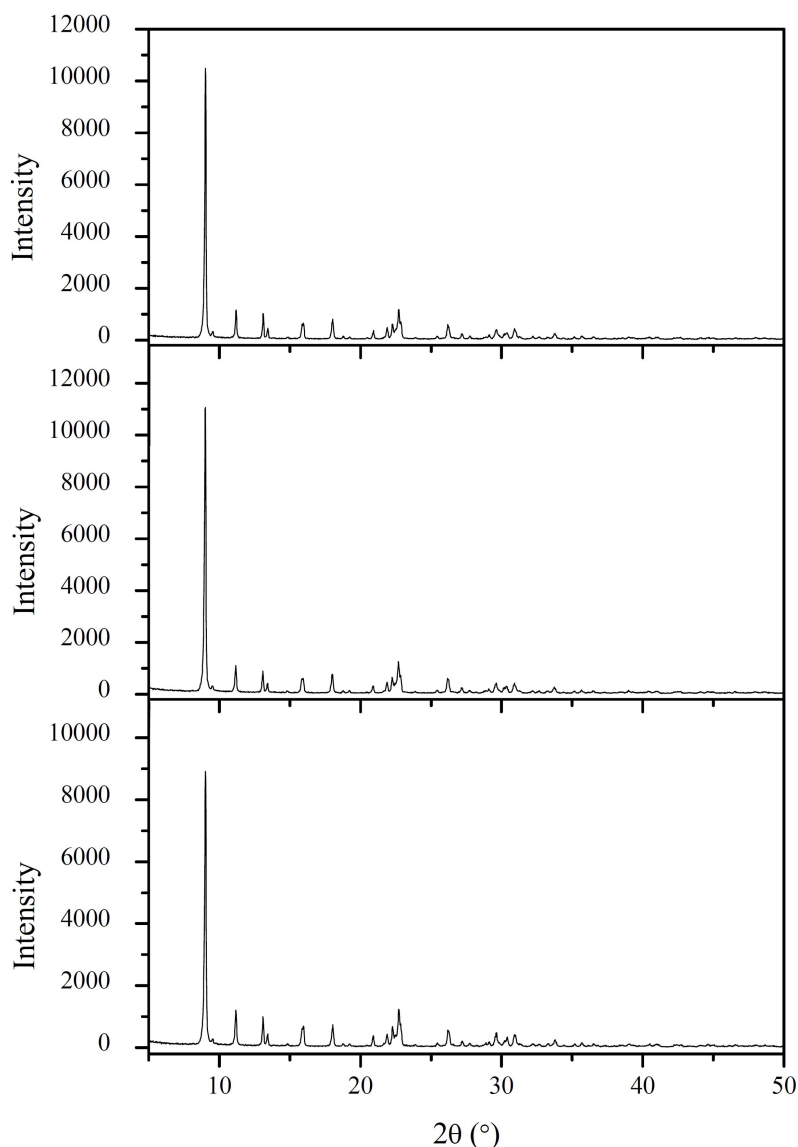


**Figure 4.9:** PXRD patterns for as-synthesized ipaCuAPO<sub>4</sub>-14F compositions; ipa0.01CuAPO<sub>4</sub>-14F (top), 0.03CuAPO<sub>4</sub>-14F (middle), and ipa0.08CuAPO<sub>4</sub>-14F (bottom).

would perhaps seem logical that their crystallization times increase. Other attempts at incorporating metals in the AFN topology have reported lengthy crystallization times<sup>10,31,32</sup> indicating that this process is generally time consuming. The presence of AlPO<sub>4</sub>-14 in the early stages of crystallization can thus be an indication that copper favors the impurities. A useful relation between crystallization times and copper content was determined to be 24 h of crystallization for every 0.01 mol copper in the gel.

### **calcined dehydrated**

Figure 4.10 shows the diffraction patterns for the three calcined dehydrated CuAPO<sub>4</sub>-14F compositions. The samples were calcined in a preheated oven at 600°C for 3 h. The compositions

show diffraction patterns similar to that of calcined dehydrated  $\text{AlPO}_4\text{-14F}$ . There is also a noteworthy increase in relative intensity of peaks in the  $0.08\text{CuAlPO}_4\text{-14F}$  sample from 20 to  $25^\circ$ . Upon calcination the samples changed color from turquoise to light green. The color change of copper-containing Zeotypes induced by calcination has previously been reported by several authors, and the products reported are either gray<sup>111</sup>, or green (varying intensities reported)<sup>112,106</sup>. The gray color has been attributed to octahedral coordination of copper (no tetragonal distortion)<sup>111</sup>, and the green color has been attributed to tetrahedrally coordinated copper<sup>106</sup>.

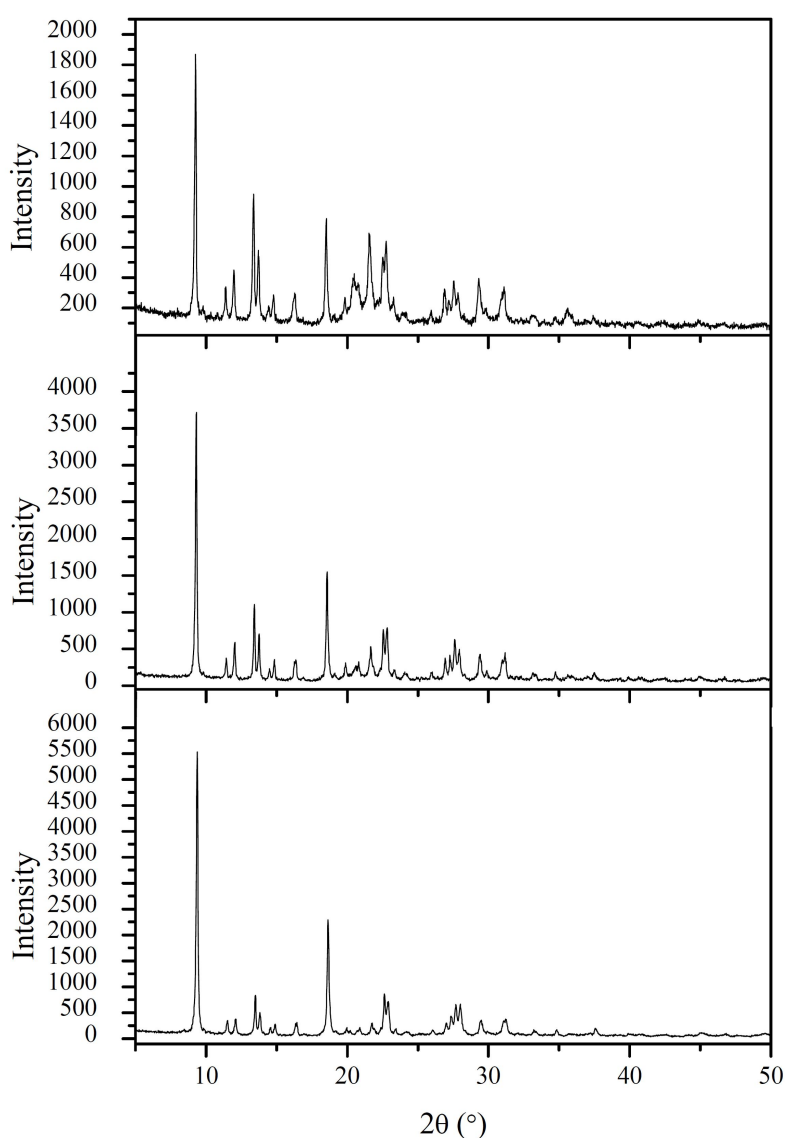


**Figure 4.10:** PXRD patterns for calcined dehydrated  $\text{CuAlPO}_4\text{-14F}$  compositions;  $0.08\text{CuAlPO}_4\text{-14F}$  (top pattern),  $0.03\text{CuAlPO}_4\text{-14F}$  (middle pattern), and  $0.01\text{CuAlPO}_4\text{-14F}$  (bottom pattern).

### calcined partially hydrated

Figure 4.11 shows the diffraction patterns for the three  $\text{CuAlPO}_4\text{-14F}$  compositions after calcination by the method proposed by Mathisen et al.<sup>106</sup>. As mentioned previously, this procedure allows for partial hydration of the samples. The patterns are similar to that of calcined partially-hydrated  $\text{AlPO}_4\text{-14F}$ . There are two major distinctions, however:

1. In calcined partially-hydrated  $\text{AlPO}_4\text{-14F}$  early reflections around  $8^\circ$  was observed. There is no sign of such peaks in these patterns, which led to the notion that the copper compositions were unable to hydrate to the same extent.
2. The diffraction pattern for calcined partially-hydrated  $0.08\text{CuAlPO}_4\text{-14F}$  exhibits peaks consistent with tridymite, indicating that some of the phases has undergone a transition upon hydration.

The tridymite peaks observed for  $0.08\text{CuAlPO}_4\text{-14F}$  may indicate that the copper is situated in  $\text{AlPO}_4\text{-14A}$  and/or  $\text{AlPO}_4\text{-15}$ . These materials have been shown to be thermally unstable<sup>114,115</sup>, and the presence of copper may lead to further instability. A structure collapse could trap the copper, effectively preventing it from rehydrating.

The samples were left in moist air for 72 h (as with  $\text{AlPO}_4\text{-14F}$ ) to see if the early diffraction peaks appeared. The diffraction patterns for the three copper compositions after hydration in air for 72 h is shown in figure 4.12. It can be observed that even after standing in moist air for 72 hours, only  $0.01\text{CuAlPO}_4\text{-14F}$  shows signs of the early diffraction peak around  $8^\circ$ . This copper sample is also the only one that regained the turquoise color lost during calcination. Thus, the presence of copper in the synthesis gel somehow alters the water uptake by the crystal lattice. It is also quite intriguing to observe that the tridymite peaks found earlier in the pattern for  $0.08\text{CuAlPO}_4\text{-14F}$  have disappeared, making the region less definable.

---

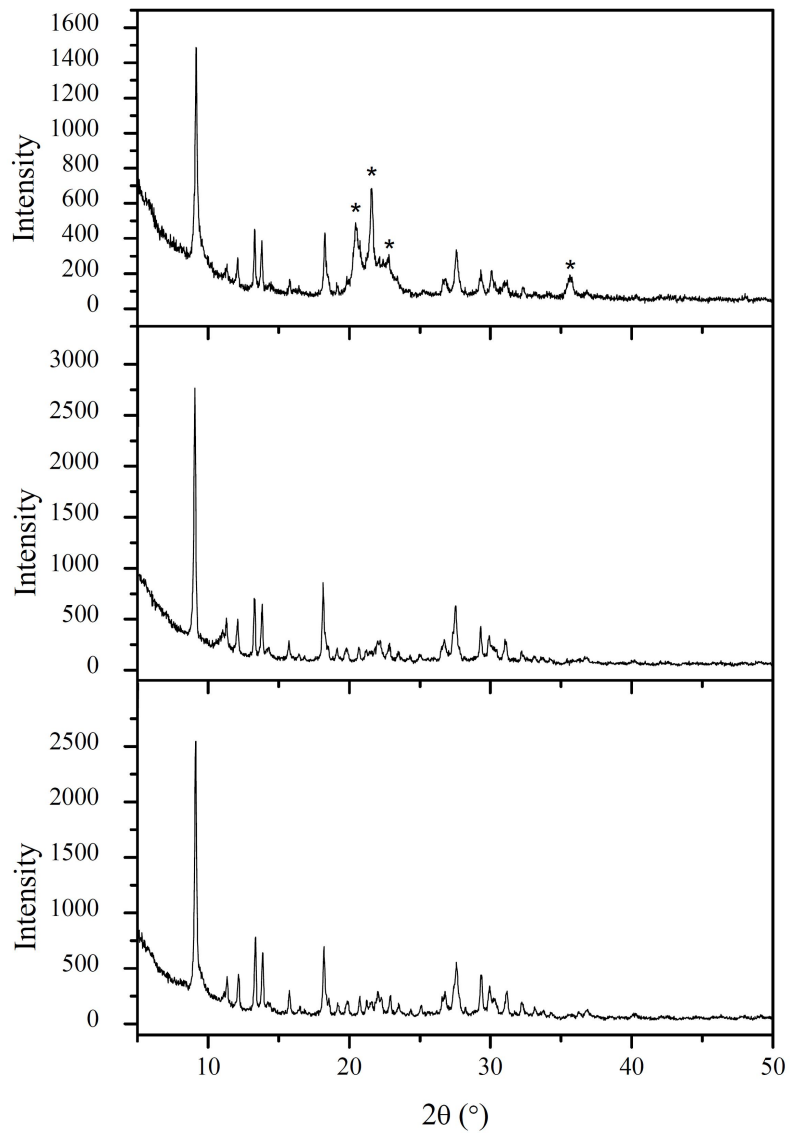


**Figure 4.11:** PXRD patterns for calcined partially-hydrated CuAPO<sub>4</sub>-14F compositions; 0.08CuAPO<sub>4</sub>-14F (top), 0.03CuAPO<sub>4</sub>-14F (middle), and 0.01CuAPO<sub>4</sub>-14F (bottom). The \* indicates reflections from a tridymite phase.

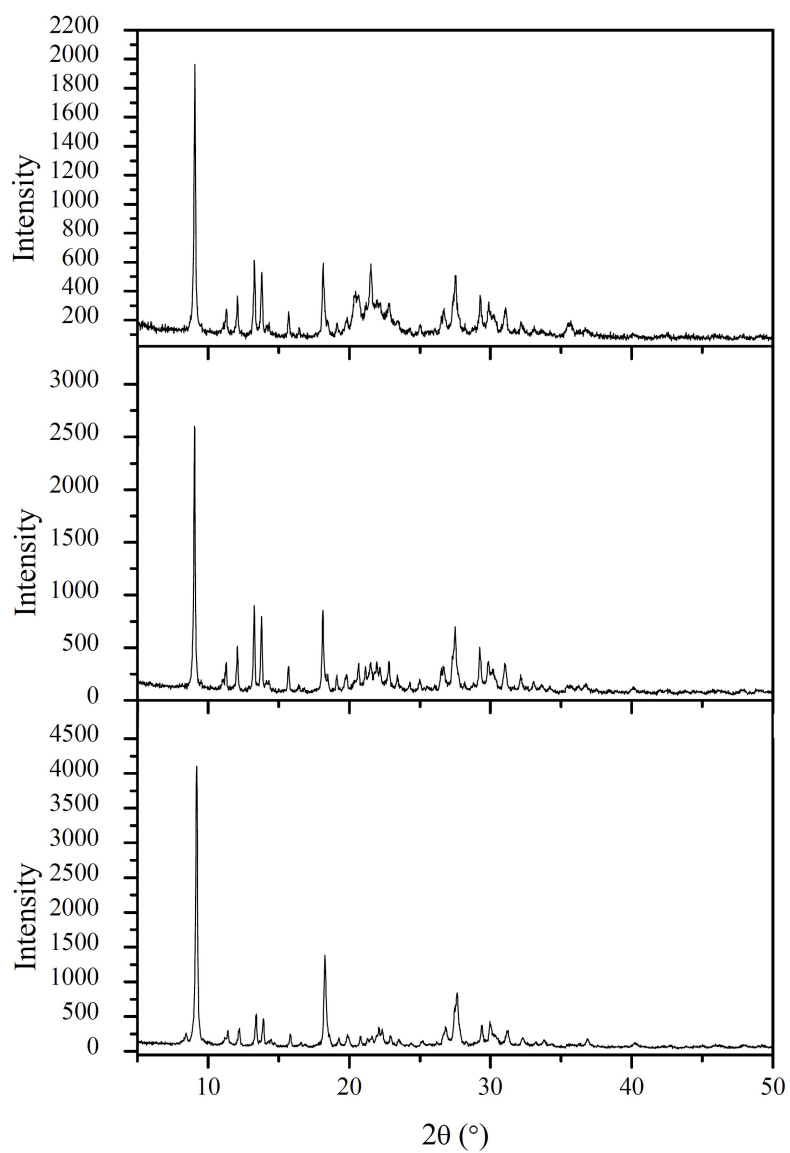


**Figure 4.12:** PXRD patterns for calcined  $\text{CuAPO}_4\text{-14F}$  compositions hydrated for 72 h;  $0.08\text{CuAPO}_4\text{-14F}$  (top pattern),  $0.03\text{CuAPO}_4\text{-14F}$  (middle pattern), and  $0.01\text{CuAPO}_4\text{-14F}$  (bottom pattern).

### 4.1.5 tbaSAPO<sub>4</sub>-14F

#### as-synthesized

Phase-pure SAPO<sub>4</sub>-14 has not previously been reported, and was not among the SAPOs first presented in U.S. patent 4,440,871<sup>9</sup>. The patent did, however, report the crystallization of SAPO<sub>4</sub>-34 from a gel with molar oxide ratio: 1R:Al<sub>2</sub>O<sub>3</sub>:1.0P<sub>2</sub>O<sub>5</sub>:0.6SiO<sub>2</sub>:50H<sub>2</sub>O (R = isopropylamine) crystallized at 200°C for 51 h. Girnus et al.<sup>36</sup> reported the impossibility of crystallizing SAPO<sub>4</sub>-14 using piperidine. The authors reached this conclusion after having observed the formation of SAPO<sub>4</sub>-34 from a gel that crystallizes AlPO<sub>4</sub>-14 in absence of Si. Rajić et al.<sup>32</sup> reported the crystallization of CoSAPO<sub>4</sub>-14 and CoSAPO<sub>4</sub>-34 from a gel with molar oxide ratio: 1R:Al<sub>2</sub>O<sub>3</sub>:1.0P<sub>2</sub>O<sub>5</sub>:0.2Co(OAc)<sub>2</sub>:0.4SiO<sub>2</sub>:50H<sub>2</sub>O (R = isopropylamine) crystallized for periods ranging from 1 to 45 days at both low and high temperatures (125, 160, and 195°C).

The approach for synthesizing tbaSAPO<sub>4</sub>-14F was taking an AlPO<sub>4</sub>-14F gel and replacing a equimolar amounts of P with Si. The template of choice was tert-butylamine. The gels were crystallized at 200°C for the times presented in table 4.2. As with CuAPO<sub>4</sub>-14F, the crystallization time was estimated to 24 h per 0.01 mol silicon tried incorporated. However, the two compositions with the highest silicon content in the synthesis gels were synthesized using 50 mg seed crystals of tbaAlPO<sub>4</sub>-14F, and crystallized for only 24 h. The mindset of adding small amounts of tbaAlPO<sub>4</sub>-14F came from previous reports<sup>107</sup> where seed crystals of ipaAlPO<sub>4</sub>-14 were used to avoid the formation of AlPO<sub>4</sub>-17 when synthesizing pipAlPO<sub>4</sub>-14.

**Table 4.2:** Gel composition and crystallization parameters for all SAPO<sub>4</sub>-14F compositions. \*Additional 50mg tbaAlPO<sub>4</sub>-14F seed crystals in the synthesis gel (Cryst. = Crystallization)

Sample	R	Al <sub>2</sub> O <sub>3</sub>	P <sub>2</sub> O <sub>5</sub>	SiO <sub>2</sub>	H <sub>2</sub> O	Cryst. Time (days)	T (°C)
tba0.06SAPO-14F	1	1	0.94	0.12	40	6	200
tba0.08SAPO-14F*	1	1	0.92	0.16	40	1	200
tba0.20SAPO-14F*	1	1	0.80	0.40	40	1	200

The diffraction patterns obtained for the tbaSAPO<sub>4</sub>-14F compositions are shown in figure 4.13. There is a noteworthy difference between the patterns of the samples made with seeding and the one without, which is highlighted in the pattern for tba0.06SAPO<sub>4</sub>-14F. As mentioned, previous attempts<sup>9,36</sup> at crystallizing the AFN topology in the presence of Si has resulted in the formation of SAPO<sub>4</sub>-34, which is of CHA topology. The difference between the preparations of this work and those previously reported is that Si is replacing P in the molar oxide ratio, instead of being added “in excess”. The purpose of adding Si to the gel is that it hopefully replaces some of the P in the finished product. It thus seems logical to decrease the phosphorous content of the gel to provoke this desirable event.

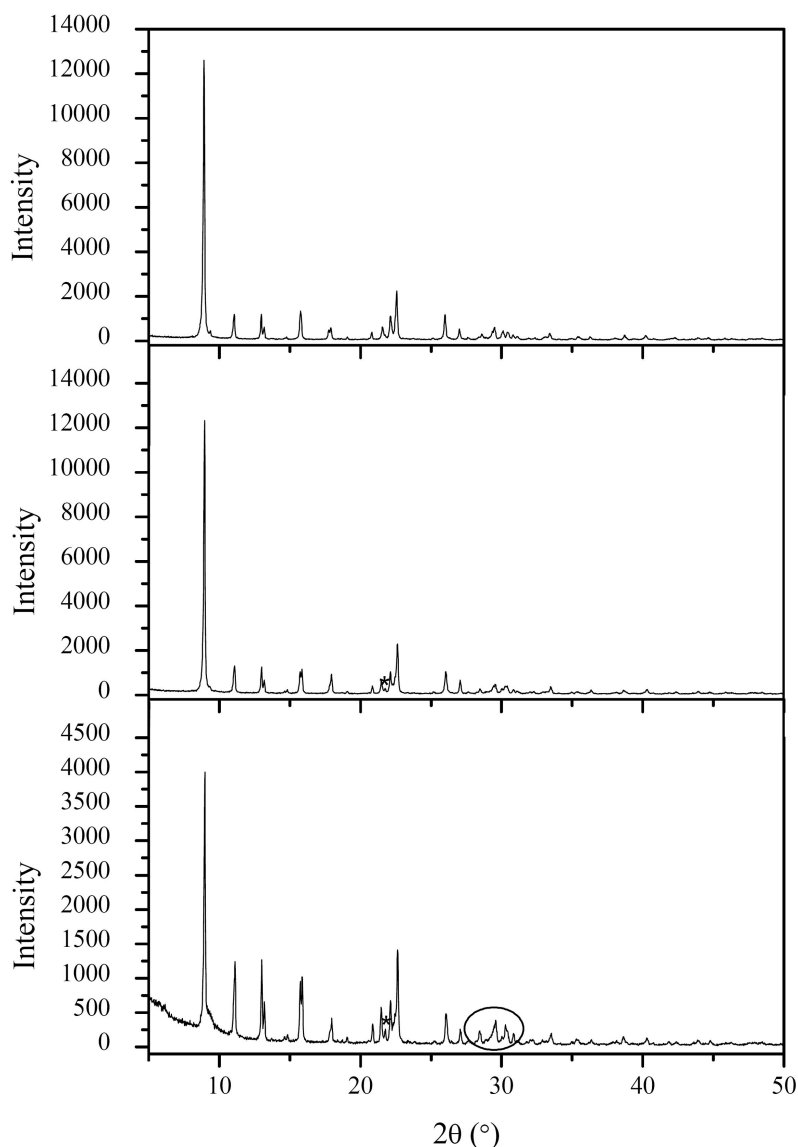


**Figure 4.13:** PXRD patterns for as-synthesized SAPO<sub>4</sub>-14F compositions; tba0.20SAPO<sub>4</sub>-14F (top pattern), tba0.08SAPO<sub>4</sub>-14F (middle pattern), and tba0.06SAPO<sub>4</sub>-14F (bottom pattern). Differences between the bottom pattern and the other to are highlighted. Impurities from a contaminated template are marked with \*.

### calcined

Figure 4.14 shows the diffraction patterns for the SAPO<sub>4</sub>-14F compositions after calcination by heating them from 25 to 1000°C at a rate of 5°C/min, and dwelling for 3h. The increase in calcination temperature was introduced after insufficient mass loss was observed with TGA when using the procedure proposed by Mathisen et al.<sup>106</sup>. Samples calcined at 550°C were dark brown and the color was attributed to template molecules still residing in the pores. This was also seen as an indication that the presence of silicon had an impact on the thermal behavior and decomposition of the template. The patterns are characteristic for calcined dehydrated AlPO<sub>4</sub>-14F and indicates that the same impurities also crystallize in the presence of Si. There

are no peaks characteristic for SAPO<sub>4</sub>-34 either, indicating that the method of replacing Si prevents its crystallization. It may also be an indication that SAPO<sub>4</sub>-34 can only be synthesized using the isopropylamine template using large amounts of Si (0.6 SiO<sub>2</sub>) in the synthesis gel. There is a noteworthy increase in the relative intensity of the 0.20SAPO<sub>4</sub>-14F sample, possibly indicating that some phases have increased in quantity. The extremely high calcination temperature used also indicates that after the initial destruction the phases present are very stable. As mentioned, AlPO<sub>4</sub>-15 synthesized with hexamethylenetetraamine as template<sup>115</sup> undergoes a phase transition to tridymite during calcination. Even though this impurity is initially unstable, the exposure to 1000°C does not induce a phase transition. This also excludes the possibility of obtaining phase-pure SAPO<sub>4</sub>-14 by calcining the material to temperatures where the impurities turn amorphous.

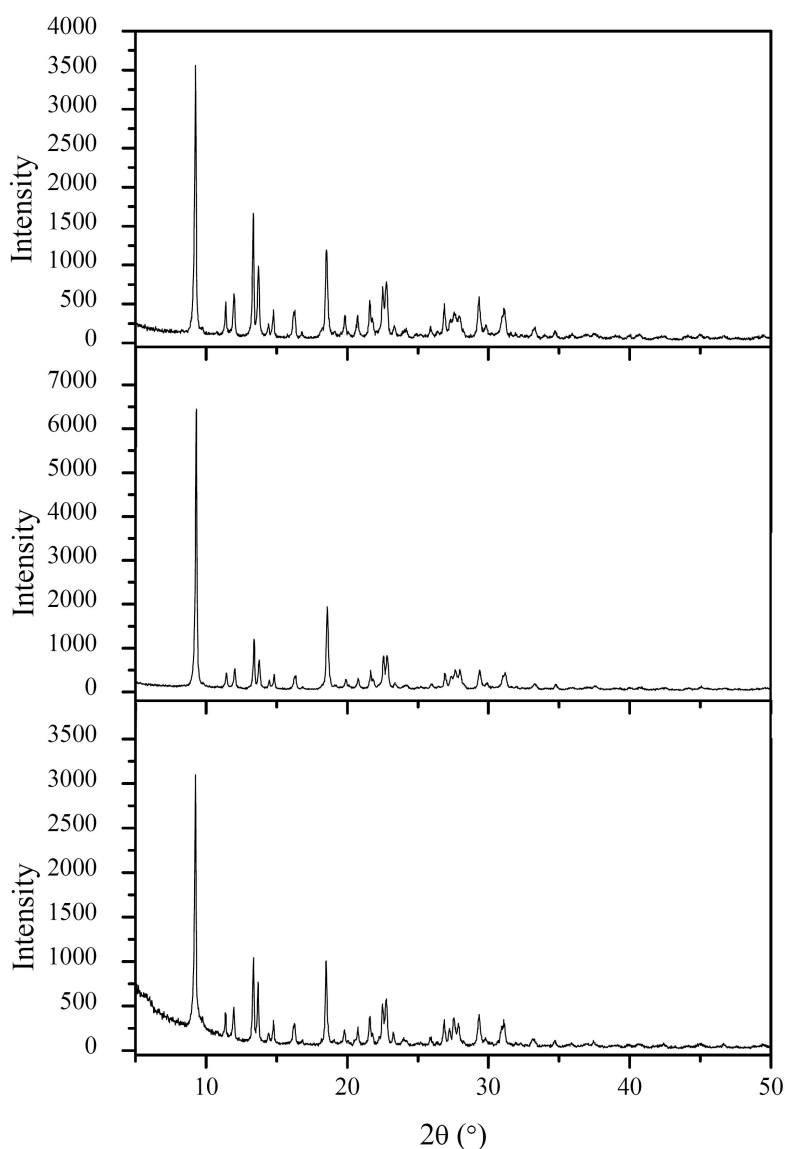


**Figure 4.14:** PXRD patterns for calcined dehydrated SAPO<sub>4</sub>-14F compositions; 0.20SAPO<sub>4</sub>-14F (top pattern), 0.08SAPO<sub>4</sub>-14F (middle pattern), and 0.06SAPO<sub>4</sub>-14F (bottom pattern).

### 4.1.6 Attempts at synthesizing phase-pure $\text{AlPO}_4\text{-14}$

Since the original preparation for  $\text{AlPO}_4\text{-14}$  by Wilson et al.<sup>6</sup> produced impurities (as pointed out by Pluth and Smith<sup>30</sup>), a great deal of effort was put into synthesizing phase-pure  $\text{AlPO}_4\text{-14}$  samples. Phase-pure samples are a necessity for disambiguous assignment of observed characteristics to one type of material. With impurities present, one can never be completely confident that the property observed is exclusive to a particular molecular sieve. The logical first step was to test other (non-patented) published synthesis procedures, such as the ones by Antonijevic-, Broach-, and Zibrowius et al. The “traditional” pseudo-boehmite was used as alumina source in all preparations (except where noted), although not all the published articles stated the reactants used in their syntheses. The other reactants used were 85% phosphoric acid, distilled water, isopropylamine, and piperidine.

#### The evaluation of published synthesis procedures for $\text{AlPO}_4\text{-14}$

**Procedures proposed by Zibrowius et al.** Zibrowius et al. have presented two preparations for  $\text{AlPO}_4\text{-14}$ : one for ipa $\text{AlPO}_4\text{-14}$ , and one for pip $\text{AlPO}_4\text{-14}$  (made respectively with isopropylamine and piperidine as templates). It should be noted that the preparation for pip $\text{AlPO}_4\text{-14}$  can be found in an article<sup>34</sup> and in an online scientific poster<sup>116</sup>, whereas the preparation for ipa $\text{AlPO}_4\text{-14}$  was only found on the online poster<sup>116</sup>. It should also be noted that the authors comprising Zibrowius et al. are not entirely the same in the article and the poster.

The preparation for ipa $\text{AlPO}_4\text{-14}$  was tested first, where the molar oxide ratio of the synthesis gel was:  $2\text{R}:\text{Al}_2\text{O}_3:\text{P}_2\text{O}_5:0.25\text{H}_2\text{SO}_4:100\text{H}_2\text{O}$  (R = isopropylamine). The crystallization time was 40 h, the temperature was  $180^\circ\text{C}$ , and the gel was aged for 1 h prior to hydrothermal treatment. The diffraction pattern for the resulting sample (after calcination in a preheated oven at  $600^\circ\text{C}$  for 3 h) is shown in figure 4.15 a). The preparation for pip $\text{AlPO}_4\text{-14}$  consisted of crystallizing a gel with the molar oxide ratio:  $2.3\text{R}:\text{Al}_2\text{O}_3:1.4\text{P}_2\text{O}_5:40\text{H}_2\text{O}$  (R = piperidine). The crystallization was carried out at  $200^\circ\text{C}$  for 24 h and 96 h. After 24 h, no powder product was obtained, and during the crystallization the mixture had formed a viscous yellow colored gel. After 96 h there was also the aforementioned gel, but it contained a small amount (50 mg) of dispersed powder. The diffraction pattern for the resulting powder sample in calcined form is shown in figure 4.15 b). The pip $\text{AlPO}_4\text{-14}$  sample was calcined with a procedure (see figure text for details) based on the TGA results published by Zibrowius et al.<sup>34</sup>. As can be seen from figure 4.15, none of the preparation methods yielded phase-pure  $\text{AlPO}_4\text{-14}$ , but yielded phases consistent with that of  $\text{AlPO}_4\text{-14F}$ . It is interesting to note, however, that the pattern for calcined  $\text{AlPO}_4\text{-14F}$  made with piperidine has different relative intensities of peaks compared to the sample made with isopropylamine. It appears as though more  $\text{AlPO}_4\text{-14}$  is present after calcination when using the piperidine template. This might be an indication that the removal of the piperidine template has a different effect on the material than the removal of isopropylamine or tert-butylamine. This may be caused by the fact that the structure of piperidine is a lot

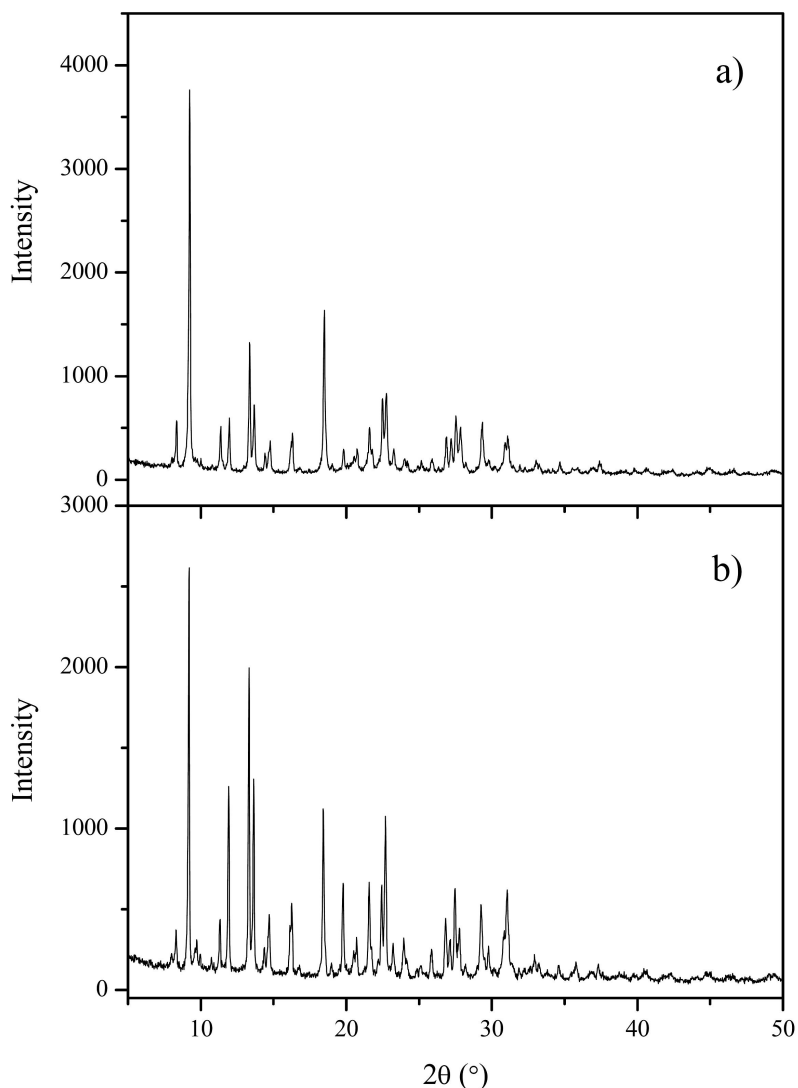
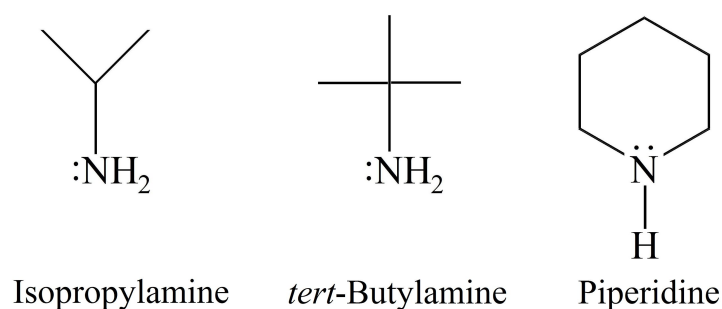


**Figure 4.15:** PXRD patterns for calcined samples obtained from the proposed preparations of Zibrowius et al. for: a) ipaAlPO<sub>4</sub>-14 calcined in a preheated oven at 600°C for 3 h, and b) pipAlPO<sub>4</sub>-14 calcined by heating the material from 25 to 800°C at a rate of 5°C/min, and then dwelling for 3 h.

different from the other two templates (see scheme 4.2). An interesting fact is that the sample of pipAlPO<sub>4</sub>-14 used for the work behind the poster was supplied by one of the researchers behind the original article on pipAlPO<sub>4</sub>-14. What is more intriguing is that the sample contained an impurity, more specifically 6% Augelite (as determined by quantitative Rietveld analysis). This is an indication that the procedure presented for pipAlPO<sub>4</sub>-14 is flawed with respect to reproducibility. This is especially evident as even one of the co-authors presenting the original preparation had trouble obtaining a phase-pure product.

**Procedure proposed by Antonijevic et al.** The preparation by Antonijevic et al.<sup>107</sup> comprised of reversing the order of reactants added (with respect to the preparations of Wilson et al.<sup>6</sup>), this



Scheme 4.2

time starting with water and alumina as opposed to water and phosphoric acid. The molar oxide ratio of the synthesis gel used was: 1R:Al<sub>2</sub>O<sub>3</sub>:P<sub>2</sub>O<sub>5</sub>:35H<sub>2</sub>O (R = isopropylamine), crystallized at 160°C for 10 hours. The resulting diffraction pattern for the as-synthesized sample obtained is shown in figure 4.16 a). From the diffraction pattern, peaks of AlPO<sub>4</sub>-14 and tridymite was observed. The presence of tridymite was again seen as a precursor to AlPO<sub>4</sub>-14 resulting from the crystallization not reaching completion within the ten hours. The same gel crystallized for 24 h yields AlPO<sub>4</sub>-14F as shown in figure 4.16 b) and c). The shorter crystallization time only slows down the crystallization process, and does not prevent impurities from forming.

#### **Published procedure proposed by Broach et al. and the issue of autoclaves with stirring**

The first reported case of phase-pure AlPO<sub>4</sub>-14 was published in the conference proceedings of the sixth international Zeolite conference<sup>29</sup>. The preparation introduced stirred autoclaves, crystallization time and temperature of respectively 30 h and 175°C. The molar oxide ratio of the synthesis gel was: 1R:Al<sub>2</sub>O<sub>3</sub>:P<sub>2</sub>O<sub>5</sub>:35H<sub>2</sub>O, and isopropylamine was used as template. As only static autoclaves were available at the laboratory, stirred autoclaves were improvised by placing a suitable sized autoclave on a magnetic stirrer, and using the hot-plate to increase the temperature. The autoclaves were somewhat insulated with aluminum foil to avoid too much radiant heat loss to the surroundings. A problem arose when trying to stir the viscous gel inside the Teflon liner, and more so when trying to close the autoclave. After numerous attempts, the idea of stirring this type of viscous gel during crystallization had to be abandoned. The same procedure was performed without stirring to see if these new parameters (longer crystallization time and lower crystallization temperature) would yield phase-pure AlPO<sub>4</sub>-14 without stirring. The diffraction patterns for the obtained sample, both as-synthesized and calcined, is shown in figure 4.17. The result of this was the unwanted crystallization of AlPO<sub>4</sub>-14F, indicating that the parameters (time and temperature) had little effect on the phases formed.

#### **Procedures tested in this thesis work**

After the exhaustive approach of testing the major part of the published synthesis procedures for AlPO<sub>4</sub>-14, the next step was taking the published procedures and varying the synthesis

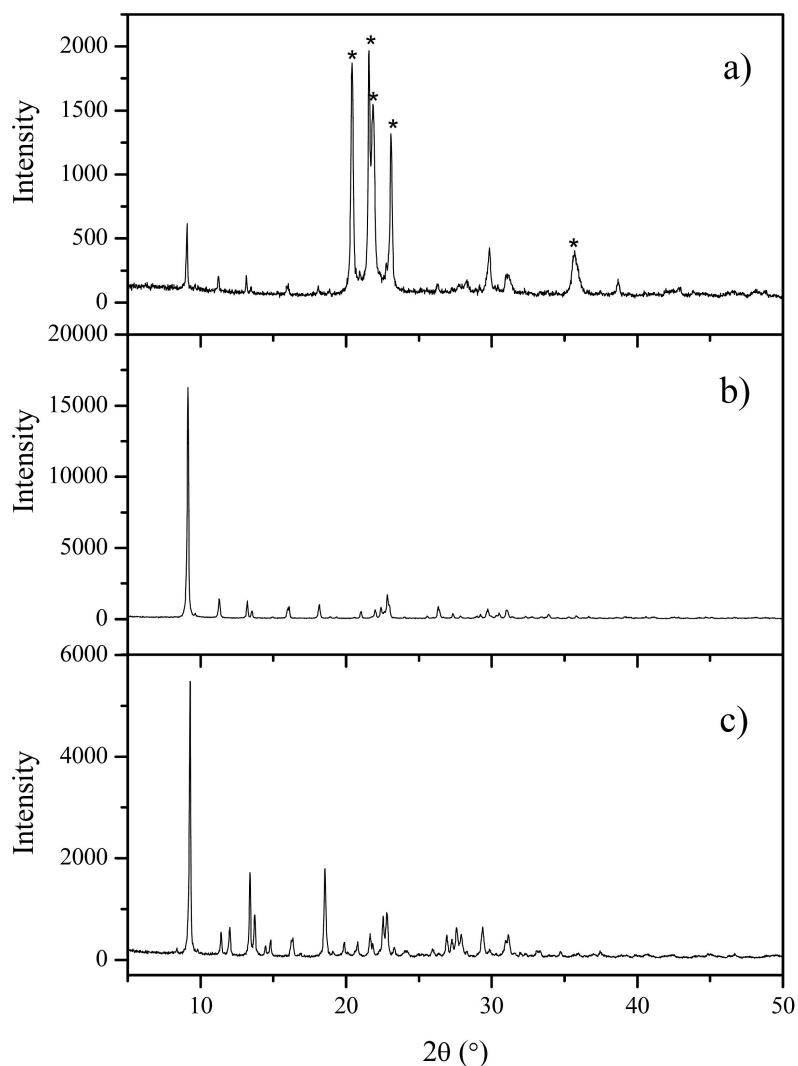


**Figure 4.16:** PXRD pattern for a sample obtained using a preparation proposed by Antonijevic et al.: a) crystallized at 160°C for 10 hours (as-synthesized); b) crystallized at 160°C for 24 hours (as-synthesized); c) same as b) after calcination at 600°C for 2 h in a preheated oven. The \* indicates peaks consistent with tridymite.

parameters to see if a more positive result could be obtained. Since varying the temperature had little effect (see above) it was kept constant and the attention was directed towards altering the molar oxide ratio of the gel. The variables tested were: Al content, water content, template content, addition of acids ( $\text{H}_2\text{SO}_4$ ,  $\text{CH}_3\text{COOH}$ ), stirring (where possible), and aluminum source. The starting point for the parameter testing was the preparation for  $\text{ipaAlPO}_4\text{-14F}^6$ , using a gel of molar oxide ratio of  $1\text{R}:\text{Al}_2\text{O}_3:\text{P}_2\text{O}_5:40\text{H}_2\text{O}$  (R = isopropylamine) crystallized at 200°C for 24 h. As none of the published or patented preparations yielded phase-pure  $\text{AlPO}_4\text{-14}$ , this preparation was seen as a good a starting point as any.

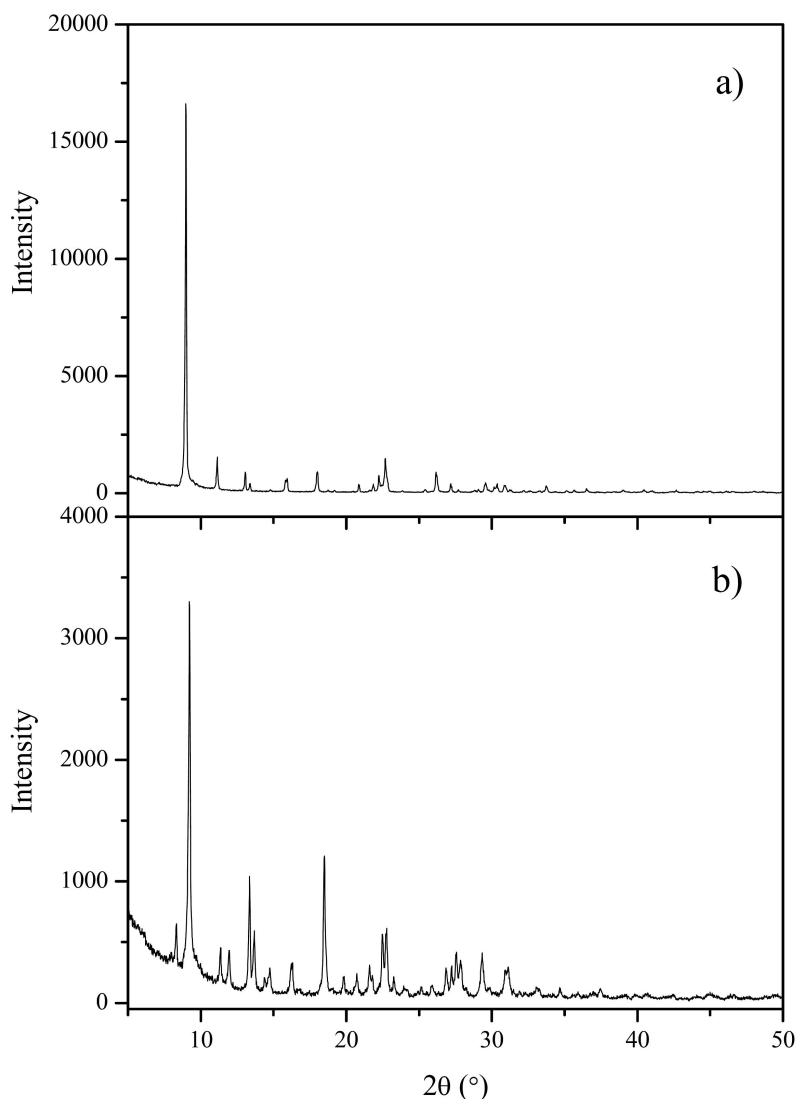


**Figure 4.17:** PXRD pattern for a sample obtained using a molar oxide ratio: 1R:Al<sub>2</sub>O<sub>3</sub>:P<sub>2</sub>O<sub>5</sub>:35H<sub>2</sub>O crystallized at 175°C for 30 h: a) as-synthesized; b) calcined at 600°C for 3 h in a preheated oven.

**Parameter 1: The presence of copper or silicon in the synthesis gel** During the work with first generation AlPO<sub>4</sub>-14, a natural progression was to try to incorporate copper or silicon into the framework. This resulted in the CuAPO<sub>4</sub>-14F and SAPO<sub>4</sub>-14F compositions respectively. The results obtained (as shown in previous sections) indicated that no other phases than AlPO<sub>4</sub>-14F or tridymite was favored during the crystallization of these materials. Also, the lowering of crystallization temperature to 150°C in the case of the CuAPO<sub>4</sub>-14F compositions did not have a profound effect on the phases formed either.

**Parameter 2: The aluminum and phosphorous ratio** The aluminum content of the synthesis gel was altered to see if there was a correlation between it and phases formed. When crystallizing a gel of molar oxide ratio: 1R:0.75Al<sub>2</sub>O<sub>3</sub>:P<sub>2</sub>O<sub>5</sub>:40H<sub>2</sub>O at 200°C for 24 h, the

diffraction pattern for the as-synthesized sample had reflections reminiscent of the “impurity”  $\text{AlPO}_4\text{-14A}$  (in addition to a tridymite phase). This eventually led to a series of experiments concerned with obtaining phase-pure  $\text{AlPO}_4\text{-14A}$  (see subsection 4.1.7). It is obvious from the diffraction pattern in figure 4.18 a) that a low alumina content favors one of the impurities, and naturally the next step was to try to add more alumina to possibly promote the crystallization of  $\text{AlPO}_4\text{-14}$ . Thus, gels with molar oxide composition:  $1\text{R}:1.15\text{Al}_2\text{O}_3:\text{P}_2\text{O}_5:40\text{H}_2\text{O}$  and

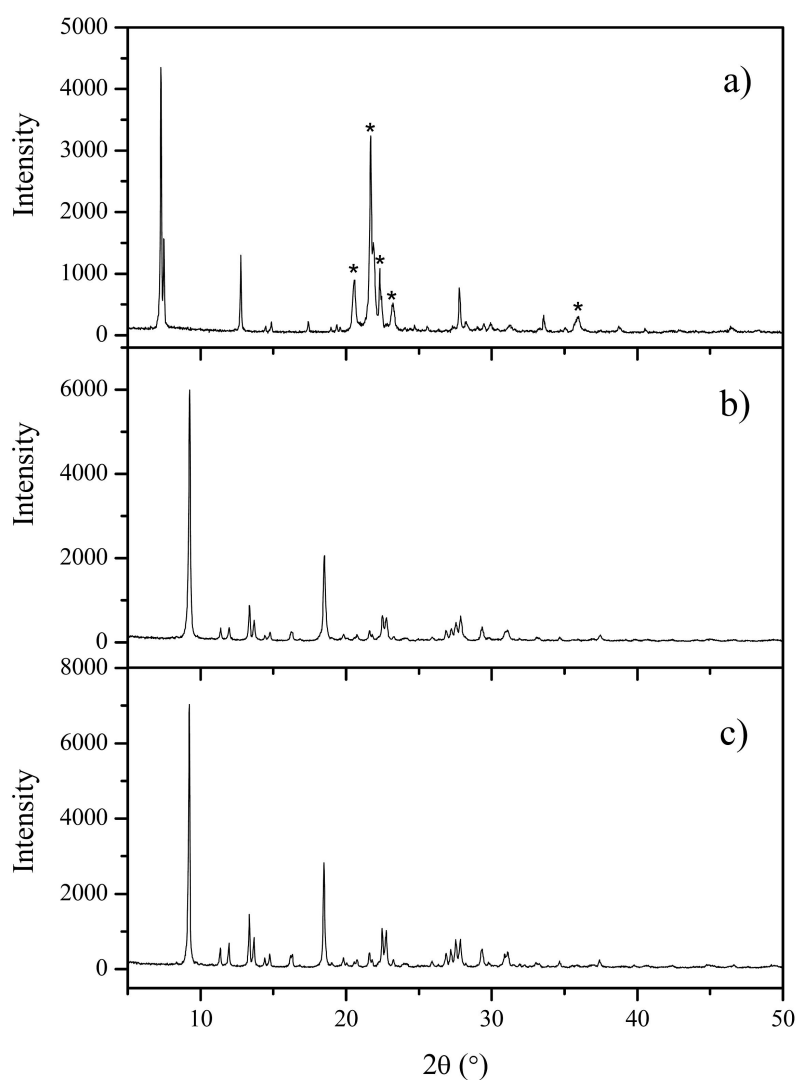


**Figure 4.18:** PXRD patterns samples obtained from a gels crystallized for 24 hours at  $200^\circ\text{C}$ , and having the molar oxide ratios: a)  $1\text{R}:0.75\text{Al}_2\text{O}_3:\text{P}_2\text{O}_5:40\text{H}_2\text{O}$  (as-synthesized); b)  $1\text{R}:1.15\text{Al}_2\text{O}_3:\text{P}_2\text{O}_5:40\text{H}_2\text{O}$  (calcined); c)  $1\text{R}:1.5\text{Al}_2\text{O}_3:\text{P}_2\text{O}_5:40\text{H}_2\text{O}$  (calcined). The samples in (b) and (c) were calcined in a preheated oven at  $600^\circ\text{C}$  for 3 h. The \* indicates peaks that are in agreement with a tridymite phase.

$1\text{R}:1.5\text{Al}_2\text{O}_3:\text{P}_2\text{O}_5:40\text{H}_2\text{O}$  was crystallized for 24 h at  $200^\circ\text{C}$ . Although low alumina content of the synthesis gels favor  $\text{AlPO}_4\text{-14A}$ , the diffraction patterns in figure 4.18 show that high alumina content does not favor any of the three phases, and  $\text{AlPO}_4\text{-14F}$  is formed.

**Parameter 3: The water content of the synthesis gel** The water content of the gel was modified with respect to that of the original preparation:  $1\text{R}:\text{Al}_2\text{O}_3:\text{P}_2\text{O}_5:40\text{H}_2\text{O}^6$ . Figure 4.19 shows the diffraction pattern for an as-synthesized sample crystallized at  $200^\circ\text{C}$  for 24h from a gel with molar oxide ratio:  $1\text{R}:\text{Al}_2\text{O}_3:\text{P}_2\text{O}_5:25\text{H}_2\text{O}$ . As can be seen from the figure, the reduced water content of the synthesis gel favored the  $\text{AlPO}_4\text{-14A}$  phase as well as the  $\text{AlPO}_4\text{-14}$  phase. Usually, the remnants of the  $\text{AlPO}_4\text{-14A}$  phase is only visible in the calcined samples, and then only a few peaks are present (see figure 4.3). In the diffraction pattern for the as-synthesized sample obtained from this composition, characteristic peaks of as-synthesized  $\text{AlPO}_4\text{-14A}$  are clearly visible. This indicates that synthesis gels with low water content shift the conditions to favor impurity phases as well as the intended one, and that water content plays a role in controlling the phases formed. Figure 4.20 a) and b) shows that increasing the water content only serves to promote tridymite.

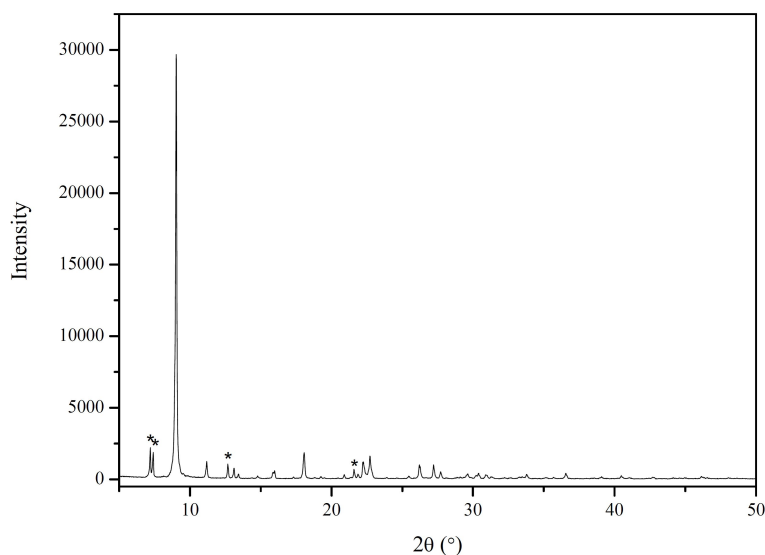


**Figure 4.19:** PXRD patterns for an as-synthesized sample obtained from a gel with the molar oxide ratio:  $1\text{R}:\text{Al}_2\text{O}_3:\text{P}_2\text{O}_5:25\text{H}_2\text{O}$ , crystallized for 24 hours at  $200^\circ\text{C}$ . The \* indicates peaks from the phase  $\text{AlPO}_4\text{-14A}$ .

**Parameter 4: The template content of the synthesis gel** Figure 4.21 shows the effect of altering the template content of the synthesis gel, showing both the effect of reducing as well as increasing it. As the template content is lowered, a tridymite phase co-crystallizes in addition to the  $\text{AlPO}_4\text{-14F}$  phases. Increased template content of the synthesis gel has initially no effect (2R) and  $\text{AlPO}_4\text{-14F}$  crystallizes. When the template content is further increased, however, only tridymite crystallizes.

**Parameter 5: The effect of additional acids** Adding an additional acid (besides phosphoric acid) to the synthesis gels was done to modify their initial pH, and to see if that would affect the

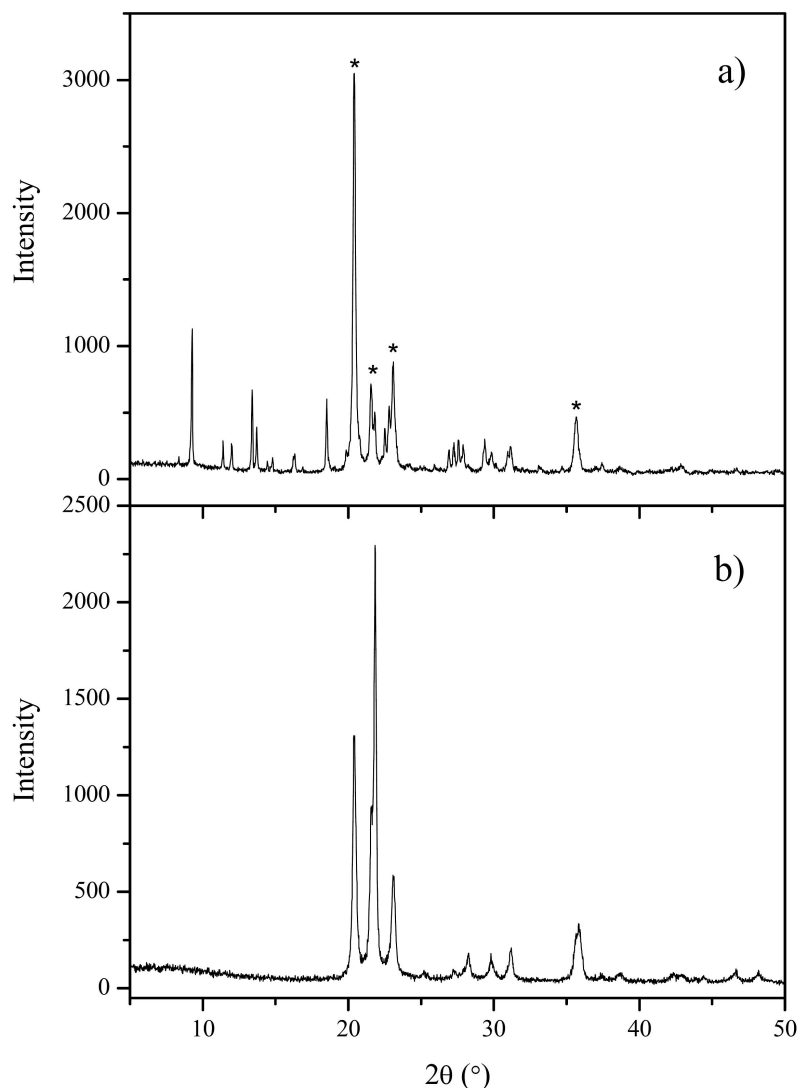


**Figure 4.20:** PXRD pattern for calcined samples obtained from a gel with the molar oxide ratios: a) 1R:Al<sub>2</sub>O<sub>3</sub>:P<sub>2</sub>O<sub>5</sub>:80H<sub>2</sub>O; b) 1R:Al<sub>2</sub>O<sub>3</sub>:P<sub>2</sub>O<sub>5</sub>:120H<sub>2</sub>O. The \* indicates peaks consistent with a tridymite phase. Both samples were calcined in a preheated oven at 600°C for 3 h.

phases formed. Two acids were tested: sulfuric and acetic acid. As can be seen in figure 4.22 a) the presence of 0.25 mol of sulfuric acid caused a tridymite phase to form in addition to low amounts of AlPO<sub>4</sub>-14F (very low intensity peaks). Increasing the crystallization time (figure 4.22 b)) or the H<sub>2</sub>SO<sub>4</sub> content further (figure 4.22 c)), resulted in phase-pure tridymite. It is interesting to note that the preparation presented by Zibrowius et al.<sup>116</sup> suggested a gel with high water and template content and the adding of sulfuric acid (assumably to regulate the pH), when neither seem to have a positive effect on the crystallization of AlPO<sub>4</sub>-14. The presence of acetic acid has a more dramatic effect than the co-crystallization of tridymite than the presence of sulfuric acid as shown above. Figure 4.23 shows that its presence has resulted in a pattern not characteristic for any of the three phases constituting AlPO<sub>4</sub>-14F. The results indicate that the

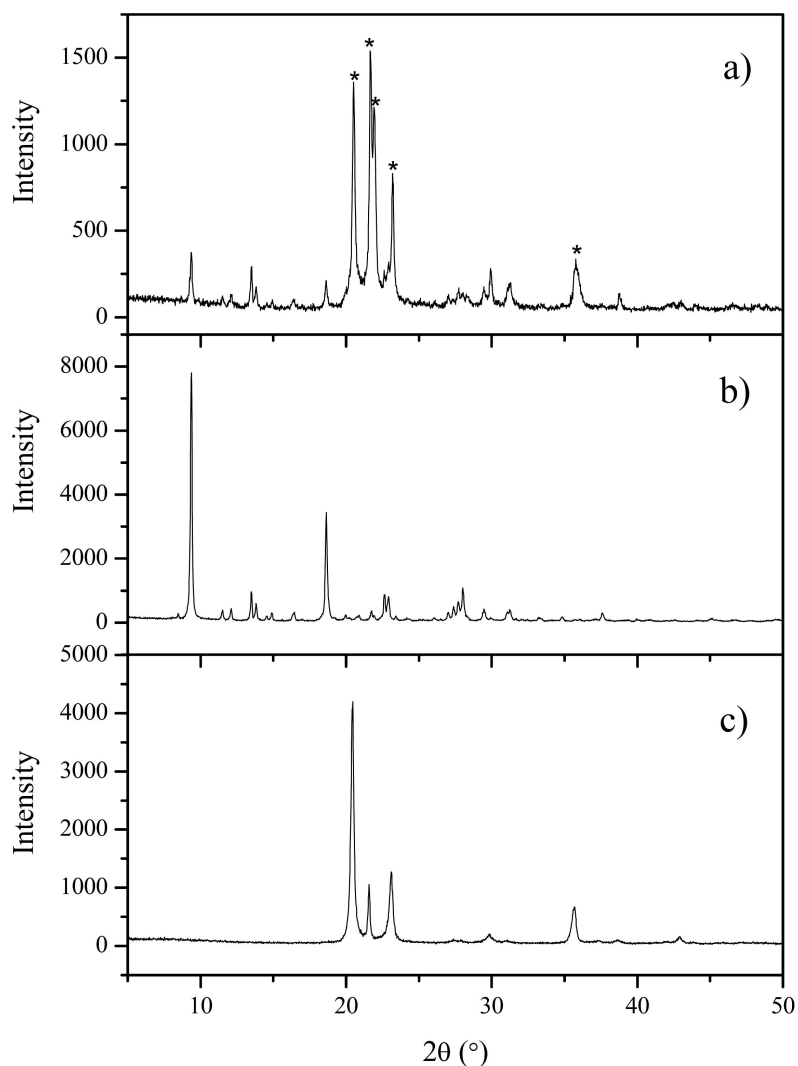


**Figure 4.21:** PXRD patterns for calcined samples obtained from gels crystallized for 24 hours at 200°C, and having the molar oxide ratios: a) 0.5R:Al<sub>2</sub>O<sub>3</sub>:P<sub>2</sub>O<sub>5</sub>:40H<sub>2</sub>O (pH of gel = 1), b) 2R:Al<sub>2</sub>O<sub>3</sub>:P<sub>2</sub>O<sub>5</sub>:40H<sub>2</sub>O (pH of gel = 5), and c) 3R:Al<sub>2</sub>O<sub>3</sub>:P<sub>2</sub>O<sub>5</sub>:40H<sub>2</sub>O (pH of gel = 7). The calcination process consisted of heating the materials in a preheated oven at 600°C for 3 h.

addition of acids other than phosphoric acid is not beneficial for the crystallization of AlPO<sub>4</sub>-14. It is worth noting, however, that the addition of sulfuric acid reduced the viscosity of the gels to the point where they are perhaps better described as mixtures.

**Parameter 6: The effect of stirring** The problem with stirring during crystallization was directly linked to the viscosity of the gels. The preparation proposed by Broach et al.<sup>29</sup> involved crystallizing a highly viscous gel, something that was not possible with the improvised autoclaves. As was mentioned above, the adding of sulfuric acid drastically reduced the viscosity, and was seen as an opportunity to test the effect of stirring during crystallization. Therefore, a

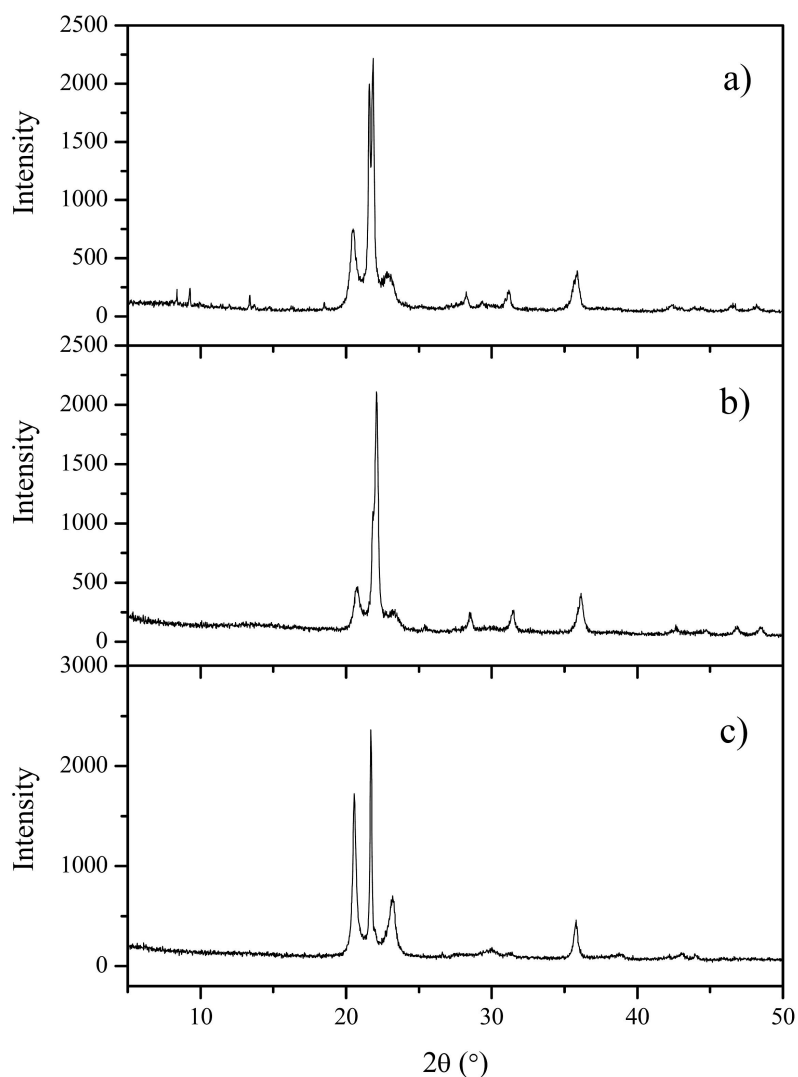


**Figure 4.22:** PXRD patterns for as-synthesized samples obtained from gels of varying molar oxide ratio and  $\text{H}_2\text{SO}_4$  content: a)  $1\text{R}:\text{Al}_2\text{O}_3:\text{P}_2\text{O}_5:0.25\text{H}_2\text{SO}_4:40\text{H}_2\text{O}$  (pH of mixture = 3) crystallized for 24 h at  $200^\circ\text{C}$  (pH of mixture = 2-3); b) same as (a) crystallized for 48 h; c)  $1\text{R}:\text{Al}_2\text{O}_3:\text{P}_2\text{O}_5:0.5\text{H}_2\text{SO}_4:40\text{H}_2\text{O}$  (pH of mixture = 2).

gel with molar oxide ratio:  $\text{R}:\text{Al}_2\text{O}_3:\text{P}_2\text{O}_5:0.25\text{H}_2\text{SO}_4:40\text{H}_2\text{O}$  ( $\text{R}$  = isopropylamine) was crystallized with stirring for 24 h at  $200^\circ\text{C}$ . It is obvious from figure 4.24 a) that stirring has an effect when compared to the unstirred synthesis (see figure 4.22 b)). As was shown above, the same preparation without stirring yielded  $\text{AlPO}_4\text{-14}$  and tridymite. With stirring, there is less tridymite as well as some low-intensity peaks of  $\text{AlPO}_4\text{-14}$ . This was seen as an indication that the stirring had partially counteracted the effect of the sulfuric acid (possibly diluting it), but it still did not lead to phase-pure  $\text{AlPO}_4\text{-14}$ .

The preparation by Zibrowius et al.<sup>34</sup> for pip $\text{AlPO}_4\text{-14}$  yielded no product when stirring was applied. The only observable change was that a dark liquid had formed, and the pH had

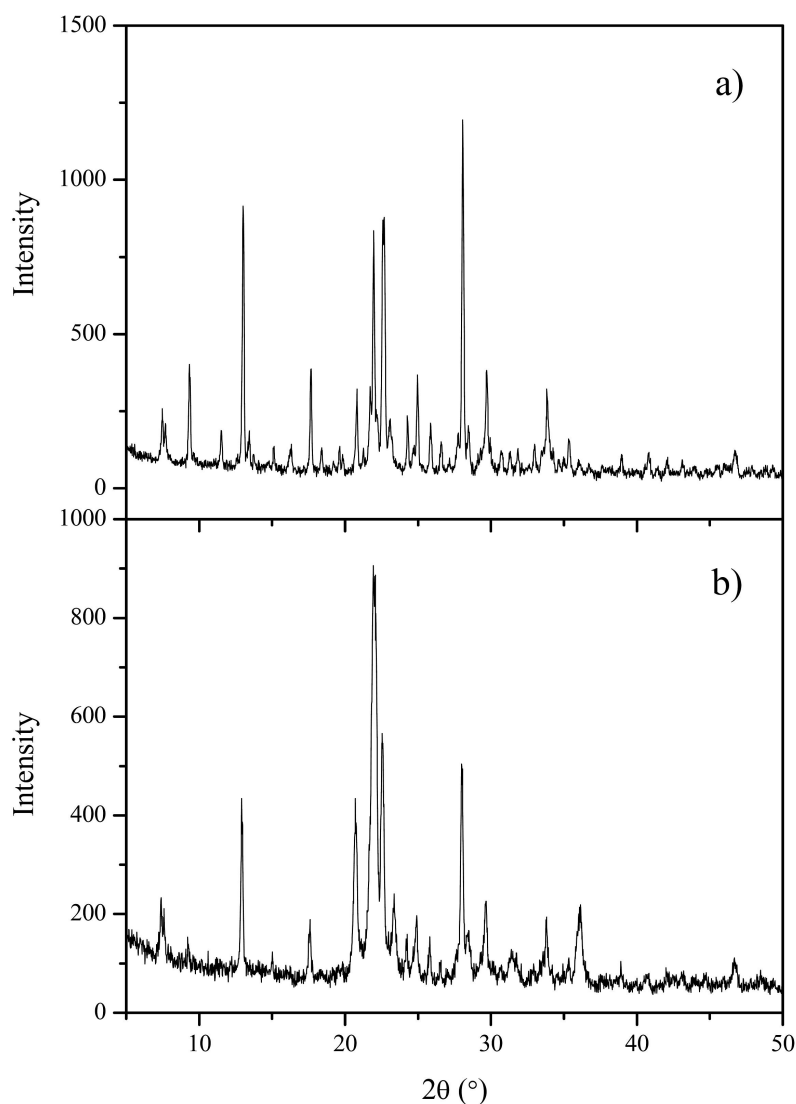


**Figure 4.23:** PXRD patterns for as-synthesized samples obtained from gels of varying molar oxide ratio and  $\text{CH}_3\text{COOH}$  content: a) R: $\text{Al}_2\text{O}_3$ : $\text{P}_2\text{O}_5$ : $0.25\text{CH}_3\text{COOH}$ : $40\text{H}_2\text{O}$  crystallized for 24 h at  $200^\circ\text{C}$ ; b) R: $\text{Al}_2\text{O}_3$ : $\text{P}_2\text{O}_5$ : $0.5\text{CH}_3\text{COOH}$ : $40\text{H}_2\text{O}$ . The pH of both gels = 3.

increased from 4.5 to 7 during crystallization. Stirring during crystallization was also applied to the preparation for ipa $\text{AlPO}_4$ -14 by the same authors. After 40 h a sample was obtained that had a pattern somewhat resembling calcined  $\text{AlPO}_4$ -14 (see figure 4.25 a) and figure text for details), but due to the varying width of observed peaks it was recognized as a blend of phases. The same preparation repeated with increased crystallization times eventually led to the formation of tridymite (see patterns in figure 4.25 b) and c).

**Parameter 7: The source for aluminum and phosphorous** The final parameter tested for the synthesis of phase-pure  $\text{AlPO}_4$ -14 was varying the chemicals used as sources for aluminum and phosphorous. The only other chemical tested as a potential phosphorous source

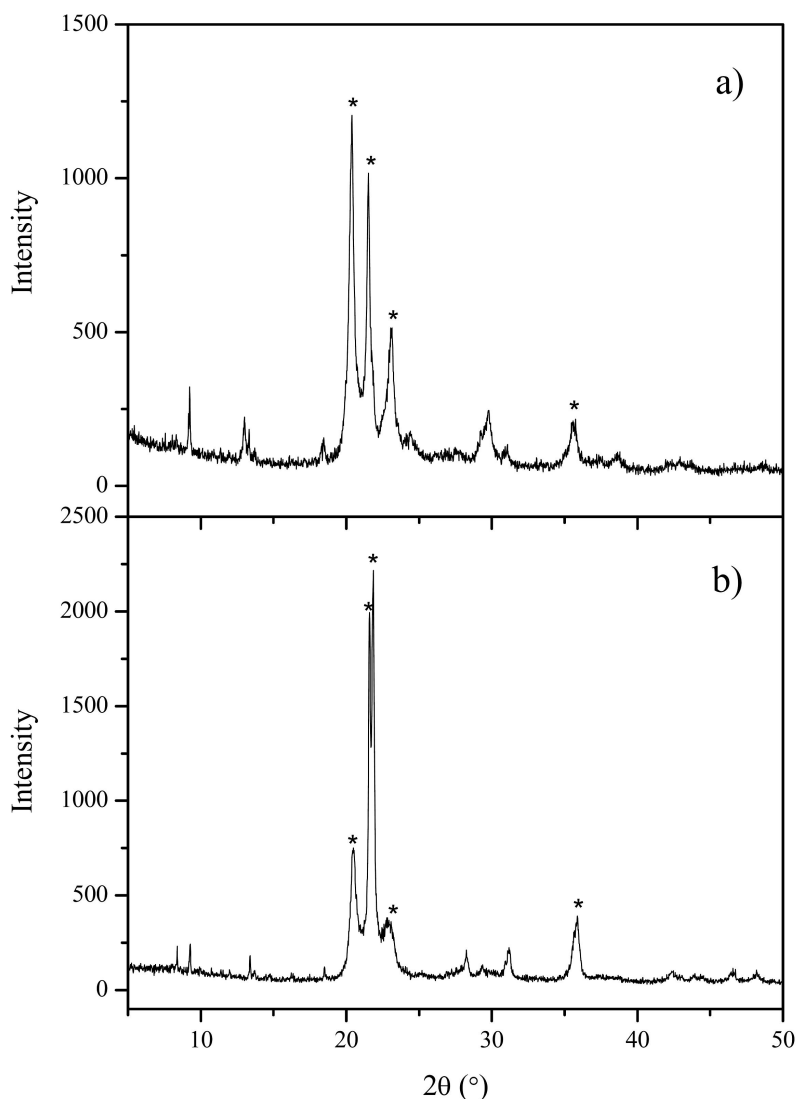


**Figure 4.24:** PXRD patterns for calcined samples obtained from a gel of molar oxide ratio:  $1\text{R}:\text{Al}_2\text{O}_3:\text{P}_2\text{O}_5:0.25\text{H}_2\text{SO}_4:40\text{H}_2\text{O}$ : a) with stirring; b) without stirring. The materials were calcined in a preheated oven at  $600^\circ\text{C}$  for 3 h.

was phosphorous pentoxide ( $\text{P}_2\text{O}_5$ ). This chemical, however, only resulted in the formation of gel products during crystallization. The chemicals tested as aluminum source were aluminum isopropoxide and hydrated alumina. Figure 4.26 shows the diffraction patterns for the samples obtained when using these chemicals and the molar oxide ratio:  $1\text{R}:\text{Al}_2\text{O}_3:\text{P}_2\text{O}_5:40\text{H}_2\text{O}$ . As the patterns indicate, the alternative sources for aluminum has little to no effect on the phases formed, and the result is  $\text{AlPO}_4\text{-14F}$ . The work on synthesizing phase-pure  $\text{AlPO}_4\text{-14}$  was abandoned.

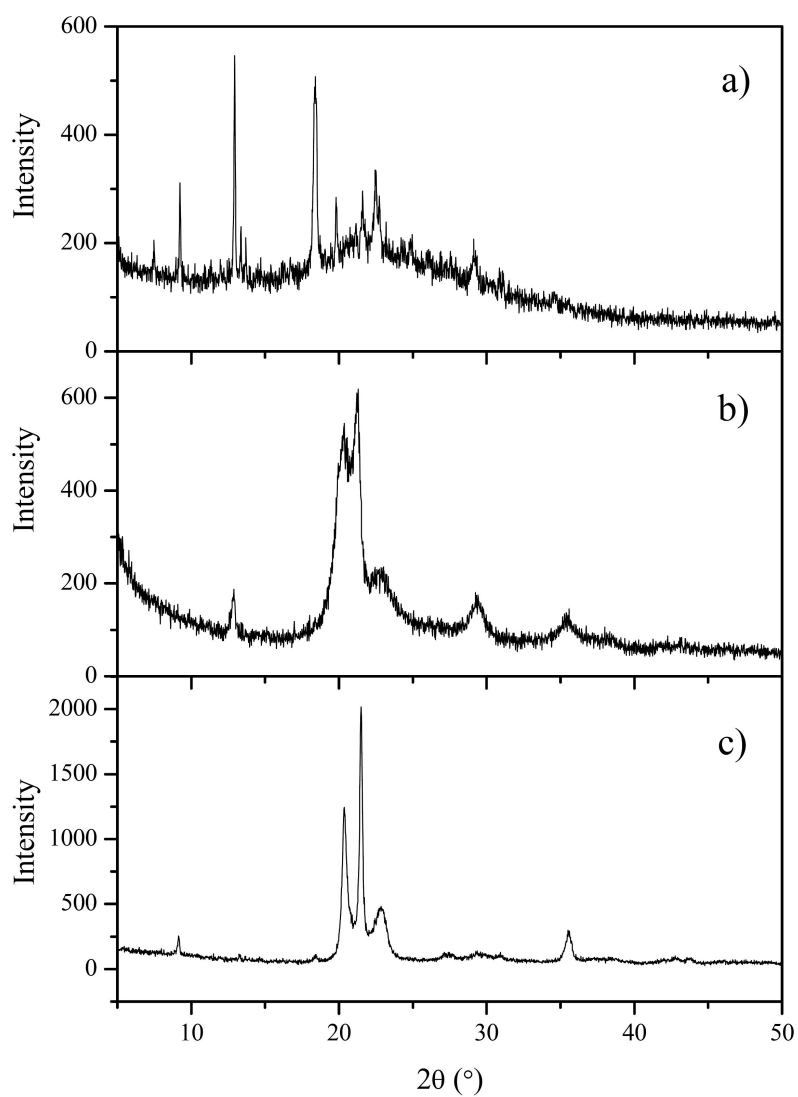


**Figure 4.25:** PXRD patterns for calcined samples obtained using improvised stirred autoclaves and gels with the molar oxide ratio:  $2R:Al_2O_3:P_2O_5:0.25H_2SO_4:100H_2O$ , aged for 1 h, crystallized at  $180^\circ C$  for: a) 40 h b) 4 h c) 96 h. The materials were calcined in a preheated oven at  $600^\circ C$  for 3 h.

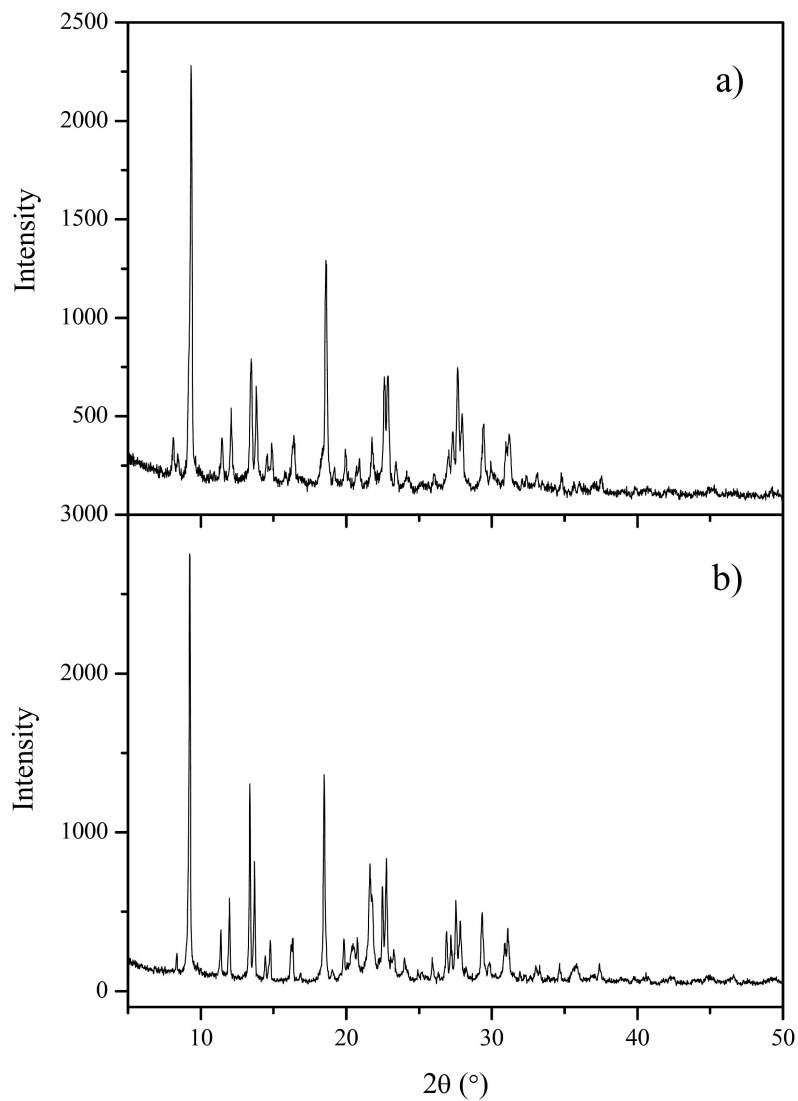


**Figure 4.26:** PXRD patterns for calcined samples obtained by crystallizing a gel with molar oxide ratio:  $1R:Al_2O_3:P_2O_5:40H_2O$  at  $200^\circ C$  for 24 h using different sources of aluminum: a) Aluminum isopropoxide; b) hydrated alumina.

### 4.1.7 ipaAlPO<sub>4</sub>-14A

#### as-synthesized

During the work with trying to synthesize phase-pure AlPO<sub>4</sub>-14, one of the variables tested was the aluminum content of the synthesis gel. From a gel of molar oxide ratio 1R:0.75Al<sub>2</sub>O<sub>3</sub>:P<sub>2</sub>O<sub>5</sub>:40H<sub>2</sub>O (R = isopropylamine) crystallized for 24 hours at 200°C, a phase was obtained that resembled AlPO<sub>4</sub>-14A more than AlPO<sub>4</sub>-14. The diffraction pattern for the product obtained is shown in figure 4.27 a).

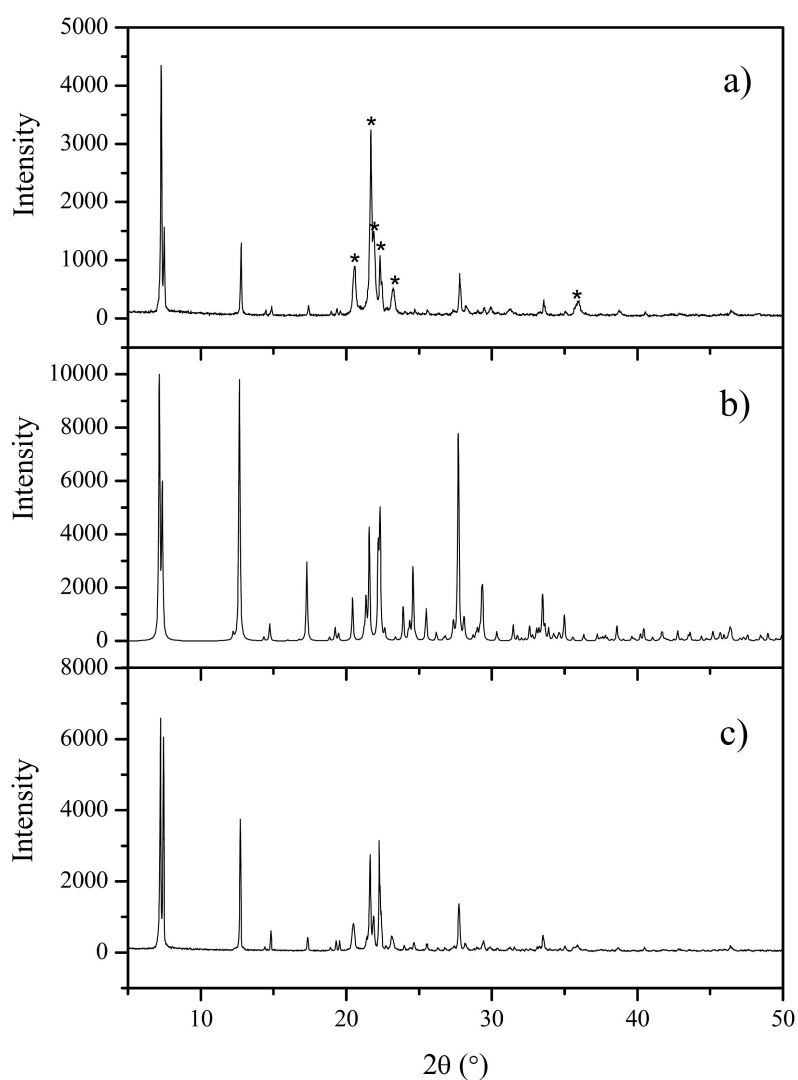


**Figure 4.27:** PXRD patterns for: an as-synthesized sample obtained from a gel with the molar oxide ratio: 1R:0.75Al<sub>2</sub>O<sub>3</sub>:P<sub>2</sub>O<sub>5</sub>:40H<sub>2</sub>O, crystallized for 24 hours at 200°C (pH of gel = 2); b) simulated pattern for ipaAlPO<sub>4</sub>-14A from single-crystal studies<sup>30</sup>; c) sample obtained using the same gel as in (a) but crystallized for 48 h. The \* indicates peaks consistent with the phase tridymite.

The reflections are roughly in agreement with that reported for AlPO<sub>4</sub>-14A by M. Goepper

and J.L. Guth<sup>114</sup>, but visible are also peaks from a dense tridymite phase that also crystallized in the time stated. Also shown is a simulated pattern for AlPO<sub>4</sub>-14A, generated from the single-crystal data published by J.J. Pluth and J.V. Smith<sup>30</sup> (the CIF written from their data is supplied in Appendix B.2.1, and the pattern was simulated using a freeware base version of the crystallographic program Mercury version 2.3<sup>117</sup>). This pattern is also representable for the powder pattern published by M. Goepper and J.L. Guth<sup>114</sup>.

To try to avoid the co-crystallization of the tridymite phase, an additional experiment was run using the same molar oxide ratio of the synthesis gel. The temperature was the same as before, but the crystallization time was increased to 48 h. The diffraction patterns for the as-synthesized sample obtained is shown in figure 4.27 c). It can be seen from this figure that an increase in crystallization time removes the tridymite phase, and more AlPO<sub>4</sub>-14A crystallizes. This supports the notion of tridymite existing as a precursor to AlPOs. The pattern in figure 4.27 c) is still somewhat inconsistent with the published diffraction pattern for AlPO<sub>4</sub>-14A, particularly around 22° where the doublet is slightly shifted (to higher angle) and the intensity is inverted. The positions of the peaks for AlPO<sub>4</sub>-14A and tridymite were not readily distinguishable after 48 h, and so no assignments were made. The difference itself may be linked to the aluminum deficiency in the molar oxide ratio.

In the article published by Goepper and Guth<sup>114</sup>, the authors mentioned in their concluding remarks that they did not fully understand the role of the hydrofluoric acid (HF). They suggested that the fluoride ions somehow regulated the concentration of aluminum and phosphorous in the reaction mixture during crystallization. In a review article, C.S. Cundy and P.A. Cox<sup>118</sup> discussed the role of mineralizers (such as OH<sup>-</sup> and F<sup>-</sup>) in the synthesis of Zeolites, and attributed the following properties as characteristic of a good mineralizer:

1. convert starting materials into mobile units (form complexes)
2. convey chemical reactivity of these mobile units
3. de-complex from the mobile units to allow the formation of stable structures

In their discussion of F<sup>-</sup> as a mineralizer, the authors highlighted the presence of Si(OH)<sub>3</sub>F and Al(OH)<sub>3</sub>F<sup>-</sup> species, which is partially relevant to the present topic. The absence of Si in AlPO syntheses excludes the Si(OH)<sub>3</sub>F species, but it is likely that the Al(OH)<sub>3</sub>F<sup>-</sup> species contribute to the crystallization of AlPO<sub>4</sub>-14A in fluoride medium. If the de-complexing stage is sufficiently slow compared to the building of the framework, this could provoke the AlPO<sub>4</sub>-14A phase in the same way as a lowering of aluminum concentration. The fact that the fluoride complexes may only hinder the transport of aluminum, and that it is not partially absent as in the sample from this work, could explain the differences in the observed diffraction patterns of the as-synthesized materials.

Although the increased crystallization time showed promise in the fact that the impurity peaks gradually faded away, time alone was not sufficient to obtain phase-pure as-synthesized

$\text{AlPO}_4\text{-14A}$  in acidic medium. Even after 9 days the pattern is still inconsistent, as shown in figure 4.28 a). In addition, peaks of  $\text{AlPO}_4\text{-14}$  have appeared, indicating that the duration of the experiment enabled its suppressed crystallization to reach a concentration high enough to be detected with PXRD.

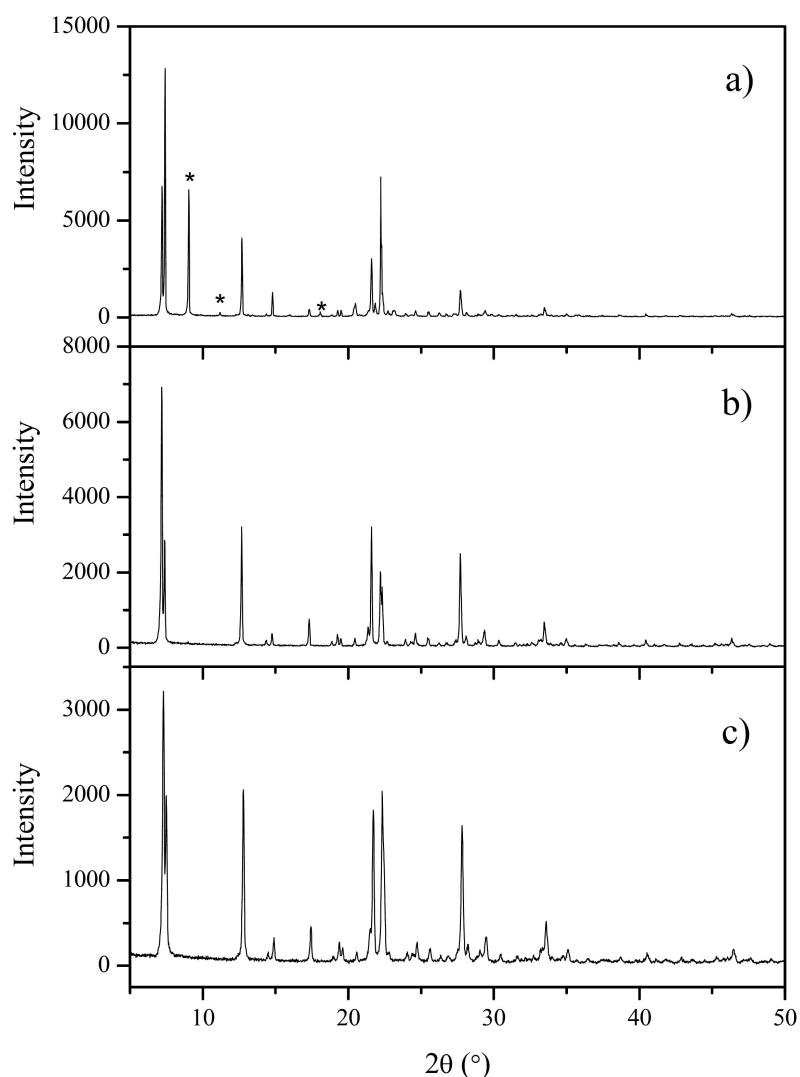


**Figure 4.28:** PXRD patterns for samples obtained from gels with the molar oxide ratios: a)  $1\text{R}:0.75\text{Al}_2\text{O}_3:\text{P}_2\text{O}_5:40\text{H}_2\text{O}$ , crystallized for 9 days at  $200^\circ\text{C}$ . The \* indicates peaks from the phase  $\text{AlPO}_4\text{-14}$ ; b)  $4\text{R}:\text{Al}_2\text{O}_3:\text{P}_2\text{O}_5:200\text{H}_2\text{O}$  (pH of mixture = 10) crystallized for 24 hours at  $200^\circ\text{C}$ ; c)  $4\text{R}:\text{Al}_2\text{O}_3:\text{P}_2\text{O}_5:200\text{H}_2\text{O}$  (pH of mixture = 10) crystallized for 144 hours at  $200^\circ\text{C}$ .

Another preparation for  $\text{ipaAlPO}_4\text{-14A}$  was found using a mixture with molar oxide ratio:  $4\text{R}:\text{Al}_2\text{O}_3:\text{P}_2\text{O}_5:200\text{H}_2\text{O}$  (R = isopropylamine) crystallized for 24 hours at  $200^\circ\text{C}$ . The mindset behind the molar oxide ratio was to increase the template and water content to push the pH of the mixture beyond neutral, and to see if an  $\text{AlPO}$  was obtainable under alkaline conditions. As a result, the mixture had an initial pH of 10, and after crystallization the pH of the liquid

phase surrounding the product powder was 11. The diffraction pattern for the sample obtained is shown in figure 4.28 b). The diffraction pattern for the as-synthesized sample indicates that, in a mixture of high pH, the phase  $\text{AlPO}_4\text{-14A}$  is favored over the phase  $\text{AlPO}_4\text{-14}$  which is completely absent. Even after 144 h, no signs of  $\text{AlPO}_4\text{-14}$  are present in the pattern (figure 4.28 c)). This also gives insight to why  $\text{AlPO}_4\text{-14F}$  contains  $\text{AlPO}_4\text{-14A}$  when the pH of the liquid phase surrounding the product is 10 after crystallization. The issue of obtaining phase-pure  $\text{AlPO}_4\text{-14}$  may then be directly related to the pH of the gel during crystallization. The problem with working with gels that are initially acidic may be that during crystallization the phosphoric acid is converted to constituent  $\text{PO}_4$  building blocks, which in turn may raise the pH of the crystallization medium.

It can be seen from the diffraction pattern that even though the crystallization time for  $\text{AlPO}_4\text{-14A}$  was only 24 hours, no tridymite impurity phase is present. In contrast to the patterns obtained from samples synthesized under acidic conditions, this pattern is in agreement with both the published pattern by Goepper and Guth<sup>114</sup> as well as the simulated pattern<sup>30</sup>. Based on this, the material was determined to be phase-pure in as-synthesized form. The crystallization of  $\text{ipaAlPO}_4\text{-14A}$  is thus faster in alkaline medium and produces a phase-pure as-synthesized product. Also, as opposed to the preparation in acidic medium, this preparation has no aluminum deficiency in the molar oxide ratio ( $\text{Al:P} = 1$ ), which may indicate that the high pH somehow alters the mobility of the aluminum ions. It is probable that the  $\text{OH}^-$  ions act as mineralizers, and that their presence has a similar effect on the crystallization process as the  $\text{F}^-$  ions discussed previously.

Figure 4.29 a) shows a sample synthesized using the same preparation as above, but this time with the improvised stirred autoclave. The pattern is characteristic for  $\text{AlPO}_4\text{-14A}$ , but a peak of  $\text{AlPO}_4\text{-14}$  have appeared along with a drop in the overall intensity of observed peaks. This indicates that stirring promotes the  $\text{AlPO}_4\text{-14}$  phase in a mixture with a molar oxide ratio that would otherwise favor  $\text{AlPO}_4\text{-14A}$ . This also supports a hypothesis that stirred autoclaves is a necessity for obtaining phase-pure  $\text{AlPO}_4\text{-14}$ .

A preparation using less water in a synthesis gel was also tested (molar oxide ratio:  $4.36\text{R}:\text{Al}_2\text{O}_3:\text{P}_2\text{O}_5:40\text{H}_2\text{O}$ ), and also resulted in phase-pure as-synthesized  $\text{AlPO}_4\text{-14A}$  as can be seen in figure 4.29 b). The simulated pattern is shown in figure 4.29 c) to enable direct comparison.

As-synthesized  $\text{AlPO}_4\text{-14A}$  possesses some interesting structural features and a discussion of these is relevant for the following characterization of the material (and first generation (F) sieves). Normally, AlPOs are constructed of strictly alternating  $[\text{PO}_4]^{3-}$  and  $[\text{AlO}_4]^{5-}$  tetrahedra, making them charge neutral<sup>7</sup>. The substitution for some of the  $[\text{PO}_4]^{3-}$  by  $[\text{SiO}_4]^{4-}$  tetrahedra in SAPOs is well known, and results in acid sites in the form of Si-OH-Al linkages (bridging hydroxyls)<sup>92</sup>. In the case of  $\text{AlPO}_4\text{-14}$ , the presence of occluded template,  $\text{H}_2\text{O}$ , and  $\text{OH}^-$  in the material's pores causes five- and six-coordination of some Al sites. These higher coordinated Al sites are, however, removed upon calcination resulting in only four-coordinated Al species<sup>29</sup>.

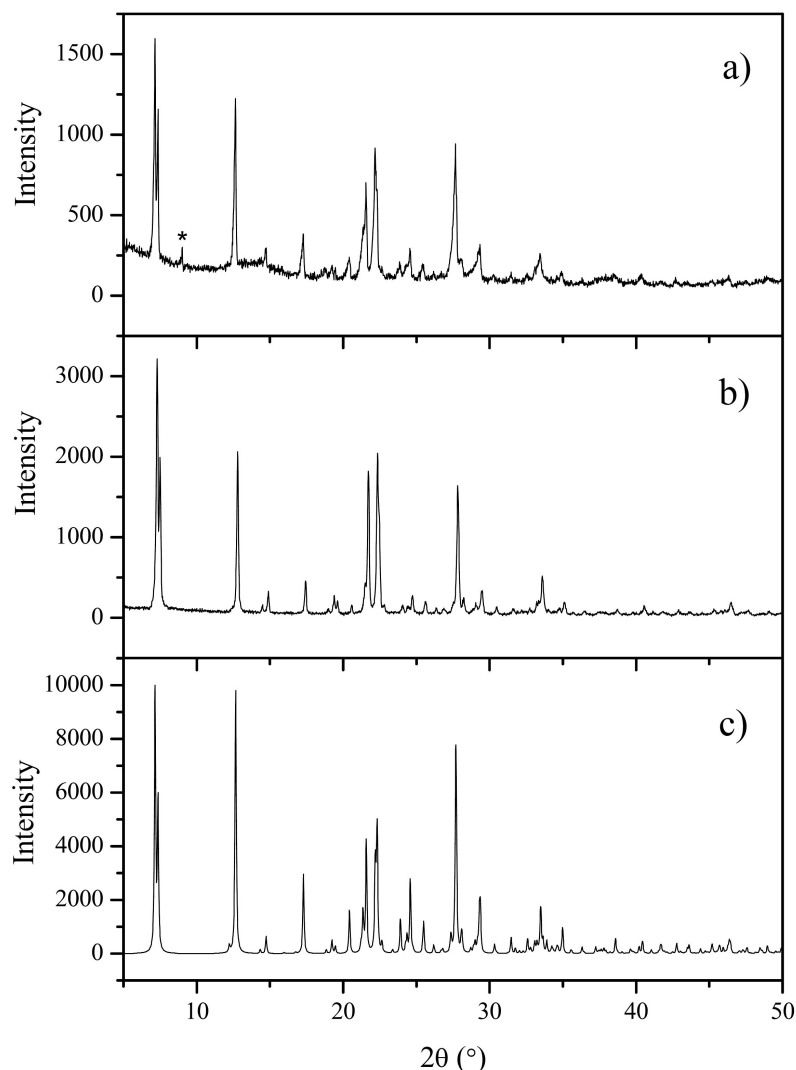


**Figure 4.29:** PXRD patterns for: a) a sample obtained from a mixture with molar oxide ratio: 4R:Al<sub>2</sub>O<sub>3</sub>:P<sub>2</sub>O<sub>5</sub>:200H<sub>2</sub>O (pH of mixture = 10) crystallized with stirring for 24 hours at 200°C. The \* indicates a peak consistent with AlPO<sub>4</sub>-14; b) a sample of ipaAlPO<sub>4</sub>-14A, obtained from a mixture with the molar oxide ratio: 4.36R:Al<sub>2</sub>O<sub>3</sub>:P<sub>2</sub>O<sub>5</sub>:40H<sub>2</sub>O (pH of mixture = 10), crystallized for 24 hours at 200°C; c) simulated pattern<sup>30</sup> for as-synthesized ipaAlPO<sub>4</sub>-14A.

The structure elucidation of AlPO<sub>4</sub>-14A by J.J. Pluth and J.V. Smith<sup>30</sup>, revealed a rather peculiar structure unit, namely an Al<sub>3</sub>P<sub>2</sub>O<sub>18</sub>H<sub>2</sub> cluster containing two tetrahedral P(4), one tetrahedral Al(1), and two octahedral Al(4) species. An excellent illustration of this cluster can be found in the article by Brouwer et al.<sup>119</sup>, and has been tried re-illustrated in figure 4.30. The five species form three 4-rings, where the two octahedral Al(4) species are connected to the tetrahedral Al(1) via bridging hydroxyls, or Al-OH-Al linkages. In a simplified manner, one can think of these linkages as Si-OH-Al linkages where the Si has been replaced by Al.

As pointed out by Brouwer et al.<sup>119</sup>, since the octahedral Al species are not the result of

coordination to occluded species in the pores, calcination should theoretically not lead to their destruction. The two Al-OH-Al sites are crystallographically equivalent, and is consistent with  $^1\text{H}$  MAS NMR<sup>119</sup> findings showing one resonance at 5 ppm.

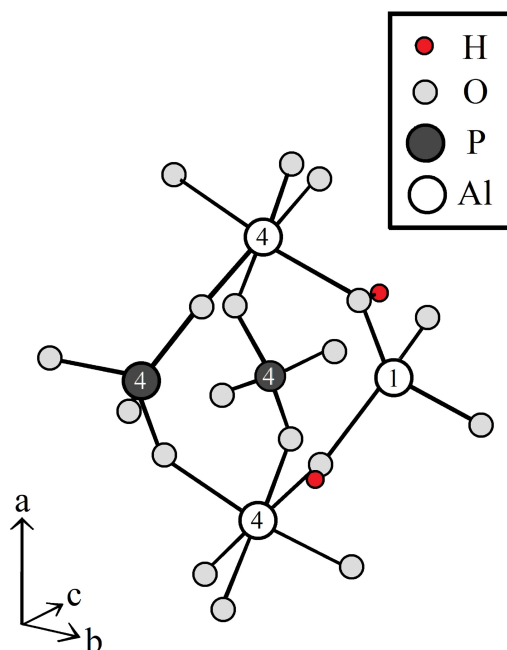


**Figure 4.30:** An illustration of the  $\text{Al}_3\text{P}_2\text{O}_{18}\text{H}_2$  cluster found in as-synthesized  $\text{AlPO}_4$ -14A.

### calcined

Figure 4.31 a) shows the diffraction pattern for a sample of  $\text{AlPO}_4$ -14A obtained from a gel with the molar oxide ratio:  $4\text{R}:\text{Al}_2\text{O}_3:\text{P}_2\text{O}_5:200\text{H}_2\text{O}$  after calcination at  $600^\circ\text{C}$  for 3 hours. The pattern is distinctly different than the as-synthesized pattern, showing loss of intensity and a broad background. The calcination process has also revealed some peaks from calcined  $\text{AlPO}_4$ -14F, which may be the impurity peaks reported by Goepper and Guth<sup>114</sup> in their calcined sample made with HF. One may argue that the structural studies (NMR study by Brouwer et al.<sup>119</sup>) on their  $\text{AlPO}_4$ -14A sample should not have been published when calcination reveals impurities that may give erroneous data. The pattern also enables assignments of peaks in first generation samples, and also shows that no phase transition to tridymite occurs during calcination.

The benefit of crystallizing a gel with a relatively lower water content can be seen in figure 4.31 b), showing the diffraction pattern for a calcined sample crystallized from a gel with the molar oxide ratio:  $4.36\text{R}:\text{Al}_2\text{O}_3:\text{P}_2\text{O}_5:40\text{H}_2\text{O}$  (temperature =  $200^\circ\text{C}$ , crystallization time = 24 h). The figure shows that although parts of the material have been lost during calcination, none of the previous mentioned  $\text{AlPO}_4$ -14F peaks have appeared. This shows that regardless of the pH of the gel, low water content favors the  $\text{AlPO}_4$ -14A phase. This preparation not only leads to  $\text{AlPO}_4$ -14A without the use of HF, but also prevents the formation of  $\text{AlPO}_4$ -14F impurity phases. Also, the aging step ( $20^\circ\text{C}$  for 1 h) prior to crystallization proposed by

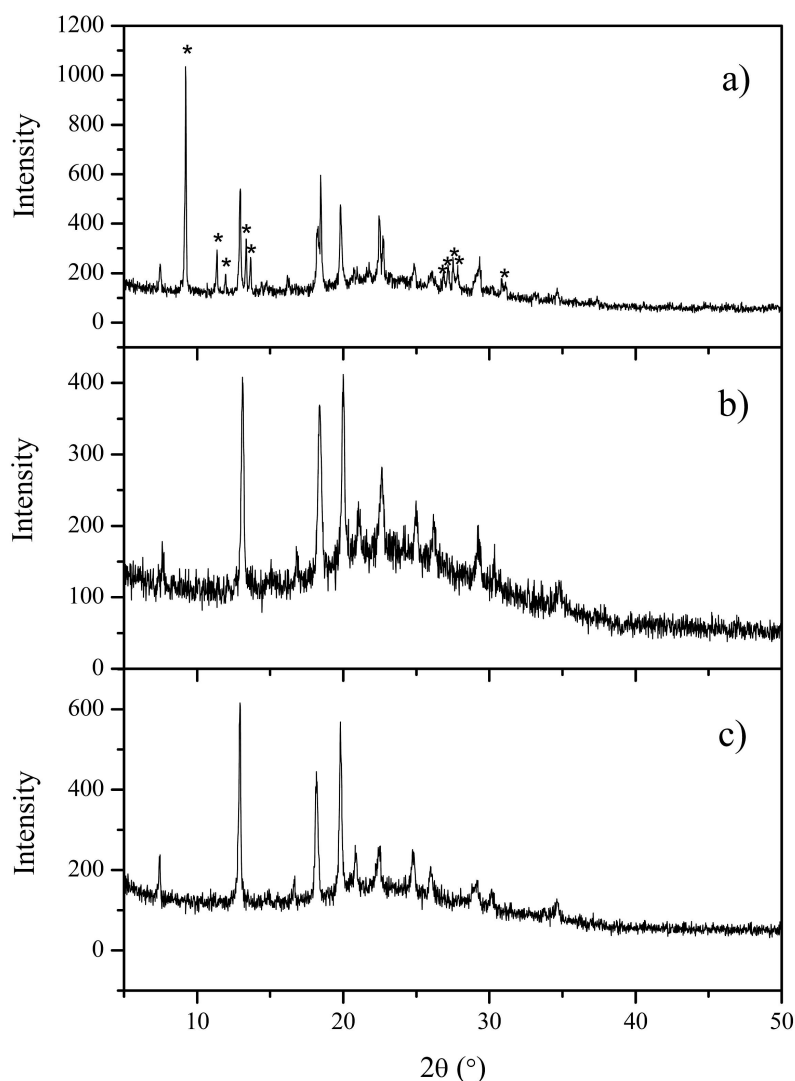


**Figure 4.31:** The PXRD patterns for calcined samples obtained from gels (pH = 10 in both cases) with the molar oxide ratios: a) 4R:Al<sub>2</sub>O<sub>3</sub>:P<sub>2</sub>O<sub>5</sub>:200H<sub>2</sub>O crystallized for 24 h at 200°C; b) 4.36R:Al<sub>2</sub>O<sub>3</sub>:P<sub>2</sub>O<sub>5</sub>:40H<sub>2</sub>O crystallized for 24 h at 200°C. Both samples were calcined in a preheated oven at 600°C for 3 h. c) same as b) calcined by heating the material from 25 to 550°C at a rate of 1°C/min, and dwelling for 3 h. The \* indicates peaks that are in agreement with calcined AlPO<sub>4</sub>-14F.

Goepper and Guth<sup>114</sup> is not necessary when using the preparation from this work. The sample made with the molar oxide ratio: 4.36R:Al<sub>2</sub>O<sub>3</sub>:P<sub>2</sub>O<sub>5</sub>:40H<sub>2</sub>O (R = isopropylamine) will from hereon be referred to as AlPO<sub>4</sub>-14A. The diffraction pattern shown in figure 4.31 b) is the first ever reported diffraction pattern for phase-pure calcined AlPO<sub>4</sub>-14A. It is, however, uncertain how much of the original structure is left after the destructive process of calcination, and how this might affect the material's behavior as a potential catalyst. Of particular interest is the preservation of the Al-OH-Al sites. The material was also calcined by slow heating, but it can be seen from figure 4.31 c) that it had little effect.

To get a more defined diffraction pattern the sample was analyzed with PXRD for a second time. The slit was changed from 0.2 to 0.6 mm and the detector count time was increased fourfold. The resulting diffraction patterns (with and without background subtraction) is shown in figure 4.32. The difference between the patterns before and after background subtraction is remarkable. The unprocessed pattern shows a broad background feature starting at  $5^\circ$ , peaking at  $25^\circ$ , and continuing until  $40^\circ$ . This clearly demonstrates the magnitude of calcination on the material, since such a broad feature is characteristic for amorphous materials<sup>120</sup>.

Table 4.3 lists the experimental  $2\theta$  and corresponding d-spacings observed in this pattern, from hereon attributed to calcined  $\text{AlPO}_4$ -14A. It was noted that quite a few of the observed peaks were consistent with that of  $\text{AlPO}_4$ -5, indicating that the calcined structure of  $\text{AlPO}_4$ -14A may be a variation of the AFI topology. The indexing of these values to (possibly) a monoclinic unit cell is beyond the scope of this work.

**Table 4.3:** Experimental  $2\theta$  and d-spacings observed for calcined  $\text{AlPO}_4$ -14A.

$2\theta$ ( $^\circ$ )	d-spacing ( $\text{\AA}$ )
7.553	11.696
12.989	6.8102
16.674	5.312
18.243	4.859
19.812	4.478
20.943	4.238
22.513	3.946
24.487	3.580
26.015	3.422
29.153	3.061
30.138	2.963
34.626	2.588

### 4.1.8 ipaSAPO<sub>4</sub>-43

#### as-synthesized and calcined

The possibility for synthesizing SAPO<sub>4</sub>-14A was briefly investigated. Since the material naturally contains bridging hydroxyls, it was of interest to see if silicon could be incorporated into the already existing sites. The first attempt at incorporation was carried out by replacing equimolar amounts of aluminum with silicon in the molar oxide ratio of the synthesis gel. Thus, a gel with molar oxide ratio: 4.36R:0.80Al<sub>2</sub>O<sub>3</sub>:1.00P<sub>2</sub>O<sub>5</sub>:0.40SiO<sub>2</sub>:40.00H<sub>2</sub>O, was crystallized at 200°C for 24h. The initial pH of the gel was 9, and increased to 11 during crystallization. This preparation, however, resulted in the crystallization of a material identified as SAPO<sub>4</sub>-43 (see figure 4.33) a), which is of GIS topology.

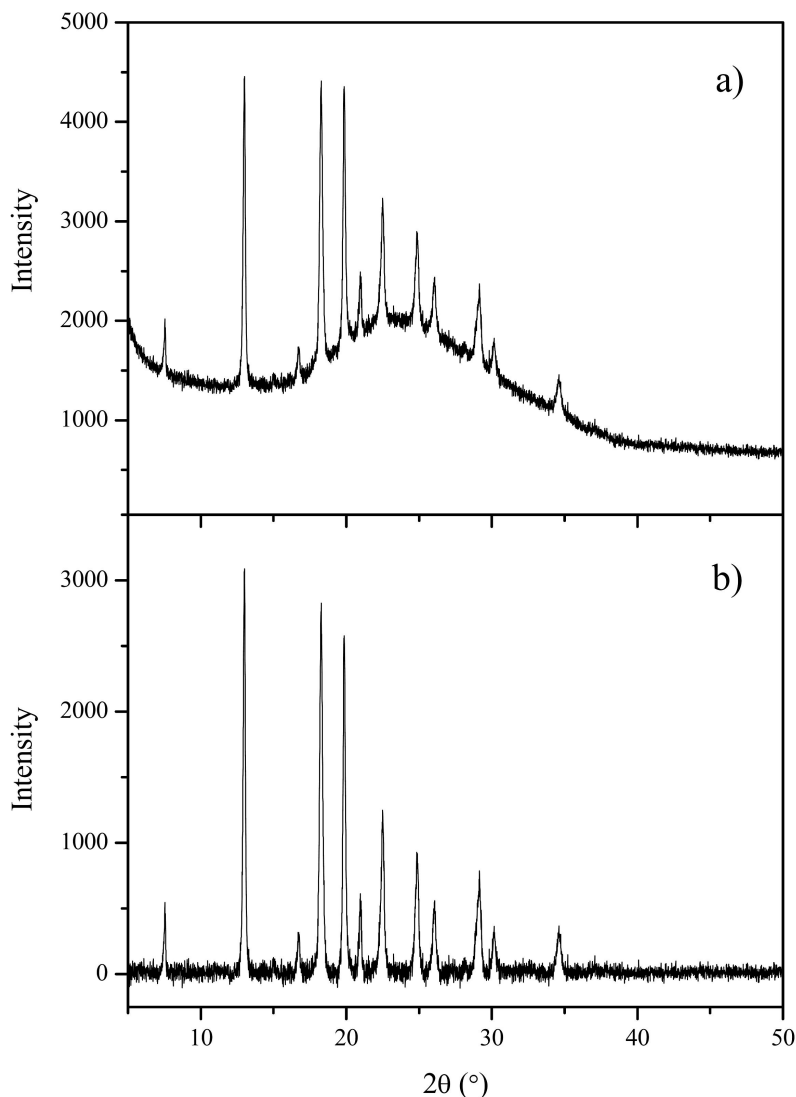


**Figure 4.32:** The PXRD patterns for a calcined  $\text{AlPO}_4$ -14A using a larger slit and longer counting time: a) pattern with background; b) background subtracted pattern.

The as-synthesized material was deemed phase-pure by comparing it to the pattern presented for  $\text{ipaSAPO}_4$ -43 by Akporiaye et al.<sup>121</sup>. It was also in great agreement with a simulated pattern<sup>122</sup> for  $\text{dpaMAPO}_4$ -43 (dpa = di-n-propylamine) which is shown in figure 4.33 b). The diffraction pattern for the calcined sample is shown in figure 4.33 c). The calcination process leads to a complete structural failure, which is consistent with that observed previously by Akporiaye et al.<sup>121</sup>. These authors also performed *in-situ* PXRD on their sample, which showed that the reflections broadened with increasing temperature. Their experiments did not, however, show an actual phase transition to a denser phase (e.g. Tridymite or Berlinite). The structural failure has also been observed for  $\text{dpaMAPO}_4$ -43 in the work done by D.B. Akolekar and S. Kaliaguine<sup>123</sup>. The authors employed several different calcination methods but was unsuccessful in preserving the structure during calcination. They opened for the possibility that magne-

sium and silicon were sources for instability, pointing to observations made for MAPO<sub>4</sub>-36 and SAPO<sub>4</sub>-5.

Since the previous work on the GIS topology indicates a problem with thermal stability, milder calcination procedures were also tested. Figure 4.34 a) shows the diffraction pattern for the sample calcined using the method proposed by Mathisen et al.<sup>106</sup>. It can be seen from the figure that heating the material using this procedure has little effect, and it is still amorphous after calcination. Another procedure was developed where the sample was heated slowly from 25°C to 400°C. The resulting diffraction pattern shown in figure 4.34 b), and it can be seen that this procedure preserves some of the material. The diffraction pattern does not, however, show easily recognizable peaks that could be assigned to SAPO<sub>4</sub>-43. It does show, however, that the removal of the occluded template is dependent on the heating rate used, as well as

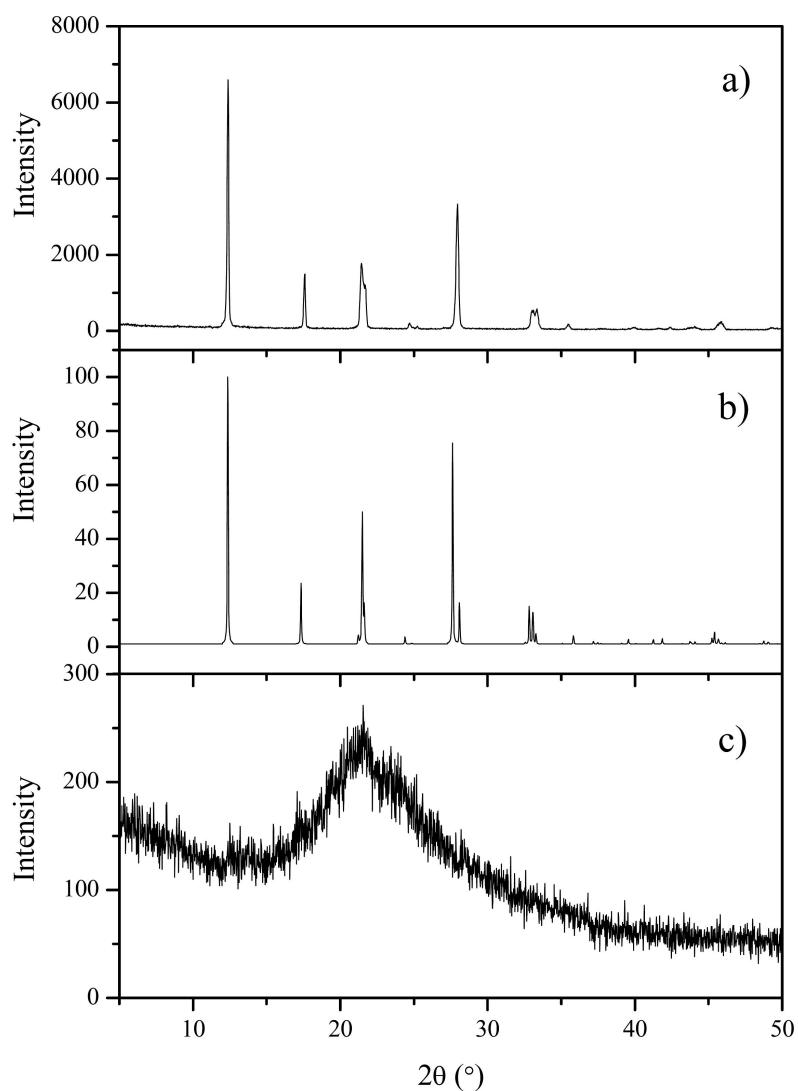


**Figure 4.33:** PXR D pattern for a sample of ipaSAPO<sub>4</sub>-43: a) as-synthesized; b) simulated pattern for dpaMAPO<sub>4</sub>-43; c) calcined in a preheated oven at 600°C for 3 h.

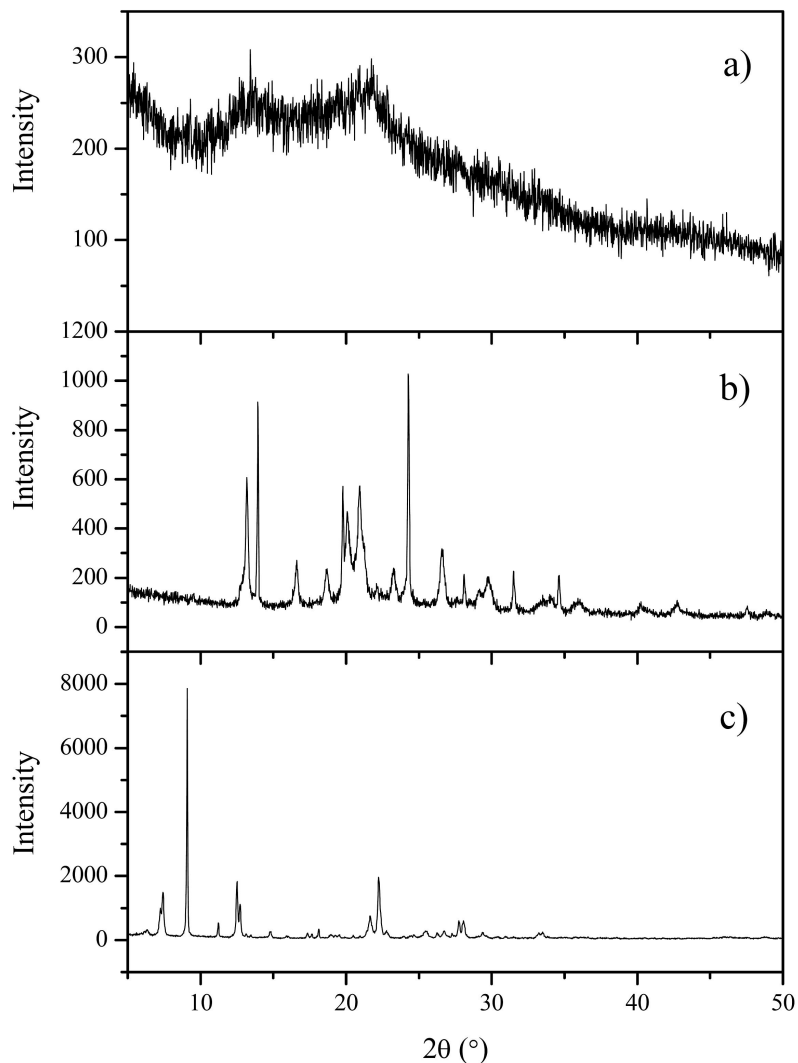


**Figure 4.34:** PXRD pattern for: a) SAPO<sub>4</sub>-43 calcined by heating the material from 25 to 550°C at a rate of 1°C/min; b) SAPO<sub>4</sub>-43 calcined by heating the material from 25 to 400°C at a rate of 1°C/min (both samples were kept at the aforementioned temperatures for 24 h); c) a sample obtained from a gel with molar oxide ratio: 4.85R:Al<sub>2</sub>O<sub>3</sub>:0.95P<sub>2</sub>O<sub>5</sub>:0.1SiO<sub>2</sub>:40.00H<sub>2</sub>O crystallized at 200°C for 24 h.

the final temperature. Another preparation investigated for the crystallization of SAPO<sub>4</sub>-14A involved crystallizing a gel with molar oxide ratio: 4.36R:1.00Al<sub>2</sub>O<sub>3</sub>:0.95P<sub>2</sub>O<sub>5</sub>:0.1SiO<sub>2</sub>:40H<sub>2</sub>O at 200°C for 24 h. This preparation, however, lead to a sample with the unrecognizable pattern shown in figure 4.34 c)).

The transformation of ipaAlPO<sub>4</sub>-14A to ipaSAPO<sub>4</sub>-43 with the adding of silicon is similar to an observation made by Girnus et al.<sup>36</sup>. The authors showed that crystallizing an AlPO<sub>4</sub>-14 gel in the presence of silicon yielded SAPO<sub>4</sub>-34. It is obvious that the presence of silicon has a profound structure directing effect, though the specificity of this effect has yet to be established. When synthesizing SAPOs in alkaline mixtures, interactions between silicon and

the mineralizer  $\text{OH}^-$  can not be ignored either.

### Vermiculite

In their work with ipaSAPO<sub>4</sub>-43, Akporiaye et al.<sup>121</sup> also presented a diffraction pattern for an unknown phase that crystallized at low temperatures. This phase was also obtained in this work while experimenting with the discovered ipaSAPO<sub>4</sub>-43 preparation. The gel with molar oxide ratio: 4.36R:0.80Al<sub>2</sub>O<sub>3</sub>:1.00P<sub>2</sub>O<sub>5</sub>:0.40SiO<sub>2</sub>:40.00H<sub>2</sub>O was crystallized at 150°C for 168 h, and produced a sample that had the diffraction pattern shown in figure 4.35. Also supplied in the figure is an inset showing the fine structure “hidden” by the intense low angle peak. The pattern is in agreement with that reported by Akporiaye et al.<sup>121</sup>, and was also consistent with the mineral Vermiculite. The material may very well be a SAPO in its own right. An identical phase was obtained from an AlPO<sub>4</sub>-14A gel treated at the same temperature for 72 h, indicating that an AlPO version is also obtainable.

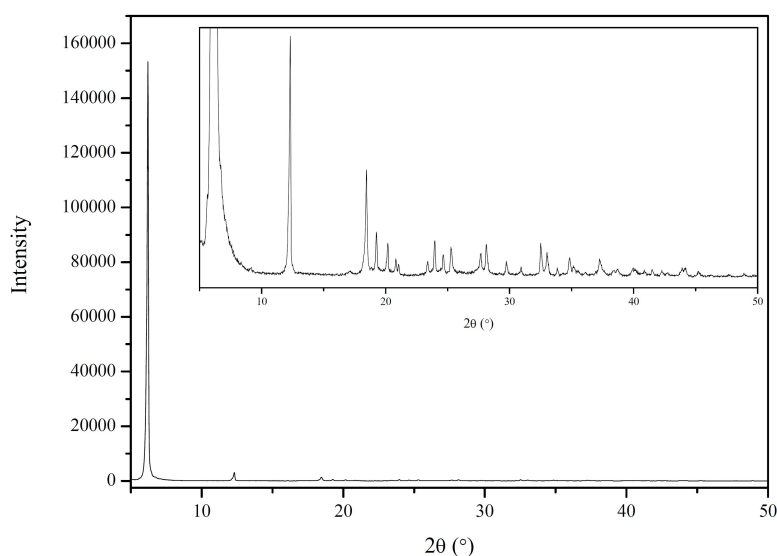


**Figure 4.35:** PXRD pattern for a sample obtained from a gel with molar oxide ratio: 4.85R:Al<sub>2</sub>O<sub>3</sub>:0.80P<sub>2</sub>O<sub>5</sub>:0.40SiO<sub>2</sub>:40.00H<sub>2</sub>O crystallized at 150°C for 168 h. Inset: A view of the fine structure of diffraction peaks “hidden” by the intense low angle peak.

### 4.1.9 dpaAlPO<sub>4</sub>-11 and dpaSAPO<sub>4</sub>-43

#### as-synthesized and calcined

The potential for synthesizing AlPOs and SAPOs in alkaline mixtures (with a more stable pH) was put to the test using another common template, namely di-n-propylamine. Di-n-propylamine, or simply dpa, was replaced with isopropylamine in the preparations for ipaAlPO<sub>4</sub>-14A, and ipaSAPO<sub>4</sub>-43. Thus, gels with molar oxide ratios (R = di-n-propylamine):

- 4.36R:Al<sub>2</sub>O<sub>3</sub>:P<sub>2</sub>O<sub>5</sub>:40H<sub>2</sub>O
- 4.36R:0.8Al<sub>2</sub>O<sub>3</sub>:P<sub>2</sub>O<sub>5</sub>:0.4SiO<sub>2</sub>:40H<sub>2</sub>O

were crystallized at 200°C for 72 h respectively. Figure 4.36 and figure 4.37 shows the diffraction patterns for the resulting samples.

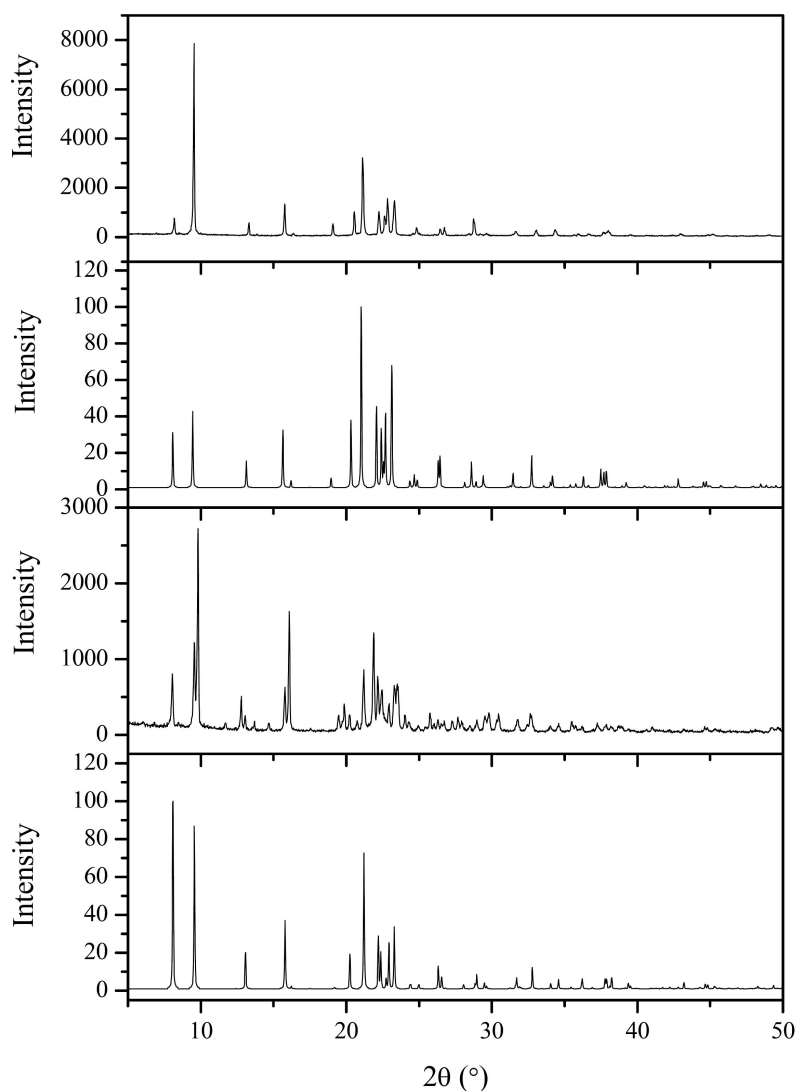


**Figure 4.36:** PXRD patterns for: a) sample of as-synthesized dpaAlPO<sub>4</sub>-11; b) simulated pattern<sup>124</sup> for as-synthesized dipaMnAPO<sub>4</sub>-11 c) same as (a)) after calcination in a preheated oven at 600°C for 10 h; d) simulated pattern<sup>125</sup> for calcined AlPO<sub>4</sub>-11.

The product from the AlPO preparation was identified by a database search as dpaAlPO<sub>4</sub>-11. It can be seen from figure 4.36 that although dpaAlPO<sub>4</sub>-11 was synthesized under alkaline conditions, the more stable pH did not prevent additional phases to form. This is evident from the additional peaks appearing after calcination of the sample (4.36 c)). It is possible that a shorter or longer crystallization time will yield either phase-pure AlPO<sub>4</sub>-11, or another phase.

The SAPO preparation yielded sample that was identified as phase-pure dpaSAPO<sub>4</sub>-43 by virtue of having an identical diffraction pattern (see figure 4.37 a) and b)) to that of dipaMAPO<sub>4</sub>-43 (dipa = di-isopropylamine)<sup>122</sup> (.CIF files for a range of topologies are available via <http://www.iza-structure.org/databases/><sup>3</sup>). It is interesting to note the differences between the diffraction patterns for dpaSAPO<sub>4</sub>-43 and ipaSAPO<sub>4</sub>-43 in the way that dpaSAPO<sub>4</sub>-43 seems to have some peaks more defined.

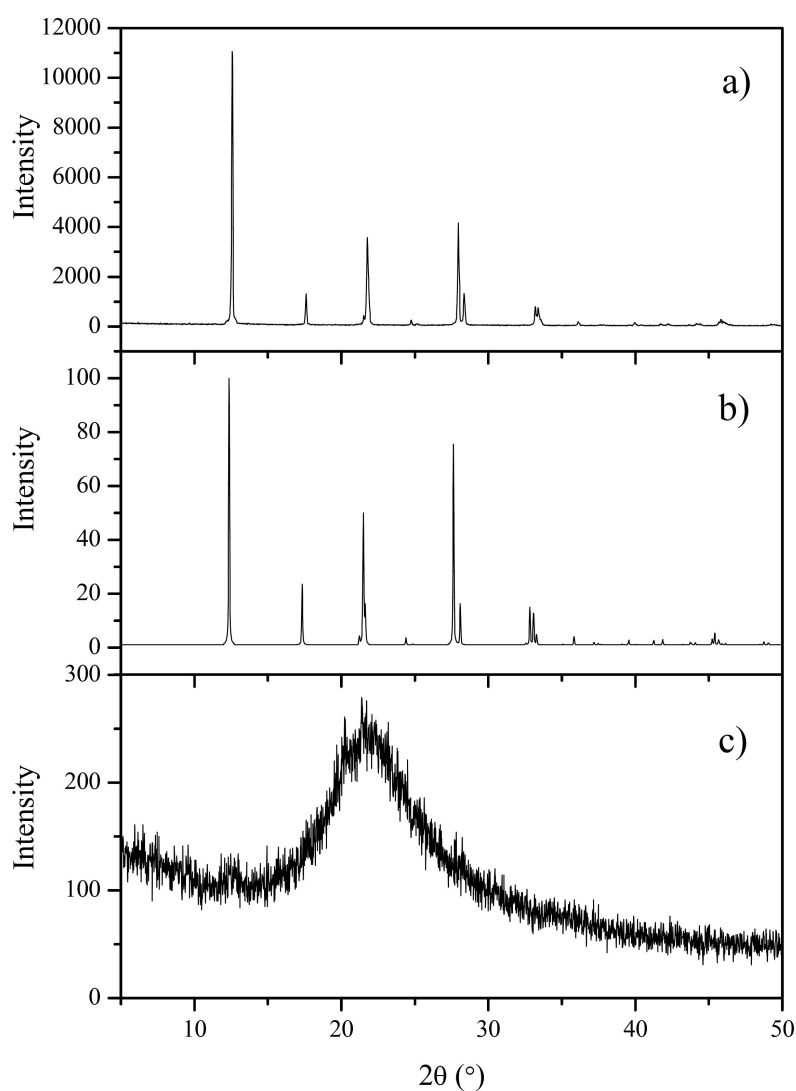


**Figure 4.37:** PXR D patterns for: a) an as-synthesized sample of dpaSAPO<sub>4</sub>-43; b) simulated pattern<sup>122</sup> for as-synthesized dipaMAPO<sub>4</sub>-43; c) same as (a)) after calcination in a preheated oven at 600°C for 3 h.

The di-n-propylamine template has prior to this work been shown to crystallize dpaSAPO<sub>4</sub>-43 both as impurity and as a product. Ma et al.<sup>126</sup> obtained dpaSAPO<sub>4</sub>-43 in an attempt at synthesizing dpaSAPO<sub>4</sub>-41 using phosphorous acid (H<sub>3</sub>PO<sub>3</sub>). Their sample originated from a gel with molar oxide ratio: 4R:0.85Al<sub>2</sub>O<sub>3</sub>:2H<sub>3</sub>PO<sub>3</sub>:0.3SiO<sub>2</sub>:95.4H<sub>2</sub>O, crystallized at 200°C for 8 days. The molar oxide ratio is similar to the one from this work in that a large amount of tem-

plate has been used, and that  $Al + Si = 1$ . The most obvious difference is the phosphorous source which indicates that it too has a profound structure directing effect. The authors also discovered that using a mixture of  $H_3PO_3$  and  $H_3PO_4$  led to a significant reduction in crystallization times for  $SAPO_4-41$ , and samples were obtainable after only 12 h. The di-*n*-propylamine template is notorious for being able to crystallize a range of  $SAPO_4-n$  ( $n = 11, 31, 41, 43, 46$ ),  $MAPO_4-n$  ( $n = 43, 11, 50$ )<sup>123</sup>, and  $CoAPO_4-n$  ( $n = 43, 50$ ) materials<sup>126,127,128,61,123,129,130</sup>

The preparation for  $dpaSAPO_4-43$  discovered in this work is superior to that discovered by Ma et al.<sup>126</sup> in terms of crystallization time. The authors did not, however, present a diffraction pattern for the  $SAPO_4-43$  sample obtained with  $H_3PO_3$ , so no further comparison is possible. The sample was probably discarded due to the previous reports<sup>121,66,123</sup> on the thermal instability of Zeotypes with the GIS topology. Another occurrence of  $dpaSAPO_4-43$  was reported by Kong et al.<sup>127</sup>, this time discovered as an impurity in the synthesis of  $SAPO_4-46$ .

As previously observed for  $ipaSAPO_4-43$ , calcining  $dpaSAPO_4-43$  in a preheated oven results in the destruction of the material (see figure 4.37 c). However, when heating the material from 25 to 550°C at a rate of 1°C/min, and then dwelling for 24 h, a large part of the material remains intact (see figure 4.38 a)). The heating rate utilized by Akolekar and Kaliaguine<sup>123</sup> for  $MAPO_4-43$  was 2°C/min, a rate that might just be too high for preserving of the material during calcination. It is of course also possible that the nature of  $MAPO_4-43$  is different from  $SAPO_4-43$ , and that the type of template is not the only source for thermal instability. The influence of heating rate on thermal stability was investigated further by performing an additional calcination experiment. This time, a rate of 0.5°C/min was used, and the resulting diffraction pattern for the sample is shown in figure 4.38 b). As can be seen from the figure, lowering the rate from 1°C/min to 0.5°C/min is further beneficial for the structure, leaving definable peaks with only minor signs of broadening. Figure 4.38 c) shows the diffraction pattern for the as-synthesized material for an easier comparison of patterns.

On going from as-synthesized to the calcined form, several distinct changes occur in the material's diffraction pattern. First off, here is an obvious intensity reduction visible in the first peak indicating some unavoidable destruction of the material. The second peak (going from left to right in the diffraction pattern) is shifted to a higher  $2\theta$  value, indicating a reduction of the *d*-spacing of the corresponding plane. Since this material's thermal stability can undoubtedly be linked to template removal, any shifts in peak positions may equally be attributed to this. At roughly 22° there is a peak in the as-synthesized pattern which has a barely visible shoulder at lower angle. In the pattern for the calcined material these peaks are separated, and the intensity is distributed more evenly between them. Similar changes are observed for the doublets and multiplet at respectively 28° and 34°.

The crystallinity of the material after calcination is far superior to that reported previously<sup>123,121</sup> for  $SAPO_4-43$ . Samples of  $dpaSAPO_4-43$  calcined by heating them from 25 to 550°C at a rate of 0.5°C, and then dwelling for 24 h, will from hereon be referred to as calcined dehydrated  $SAPO_4-43$ . The pattern represents the first ever reported diffraction pattern for cal-

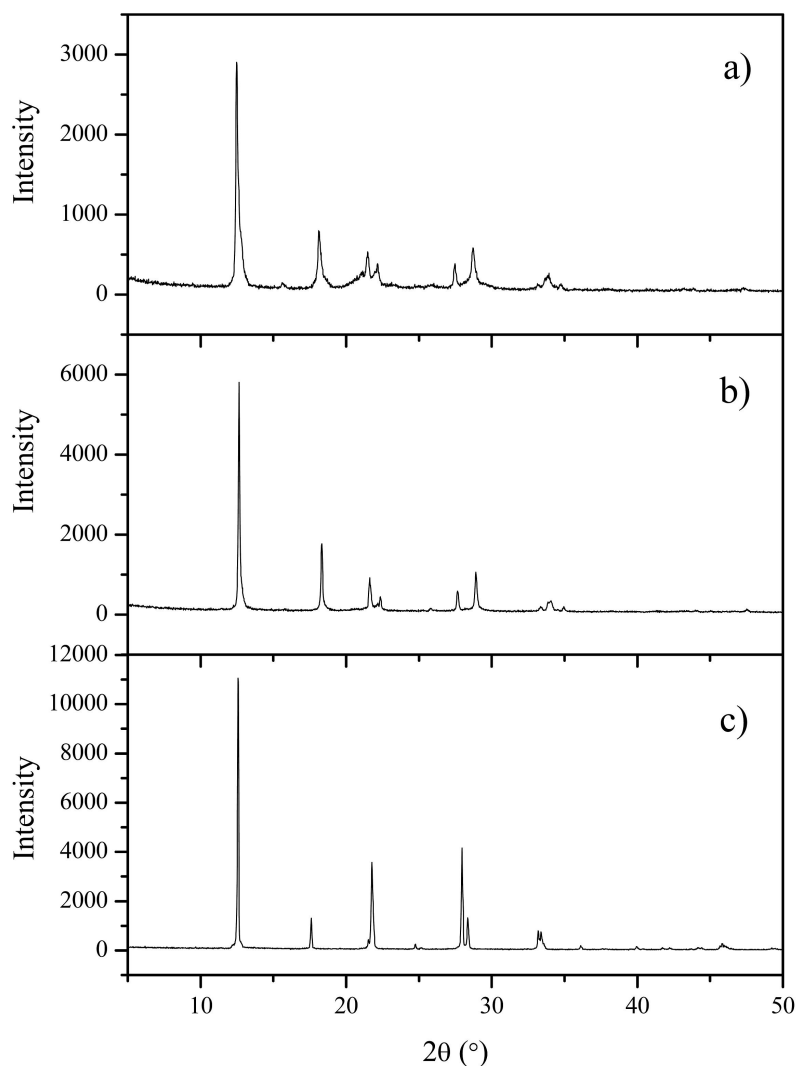


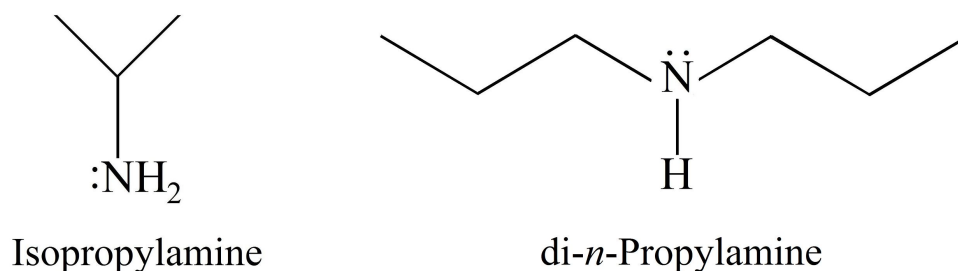
**Figure 4.38:** PXRD patterns for samples of dpaSAPO<sub>4</sub>-43 calcined by heating them from 25 to 550° at different rates: a) 1°C/min; and b) 0.5°C/min. The samples were kept at 550°C for 24 h.

cined dehydrated (or hydrated for that matter) SAPO<sub>4</sub>-43 synthesized using di-n-propylamine as template, and is more defined in terms of visible peaks and intensity than any previous reported pattern for calcined SAPO<sub>4</sub>-43. Table 4.4 lists the observed  $2\theta$ , d-spacings, and relative intensities for calcined dehydrated SAPO<sub>4</sub>-43 (determined using a peak search function in the diffraction software EVA, a part of the DIFFRAC<sup>plus</sup> software suite by Bruker AXS).

The difference in thermal stability between ipaSAPO<sub>4</sub>-43 and dpaSAPO<sub>4</sub>-43 is intriguing. From the structures of the two template amines (see scheme 4.3) one would probably assume that the larger di-n-propylamine would (if leaving the material with its structure intact) lead to a greater destruction of the crystal lattice. As has been shown in this thesis work, this is not the case, and removal of dpa molecules is less destructive.

**Table 4.4:** Experimental  $2\theta$  and d-spacings observed for calcined dehydrated SAPO<sub>4</sub>-43.

$2\theta$ (°)	d (Å)	$I/I_0 \times 100$
12.656	6.98885	100
18.319	4.83902	30.6
21.625	4.1061	15.9
22.356	3.97349	7.7
25.812	3.44883	2.7
27.652	3.22337	10.1
28.909	3.08596	18.2
33.376	2.68244	3.4
34.058	2.63029	6
34.939	2.56597	3.4
44.07	2.05318	1.8
45.063	2.01021	1.8
47.528	1.91154	2.4

**Scheme 4.3**

A previous TGA study<sup>123</sup> on MAPO<sub>4</sub>-43 shows an abrupt mass loss step at 500°C. Similar abrupt mass loss steps have also been observed<sup>114,129</sup> for the unstable structures AlPO<sub>4</sub>-14A and MAPO<sub>4</sub>-50, although at different temperatures. A general trend is the reports of also subjecting the samples to the same thermal treatment in inert atmosphere, though the structures still collapse. This indicates that the structural instability is not dependent on heat evolved. AlPO<sub>4</sub>-14A and MAPO<sub>4</sub>-50 both have larger pores than SAPO<sub>4</sub>-43, indicating that the template can more easily diffuse out of their crystal lattices. This is especially evident for AlPO<sub>4</sub>-14 where the template is located within 5 Å of the Al and P atoms in the surrounding “cage”<sup>119</sup>. It is also interesting to note that templates can crystallize materials with pore diameters substantially larger than the amine itself. The main pores in the AFY topology (AlPO<sub>4</sub>-50) have 12-ring openings (see figure 4.39), while the GIS topology only has 8-ring pore openings. One could then easily assume that the larger pores of the AFY topology could lead to an easier removal of the template, and that it would be more thermally stable than the GIS topology. As shown indirectly with AlPO<sub>4</sub>-14F samples, AlPO<sub>4</sub>-14 undergoes partial destruction upon removal of the isopropylamine and tert-butylamine templates. However, the same sample appears to have “more” AlPO<sub>4</sub>-14 after calcination when synthesized with the bulkier piperidine template.

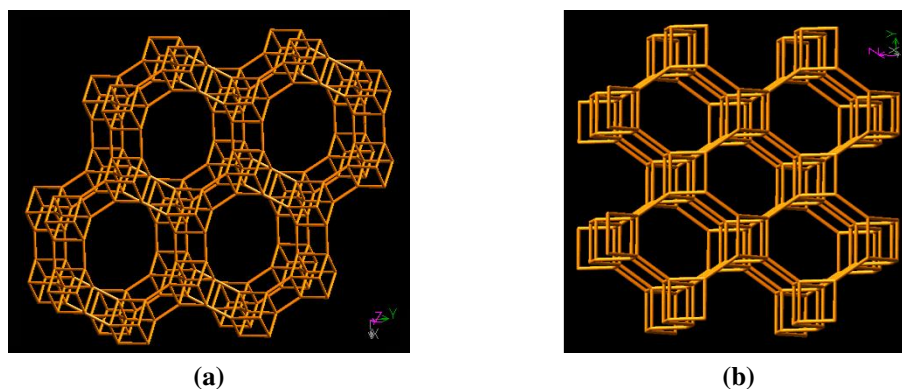


**Figure 4.39:** Images illustrating parts of structure of two topologies:<sup>3</sup> a) AFY; b) GIS.

All these facts suggest that smaller pores, or pores of size similar to the template, leads to the materials being more preserved during calcination. This further indicates that the stability is linked to the diffusivity of organic species leaving the pores, and that molecules of lower diffusivity causes less destruction upon leaving the crystal lattice. The governing factor for thermal stabilities of AlPOs and SAPOs is then the rate at which the template leaves the pores, with low rates being less destructive. The only way to really test this would be to crystallize unstable samples with geometrically larger templates. Another way of validating the hypothesis would be to synthesize thermally stable Zeotypes using templates much smaller than the pore apertures. This would, given that the hypothesis holds, cause them to undergo destruction during the calcination procedure. Unfortunately this is easier said than done, and thermally unstable AlPOs and SAPOs can be considered “exceptions to the rule”. SAPO<sub>4</sub>-34 is a thermally stable Zeotypes with 8-ring pores, not much different from AlPO<sub>4</sub>-14. It has also been shown<sup>9</sup> to crystallize in the presence of isopropylamine, making possible a direct evaluation of the hypothesis. Unfortunately, ipaSAPO<sub>4</sub>-34 has received little characterization, and SAPO<sub>4</sub>-34 is usually synthesized with bulkier/larger templates.

#### 4.1.10 Augelite and pipSAPO<sub>4</sub>-20

##### as-synthesized

The same approach to synthesizing dpaAlPO<sub>4</sub>-11 and dpaSAPO<sub>4</sub>-43 was applied to the piperidine template. This template has previously been shown to yield AlPO<sub>4</sub>-14<sup>34</sup>, and it was therefore desirable to test what crystallization products this template would yield in alkaline mixtures. Thus, gels with the molar oxide ratios (R = piperidine):

- 2.92R:Al<sub>2</sub>O<sub>3</sub>:P<sub>2</sub>O<sub>5</sub>:40H<sub>2</sub>O
- 3.00R:0.8Al<sub>2</sub>O<sub>3</sub>:P<sub>2</sub>O<sub>5</sub>:0.4SiO<sub>2</sub>:40H<sub>2</sub>O

were crystallized at 200°C for 36 and 72 h respectively. The template content was adjusted to ensure an initial pH of 10 in the synthesis gels. Figure 4.40 a) shows that the AlPO preparation

crystallized Augelite, as was determined by a database search. Two peaks due to unknown impurities were also observed.

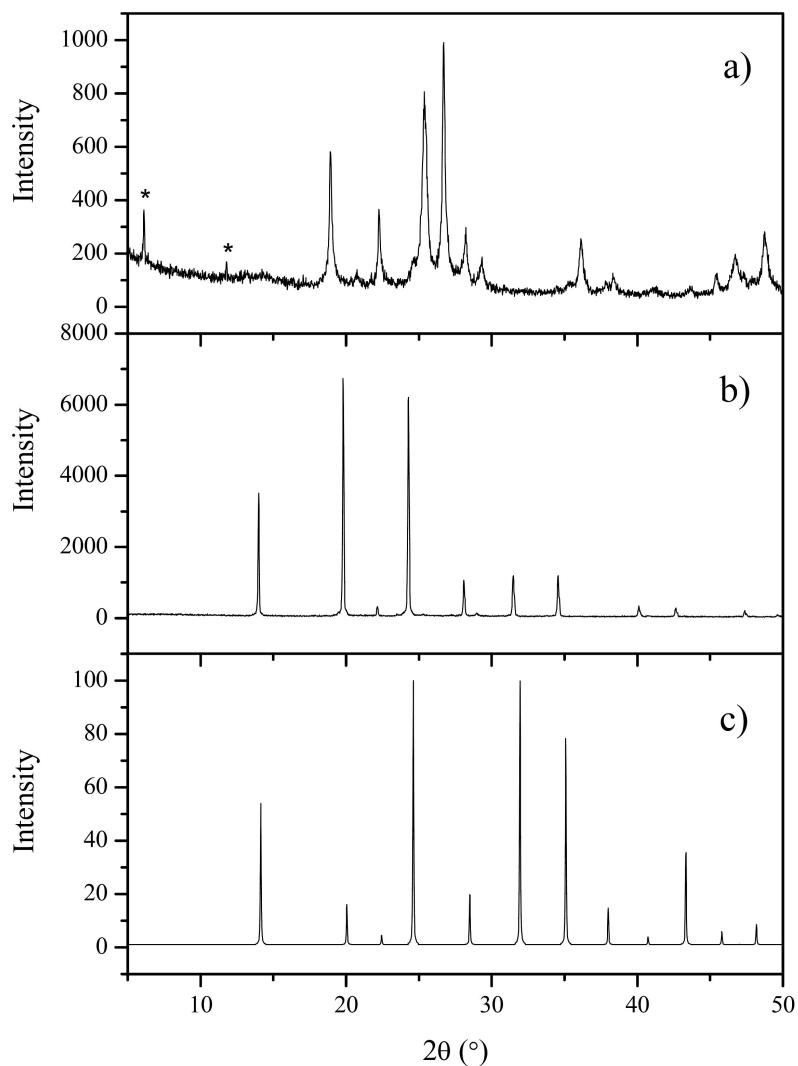


**Figure 4.40:** PXRD patterns for: a) as-synthesized Augelite; b) as-synthesized pipSAPO<sub>4</sub>-20; c) simulated pattern for sodalite octahydrate<sup>131</sup>. Peaks due to impurities are marked with \*.

Figure 4.40 b) shows the diffraction pattern for the sample obtained using the SAPO preparation. The sample was identified as pipSAPO<sub>4</sub>-20 by virtue of having a diffraction pattern in agreement with that of sodalite octahydrate shown in figure 4.40 c). The preparation is incidentally similar to one presented in a previous study by Dimitriu et al.<sup>132</sup> (though their intended material was SAPO<sub>4</sub>-34). Additional experiments were performed using variations of the above SAPO preparation, and the samples obtained had the diffraction patterns shown in figure 4.41. The parameters tested were the replacement of silicon by either aluminum or phosphorous, as well as silicon added “in excess”. In the case of the SAPO preparation combined with the isopropylamine template, altering the molar oxide ratio by having silicon replacing phosphorous

resulted in what is most likely a blend of SAPOs. However, as shown in figure 4.41, the piperidine template ensures that pipSAPO<sub>4</sub>-20 always crystallizes even though the molar oxide ratio is drastically altered.

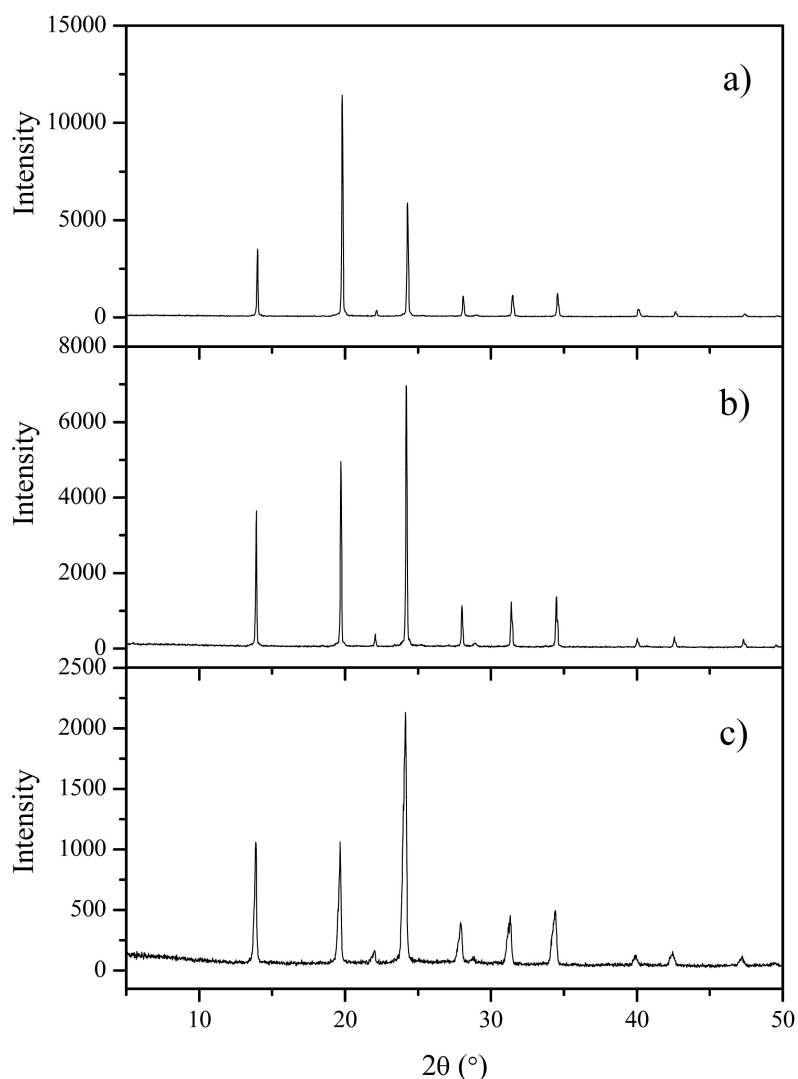


**Figure 4.41:** PXR D patterns for samples of as-synthesized pipSAPO<sub>4</sub>-20 crystallized at 200°C for 24 h from gels with the molar oxide ratios: a) 3.53R:Al<sub>2</sub>O<sub>3</sub>:P<sub>2</sub>O<sub>5</sub>:0.4SiO<sub>2</sub>:40H<sub>2</sub>O; b) 3.36R:Al<sub>2</sub>O<sub>3</sub>:0.8P<sub>2</sub>O<sub>5</sub>:0.4SiO<sub>2</sub>:40H<sub>2</sub>O; c) 3.36R:0.8Al<sub>2</sub>O<sub>3</sub>:P<sub>2</sub>O<sub>5</sub>:1SiO<sub>2</sub>:40H<sub>2</sub>O.

#### 4.1.11 tbaAlPO<sub>4</sub>-15 and tbaSAPO<sub>4</sub>-20

It was desirable to test the high pH approach with all templates that previously have been reported to yield AlPO<sub>4</sub>-14. Thus, gels containing tert-butylamine and having the molar oxide ratios:

- 4.36R:Al<sub>2</sub>O<sub>3</sub>:P<sub>2</sub>O<sub>5</sub>:40H<sub>2</sub>O

- 4.36R:0.8Al<sub>2</sub>O<sub>3</sub>:P<sub>2</sub>O<sub>5</sub>:0.4SiO<sub>2</sub>:40H<sub>2</sub>O

were crystallized at 200°C for 24 h. Figure 4.42 a) shows that the product of the AlPO preparation was impure tbaAlPO<sub>4</sub>-15 when compared to the reflections from a simulated pattern. This

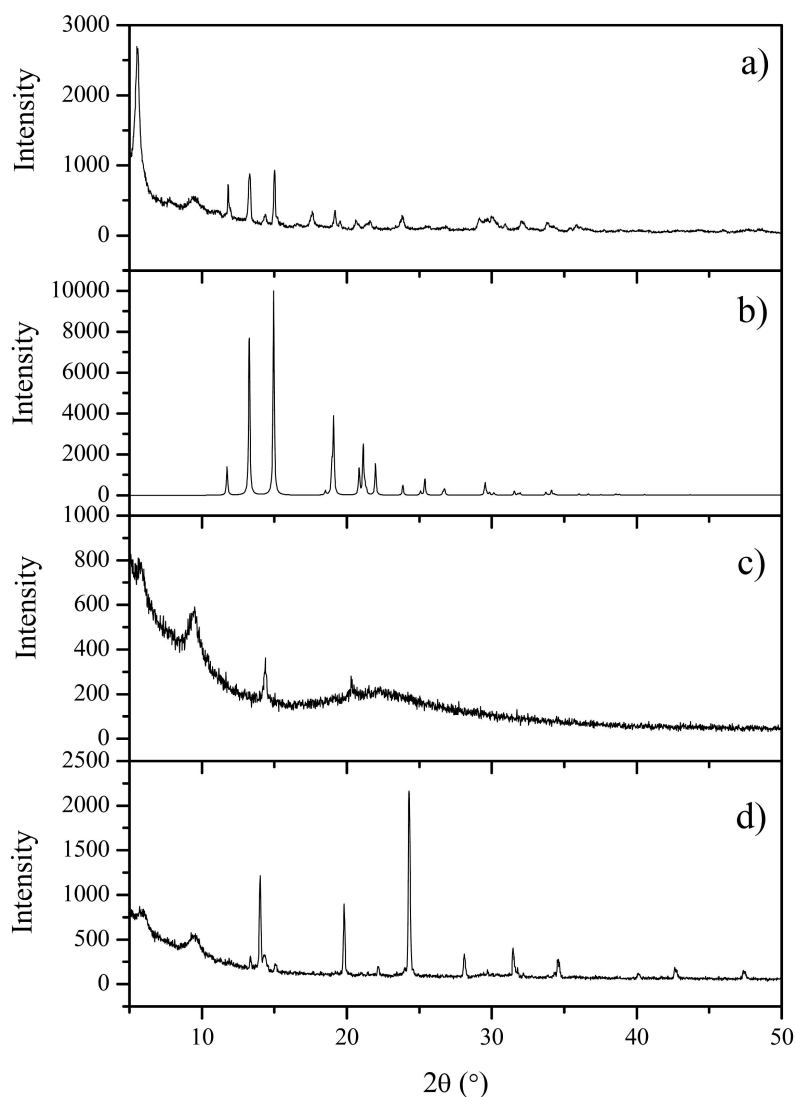


**Figure 4.42:** PXRD patterns for: a) impure as-synthesized tbaAlPO<sub>4</sub>-15 sample obtained after 24 h; b) simulated pattern for tbaAlPO<sub>4</sub>-15 from single-crystal studies<sup>133</sup>; c) same as (a) after calcination by heating the material from 25 to 550°C at a rate of 1°C/min, and finally dwelling for 24 h; d) as-synthesized tbaSAPO<sub>4</sub>-20.

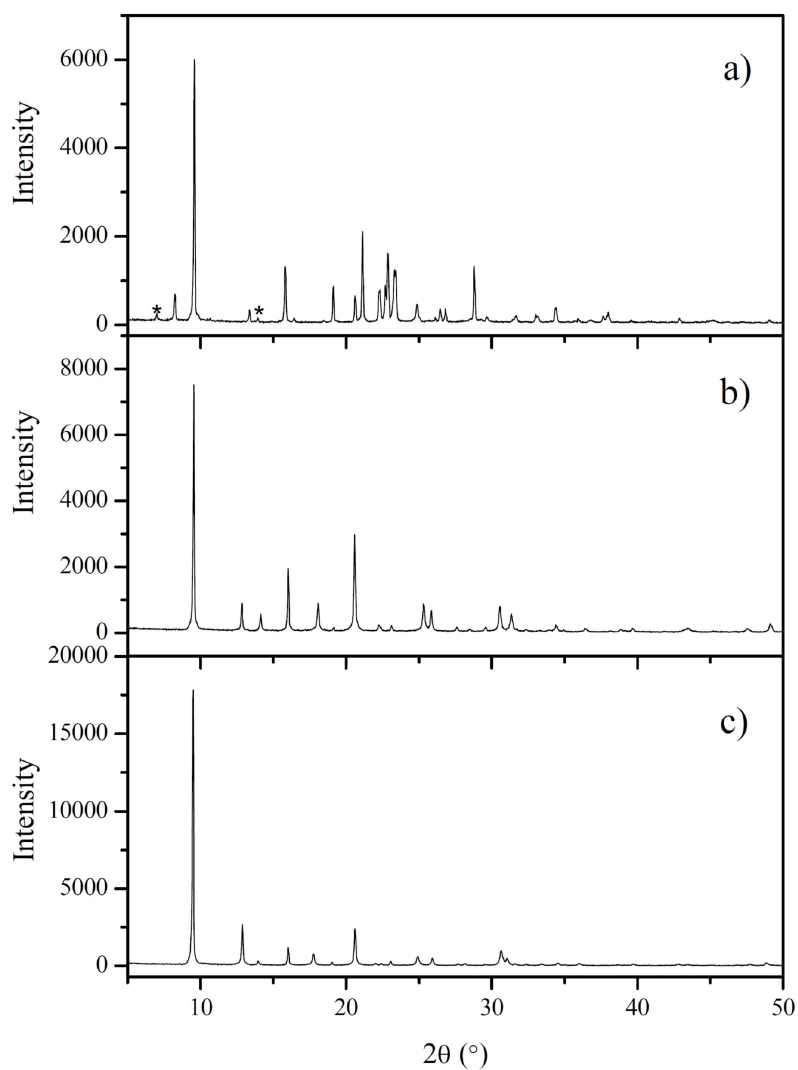
indicates that the isopropylamine and tert-butylamine templates behave quite differently in alkaline mixtures than in then in acidic ones. Under acidic conditions, the templates are both able to crystallize AlPO<sub>4</sub>-14F. However, when the pH value is above 7 these two templates no longer crystallize the same phases, but seem to choose either AlPO<sub>4</sub>-14A (ipa) or AlPO<sub>4</sub>-15 (tba). When crystallizing tbaAlPO<sub>4</sub>-15 there is a competing phase with characteristic peaks at low 2θ angles. This unknown phase might be similar to the Vermiculite phase mentioned previously.

Figure 4.42 c) shows the diffraction pattern for the tbaAlPO<sub>4</sub>-15 sample after calcination. The pattern indicates that the materials thermally unstable, and that there is no difference in thermal stability for tbaAlPO<sub>4</sub>-15 when crystallized under alkaline conditions compared acidic conditions.

The SAPO preparation yielded (see figure 4.42 d)) tbaSAPO<sub>4</sub>-20 with some minor impurities (not assigned), which is quite different from the resulting SAPO<sub>4</sub>-43 when using the isopropylamine template. In the presence of Si these two templates crystallize topologies completely different from those encountered under acidic conditions.

#### 4.1.12 dipaAlPO<sub>4</sub>-11 and dipaSAPO<sub>4</sub>-34

The di-isopropylamine (or dipa) template was also tested. The molar oxide ratios for dipa was identical to those tested for dpa, but some modifications were made when using the SAPO preparation (vide infra). Figure 4.43 shows the diffraction patterns for the samples obtained. The AlPO preparation yielded AlPO<sub>4</sub>-11 after 72 h (see figure 4.43 a)), but in contrast to the sample made with dpa, this sample showed impurities in the as-synthesized form. It is possible that reducing the crystallization time for both the dpa and dipa preparations would yield phase-pure AlPO<sub>4</sub>-11, but this was not tested. The SAPO preparation first yielded only a small amount of product (100 mg) after 24 h, which was then used as seed crystals in the same preparation performed a second time. The product from the second experiment was identified as dipaSAPO<sub>4</sub>-34, by virtue of having a diffraction pattern for the calcined sample in agreement with a simulated pattern for chabazite<sup>134</sup> (see figure 4.43 b)). In contrast to the majority of samples previously mentioned, SAPO<sub>4</sub>-34 increases in intensity upon calcination.



**Figure 4.43:** PXRD patterns for samples obtained using the di-isopropylamine template: a) as-synthesized dipaAlPO<sub>4</sub>-11; b) as-synthesized dipaSAPO<sub>4</sub>-34; c) SAPO<sub>4</sub>-34 calcined by heating the sample from 25 to 600°C at a rate of 5°C/min, then dwelling for 24 h. The \* indicates peaks from an unknown impurity.

### 4.1.13 Unidentified phase

Using methylamine as template and a mixture with molar oxide ratio: 4.36R:Al<sub>2</sub>O<sub>3</sub>:P<sub>2</sub>O<sub>5</sub>:40H<sub>2</sub>O, a sample was obtained with a pattern that did not produce a satisfactory database match for any previously reported AIPO. The pattern is shown in figure 4.44, both as-synthesized and after calcination in a preheated oven at 600°C for 3 h. The preheated oven approach is sufficient to induce a transition from the unidentified phase to a tridymite phase. Modifying the calcination (i.e. using a lower heating rate) procedure may preserve the material, but was not tested.

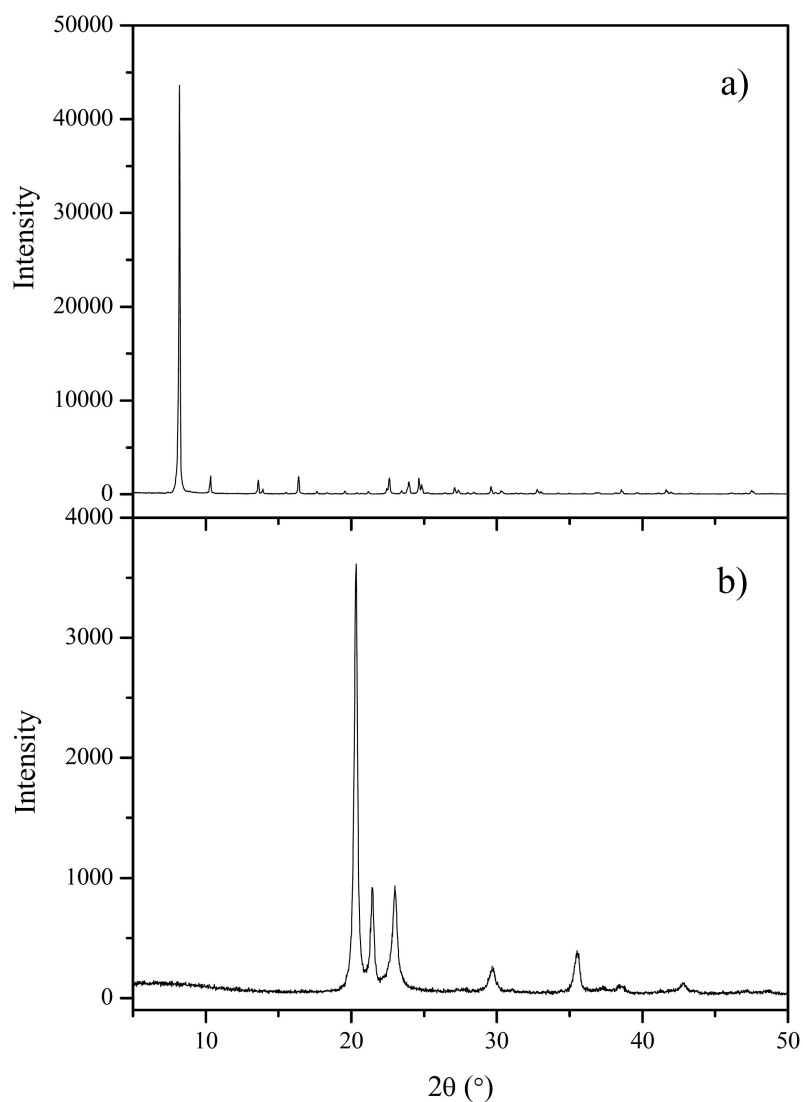


**Figure 4.44:** PXRD pattern for an unidentified sample obtained from a mixture with molar oxide ratio: 4.36R:Al<sub>2</sub>O<sub>3</sub>:P<sub>2</sub>O<sub>5</sub>:40H<sub>2</sub>O crystallized at 200°C for 24 h: a) as-synthesized; b) calcined in a preheated oven at 600°C for 3 h.

#### 4.1.14 teaAlPO<sub>4</sub>-5 and teaSAPO<sub>4</sub>-18

The template triethylamine, or tea, was the final template tested using the molar oxide ratios of ipaAlPO<sub>4</sub>-14A and ipaSAPO<sub>4</sub>-43. Thus, two gels of composition:

- 10R:Al<sub>2</sub>O<sub>3</sub>:P<sub>2</sub>O<sub>5</sub>:40H<sub>2</sub>O
- 10R:0.8Al<sub>2</sub>O<sub>3</sub>:P<sub>2</sub>O<sub>5</sub>:0.4SiO<sub>2</sub>:40H<sub>2</sub>O (R = triethylamine)

were both crystallized at 200°C for 48 h. The high template content of the synthesis gels resulted from the attempt to push the pH of the gel to above 7. This resulted in the formation of a two phase system after stirring was discontinued, and prior to sealment in a Teflon lined autoclave. The two phase system consisted of an almost clear liquid phase at the top (pH = 7), and a white gel at the bottom (pH = 8). Stirring during crystallization may have prevented this, but was not tested.

##### teaAlPO<sub>4</sub>-5

**as-synthesized and calcined** Figure 4.45 a) shows the diffraction pattern for a sample obtained using the above AlPO preparation. From the pattern, peaks of AlPO<sub>4</sub>-5 was identified, along with some peaks reminiscent of AlPO<sub>4</sub>-14A. Since AlPO<sub>4</sub>-14A is thermally unstable, it was of interest to investigate if the instability is linked to the actual template used to crystallize the specific topology. To push the phase towards AlPO<sub>4</sub>-14A, 100 mg of ipaAlPO<sub>4</sub>-14A was added as seed crystals in the aforementioned gel composition. Figure 4.45 b) shows the diffraction pattern for the sample obtained with seeding and crystallization of the gel at 200°C for 24 h. Figure 4.45 c) shows the diffraction pattern for the same sample after calcination (see figure text for details). The sample was identified by a database search as AlPO<sub>4</sub>-5, and subsequently determined to be phase-pure by comparing the pattern with a generated pattern from a single crystal study by Qiu et al.<sup>135</sup>. The seeding with 100 mg of AlPO<sub>4</sub>-14A proved unsuccessful, and seems to have little effect on the phase formed. It is possible that the same gel would have yielded AlPO<sub>4</sub>-5 after 24 h even without the seed crystals, but this was not investigated.

##### teaSAPO<sub>4</sub>-18

**as-synthesized and calcined** Figure 4.46 a) shows the diffraction pattern for the sample obtained from the the SAPO preparation. A database search identified the reflections as somewhat consistent with as-synthesized AlPO<sub>4</sub>-18. The material was identified as phase-pure SAPO<sub>4</sub>-18 by virtue of having diffraction patterns (4.46 a) and b)) identical to that reported by Chen et al.<sup>97</sup>. The authors highlighted the co-crystallization of unknown silicon compounds during the crystallization of SAPO<sub>4</sub>-18 leading to the differences in the diffraction patterns for as-synthesized SAPO<sub>4</sub>-18 and AlPO<sub>4</sub>-18.

The similarities between the as-synthesized sample and the one reported by Chen et al.<sup>97</sup>, suggests that the same “silicon impurities” crystallize with the preparation used in this thesis

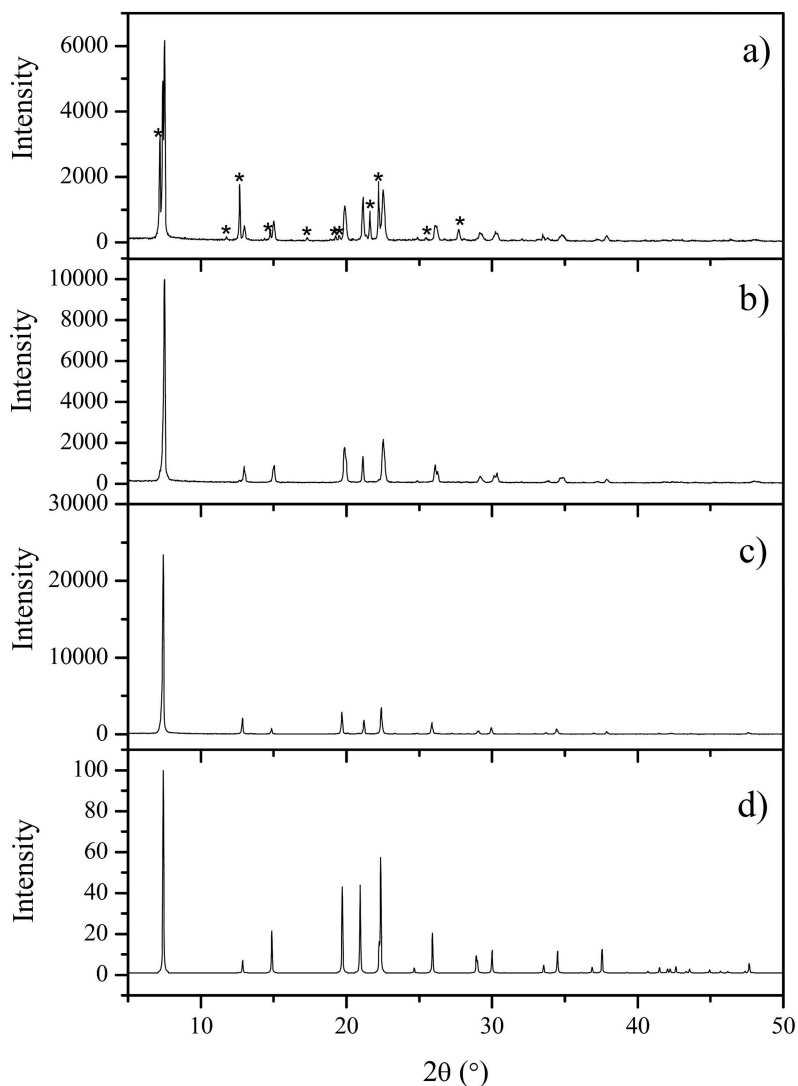


**Figure 4.45:** PXRD patterns for: a) a sample obtained from a gel with molar oxide ratio:  $10\text{R}:\text{Al}_2\text{O}_3:\text{P}_2\text{O}_5:40\text{H}_2\text{O}$  ( $\text{R}$  = triethylamine) crystallized at  $200^\circ\text{C}$  for 48 h; b) as-synthesized  $\text{teaAlPO}_4\text{-5}$ ; c) same as (b) after calcination by heating it from  $25$  to  $600^\circ\text{C}$  at a rate of  $5^\circ\text{C}/\text{min}$ , and finally dwelling for 24 h; d) simulated pattern for tetrapropylammonium fluoride  $\text{AlPO}_4\text{-5}$ . The \* indicates peaks from an impurity (somewhat consistent with  $\text{AlPO}_4\text{-14A}$ ).

work. The authors also stated that the crystallization temperature played an important role in the formation of  $\text{AlPO}_4\text{-18}$  and  $\text{SAPO}_4\text{-18}$ , claiming that only dense phases would form at  $200^\circ\text{C}$  or above. The  $\text{SAPO}_4\text{-18}$  obtained in this thesis work was crystallized at  $200^\circ\text{C}$ , indicating that perhaps this alternate approach to synthesizing this sieve is less temperature dependent. The high pH and triethylamine template may also play a role in the ability for this topology to crystallize at higher temperatures than that reported earlier.

The calcination process was reported by Chen et al.<sup>97</sup> to eliminate the extra silicon phases, and it can be seen in figure 4.46 b) that the diffraction pattern for the calcined sample has

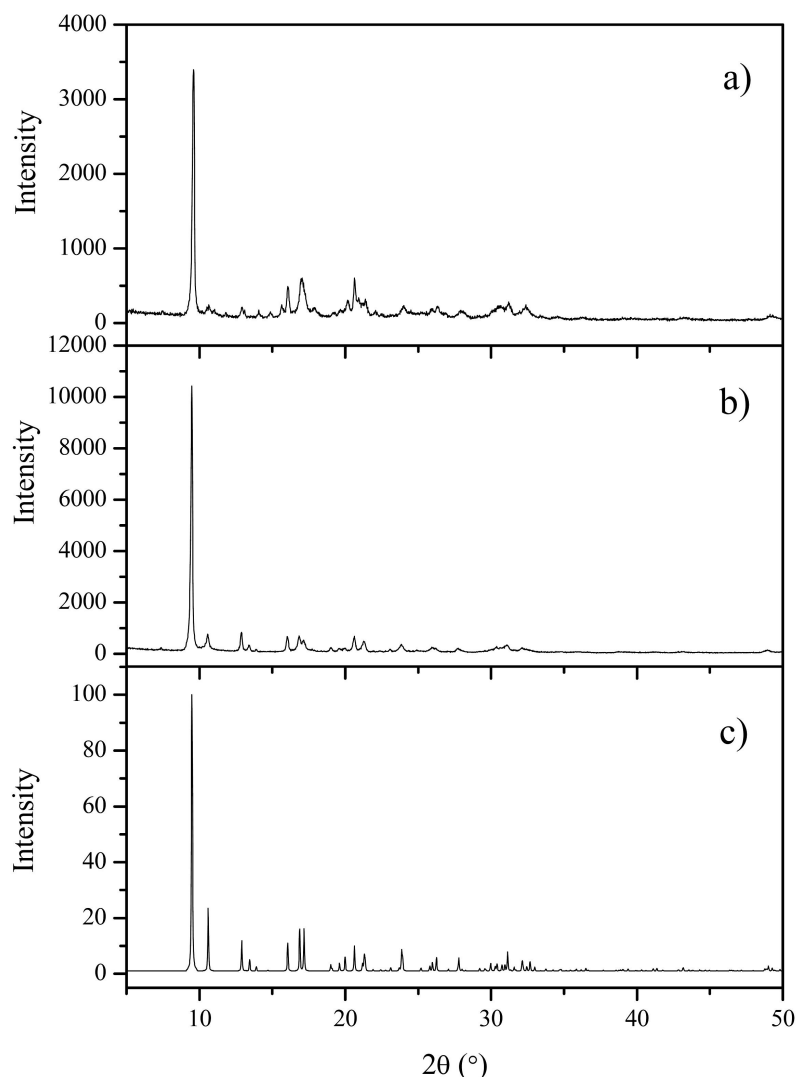


**Figure 4.46:** PXRD pattern for: a) an as-synthesized sample of teaSAPO<sub>4</sub>-18; b) same as a(a) calcined by heating it from 25°C to 600°C at a rate of 5°C/min, and then dwelling for 24 h; c) simulated pattern<sup>136</sup> for calcined AlPO<sub>4</sub>-18.

fewer peaks than the as-synthesized sample. The general observation for other topologies has been that the calcination process reveals (if any) impurities and is somewhat detrimental to the crystal lattice. The situation is quite the opposite for SAPO<sub>4</sub>-18, where the calcination process has removed impurities and actually increased the intensity of the peaks. This was seen as an indication that the calcination process is actually quite beneficial for the material. Chen et al.<sup>97</sup> employed a stream of dry oxygen at 550°C as the calcination procedure. The sample obtained in this work seems to have no special requirements when it comes to template removal at all, and this could be due to the use of triethylamine as the template. The method used here was heating the material from 25 to 600°C at a rate of 5°C/min (in atmospheric air), and then dwelling for 24 h. PXRD indicates that the method of this work is an acceptable one, with no apparent

destruction of the material.

#### 4.1.15 dpaipaSAPO<sub>4</sub>-43

#### 4.1.16 as-synthesized and calcined

As is evident from the SEM images in chapter 4.3 the preparations for AlPOs and SAPOs discovered in this thesis work generally yields large ( $\approx 20\mu\text{m}$ ) crystallites. This presents a problem for transmission mode (IR beam travels through the sample) FT-IR investigations since the transmission is dependent on the thickness of samples studied<sup>137</sup>. Accommodating the crystallite sizes requires the preparation of extremely thin wafers to minimize absorption, which is easier said than done.

The use of dual templates has previously proved beneficial for a number of aspects in the synthesis of SAPO<sub>4</sub>-34, including: crystallite size, reduction in template expenses, BET surface area, increase in catalytic activity/selectivity and distribution of acid centers<sup>138</sup>. The two preparations discovered for SAPO<sub>4</sub>-43 in this thesis work is identical in terms of molar oxide ratio, chemicals used, pH, and temperature, and differs only in time and type of template. This was seen as an indication that these two templates were suitable for the dual template approach, and was aimed at obtaining SAPO<sub>4</sub>-43 with smaller crystallites more suitable for FT-IR studies. Therefore, a gel with molar oxide ratio: 3R1:0.2R2:0.8Al<sub>2</sub>O<sub>3</sub>:P<sub>2</sub>O<sub>5</sub>:0.4SiO<sub>2</sub>:40H<sub>2</sub>O (R1 = di-n-propylamine, R2 = isopropylamine) was crystallized for 24 h at 200°C. The result was named dpaipaSAPO<sub>4</sub>-43 and the diffraction pattern for the as-synthesized sample is shown in figure 4.47 a).

The differences in the diffraction patterns for as-synthesized SAPO<sub>4</sub>-43 made with di-n-propylamine and isopropylamine makes it possible to determine which template resides in the pores of the product. The pattern is characteristic for SAPO<sub>4</sub>-43 made with di-n-propylamine, which seems logical when more moles of this template is present in the synthesis gel. An interesting aspect of the synthesis is the fact that the sample was obtained after only 24 h of crystallization when normally the dpa template requires 72 h to crystallize dpaSAPO<sub>4</sub>-43. Isopropylamine readily crystallizes ipaSAPO<sub>4</sub>-43 in 24 h, and its presence may have altered the effectiveness of the di-n-propylamine template.

The sample was calcined using the calcination procedure developed for dpaSAPO<sub>4</sub>-43, and the diffraction pattern for the calcined material in figure 4.47 b) validates this procedure. The diffraction pattern shows that the dpaipaSAPO<sub>4</sub>-43 sample is stable upon calcination, indicates that the majority of template present in the pores of the material is in fact di-n-propylamine. This is beneficial since the removal of the isopropylamine template is impossible without destroying the structure. Crystallizing the same gel in the absence of isopropylamine only results in the formation of viscous gels and no powder product. In the synthesis of dpaipaSAPO<sub>4</sub>-43 the di-n-propylamine brings thermal stability, and the isopropylamine brings fast crystallization.

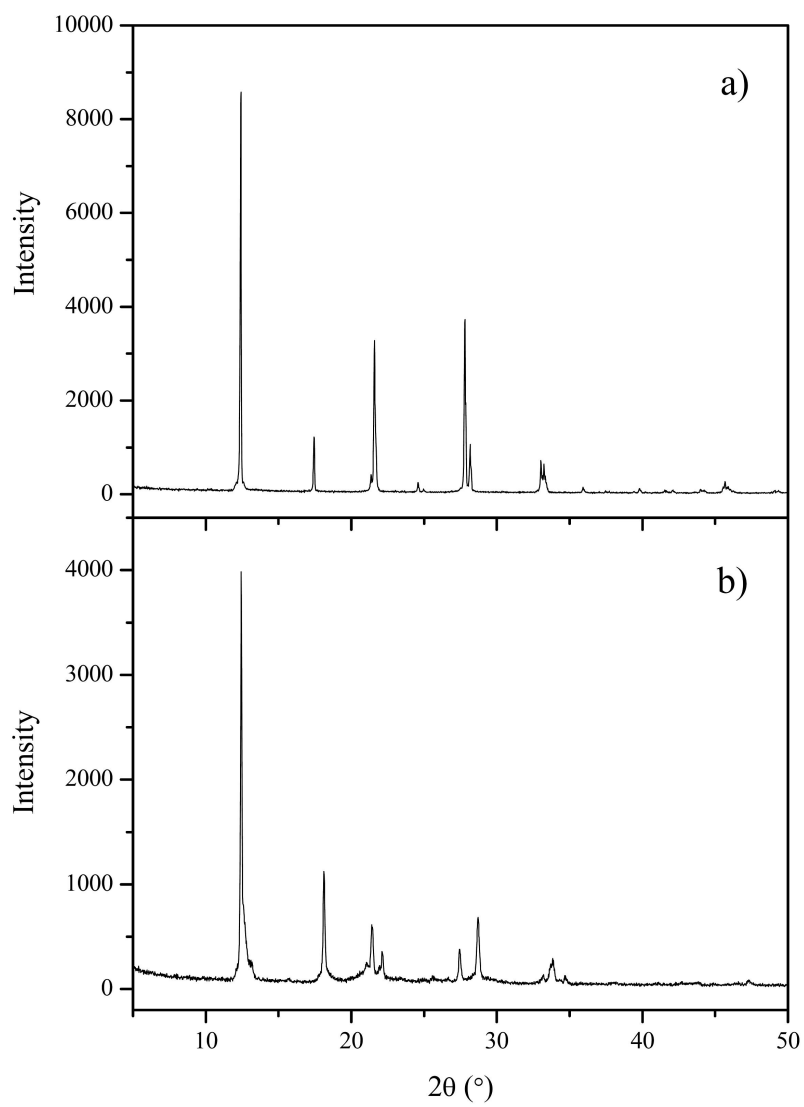


**Figure 4.47:** PXRD pattern for dpaipaSAPO<sub>4</sub>-43: a) as-synthesized b) calcined by heating the material from 25 to 550°C at a rate of 0.5°C/min. The sample was kept at 550°C for 24 h.

## 4.2 ICP-MS

### 4.2.1 First generation molecular sieves

Table 4.5 lists various ratios with respect to moles of elements found in first generation sieves. For the elements aluminum and phosphorous, the general trend is a surplus of phosphorous indicated by Al/P ratios lower than 1 (the value of P is larger than the value of Al). These ratios vary somewhat sporadically between 0.95 and 0.90 for the different compositions. Also included in the table are (Al+P)/Si and (Al+P)/Cu ratios. These indicate the ratio of elements originally present in the framework and those tried incorporated. The Al/P ratios for the SAPO<sub>4</sub>-14F compositions decrease with increasing silicon content in the gel, which may indicate that Si successively replaces more P. The use of seed crystals seems to benefit the Si uptake for the 0.08SAPO<sub>4</sub>-14F and 0.20SAPO<sub>4</sub>-14F samples. The 0.20SAPO<sub>4</sub>-14F sample obtained after 24 with seeding has the same mole fraction of Si as the 0.06SAPO<sub>4</sub>-14F sample obtained after 6 days. In this case, seeding not only promotes the crystallization of the AlPO<sub>4</sub>-14F lattice, but seems to affect the Si uptake as well. The CuAPO<sub>4</sub>-14F compositions show a steady increase in the mole fraction of copper reflecting the composition of their synthesis gels. A copper mole fraction of 0.012 in the 0.08CuAPO<sub>4</sub>-14F sample may be the limit for these compositions since this sample showed tridymite peaks after calcination. There is a dramatic difference between the (Al+P)/Cu ratios of the samples 0.01CuAPO<sub>4</sub>-14F and 0.03CuAPO<sub>4</sub>-14F, showing a difference of roughly 300. The crystallization times for these samples were respectively 24 and 72 h, and the difference may be an indication that the initial uptake of copper into the AlPO<sub>4</sub>-14F is framework is low.

**Table 4.5:** Elemental analysis of first generation molecular sieves. Experimentally obtained values are supplied in appendix A.1.

Sample	Al/P	(Al+P)/Si	(Al+P)/Cu	Si/(Si+Al+P)	Cu/(Cu+Al+P)
AlPO <sub>4</sub> -14F	0.92	-	-	-	-
0.01CuAPO <sub>4</sub> -14F	0.91	-	398	-	0.003
0.03CuAPO <sub>4</sub> -14F	0.93	-	99	-	0.010
0.08CuAPO <sub>4</sub> -14F	0.90	-	80	-	0.012
0.06SAPO <sub>4</sub> -14F	0.91	51	-	0.019	-
0.08SAPO <sub>4</sub> -14F	0.95	83	-	0.012	-
0.20SAPO <sub>4</sub> -14F	0.94	53	-	0.019	-

### 4.2.2 Various other compositions

Table 4.6 lists the results from the elemental analysis of various AlPOs and SAPOs synthesized with preparations discovered in this thesis work. For the two AlPO samples, AlPO<sub>4</sub>-14A and

AlPO<sub>4</sub>-5, the Al/P ratio is in favor of P as observed for the first generation sieves. All SAPOs (except for ipaSAPO<sub>4</sub>-20) were synthesized from a gel with the generalized molar oxide ratio:

- xR:0.8Al<sub>2</sub>O<sub>3</sub>:P<sub>2</sub>O<sub>5</sub>:0.4SiO<sub>2</sub>:40H<sub>2</sub>O

crystallized at 200°C for y h. When examining the results for the various SAPOs synthesized using this surplus template approach, an immediate observation is that the Al/P ratio is shifted in favor of Al. This is consistent with the sieves favoring the silicon present in the synthesis gels, thus effectively rejecting some of the phosphorous. The fact that P is in excess in the molar oxide ratio seems to have little effect, and only SAPO<sub>4</sub>-18 has an Al/P ratio equal to 1. Common values for the mole fraction of Si in SAPO<sub>4</sub>-34 is 0.1, and it has been pointed out that synthesizing samples with a lower mole fraction is difficult<sup>97</sup>. The sample in this thesis work has a mole fraction of 0.074, which is significantly lower than the norm.

**Table 4.6:** Elemental analysis of various AlPOs and SAPOs. Experimentally obtained values are supplied in appendix A.1.

Sample	Al/P	(Al+P)/Si	Si/(Si+Al+P)	Al/(Si+Al+P)	P/(Si+Al+P)
ipaAlPO <sub>4</sub> -14A	0.93	-	-	0.483	0.517
teaAlPO <sub>4</sub> -5	0.91	-	-	0.477	0.523
ipaSAPO <sub>4</sub> -43	1.36	5	0.163	0.482	0.355
dpaSAPO <sub>4</sub> -43	1.20	10	0.090	0.496	0.414
pipSAPO <sub>4</sub> -20	1.15	11	0.086	0.486	0.425
dipaSAPO <sub>4</sub> -34	1.03	13	0.074	0.469	0.457
ipaSAPO <sub>4</sub> -20	1.26	15	0.061	0.523	0.415
teaSAPO <sub>4</sub> -18	1.00	31	0.031	0.486	0.483

It is interesting to note that the ipaSAPO<sub>4</sub>-20 sample made with only a fourth of SiO<sub>2</sub> (molar oxide ratio: 4.36R:Al<sub>2</sub>O<sub>3</sub>:0.95P<sub>2</sub>O<sub>5</sub>:0.1SiO<sub>2</sub>:100H<sub>2</sub>O) has a mole fraction twice as large as teaSAPO<sub>4</sub>-18. What is more interesting is that the two SAPO<sub>4</sub>-43 samples also differ greatly in their mole fractions of Si. The sample made with isopropylamine has an Si/(Si+Al+P) of 0.163, the one made with di-n-propylamine has a Si/(Si+Al+P) of only 0.09. As the samples were synthesized under near identical conditions (the crystallization times were 24 (ipa) and 72 h (dpa)), it seems that the template itself may play a role in the sample's Si uptake. This would explain the higher Si uptake for ipaSAPO<sub>4</sub>-20 when considering the fact that less Si was present in the synthesis gel. One could therefore range the templates in order of Si uptake by the samples. The low Si uptake of the SAPO<sub>4</sub>-14F compositions indicate that the Si uptake may be topology dependent as well as template dependent. It may also indicate that the Si uptake under low and high pH conditions are different.

Previous studies on SAPO<sub>4</sub>-43 and MAPO<sub>4</sub>-43 have shown that the GIS topology favors incorporation of rather large amounts of respectively Si and Mg. The two ipaSAPO<sub>4</sub>-43 samples synthesized by Akporiaye<sup>121</sup> and Hernández-Maldonado et al.<sup>66</sup> had similar Si/(Si+Al+P)

ratios of respectively 0.20 and 0.19 (avg. value, not to be confused with the wt% ratios presented in the article<sup>66</sup>, indicating good reproducibility of the procedure by Akporiaye et al. in terms of composition. The Si/(Si+Al+P) ratio of the ipaSAPO<sub>4</sub>-43 sample obtained in this work is lower (0.163), which is reflected in the number of moles of Si present (0.2 mol SiO<sub>2</sub> vs. 0.7 mol SiO<sub>2</sub>) in the synthesis gel. This could also indicate that lower temperatures and longer crystallization times enable a larger Si uptake. The Mg/(Mg+Al+P) ratio was 0.11 for the MAPO<sub>4</sub>-43 sample made by Akolekar et al.<sup>123</sup>, which was made with 0.3 mol MgO in the synthesis gel.

SAPO<sub>4</sub>-18 has previously been synthesized using *N,N*-diisopropylethylamine and tetraethylammonium hydroxide (TEAOH) as templates<sup>97,139</sup>. Chen et al.<sup>93</sup> synthesized several SAPO<sub>4</sub>-18 samples using *N,N*-diisopropylethylamine and varying moles of SiO<sub>2</sub> in the synthesis gels. One of their samples were synthesized from a gel with molar oxide ratio:

1.6R:Al<sub>2</sub>O<sub>3</sub>:0.1SiO<sub>2</sub>:0.95P<sub>2</sub>O<sub>5</sub>:50H<sub>2</sub>O, which was crystallized for 8 days. This sample had an Si/(Si+Al+P) ratio of 0.028, which is closest to the sample synthesized with triethylamine in this thesis work. In one way, the triethylamine template seems to be more efficient at incorporating (incorporation has been proven for this sample, see FT-IR section) Si given that the crystallization time for the sample obtained in this thesis work was only 48 h. From another viewpoint, the sample synthesized by Chen et al. had a larger Si/(Si+Al+P) ratio despite having only half the amount of Si in the synthesis gel. Another sample synthesized by the authors using a molar oxide ratio of: 1.6R:Al<sub>2</sub>O<sub>3</sub>:0.2SiO<sub>2</sub>:0.95P<sub>2</sub>O<sub>5</sub>:50H<sub>2</sub>O (the same amount of SiO<sub>2</sub> used to obtain the sample from this work) had an Si/(Si+Al+P) ratio of 0.047, which is a little less than double that of the previous sample. It is uncertain if the procedure using triethylamine would yield a higher Si content after additional crystallization times (i.e. not tested in this thesis work), or if doubling or tripling the SiO<sub>2</sub> content of the synthesis gel would produce samples with twice and three times larger Si/(Si+Al+P) ratios. It could, however, provide a route to obtaining high Si content SAPO<sub>4</sub>-18 faster than previously reported.

## 4.3 SEM

### 4.3.1 ipaAlPO<sub>4</sub>-14F

#### as-synthesized and calcined dehydrated

Figure 4.48 a) shows a SEM image of a sample of as-synthesized ipaAlPO<sub>4</sub>-14F. The image shows a collection of crystallites of varying sizes and habits. The largest and most defined crystallites are of tabular habit, approximately 40  $\mu\text{m}$  in size, and are surrounded by smaller less-defined crystallites 10  $\mu\text{m}$  in size. The habits of the largest crystallites are consistent with that reported for AlPO<sub>4</sub>-14<sup>34</sup> and AlPO<sub>4</sub>-14F<sup>140</sup>, but the broad size distribution is not. Usually, a narrow size distribution with 10  $\mu\text{m}$  crystallites is observed. This may be a result of the non-ideal synthesis procedure<sup>6</sup>. The largest crystallites were attributed to AlPO<sub>4</sub>-14. The observation made with PXRD was that the sample is phase-pure in as-synthesized form, but contains impurities after calcination. Since AlPO<sub>4</sub>-14A and AlPO<sub>4</sub>-15 co-crystallize, and are not the result of a phase transition, this can perhaps best be explained by these large crystallites making the net reflections count in favor of AlPO<sub>4</sub>-14. The reflections from the impurity crystallites are then averaged out, giving the “illusion” that the sample is pure.

Figure 4.48 b) shows a SEM image of the same sample after calcination in a preheated oven at 600°C for 3 h. It can be seen that calcination has reduced the size of the largest crystallites from 40  $\mu\text{m}$  to 10  $\mu\text{m}$ . PXRD showed that calcination lead to reduced intensity of diffracted peaks, as well as the appearance of “extra” peaks. The reduction in intensity thus manifests itself in the size of the composite crystallites. This supports the hypothesis that the large size of the crystallites in as-synthesized samples prevent any impurities of being observed with PXRD.

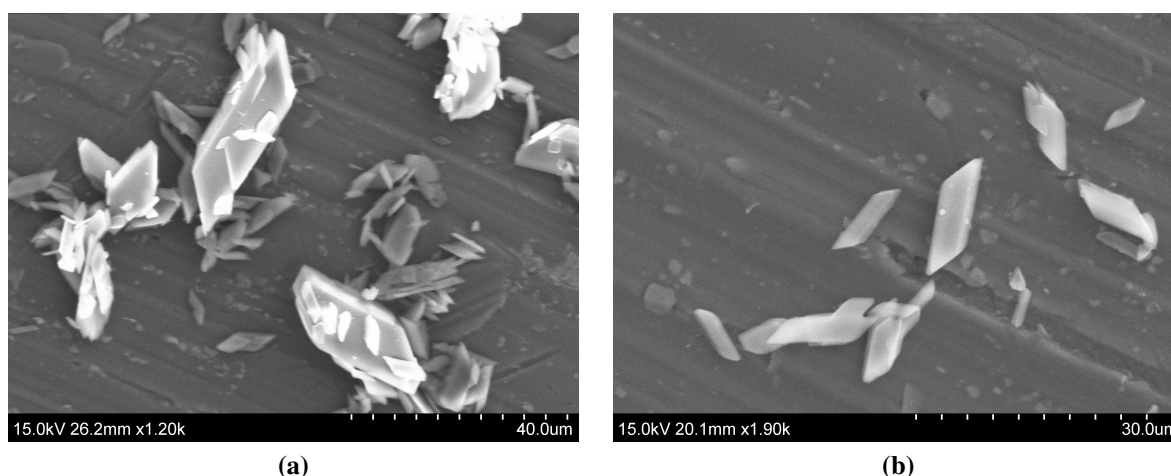


**Figure 4.48:** SEM images of a collection of crystallites in a sample of: a) as-synthesized ipaAlPO<sub>4</sub>-14F; b) calcined dehydrated AlPO<sub>4</sub>-14F.

**calcined partially-hydrated**

Figure 4.49 shows SEM images of a sample of calcined partially-hydrated  $\text{AlPO}_4\text{-14F}$ . As the images indicate, the preparation proposed by Wilson et al.<sup>6</sup> is indeed a flawed one. This is evident since the various crystallites were found in such a small (less than 20 mg) sample. The hydration seems to have affected some of the crystallites more than others, namely those of tabular habit previously attributed to  $\text{AlPO}_4\text{-14}$ . Some of these have, upon hydration, lost the clear cut edges and now have a more smooth appearance (figure 4.49 a)). Other  $\text{AlPO}_4\text{-14}$  crystallites appear to be less affected (figure 4.49 b)). The presence of both affected and unaffected crystallites of  $\text{AlPO}_4\text{-14}$  was attributed to the partial-hydration of the sample. The water-framework interactions reported by Yang et al.<sup>35</sup> for this material, seem to have repercussions beyond the area of PXRD. The observed low angle peak at  $8^\circ$  in the diffraction pattern may result from these altered crystallites. Also visible are some needle or stick type of crystallites attributed<sup>114</sup> to  $\text{AlPO}_4\text{-14A}$  (figure 4.49 c)), and some truncated cubes attributed<sup>141</sup> to  $\text{AlPO}_4\text{-15}$  (figure 4.49 d)).

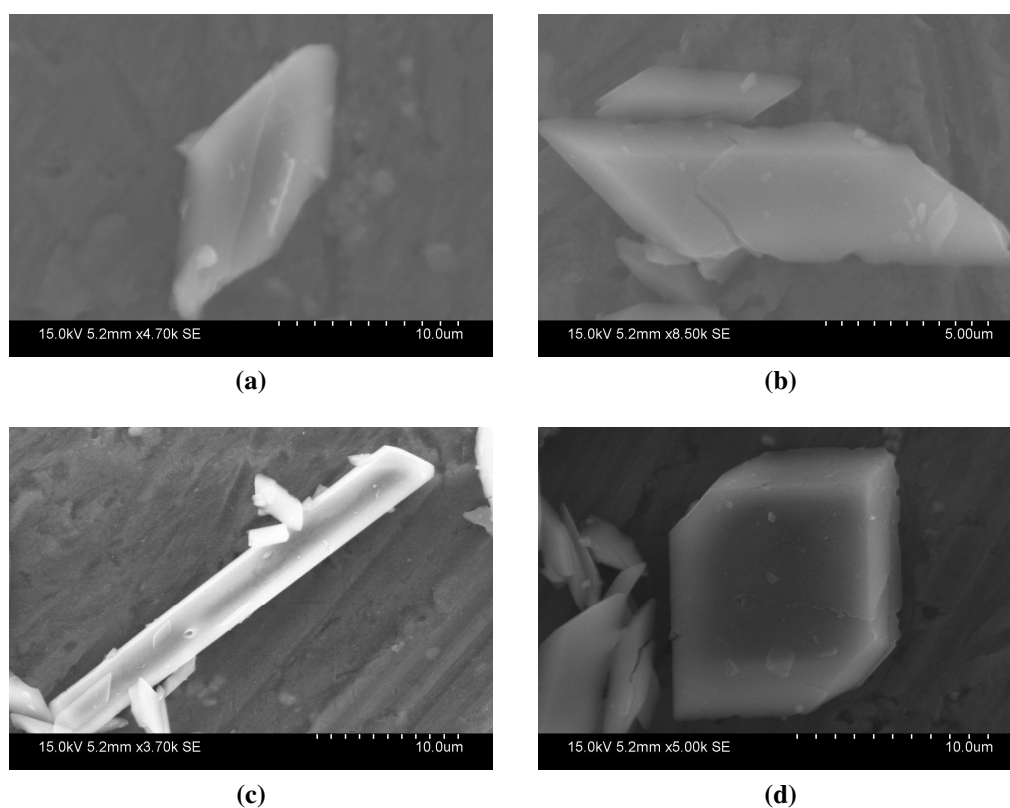


**Figure 4.49:** Sem images of crystallites with various shapes and sizes found in a sample of calcined partially-hydrated  $\text{AlPO}_4\text{-14F}$ .

### 4.3.2 ipaCuAPO<sub>4</sub>-14F

#### as-synthesized and calcined

Figure 4.50 a) shows a SEM image of a sample of as-synthesized ipa0.1CuAPO<sub>4</sub>-14F. The presence of copper acetate in the synthesis gel seems to have altered the shapes of the crystallites, making some of them appear of truncated rectangular shape rather than the tabular shape found in AlPO<sub>4</sub>-14F. Although this shape is dominating, several crystallites have a more distorted appearance and lack of a definable shape. The distribution of crystallite sizes is broad, with the largest ones reaching 4 μm. Previous SEM reports on copper containing Zeotypes have shown the formation of crystallite agglomerates. Muñoz et al.<sup>109</sup> reported agglomerates of hexagonal CuAPO<sub>4</sub>-5 crystallites with sizes ranging from 10-20 μm when using copper oxide as transition metal source. Also reported by the authors was the formation of individual hexagonal crystallites having the same size as the clusters. Mathisen et al.<sup>106</sup> synthesized CuAPO<sub>4</sub>-5 crystallite agglomerates with similar size and shape as those reported by Muñoz et al., but also tested copper acetate as transition metal source. Their SEM images showed that samples containing smaller amounts of copper formed agglomerates of smaller sizes (respectively 10 and 6 μm).

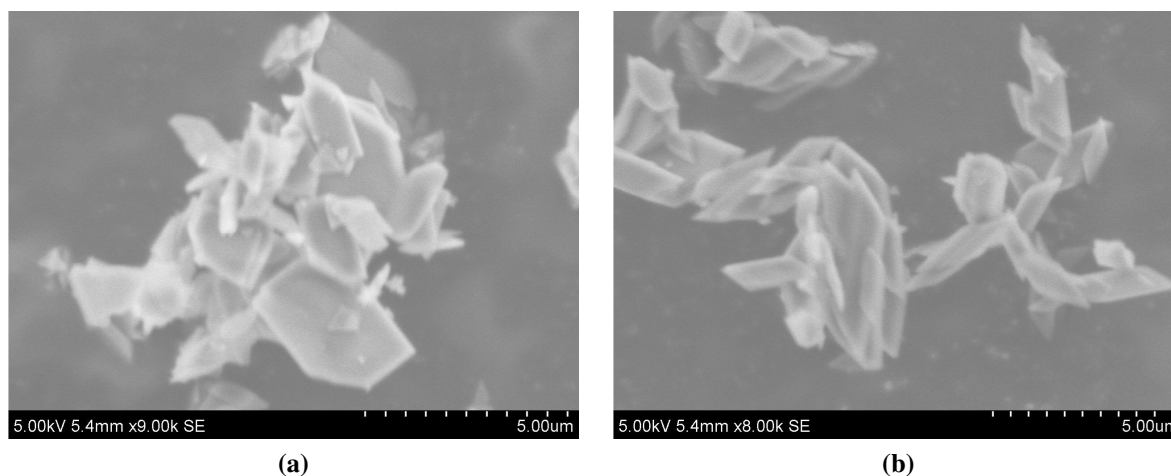


**Figure 4.50:** SEM images of a collection of crystallites in samples of as-synthesized: a) ipa0.01CuAPO<sub>4</sub>-14F ; b) ipa0.03CuAPO<sub>4</sub>-14F

Figure 4.50 b) shows a SEM image of a sample of as-synthesized ipa0.03CuAPO<sub>4</sub>-14F. The crystallites of this sample were found to be more defined in terms of size and shape when compared to those found in ipa0.01CuAPO<sub>4</sub>-14F. They also appear to be slightly larger, about 5 μm. The increased size may be due to the threefold increase in crystallization. This would indicate that the copper acetate perhaps acts as a size inhibitor. This may also be an indication that the initial presence of copper has a larger impact on the crystallization than copper in larger amounts. The presence of copper acetate in low amounts does not seem to cause agglomeration of crystallites.

Figure 4.51 a) shows a SEM image of a sample of calcined 0.01CuAPO<sub>4</sub>-14F. The crys-

tallites, of varying size and shape, seems to have suffered some damage by the calcination procedure most evident in what appears to be cracked/partial crystallites. This is consistent with the PXRD findings that showed similar intensity loss after calcination for  $\text{CuAPO}_4\text{-14F}$  and  $\text{AlPO}_4\text{-14F}$  samples. The presence of copper does not seem to have a stabilizing effect on the samples. It is worth noting that the crystallites are, discarding cracks, roughly the same size as that observed in the as-synthesized sample. In the case of  $\text{AlPO}_4\text{-14F}$ , the large crystallites found in as-synthesized sample were reduced upon calcination. In the  $\text{CuAPO}_4\text{-14F}$  samples the crystallite size is already reduced by the presence of copper acetate. The destruction of these could then perhaps involve another mechanism than for  $\text{AlPO}_4\text{-14F}$ . Figure 4.51 b) shows a SEM image of a sample of calcined  $0.03\text{CuAPO}_4\text{-14F}$ . In this sample the crystallites are not cracked, as observed for  $0.01\text{CuAPO}_4\text{-14F}$ , but seem to be physically separated from each other. This is evident from their poorly definable shapes and the broad distribution of sizes.

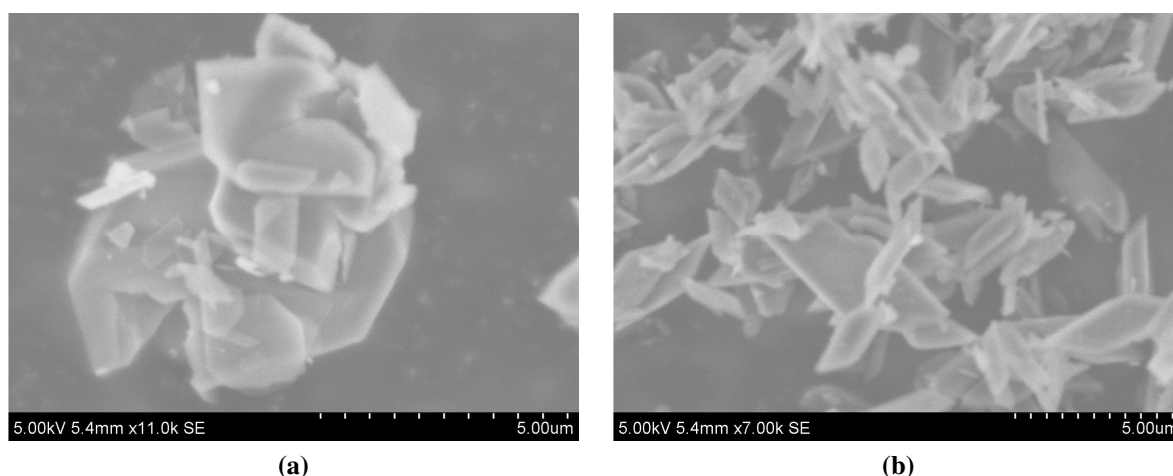


**Figure 4.51:** SEM images of a collection of crystallites in a sample of calcined: a)  $0.01\text{CuAPO}_4\text{-14F}$ ; b)  $0.03\text{CuAPO}_4\text{-14F}$

Agglomeration of crystallites readily occurs in as-synthesized  $0.08\text{CuAPO}_4\text{-14F}$ , and is not removed by calcination. (see figure 4.52 a) and b)). The increasing presence of copper has apparently two effects on  $\text{CuAPO}_4\text{s}$ : the first one being a decrease in crystallite sizes; the second being the agglomeration of the already small crystallites. The fact that the crystallization time for this sample was 8 days was seen as an additional illustration of the size suppressing role of the copper acetate. Samples of  $\text{AlPO}_4\text{-14F}$  displayed crystallites  $40\ \mu\text{m}$  in size after just 24 h of crystallization, indicating that at least large  $\text{AlPO}_4\text{-14}$  crystallites are to be expected. One would then expect the crystallites in  $0.08\text{CuAPO}_4\text{-14F}$  to substantially increase in size when given an additional 7 days of crystallization.

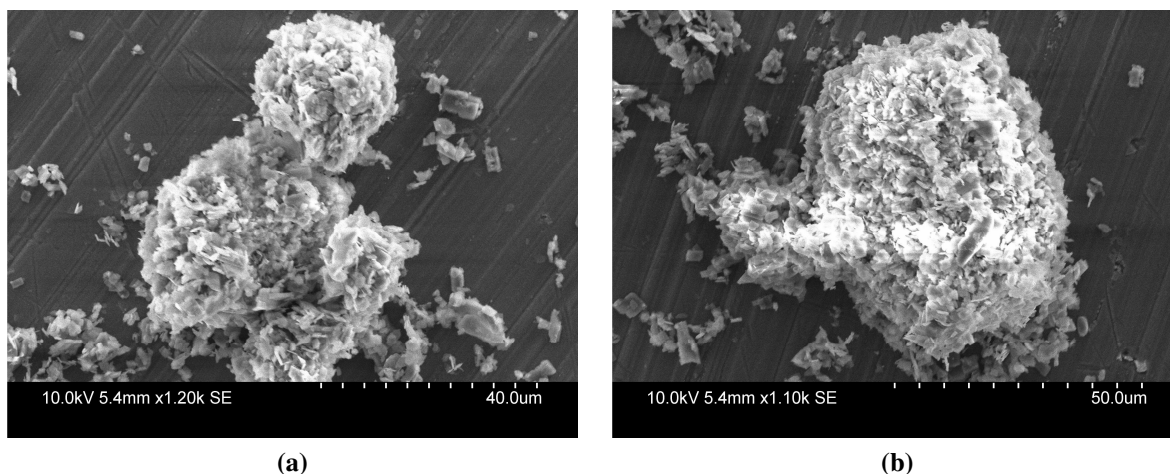


**Figure 4.52:** SEM images of a collection of crystallites in a sample of  $0.08\text{CuAlPO}_4\text{-14F}$ : a) as-synthesized; b) calcined

### 4.3.3 $\text{ipaAlPO}_4\text{-14A}$

#### as-synthesized and calcined

Figure 4.53 a) shows a SEM image of a sample of  $\text{AlPO}_4\text{-14A}$ . The image shows a stick shaped crystallite at least  $40\ \mu\text{m}$  in length, which itself is surrounded by smaller similar shaped crystallites. Since the sample was proven phase-pure with PXRD it is logical to only observe one type of crystallite. By further inspection, the large crystallite seems to be composed of smaller crystallites, and the surrounding crystallites may be compositional parts that have been broken off. The stick type crystallite is in agreement with that observed by M. Goepper and J.L. Guth<sup>114</sup> for their impure  $\text{AlPO}_4\text{-14A}$  sample obtained in fluoride medium. Figure 4.53 b) shows a SEM image of crystallites in a sample of calcined  $\text{AlPO}_4\text{-14A}$ . It can be seen that the calcination process has reduced the crystallite sizes and they now tend to bunch together.

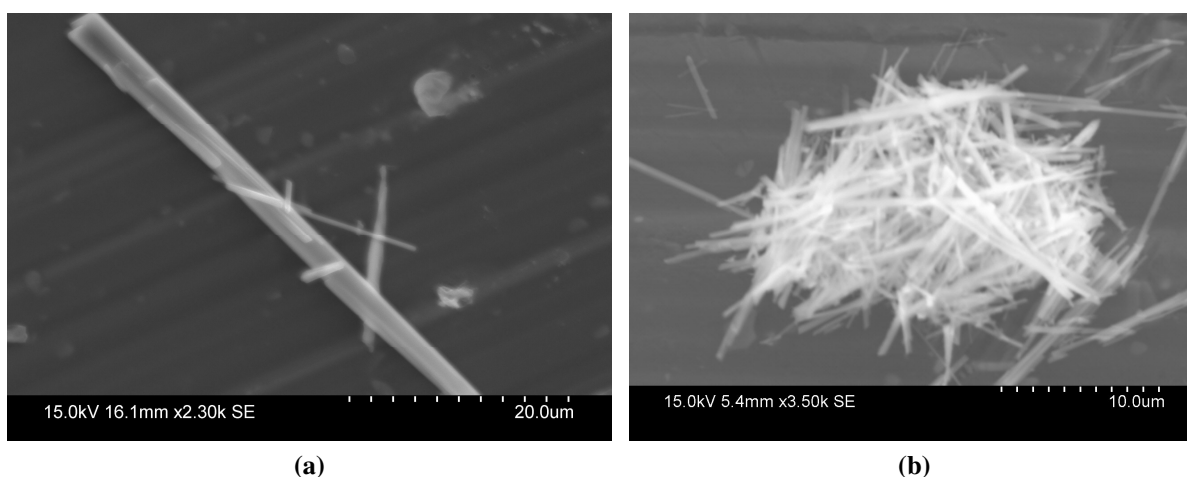


**Figure 4.53:** SEM images of a collection of crystallites in samples of  $\text{AlPO}_4\text{-14A}$ : a) as-synthesized; b) calcined

The small crystallites observed are believed to be parts of the larger crystallites found in the as-synthesized sample. Their irregular shapes seem to support this. The destroyed crystallites reflect the PXRD results, and may indicate that parts of the actual crystallites are amorphous. This mindset comes from only observing a homogeneous mixture of broken crystallites and no other species that could be defined as “amorphous” material. The same destruction was not observed for the stick type crystallites found in calcined partially-hydrated  $\text{AlPO}_4\text{-14F}$ , indicating that the thermal events maybe somehow dependent on how much of a particular crystallite is present. Another possible explanation is that the crystallites observed in  $\text{AlPO}_4\text{-14F}$  belong to another unknown impurity, one that is thermally stable. It could also indicate that  $\text{AlPO}_4\text{-14A}$  samples synthesized in acidic gels are more thermally stable. These SEM images shown here indicate that  $\text{AlPO}_4\text{-14A}$  is still present after calcination.

#### 4.3.4 ipaSAPO<sub>4</sub>-43

##### as-synthesized and calcined

Figure 4.54 a) shows a SEM image of a sample of as-synthesized ipaSAPO<sub>4</sub>-43. The image shows well formed octahedrally shaped crystallites in agreement with that previously reported by Akporiaye et al.<sup>121</sup>. The sizes of the crystallites vary from 20  $\mu\text{m}$  to 1  $\mu\text{m}$ , indicating a broad distribution. Also observed is the inter growth of crystallites, showing that the sample of this work is of roughly the same quality as that reported in the literature. The crystallites show no indication of being composed of smaller units as was observed previously for ipaAlPO<sub>4</sub>-14A.

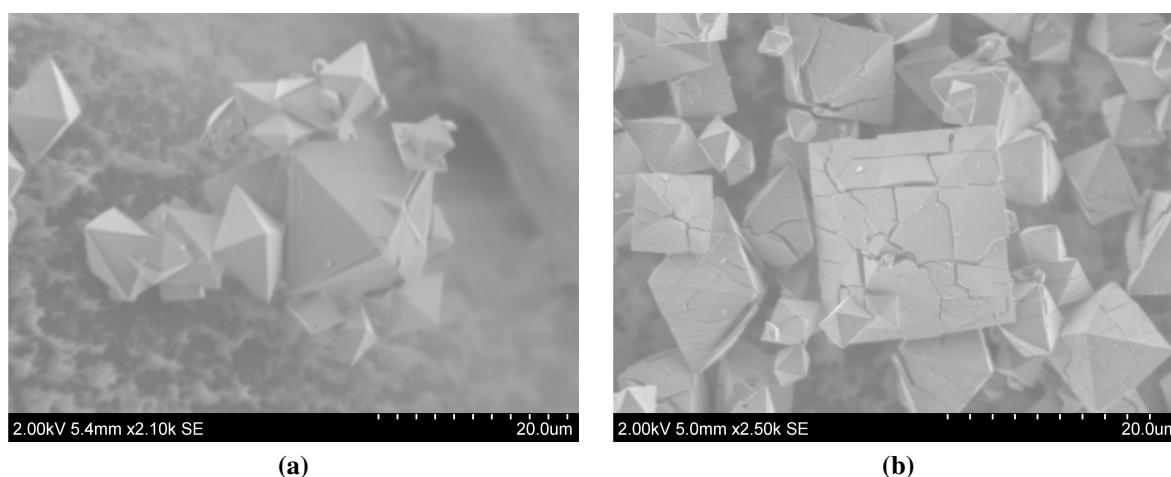


**Figure 4.54:** SEM images of a collection of crystallites in samples of ipaSAPO<sub>4</sub>-43: a) as-synthesized; b) calcined in a preheated oven at 600°C for 10 h.

Although Akporiaye et al.<sup>121</sup> highlighted the destruction of SAPO<sub>4</sub>-43 during calcination, they did not show what happened to the individual crystallites. Figure 4.54 b) shows that the calcination process has not induced a phase transition, which is consistent with PXRD results. It has, however, caused the individual crystallites to literally crack and deform. The broadening

of the PXRD peaks during calcination (observed by Akporiaye et al.<sup>121</sup> with *in-situ* studies) can then be understood by the formation of cracks causing crystal planes to get shifted relative to each other. This in turn has a distorting effect on the long range order of the material, leading to increasingly broader PXRD peaks until the point where they completely fade away. Also tested was a calcination procedure consisting of heating the material from 25 to 550°C at a rate of 1°C/min, and then dwelling for 24 h at 550°C. PXRD revealed that this alternate calcination route does not prevent the destruction of the material, and it can be seen in figure 4.55 that the crystallites are destroyed. The removal of the isopropylamine template is apparently so brutal that cracks are bound to occur.

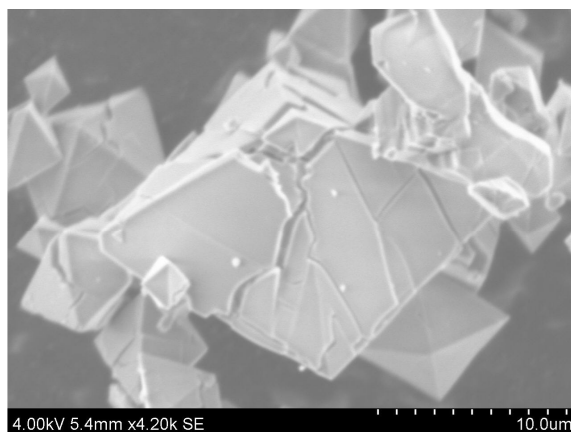


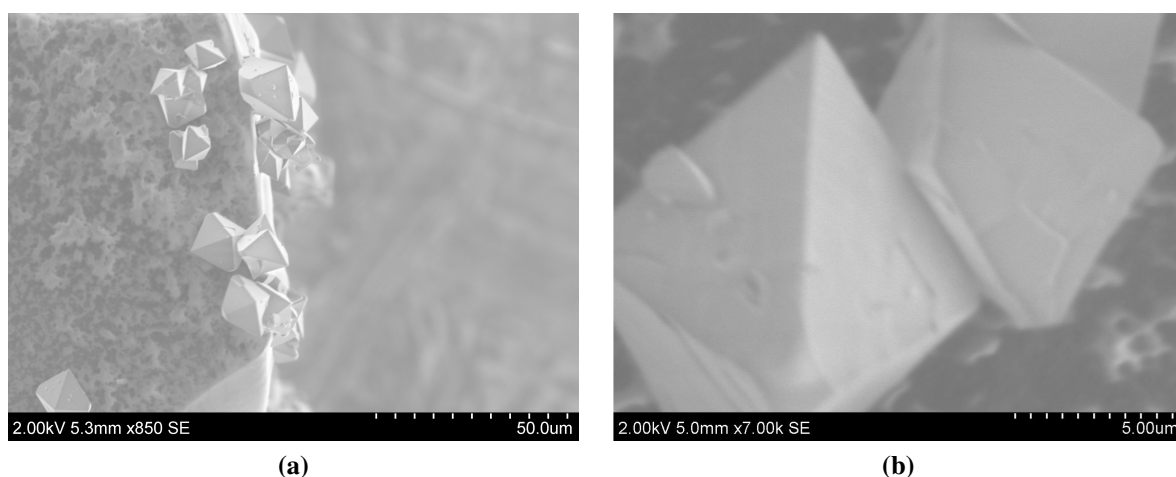
**Figure 4.55:** A SEM image of crystallites found in a sample of ipaSAPO<sub>4</sub>-43 after calcination by heating the material from 25 to 550°C at a rate of 1°C/min and dwelling for 24 h at 550°C.

### 4.3.5 dpaSAPO<sub>4</sub>-43

#### as-synthesized and calcined

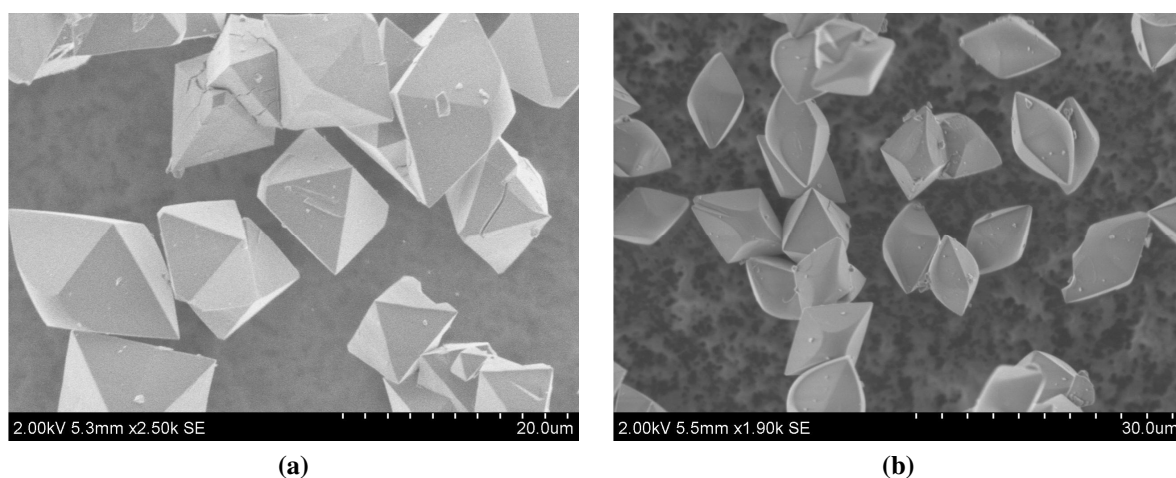
Figure 4.56 a) shows a SEM image of a sample of as-synthesized dpaSAPO<sub>4</sub>-43. The image shows well formed octahedral crystallites such as those found for ipaSAPO<sub>4</sub>-43. A distinction can be made, however, in that these crystallites were found to have a degree of truncation of some of their edges. This could, in addition to the different templates used, explain the differences observed in the diffraction patterns for the two as-synthesized versions of SAPO<sub>4</sub>-43. PXRD showed that calcination of dpaSAPO<sub>4</sub>-43 in a preheated oven also turns this version amorphous. When removing the di-n-propylamine template, the crystallites are somewhat more preserved as can be seen in figure 4.56 b). However, there are still visible cracks running through the crystallites, probably causing a distortion of the long range order (i.e. no peaks visible with PXRD). The SEM images presented by MAPO<sub>4</sub>-43 by Akolekar et al.<sup>123</sup> also showed similar cracked crystallites. These authors suggested that thermal instability was linked to magnesium content and considered their crystallites to be preserved.

Figure 4.57 a) shows a SEM image of sample of dpaSAPO<sub>4</sub>-43 after calcination by heating the material from 25 to 550°C at a rate of 1°C/min and dwelling for 24 h at 550°C. The images



**Figure 4.56:** SEM images of a collection of crystallites in samples of dpaSAPO<sub>4</sub>-43: a) as-synthesized; b) calcined in a preheated oven at 600°C for 10 h.

show that, while some crystallites have cracked and coalesced, the milder calcination method has left other crystallites unharmed. This was not the case for ipaSAPO<sub>4</sub>-43, where such a milder calcination procedure had little effect on the preservation of the crystallites. The removal of these two templates, isopropylamine and di-*n*-propylamine, are thus obviously of differing nature although they promote the crystallization of the same material. Figure 4.57 b) shows a SEM image of a sample of dpaSAPO<sub>4</sub>-43 after calcination by heating the material from 25 to 550°C at a rate of 0.5°C/min (dwelling at 550°C for 24 h). Decreasing the heating rate further leads to near full preservation of the crystallites which hardly show any sign of cracks or coalescing.

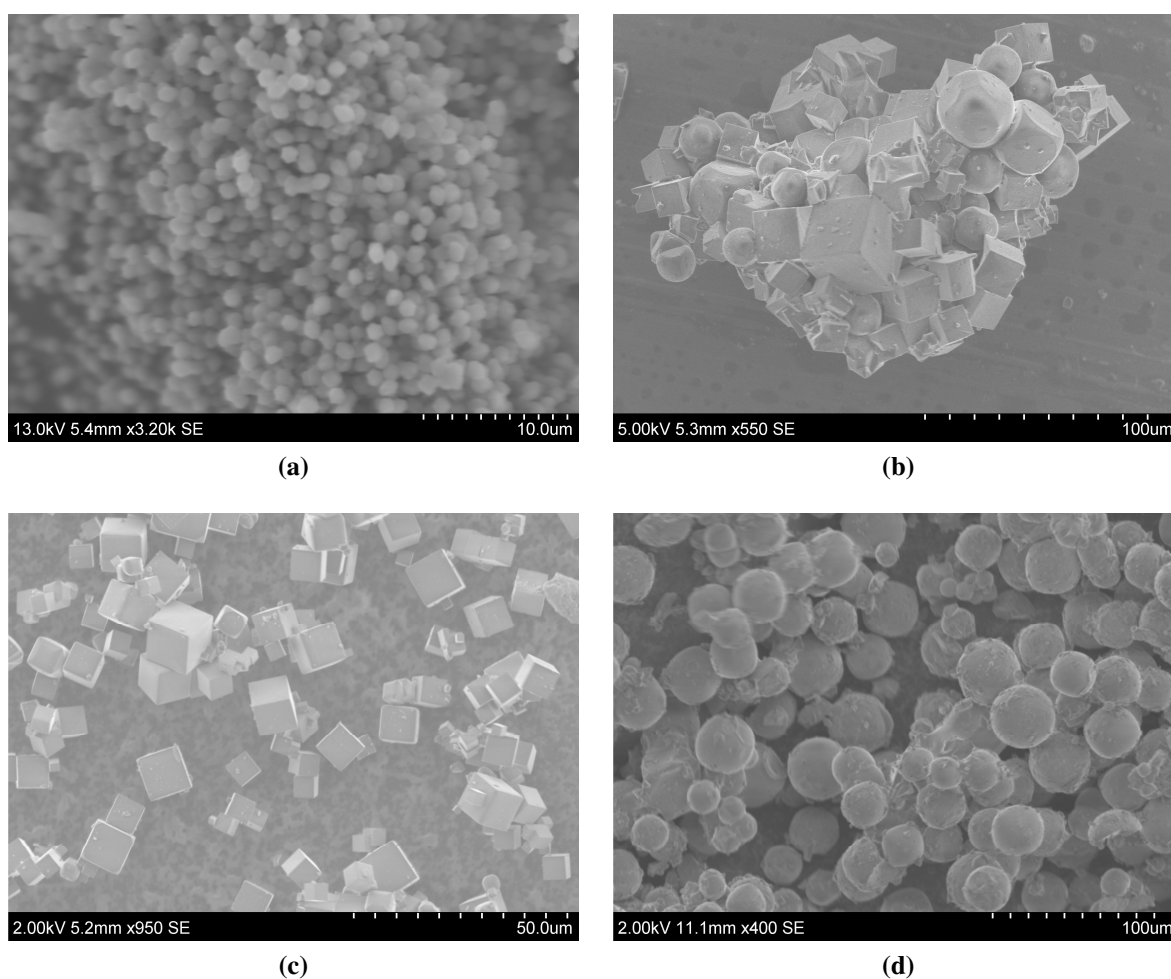


**Figure 4.57:** SEM images of a collection of crystallites in samples of dpaSAPO<sub>4</sub>-43 calcined by heating them from 25 to 550°C at different rates: a) 1°C/min; b) 0.5°C/min.

### 4.3.6 Augelite and pipSAPO<sub>4</sub>-20

#### as-synthesized

Figure 4.58 a) a SEM image of a sample of Augelite. The image shows a narrow size distribution with approximately 1 $\mu$ m sized crystallites. No definable shape was observed. The small size could probable account for the somewhat broad peaks observed with PXRD, and there was no sign of crystallites that might belong to the impurities.



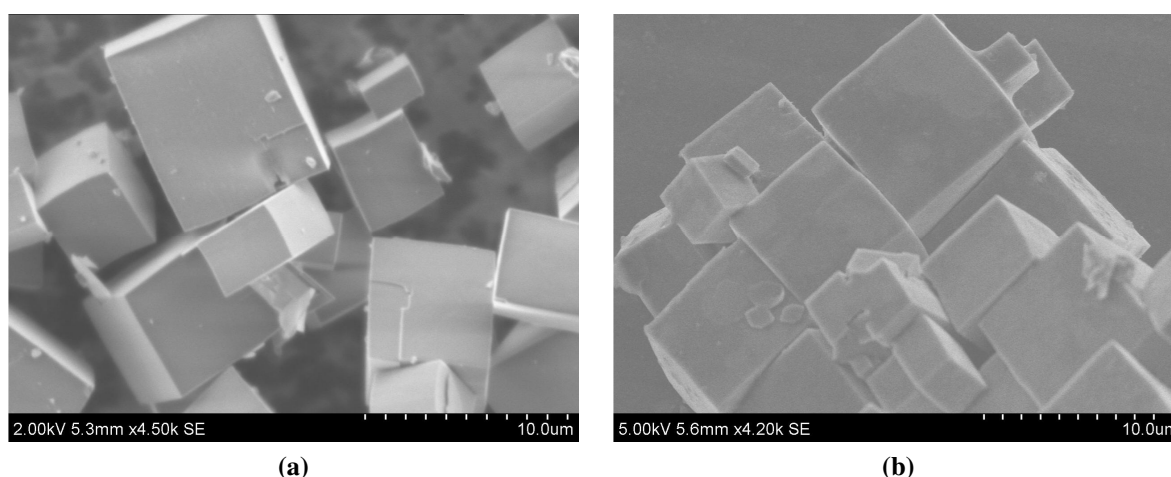
**Figure 4.58:** SEM images for: a) as-synthesized Augelite; b) as-synthesized pipSAPO<sub>4</sub>-20 obtained from a gel with molar oxide ratio: 5.18R:0.8Al<sub>2</sub>O<sub>3</sub>:P<sub>2</sub>O<sub>5</sub>:0.4SiO<sub>2</sub>:40H<sub>2</sub>O crystallized at 200°C for 72 h; c) same as (b)) using a gel with molar oxide ratio: 3.36R:Al<sub>2</sub>O<sub>3</sub>:0.8P<sub>2</sub>O<sub>5</sub>:0.4SiO<sub>2</sub>:40H<sub>2</sub>O; b) same as (b)) using a gel with molar oxide ratio: 3.36R:0.8Al<sub>2</sub>O<sub>3</sub>:P<sub>2</sub>O<sub>5</sub>:1SiO<sub>2</sub>:40H<sub>2</sub>O.

Figure 4.58 b) shows a SEM image of a sample of as-synthesized pipSAPO<sub>4</sub>-20. It shows an agglomeration of crystallites in the shape of cubes, spheres, and dice. The size distribution also seems broad, with some of the largest crystallites approaching sizes of 50  $\mu$ m. The presence of several types of crystallites is inconsistent with the PXRD results that indicated no other phase than SAPO<sub>4</sub>-20. Samples from two of the additional preparations found for pipSAPO<sub>4</sub>-20 were also characterized using SEM, and the images for these are shown in figure 4.58 c) and d) (see

figure text for details). It can be seen that in gels where silicon replaces phosphorous (figure 4.58 c)) the crystallites are of mostly cubic habit. In gels where the silicon is added “in excess” the crystallites favor a more spherical habit. This was seen as a further indication that all as-synthesized SAPO<sub>4</sub>-20 samples were phase-pure, and that the crystal habit varies with silicon content in the synthesis gel.

### 4.3.7 dipaSAPO<sub>4</sub>-34

Figure 4.59 a) shows a SEM image of as-synthesized dipaSAPO<sub>4</sub>-34. The sample is composed of crystallites with rectangular cuboid shape with sizes ranging from 2 to 10 μm. Figure 4.59 b) shows that crystallites are completely unaffected by the calcination process. This is consistent with that observed with PXRD showing an intensity increase after calcination.



**Figure 4.59:** SEM images for samples of dipaSAPO<sub>4</sub>-34: a) as-synthesized; b) calcined

### 4.3.8 teaSAPO<sub>4</sub>-18

Figure 4.60 shows SEM images of as-synthesized and calcined samples of teaSAPO<sub>4</sub>-18. The SAPO<sub>4</sub>-18 sample is composed of rectangular crystallites with sizes ranging from 500 nm to 2.5 μm. These findings are consistent with that of previous reports<sup>139,97</sup> on SAPO<sub>4</sub>-18, where crystallites of similar size and shape were obtained using the templates *N,N*-diisopropylethylamine and tetraethylammonium hydroxide (TEAOH). The sizes are, however, not consistent with that observed for most other samples synthesized in alkaline mixtures. This indicates that the topology itself may play a role in the size of the crystallites formed, and shows that high pH mixtures do not exclusively produce large crystallites. As observed previously for dipaSAPO<sub>4</sub>-34, the crystallites of SAPO<sub>4</sub>-18 suffer no damage as a result of calcination.

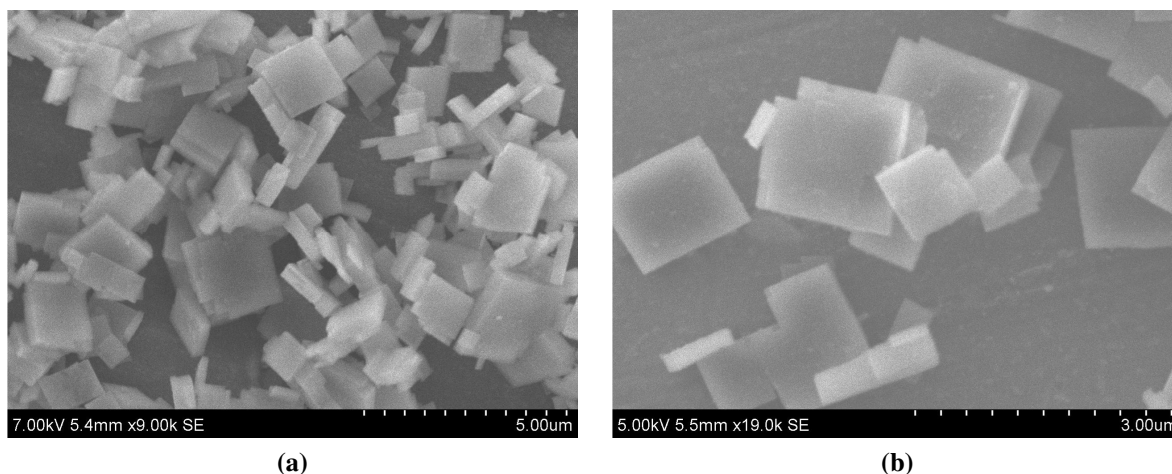


**Figure 4.60:** SEM images for samples of teaSAPO<sub>4</sub>-18: a) as-synthesized; b) calcined

### 4.3.9 Unidentified phase

Figure 4.61 shows a SEM image of the unidentified sample made with methylamine as template and a mixture with molar oxide ratio: 4.36R:Al<sub>2</sub>O<sub>3</sub>:P<sub>2</sub>O<sub>5</sub>:40H<sub>2</sub>O crystallized for 24 h at 200°C. The image shows irregular shaped plates with sizes varying from 1 to 5 μm.

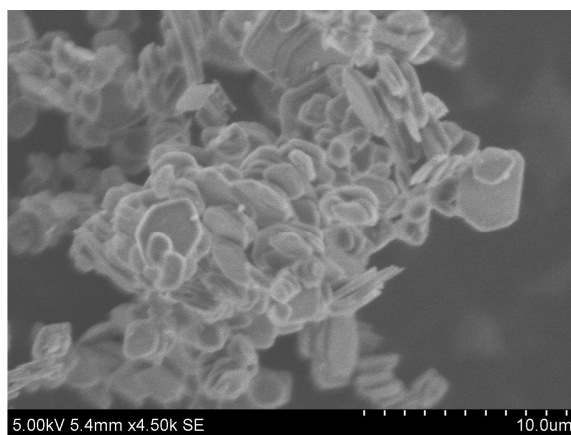


**Figure 4.61:** A SEM image of crystallites found in an unidentified as-synthesized sample made with methylamine.

### 4.3.10 dpaipaSAPO<sub>4</sub>-43

The dual template approach was primarily aimed at synthesizing smaller crystallites of SAPO<sub>4</sub>-43 more suitable for FT-IR studies. Figure 4.62 shows the SEM images for the sample in as-synthesized and calcined form. The crystallites display the octahedral shape characteristic for SAPO<sub>4</sub>-43, and the maximum size is approximately 10 μm. The crystallites also display a smooth appearance of some of their edges which is considered characteristic for SAPO<sub>4</sub>-43 samples synthesized using the di-n-propylamine template. The results thus indicate that the dual template approach effectively reduces the crystallite size by roughly 50%, and the presence

of isopropylamine does not lead to reduced thermal stability of the sample. Isopropylamine's function can then be considered a crystallization catalyst, promoting fast crystallization leading to smaller crystallites.

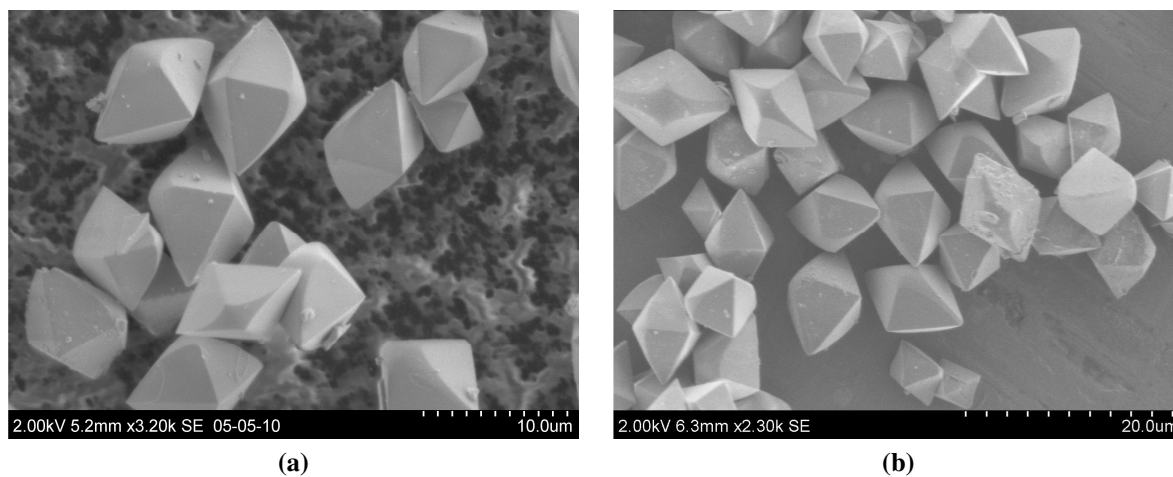


**Figure 4.62:** SEM images of a collection of crystallites in dpaipaSAPO<sub>4</sub>-43: a) as-synthesized; b) calcined by heating the sample from 25 to 550°C at 0.5°C/min.

## 4.4 TGA and DSC

### 4.4.1 ipaAlPO<sub>4</sub>-14F

Figure 4.63 shows the combined TG and DSC curves for ipaAlPO<sub>4</sub>-14F when heating a sample from 25°C to 550°C at a rate of 2°C/min. The distinctive changes occurring can roughly be assigned to three steps given by the temperature intervals: 25-100°C, 270-350°C, and 350-550°C. The TG curve shows that ipaAlPO<sub>4</sub>-14F loses 4% mass almost linearly in the temperature interval 25-100°C. The mass % lost is probably due to the removal of water adsorbed on the material's surface, a process requiring energy (endothermic)<sup>142</sup> as can be seen on the DSC curve. In the second temperature interval, an identical mass % is lost, and could be an indication of more water being removed. The interesting part is that this step is more endothermic than the previous one, as can be seen on the DSC curve. If water is removed in this step, it could be located in the pores of the material, and perhaps requiring more energy to escape. Thermal decomposition in this step is not likely based on the pseudo *in-situ* PXRD experiment that showed no structural changes prior to the interval 400 to 450°C. Any decomposition would affect the sample's unstable crystallites that are prone to partial destruction as shown with SEM.

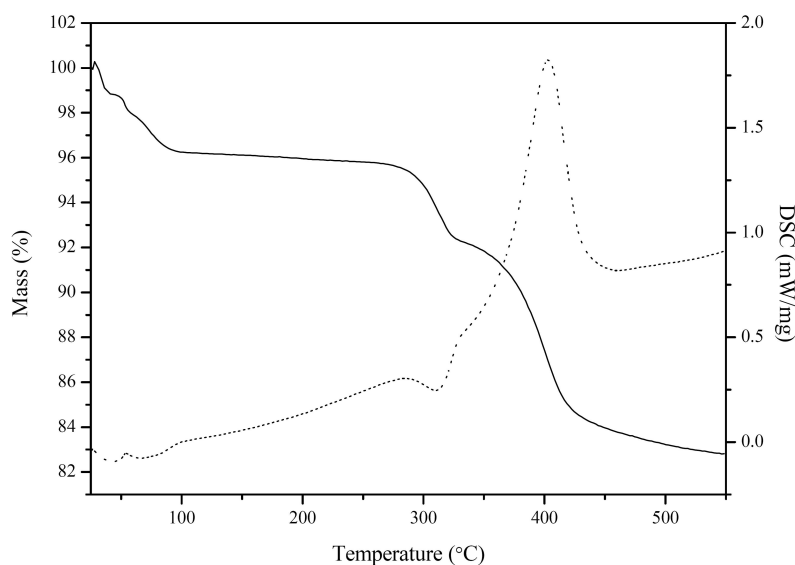
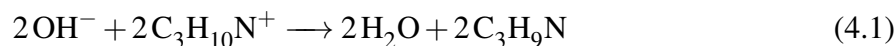


**Figure 4.63:** TG (solid line) and DSC (dotted line) curves for ipaAlPO<sub>4</sub>-14F when heating a sample from 25 to 550°C at a rate of 2°C/min.

In the final temperature interval, the mass lost is significantly larger than the previous two, and this step likely represents the removal of the isopropylamine template. This step is exothermic and is an indication that the template is removed by combustion<sup>143</sup>. From the shape of the last step one can also infer that the template is not decomposed prior to its removal. If that was the case, the curve of this step would not be smooth, but consist of smaller curves each representing the decomposed parts of the template leaving the material. The mass loss (in %)

for the temperature intervals discussed for ipaAlPO<sub>4</sub>-14F is given in table 4.7 along with theoretical mass loss data from appendix B.3.1. The theoretical values do not correspond to any definable temperature intervals, but was divided among the observed temperature intervals. The theoretical and observed mass loss steps are in agreement, indicating that OH<sup>-</sup> and H<sup>+</sup> (from the protonated template) combine and form H<sub>2</sub>O in the second temperature interval:



The values are also consistent with the template leaving the lattice intact in the temperature interval 350-450°C. Figure 4.64 shows that after reaching 550°C both TG and DSC curves approach a final value. The presence of impurities does not seem to have any effect on the AlPO<sub>4</sub>-14F sample.

**Table 4.7:** Summary of observed and theoretical mass loss for the critical temperature intervals of ipaAlPO<sub>4</sub>-14F.

Temperature interval (°C)	Mass loss (%)	Theoretical mass loss (%)
25 - 100	4	3
270 - 350	4	3
350 - 550	9	10
Total	17	16

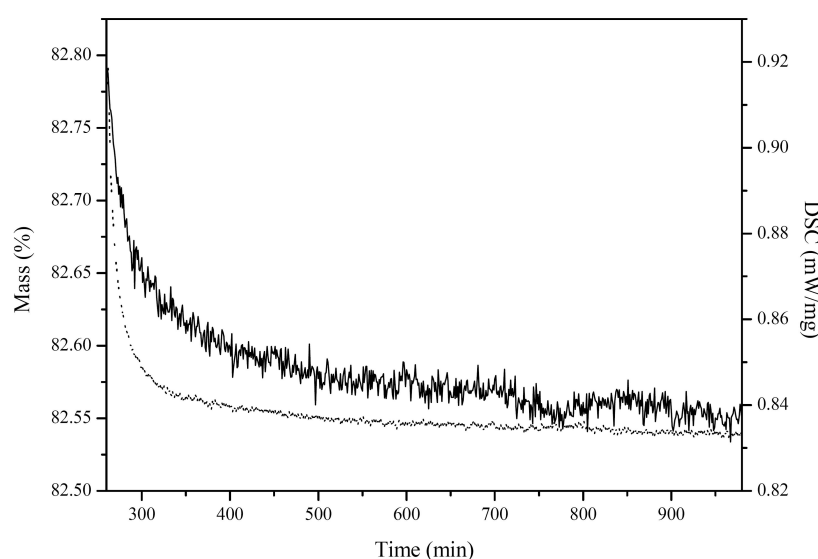
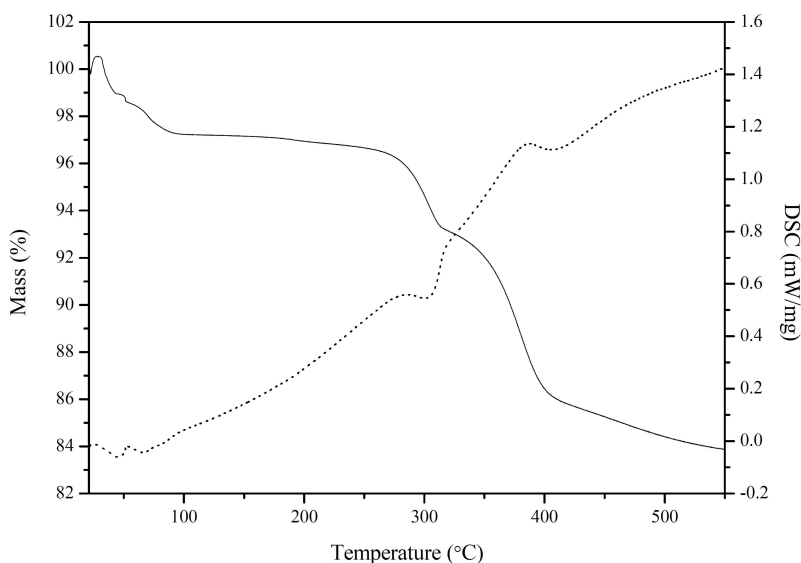


**Figure 4.64:** TG (solid line) and DSC (dotted line) curves for a sample of ipaAlPO<sub>4</sub>-14F when dwelling at 550°C for 12 hours

## 4.4.2 ipaCuAPO<sub>4</sub>-14F

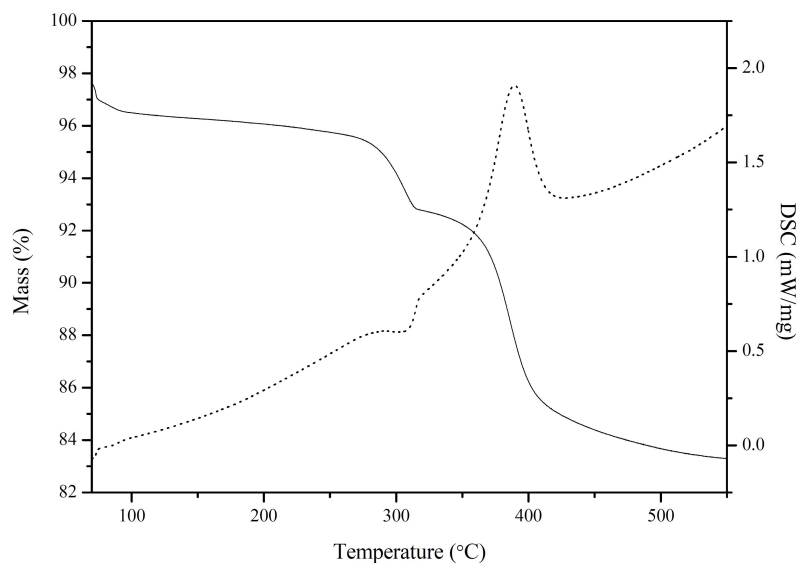
### ipa0.01CuAPO<sub>4</sub>-14F and ipa0.03CuAPO<sub>4</sub>-14F

Figure 4.65 shows TG and DSC curves for a sample of ipa0.01CuAPO<sub>4</sub>-14F during heating from 25 to 550°C at a rate of 2°C/min. The TG curve is similar to that observed for ipaAlPO<sub>4</sub>-14F, as would be expected when using the same template. The presence of copper seems to cause a less exothermic step around 400°C as indicated by the DSC curve. There is a noteworthy increase in mass at the start of the experiment, but this is more likely a result of the TGA instrument not working properly rather than an effect of copper. Figure 4.66 shows the TG and DSC curves for a sample of ipa0.03CuAPO<sub>4</sub>-14F during heating from 25 to 550°C at a rate of 2°C/min. Even though there is a large difference between the (Al+P)/Cu ratios of these samples, it has no apparent effect on their observed thermal behavior. Some difficulties with the instrument occurred when examining this sample as well, and the erroneous data obtained for the sample below 70°C was therefore discarded. The similar mass loss for the two CuAPO<sub>4</sub>-14F compositions compared to AlPO<sub>4</sub>-14F indicates that all template is removed.



**Figure 4.65:** TG (solid line) and DSC (dotted line) curves for a sample of ipa0.01CuAPO<sub>4</sub>-14F when heating a sample from 70 to 550°C at a rate of 2°C/min. Negligible mass loss observed during isothermal heating at 550°C for 12 h.

Previous studies<sup>62,144</sup> on MeAPO systems report a shift in the TG curves to higher temperatures when elements replacing than Al are present. Particularly, this behavior has been observed with DTG (differential TG, rate of mass loss) on peaks above 100°C, and unaffected peaks below this temperature was believed to involve removal of species adsorbed on the materials surfaces. The amount of metal in their samples was shown to shift the DTG peaks to higher temperatures. Kornatowski et al.<sup>62</sup> performed a rather extensive TGA study on MeAPO<sub>4</sub>-31 where a range of incorporated metals was investigated. The authors found that the presence of



**Figure 4.66:** TG (solid line) and DSC (dotted line) curves for a sample of ipa0.03CuAPO<sub>4</sub>-14F when heating a sample from 70 to 550°C at a rate of 2°C/min. Negligible mass loss observed for isothermal heating at 550°C for 12 h.

small amounts (0.01 mol Me in the synthesis gels, even less in the actual materials) of metals such as Cu, Cr, and Mn, influenced the mass loss temperature. They discovered that the critical factor for this phenomenon was the amount and not the type of metal present in the samples. To investigate if such a phenomenon was observable in the CuAPO<sub>4</sub>-14F samples of this work, the DTG curves for the two ipaCuAPO<sub>4</sub>-14F as well as that for ipaAlPO<sub>4</sub>-14F were compared (shown in figure 4.67). The DTG curve for ipaAlPO<sub>4</sub>-14F shows two peaks at 312.5 and 400°C. The presence of 0.01 mol copper in the synthesis gel for ipa0.01CuAPO<sub>4</sub>-14F results in a negative DTG temperature shift of nearly 7°C for the peak at 312.5°C, and 20°C for the peak at 400°C. This is almost an exact opposite behavior to that reported for CuAPO<sub>4</sub>-31. A further increase of copper results in a slight increase in the DTG curve. The initial decrease in DTG peaks may be an indication that the DTG curves in AlPO<sub>4</sub>-14F is shifted to what would normally be characteristic for AlPO<sub>4</sub>-14. Since no TG or DTG curves have been published for ipaAlPO<sub>4</sub>-14 (except for the calcined material<sup>35</sup>) a direct comparison is impossible. One has to consider the possibility that Al-OH-Al groups in AlPO<sub>4</sub>-14A and AlPO<sub>4</sub>-15 contributing to the removal of the template. These characteristic groups may act as acid sites in the same way as those caused by divalent metals incorporated in the lattice (replacing Al). An increase in the presence of these sites should probably produce the same behavior as an increase of Me-OH-P sites. Since, however, these sites are unavoidably present due to the impurities, the DTG curve may already have been shifted to that of pure AlPO<sub>4</sub>-14. If these sites are more acidic, and hence would cause a greater interaction than sites induced by metals, any substitution of such sites would diminish the interaction with the template during calcination. This would explain why the DTG peaks are initially negatively shifted in the presence of copper, for later to be

increased with the further increase in copper content.

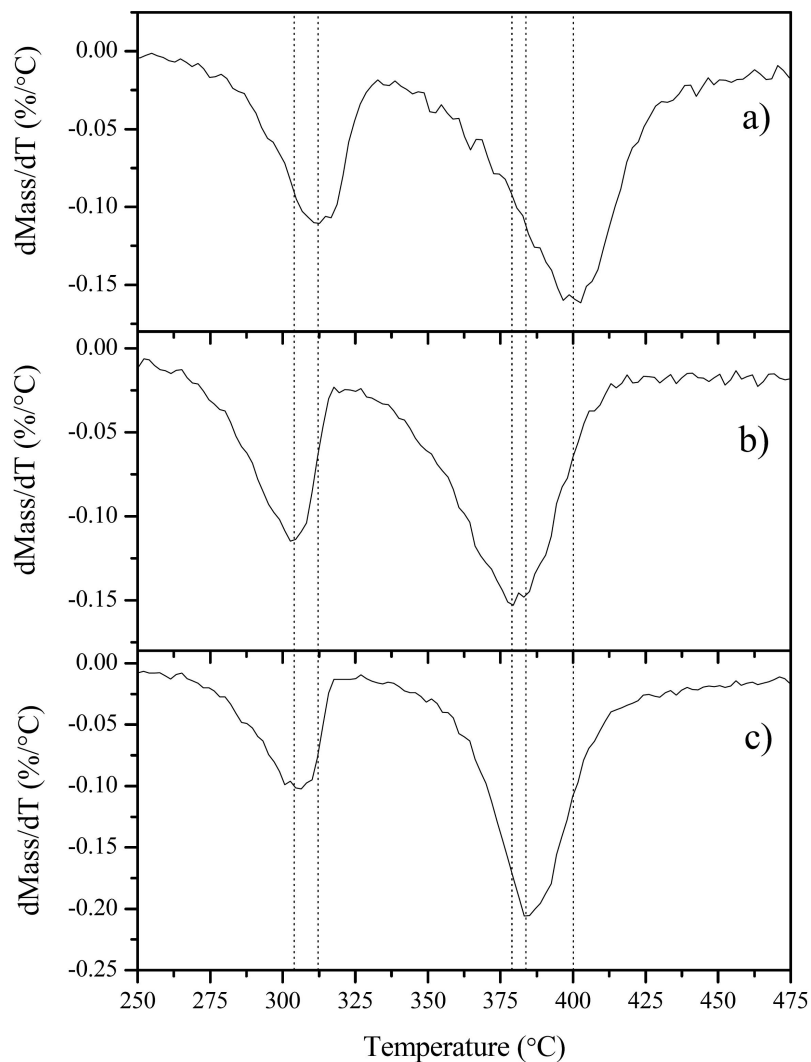


**Figure 4.67:** DTG curves for samples when heating them from 200 to 500°C at a rate of 2°C/min: a)  $\text{ipaAlPO}_4\text{-14F}$ ; b)  $\text{ipa0.01CuAPO}_4\text{-14F}$ ; c)  $\text{ipa0.03CuAPO}_4\text{-14F}$ . The dotted lines indicate approximate DTG peak minima for the three samples.

### 4.4.3 tbaAlPO<sub>4</sub>-14F

Figure 4.68 shows the TG and DSC curves for tbaAlPO<sub>4</sub>-14 when heating a sample from 25 to 550°C at a rate of 2°C/min. The two curves show expected similarities with the curves for ipaAlPO<sub>4</sub>-14F, but a few distinctions are also present. For clarity the curves are divided into the same temperature intervals as for ipaAlPO<sub>4</sub>-14F. The first distinction that can be observed is the smaller amount of water removed in the interval from 25 to 100°C.

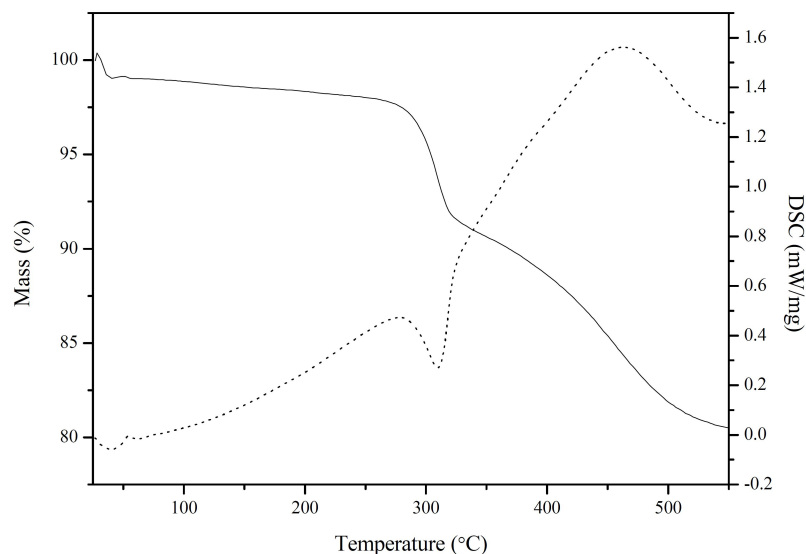


**Figure 4.68:** TG (solid line) and DSC (dotted line) curves for tbaAlPO<sub>4</sub>-14F when heating a sample from 25 to 550°C at a rate of 2°C/min.

The ipaAlPO<sub>4</sub>-14F sample has a mass loss of 4% in this interval, the tbaAlPO<sub>4</sub>-14F sample has a mass loss of only 1%. In the next interval (270-350°C), the situation is quite the opposite. In this interval the mass loss is 7%, which is a 3% increase from that observed for ipaAlPO<sub>4</sub>-14F. If this step corresponds to water removal H<sub>2</sub>O from the combination of H<sup>+</sup> (from template) and OH<sup>-</sup>, then more of these must be present in the pores of tbaAlPO<sub>4</sub>-14F than ipaAlPO<sub>4</sub>-14F. The DSC curve shows that this step is more endothermic for tbaAlPO<sub>4</sub>-14F than ipaAlPO<sub>4</sub>-14F, which is to be expected if this is the case. The pseudo *in-situ* experiment was only performed on samples containing isopropylamine, limiting the knowledge regarding the appearance of the diffraction pattern for the material at elevated temperatures. This may also be an indication that the packing of tert-butylamine differs from that of isopropylamine, and somehow incorporates more internal water. The preparation of the gel from which tbaAlPO<sub>4</sub>-14F is crystallized also differs a bit from ipaAlPO<sub>4</sub>-14F in that additional water is added after the template. This adding of water after the template may affect the final unit cell composition. The final mass loss step is the largest, and was attributed to the removal of tert-butylamine from the material's pores. This step is significantly less exothermic than that observed for isopropylamine removal. Table 4.8 summarizes the mass loss and the corresponding temperature intervals for tbaAlPO<sub>4</sub>-14. As for ipaAlPO<sub>4</sub>-14F, the theoretical and observed mass loss indicates a deprotonation of template

molecules and the subsequent formation of water (though this may be highly simplified):

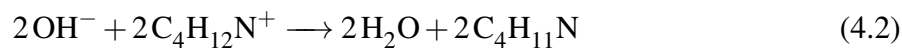
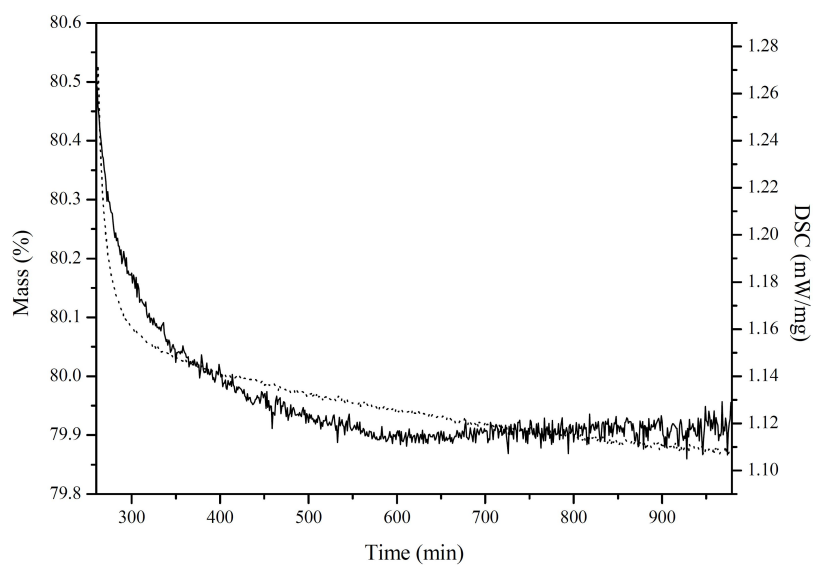


Figure 4.69 shows the TG and DSC curves for the material during isothermal heating.

**Table 4.8:** Summary of mass loss for the critical temperature intervals of tbaAlPO<sub>4</sub>-14F.

Temperature interval (°C)	Mass loss (%)	Theoretical mass loss (%)
25 - 100	1	0
270 - 350	7	6
350 - 550	12	12
Total	20	18

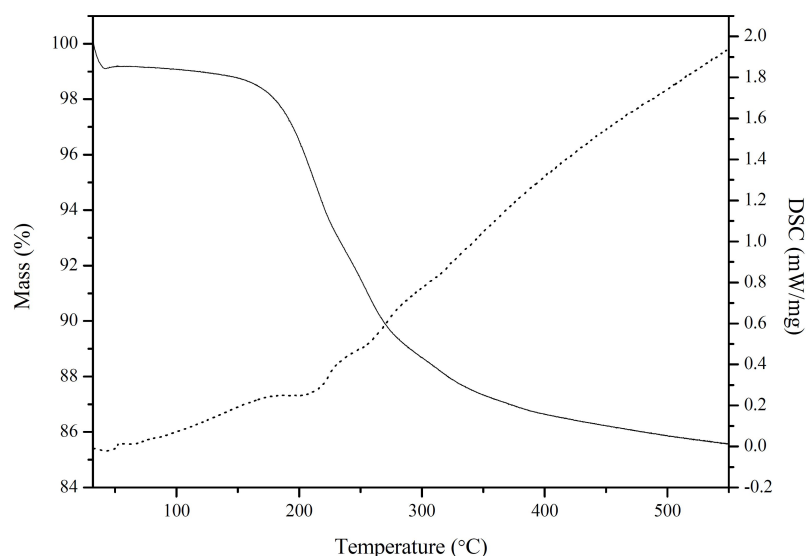


**Figure 4.69:** TG (solid line) and DSC (dotted line) curves for a sample of tbaAlPO<sub>4</sub>-14F when dwelling at 550°C for 12 hours.

#### 4.4.4 tbaSAPO<sub>4</sub>-14F

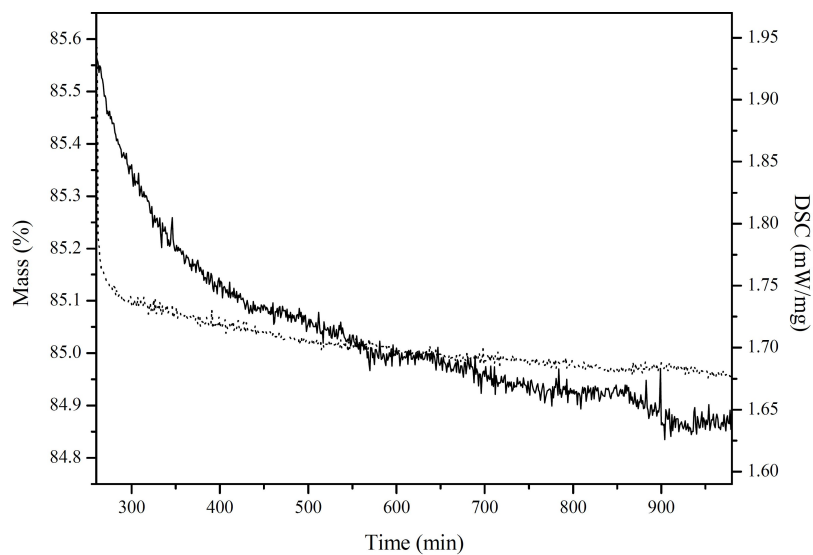
##### tba0.06SAPO<sub>4</sub>-14F

Figure 4.70 shows the TG and DSC curves for tba0.06SAPO<sub>4</sub>-14F when heating a sample from 25 to 550°C at a rate of 2°C/min. The observation made for the SAPO<sub>4</sub>-14F compositions was that the samples were still brown after calcination at 550°C for 16 h. This was seen as an indication that some of the template molecules still resided in the pores of the materials, and that higher temperatures were needed. Figure 4.70 complements this observation, showing an initial water loss of 2% between 25 to 70°C, followed by a larger mass loss of 14% between 70 and 550°C. The presence of silicon causes a shift in the TG curve, showing some of the guest molecules (template, water, hydroxide ions) leaving the lattice at lower temperatures. However, the total mass lost (14%) is less than the theoretical mass loss (18%), indicating that higher temperatures were necessary for complete calcination of the material. Figure 4.71 shows the TG and DSC curves when heating the material isothermally at 550°C for 12 h. It can be seen that little mass is lost during the isothermal heating, indicating that these mass loss events are not time dependent to any large extent.



**Figure 4.70:** TG (solid line) and DSC (dotted line) curves for a sample of tba0.06SAPO<sub>4</sub>-14F when heating a sample from 25 to 550°C at a rate of 2°C/min.

Since the observed mass loss was insufficient when heating the sample to 550°C and dwelling for 12 h, a new TGA/DSC experiment was performed. A generalized heating procedure to 1000°C at a rate of 5°C (dwelling for 3 h) was employed. The resulting TG and DSC curves are shown in figure 4.72. The increased heating rate was used to economize the experiment. The mass loss of 2% in the interval from 25 to 200°C, was attributed to desorption of water from the material's surface. The sample shows a further mass loss of 13% in the interval 200 to 700°C which, in addition to the 2% is equivalent to that observed when heating the material



**Figure 4.71:** TG (solid line) and DSC (dotted line) curves for a sample of tba0.06SAPO<sub>4</sub>-14F when dwelling at 550°C for 12 hours.

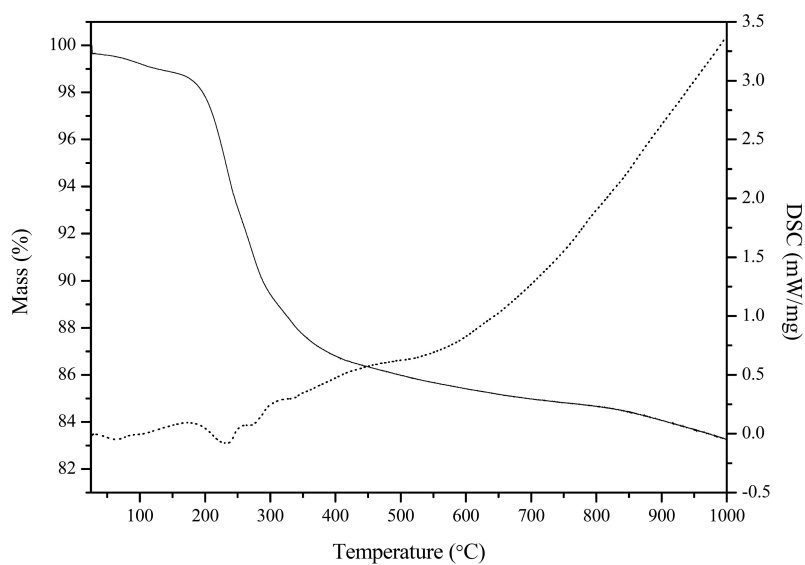


**Figure 4.72:** TG (solid line) and DSC (dotted line) curves (plotted vs. temperature) for a sample of tba0.06SAPO<sub>4</sub>-14F when heating a sample from 25 to 1000°C at a rate of 5°C/min.

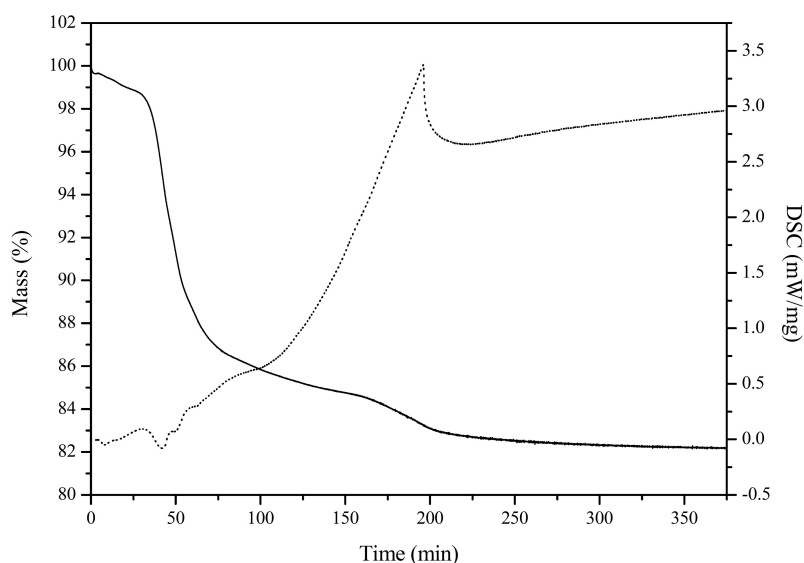


**Figure 4.73:** TG (solid line) and DSC (dotted line) curves (plotted vs. time) for a sample of tba0.06SAPO<sub>4</sub>-14F when heating a sample from 25 to 1000°C at a rate of 5°C/min, and dwelling for 3 h.

at a lower rate and dwelling for 12 h. A final mass loss step occurs, starting at 700°C and continuing to the end of the three hours of isothermal heating. The mass lost in this step is 3%. This is shown in figure 4.73, where the TG and DSC curves for the sample are shown for the entire duration of the entire experiment. The total mass lost during the experiment was 18% which is more consistent with that theoretically calculated for tbaAlPO<sub>4</sub>-14F. The calcination procedure was deemed sufficient for calcination of SAPO<sub>4</sub>-14F samples (also verified by BET surface area measurements, see chapter 4.5.1). Samples calcined at 1000°C were white which was seen as an additional indication that all template molecules were removed. The mass lost for the different temperature intervals is summarized in table 4.9.

**Table 4.9:** Summary of mass loss for the critical temperature intervals of tba0.06SAPO<sub>4</sub>-14F. \*Including mass lost during isothermal heating at 1000°C for 3 h.

Temperature interval (°C)	Mass loss (%)
25 - 100	1
250 - 700	14
700 - 1000*	3
Total	18

The thermal behavior for tbaSAPO<sub>4</sub>-14F is somewhat reflected in previous studies on SAPOs. In the work by Liu et al.<sup>145</sup> TGA was used to investigate several SAPO<sub>4</sub>-11 samples made by altering the template and phosphorous content (acidic medium only) of the synthesis gels. The TG curves for their SAPO<sub>4</sub>-11-T2 sample exhibited a similar behavior as 0.06SAPO<sub>4</sub>-14F, but differing greatly in the observed behavior to that of the other three samples investigated

(SAPO<sub>4</sub>-11-P3, SAPO<sub>4</sub>-11-P1, SAPO<sub>4</sub>-11-T4). Whereas the norm for the samples was three mass loss steps (<200°C, 200-250°C, and 300-400°C) the SAPO<sub>4</sub>-11-T2 sample exhibited only one step at roughly 150°C. The authors attributed the first mass loss step for the other samples (<200°C) to desorption of physisorbed water, and the remainder to oxidative decomposition and thermal cracking of the template. They also correlated the mass loss in the “exothermic” (no DSC curves was shown in the article for any verification of this) steps two and three with the micropore volume and acid sites, and claimed the SAPO<sub>4</sub>-11-P samples were better than SAPO-11-T samples. Even though the mass loss in steps two and three were higher for their SAPO-11-P than their SAPO-11-T2 sample (SAPO<sub>4</sub>-11-T2 was the only SAPO<sub>4</sub>-11-T sample investigated with TGA), the SAPO<sub>4</sub>-11-T2 had the largest total mass loss, and the TG measurements thus infer that this sample should have a higher micropore volume. It is also noteworthy that the authors chose to continue working with the SAPO<sub>4</sub>-11-T2 sample after showing phase impurities with PXRD, and particularly when the other SAPO<sub>4</sub>-11-T5 samples were more or less phase-pure. In a related study on MAPO<sub>4</sub>-11 compositions by Yang et al.<sup>146</sup>, the presence of either Si (a SAPO<sub>4</sub>-11 sample was made for comparison) or Mg caused a three step behavior of the template removal (shown with DTG). In the absence of these elements the template was removed in only two mass loss steps. The authors attributed the third mass loss step to the decomposition of protonated template molecules balancing the charge of the anionic lattice. The anionic lattice itself was attributed to the result of substitution of Al<sup>3+</sup> with Mg<sup>2+</sup>, and P<sup>5+</sup> with Si<sup>4+</sup>. They also showed a shift of the third mass loss step with increasing temperature, and attributed this to the increasing number and strength of the resulting Brönsted acid sites. In addition, the lower temperature step of SAPO<sub>4</sub>-11 compared to MgAPO<sub>4</sub>-11, was seen by the authors to be an indication that MgAPO<sub>4</sub>-11 had a higher acid strength than SAPO<sub>4</sub>-11. The claim of increasing temperature shift with increasing Mg content is of interesting nature when compared to 0.06SAPO<sub>4</sub>-14F. The sample has a relatively low Si content (Si/(Si+Al+P) = 0.019) and the number of possible acid sites is therefore also low. Still, an extremely high temperature is needed to remove all template species. The presence of Al-OH-Al sites (from AlPO<sub>4</sub>-14A and AlPO<sub>4</sub>-15 may contribute to this behavior, and a replacement of one of the Al in the existing Al-OH-Al linkages cannot be ruled out. Malysheva et al.<sup>65</sup> have studied the thermal behavior of butylamines on zeolite Y. Among the amines, tert-butylamine and sec-butylamine were shown to form butylammonium ions upon interacting with the acid sites (modified):



where the HOZ represents an acid site on zeolite Y (Z). The adsorbed butylammonium ions were then believed to react further forming olefins and ammonium ions:



A similar mechanism has been proposed for the calcination of TPA-ZSM-5 (TPA was some

form of tetrapropylammonium salt) by V.R. Choudhary and S.G. Pataskar<sup>64</sup>. Removal of the TPA molecule was believed to be removed by thermal cracking involving the following two simultaneous reactions:



and



The reactions were labeled as *Hofman* or *sequential Hofman* reactions/elimination involving the negatively charged lattice ( $(\text{OZ})^-$ ) and the production of olefins ( $\text{C}_3\text{H}_6$ ). The authors also opened for the possibility for the olefins to react further to hydrocarbons. Relating this to the synthesis of tbaAlPO<sub>4</sub>-14F, one can imagine that the butylammonium-hydroxide pair (see discussion regarding tbaAlPO<sub>4</sub>-14F and ipaAlPO<sub>4</sub>-14F) is formed upon perhaps similar reactions between tert-butylamine and phosphoric acid during the synthesis, thus effectively eliminating this step during the calcination of tba0.06SAPO<sub>4</sub>-14F. On the basis of this, the removal of tert-butylamine may proceed in two steps:



and



where  $(\text{OZ})^-$  is taken as the negatively charged lattice due to (assumably) incorporated Si. The first reaction occurs in the temperature interval: 200-700°C, and the second reaction occurs in the temperature interval 700°C to 1000°(and continues during the isothermal heating). The absence of any such behavior for the CuAPO<sub>4</sub>-14F samples suggests either a different local siting of Cu compared to Si, or that the behavior is dependent on the amount of Si or Cu present ( $\text{Cu}/(\text{Cu}+\text{Al}+\text{P}) = 0.003$  and  $0.01$  for  $0.01\text{CuAPO}_4\text{-14F}$  and  $0.01\text{CuAPO}_4\text{-14F}$  respectively). The reaction described by equation 4.7 may also occur more like equation 4.6:



and perhaps both reactions occur simultaneously. The high temperature step observed above 700°C could then be attributed to strongly adsorbed ammonium ions ( $\text{NH}_4^+$ ) balancing an anionic lattice. This could have implications for catalytic activity.

## 4.5 BET surface area

### 4.5.1 First generation molecular sieves

Table 4.10 lists the BET surface area for all the first generation molecular sieves (F). The samples were all calcined prior to analysis so the template prefix (e.g. ipa, tba) has been removed. The first interesting thing to note is the difference in surface area measured for a sample of  $\text{AlPO}_4\text{-14F}$  exposed to two different calcination procedures. In the first one, the sample was heated from  $25^\circ\text{C}$  to  $550^\circ\text{C}$  at a rate of  $1^\circ\text{C}/\text{min}$ . Then the sample was kept at this temperature for 17 h, before being cooled down to room temperature. This procedure resulted in a BET surface area of  $307\text{ m}^2/\text{g}$ . The other procedure consisted of exposing the sample to a preheated oven set at  $600^\circ\text{C}$  for 3 hours. This shorter, but perhaps more brutal, procedure resulted in a calcined sample with a BET surface area of  $331\text{ m}^2/\text{g}$ , an increase of  $24\text{ m}^2/\text{g}$ . This justifies the method of exposing the materials to a preheated oven instead of slowly heating them at a low rate (a preheated oven could be thought of as using the highest rate possible when using conventional heating in an oven).

**Table 4.10:** BET surface area for first generation molecular sieves after calcination. Isotherm data is supplied in appendix A.2.

Sample	BET surface area ( $\text{m}^2/\text{g}$ )	Calcination temp. ( $^\circ\text{C}$ )	Calcination time (h)
$\text{AlPO}_4\text{-14F}$	307	550	16
$\text{AlPO}_4\text{-14F}$	331	600	2
$0.01\text{CuAPO}_4\text{-14F}$	331	550	16
$0.03\text{CuAPO}_4\text{-14F}$	241	550	16
$0.06\text{SAPO}_4\text{-14F}$	306	1000	24
$0.08\text{SAPO}_4\text{-14F}$	326	1000	24
$0.20\text{SAPO}_4\text{-14F}$	313	1000	24

The  $0.01\text{CuAPO}_4\text{-14F}$  sample has a BET surface area ( $331\text{ m}^2/\text{g}$ ) identical to the  $\text{AlPO}_4\text{-14F}$  calcined in a preheated oven, even though it was calcined by slowly raising its temperature to  $550^\circ\text{C}$  ( $1^\circ\text{C}/\text{min}$ ) and kept at that temperature for 17 hours. In this case the presence of copper seem to have a positive effect on the sample's surface area. The situation is quite the opposite for the  $0.03\text{CuAPO}_4\text{-14F}$  composition, where the BET surface area is only  $241\text{ m}^2/\text{g}$ . This could be an indication that larger amounts of copper in the synthesis gel destabilizes the framework, or somehow leads to clogging of the materials pores. Increasing the amount of copper in the samples did gradually affect the crystallization as seen with PXRD, and seems to have affected the total surface area in the same process. The DTG results indicated that copper may occupy sites in the impurities, at least in the  $0.01\text{CuAPO}_4\text{-14F}$  sample. This was indicated by a negative temperature shift compared to that of  $\text{AlPO}_4\text{-14F}$ . One of the unstable impurities is  $\text{AlPO}_4\text{-14A}$  which is shown to have a surface area of only  $8\text{ m}^2/\text{g}$  (see table 4.11

and corresponding discussion), indicating that this material is not really contributing to the overall surface area. One would expect a similar surface area for  $\text{AlPO}_4\text{-15}$ , since the material has been shown by PXRD to undergo substantial destruction upon calcination. If the copper is situated in the unstable impurities in all copper samples, one would not expect this decrease in BET surface area. The decrease in BET surface area therefore indicates that copper initially (when only small amounts are present) occupy sites in impurities, and then moves on to occupy all phases present. The decrease in BET surface area for the  $0.03\text{CuAlPO}_4\text{-14F}$  sample can then be understood as the copper having started to occupy sites in  $\text{AlPO}_4\text{-14}$ , thereby effecting the main contributor to the BET surface area. This also supports the PXRD findings, where only the  $0.01\text{CuAlPO}_4\text{-14F}$  sample managed to rehydrate to some extent (low angle peaks in the diffraction pattern), and the  $0.03\text{CuAlPO}_4\text{-14F}$  and  $0.08\text{CuAlPO}_4\text{-14F}$  samples could not.

The  $\text{SAPO}_4\text{-14F}$  compositions have a similar surface area as that of  $\text{AlPO}_4\text{-14F}$ , and seem to have endured the brutal calcination at  $1000^\circ\text{C}$ . Thus, one can infer from the data that the presence of silicon does not affect the surface area in a negative way as that observed for a high copper loading. The  $0.08\text{SAPO}_4\text{-14F}$  and  $0.20\text{SAPO}_4\text{-14F}$  samples synthesized with 50 mg of  $\text{tbaAlPO}_4\text{-14F}$  as seed crystals have a slightly higher surface area than  $0.06\text{SAPO}_4\text{-14F}$  made without seed crystals. Thus, the presence of seed crystals has a slightly positive effect on the surface area of the resulting samples. It is noted that the BET surface area goes through a maximum of  $326\text{ m}^2/\text{g}$  for the  $0.08\text{SAPO}_4\text{-14F}$  sample, and then decreases to  $313\text{ m}^2/\text{g}$  for the  $0.20\text{SAPO}_4\text{-14F}$ .

### Various AlPOs and SAPOs

Table 4.11 shows the BET surface area for various AlPOs and SAPOs made with preparations discovered in this thesis work. The BET results for  $\text{AlPO}_4\text{-14A}$  is consistent with that observed with PXRD, where a large part of the material is lost or altered during the calcination process. The PXRD results also showed similarities between  $\text{AlPO}_4\text{-14A}$  and  $\text{AlPO}_4\text{-5}$ , but the two sieves have distinctly different surface areas. The stable nature of  $\text{AlPO}_4\text{-5}$  gives it a surface area of  $174\text{ m}^2/\text{g}$ , whereas  $\text{AlPO}_4\text{-14A}$  has a surface area of only  $8\text{ m}^2/\text{g}$ .

**Table 4.11:** BET surface area for first generation molecular sieves after calcination. Isotherm data is supplied in appendix A.2.

Sample	BET surface area ( $\text{m}^2/\text{g}$ )	Calcination temp. ( $^\circ\text{C}$ )	Calcination time (h)
$\text{AlPO}_4\text{-14A}$	8	600	3
$\text{SAPO}_4\text{-43}$	323	550	24
$\text{SAPO}_4\text{-34}$	591	600	24
$\text{SAPO}_4\text{-18}$	584	600	24
$\text{AlPO}_4\text{-5}$	174	600	24

The improved calcination procedure using a low heating rate ( $0.5^\circ\text{C}/\text{min}$ ) seems to have

preserved much of the porosity of SAPO<sub>4</sub>-43 (as well as crystallinity), resulting in a surface area of 323 m<sup>2</sup>/g, not much different than that observed for 0.08SAPO<sub>4</sub>-14F. Due to the unstable nature of SAPO<sub>4</sub>-43 samples made with isopropylamine, no earlier reports of surface area measurement are available for comparison.

SAPO<sub>4</sub>-34 and SAPO<sub>4</sub>-18 both have thermally stable topologies, reflected in the increase in intensity observed with PXRD after calcination. The samples also exhibit superior surface areas, 584 m<sup>2</sup>/g for SAPO<sub>4</sub>-18, and 591 m<sup>2</sup>/g for SAPO<sub>4</sub>-34.

---

## 4.6 XAS

### 4.6.1 ipa0.01CuAPO<sub>4</sub>-14F and ipa0.03CuAPO<sub>4</sub>-14F

X-ray Absorption Spectroscopy was performed on ipa0.01CuAPO<sub>4</sub>-14 and ipa0.03CuAPO<sub>4</sub>-14. The goal was to determine the oxidation state of the copper metal, observe if copper oxides had been formed during the synthesis of the materials (both determined using XANES analysis), examine the local copper multiplicities, type of nearest neighbors (oxygen, copper or T-atom), and bond lengths (determined using EXAFS analysis). Knowledge about the mentioned properties enables an evaluation regarding the incorporation of copper.

#### XANES

The normalized Cu K-edge XANES spectra (and derivatives) of the two samples and that of three models (copper tutton-salt, copper(II)oxide, and copper(I)oxide) are shown in figure 4.74. The XANES shape of the samples does not resemble either the copper(I) oxide nor the copper(II) oxide. This is particularly evident in the lack of the strong pre-edge a few eV below the edge (due to the 1s → 4p transition) characteristic for copper(II) oxide<sup>112,106</sup>. This shows that oxides has not been formed during the synthesis. The possibility of negligible amounts are also ruled out since the copper content in the samples are very low. The results indicate, however, that the copper environment resembles the Cu Tutton-salt, putting the copper in a +2 oxidation state and a tetragonally distorted octahedral environment<sup>106,111</sup>. There exists also an ever so slight pre-edge around 8979 eV (K-edge energy of Cu), attributed to the formally forbidden 1s → 3d electronic transition<sup>112,106</sup>. The presence of the pre-edge 1s → 3d peak can be explained by a distortion of perfect octahedral symmetry. The copper ions of oxidation state +2 have d<sup>9</sup> configuration, and in an octahedral field these d-electrons can be distributed in two ways; low-spin and high-spin. Degenerate and asymmetrically filled orbitals are prone to the Jahn-Teller effect: they will lower their symmetry to counteract the unstable filling of electrons. The result is local distorted octahedral symmetry, where the distortion encompasses either axial bond elongation and equatorial bond compression, or the other way around<sup>147</sup>. The XANES analysis predict similar EXAFS refinement values for both ipa0.01CuAPO<sub>4</sub>-14F and ipa0.03CuAPO<sub>4</sub>-14F.

#### EXAFS

The two models, copper(II) oxide and copper tutton-salt, were used to verify the ab initio phase-shifts and estimate the amplitude reduction factor (AFAC). The refinement was done by using computer software (EXCURV98) and crystallographic data for the models. During the refinement the experimental data for the models were fitted to a fixed set of multiplicities and the bond distances, Ef, FI, bond lengths, Debye-Waller factors, and amplitude reduction factor (AFAC) were calculated. The goal was to reduce the fit factor, R, to a low as possible value,

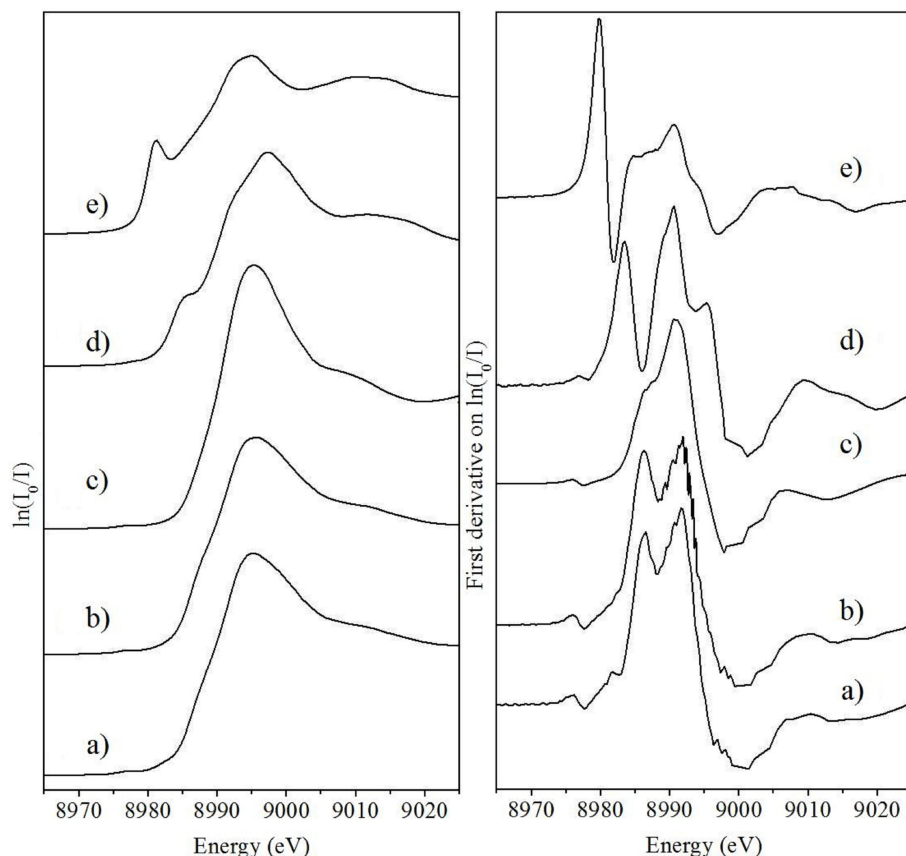


**Figure 4.74:** Normalized Cu K-edge XANES (left) and first derivatives (right) of a) 0.01CuAPO<sub>4</sub>-14F; b) 0.03CuAPO<sub>4</sub>-14F; c) copper tutton salt; d) copper(II)oxide; e) copper(I)oxide.

with values approaching the low 30's seen as acceptable. Other restraints for the refinement were maximum and minimum values for the Debye-Waller factors set at 0.03 and 0.007 respectively, and an AFAC between 0.8 and 1.0. The results of the least squares EXAFS refinement for the two models are shown in table 4.12, and the values are in agreement with previous findings<sup>148,149</sup>. The obtained experimental and theoretical  $k^3$ -weighted EXAFS and the respective Fourier transforms for Cu Tutton-salt and copper(II) oxide are shown in figure 4.75.

**Table 4.12:** Parameters from the least squares EXAFS refinement used for analysis of the Cu K-edge data. AFAC = 0.8250 for CuO and 0.8756 for Cu-Tutton salt ( $r(\text{\AA})$  (XRD) marks crystallographic values for the two compounds<sup>148,149</sup>).

Model	Shell	N	$r$ ( $\text{\AA}$ )	$r$ ( $\text{\AA}$ ) XRD	$2\sigma^2$ ( $\text{\AA}^2$ )	FI	R (%)	Ef (eV)
CuO	Cu-O	4.0	1.956(4)	1.96	0.0080(5)	7.58	37.30	-8.564
	Cu-O	2.0	-	2.78	-			
	Cu...Cu	8.0	2.934(6)	2.90	0.0282(5)			
	Cu...Cu	2.0	3.132(7)	3.08	0.0080(8)			
	Cu...Cu	2.0	3.447(5)	3.42	0.0299(4)			
Cu Tutton-salt	Cu-O	4.0	1.994(5)	2.02	0.0133(1)	8.67	33.69	-6.518
	Cu-O	2.0	2.268(1)	2.23	0.0208(6)			

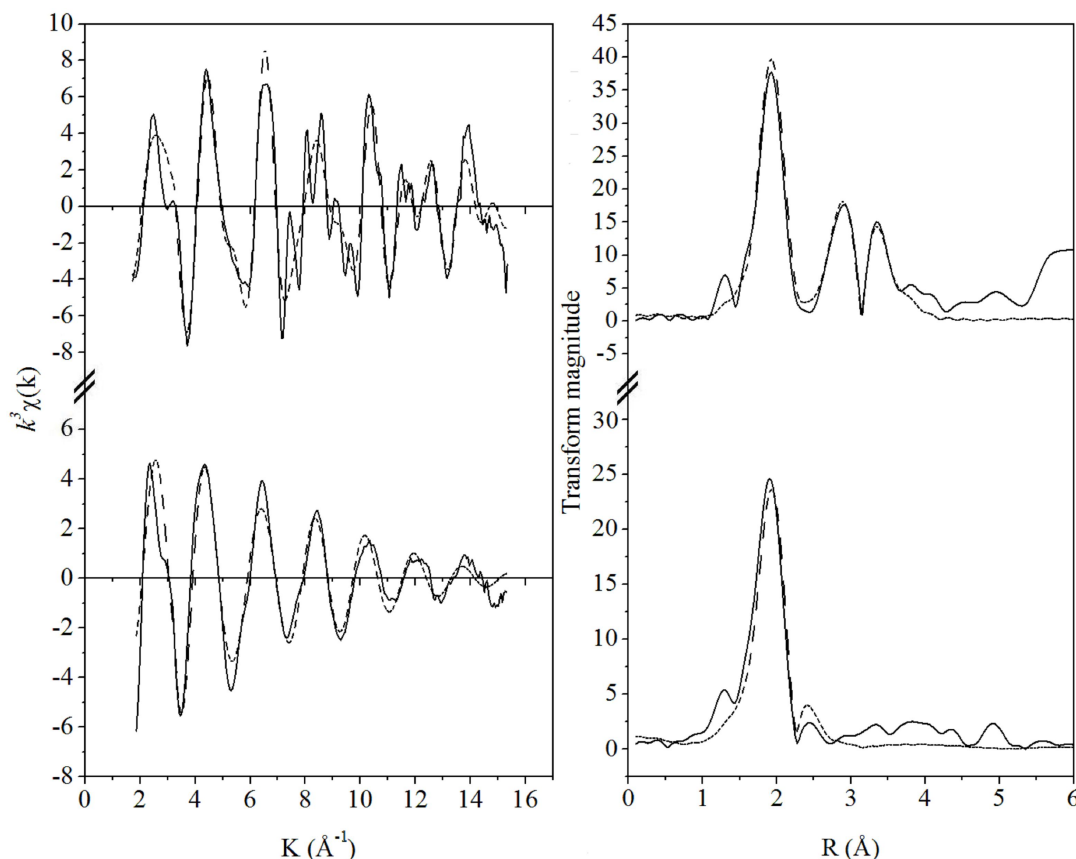


**Figure 4.75:** Experimental (solid lines) and calculated (dotted lines) for  $k^3$ -weighted EXAFS (left) and its Fourier transform (right) for copper(II) oxide (top) for Cu Tutton-salt (bottom).

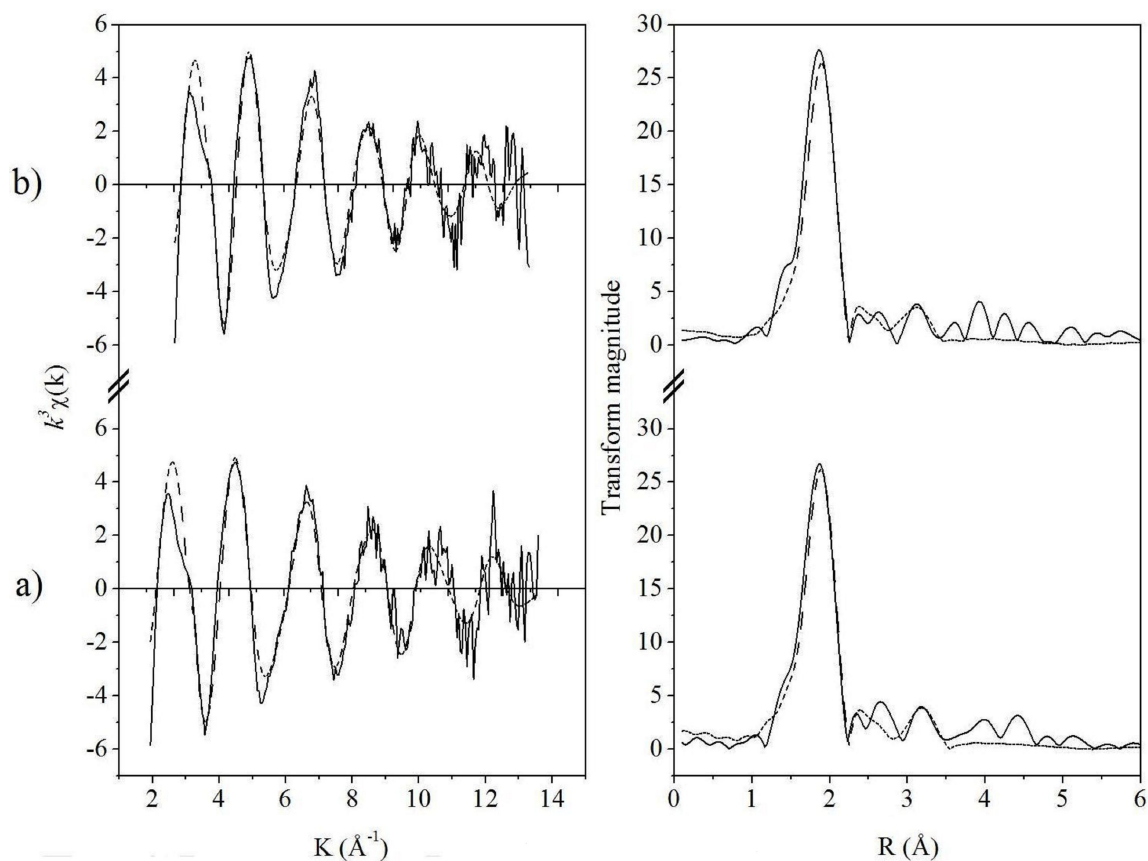
After a reasonable fit had been obtained for the models, the AFAC value for Cu Tutton-salt was transferred to the refinement of ipa0.01CuAPO<sub>4</sub>-14F and ipa0.03CuAPO<sub>4</sub>-14F. During the refinement the AFAC was held constant and the multiplicities, Ef, FI, bond lengths and Debye-Waller factors were calculated. The same restraints as for the models were used during the EXAFS refinement of the samples. The results of the least squares EXAFS refinement are shown in table 4.13. The obtained experimental and theoretical  $k^3$ -weighted EXAFS and the respective Fourier transforms for ipa0.01CuAPO<sub>4</sub>-14F and ipa0.03CuAPO<sub>4</sub>-14F are shown in figure 4.76.

The results for both ipa0.01CuAPO<sub>4</sub>-14F and ipa0.03CuAPO<sub>4</sub>-14F show a Cu-O first shell with an average multiplicity of 3.6 and a bond length of about 1.95 Å. The second shell is also a Cu-O with an average multiplicity of 2.1 and a bond length of about 2.21 Å. This makes copper six-coordinated with (multiplicity rounded up to nearest integer) four axial Cu-O bonds and two equatorial Cu-O bonds. This is consistent with the XANES findings, and the coordination of the Cu<sup>2+</sup> is of tetragonally distorted octahedral symmetry with axial elongation. The results show further that two T-atoms (the multiplicity can be rounded up to 1 per T-atom) are present in the surroundings (around 3 Å) of the copper in both samples. The presence of these is considered a proof for incorporation of copper<sup>111,106</sup>.

The first-shell (T-O) bond lengths<sup>108,30,133</sup> and co-ordination of the Al and P sites in AlPO<sub>4</sub>-

**Table 4.13:** Parameters from the Least-squares EXAFS refinement for ipa0.01CuAPO<sub>4</sub>-14F and ipa0.03CuAPO<sub>4</sub>-14F.

Sample	Shell	N	r (Å)	2σ <sup>2</sup> (Å <sup>2</sup> )	FI	R (%)	Ef (eV)
0.01CuAPO <sub>4</sub> -14F (as-synthesized)	Cu-O	3.6	1.952(3)	0.0118(7)	8.95	33.79	-5.48
	Cu-O	2.1	2.223(2)	0.0300(4)			
	Cu···T	0.6	3.073(6)	0.0296(5)			
	Cu···T	0.6	3.166(9)	0.0080(6)			
0.03CuAPO <sub>4</sub> -14F (as-synthesized)	Cu-O	3.6	1.955(0)	0.0112(6)	8.83	33.83	-5.86
	Cu-O	2.0	2.219(1)	0.0297(0)			
	Cu···T	0.6	3.132(5)	0.0071(2)			
	Cu···T	0.6	3.250(0)	0.0298(0)			

**Figure 4.76:** Experimental (solid lines) and calculated (dotted lines) for  $k^3$ -weighted EXAFS (left) and its Fourier transform (right) for 0.01CuAPO<sub>4</sub>-14F (top) and 0.03CuAPO<sub>4</sub>-14F (bottom)

14, AlPO<sub>4</sub>-14A, and AlPO<sub>4</sub>-15, were used for evaluating the site-incorporation of copper. The P-O bond distances are generally too short, and no octahedrally coordinated phosphorous species are recorded for any of the mentioned AlPOs, making phosphorous replacement of low probability. The situation is quite different for the aluminum sites that generally display longer Al-O bond distances, more in agreement with the EXAFS calculations of this work. Of particular interest is the octahedral aluminum sites reported where an axial elongation consistent

---

with that found in  $\text{CuAPO}_4\text{-14F}$  is reported. The TGA results indicated (observed by an initial negative temperature shift of the second DTG peak) that copper replaces aluminum in existing Al-OH-Al sites. However, the actual siting of copper is impossible to determine.

Calcined samples were also studied, but only large R factors (above 40) were obtained. This supports the notion that copper is occupying sites in the impurity materials, and their partial destruction results in a distortion of the copper environment. The calcined samples may have rehydrated to some extent during preparation for the XAS scans, and this may also have caused a distortion of the copper sites.

## 4.7 FT-IR

IR spectroscopy is frequently applied to investigate SAPOs. This characterization method can be used to determine, among many other things, the possible siting of Si in the frameworks of SAPOs. The mid-infrared spectrum is usually shown from 4000 to 400  $\text{cm}^{-1}$ , and can be divided further into regions characteristic for certain molecular vibrations. Of these, there is particular interest in the X-H stretching region<sup>86</sup> ranging from 4000 to 2500  $\text{cm}^{-1}$ . A discussion is first given for previous FT-IR studies of well known SAPOs.

The P-OH stretching vibration is frequently observed<sup>96,95,97,94</sup> from 3680-3670  $\text{cm}^{-1}$ , and is attributed to defects and end groups involving P. Defect sites involving aluminum, Al-OH groups, have been reported<sup>94,93,95</sup> to occur in the region from 3800 to 3760  $\text{cm}^{-1}$ . P-OH and Al-OH are observable for both AIPOs and SAPOs, but the introduction of Si usually encompasses additional absorptions and will be discussed separately.

As written in chapter 2.7.4, the incorporation of Si in AIPO frameworks can occur according to the following mechanisms<sup>92</sup>: i) Si substitution for Al; ii) Si substitution for P; iii) simultaneous substitution of two Si for one Al and one P. These three mechanisms will from now on be respectively labeled SM1, SM2, and SM3, with SM2 being the desirable mechanism since it leads to bridged hydroxyls and Brönsted acidity. The SM1 mechanism forms what is known as Si-OH defects, which are usually observed<sup>93,94,95,96</sup> near 3740  $\text{cm}^{-1}$ .

An illustration of the P-OH, Al-OH, and Si-OH groups is given in figure 4.77

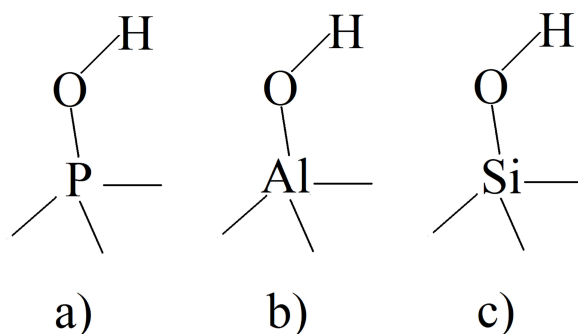


**Figure 4.77:** An illustration of various defect sites: a) P-OH; b) Al-OH; c) Si-OH. The first two may be present in both AIPOs and SAPOs, the last one may only be present in SAPOs.

The group frequencies given for P-OH, Al-OH, and Si-OH defects are only approximate and the observed wavenumbers varies between topologies. This is true to the nature of the group frequency approach, which usually deals with approximate values instead of definite ones<sup>150</sup>. Though there is a more general trend for P-OH, Al-OH, and Si-OH absorptions, the observed absorptions involving bridging hydroxyls (SM2 mechanism) are less definable. An illustration of the bridging hydroxyls are given in figure 4.78 a).

For SAPO<sub>4</sub>-11, SAPO<sub>4</sub>-31, and SAPO<sub>4</sub>-41, single absorptions involving bridging hydroxyls are observed at 3628, 3622, and 3627  $\text{cm}^{-1}$ , indicating that only one type of Brönsted acid

site is present<sup>96,94</sup>. In SAPO<sub>4</sub>-5, two absorptions have been observed<sup>96</sup> at 3628 and 3570 cm<sup>-1</sup>, both attributed to Brönsted sites. Two Brönsted sites have also been found<sup>95,97,98,99</sup> in SAPO<sub>4</sub>-34 and SAPO<sub>4</sub>-18, in this case occurring more closely at approximately 3626 and 3600 cm<sup>-1</sup>. The two bands partially overlap and are perhaps best described as a doublet. The nearly identical absorptions in the spectra of SAPO<sub>4</sub>-34 and SAPO<sub>4</sub>-18 have been attributed to the similarities between the CHA and AEI topologies<sup>93</sup>. The general consensus regarding dual Brönsted sites is that lower frequency (or wavenumber) absorptions are a result of interaction between the hydrogen and the SAPO framework<sup>96,98,97</sup>. An illustration of hydrogen bonding between bridging hydroxyls and the SAPO lattice is given in figure 4.78 b).

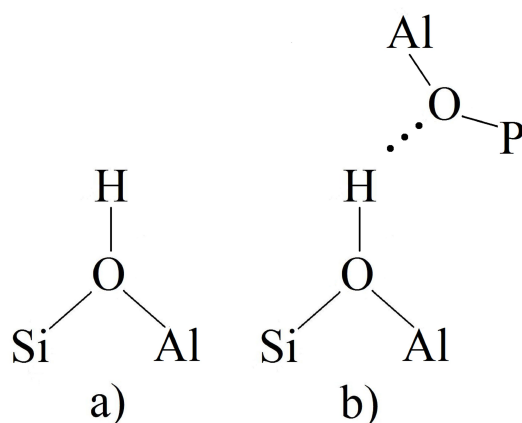


**Figure 4.78:** An illustration of two types of bridging hydroxyls: a) undisturbed Si-OH-Al linkage; b) Si-OH-Al linkage forming a hydrogen bond (represented here by three black dots) with the surrounding lattice.

### 4.7.1 SAPO<sub>4</sub>-14F

The FT-IR spectrum of phase-pure SAPO<sub>4</sub>-14 has not been reported previously. Rajic et al.<sup>32</sup> reported the IR spectrum of CoSAPO<sub>4</sub>-14, but the authors focused more on the occluded template than X-H stretching vibrations. Zibrowius et al.<sup>34</sup> reported the IR spectrum of pipAlPO<sub>4</sub>-14, but also in this case only the occluded template was investigated.

Figure 4.79 shows the FT-IR spectra of the three SAPO<sub>4</sub>-14F samples after calcination at 1000°C and after removal of re-adsorbed water. The figure shows that a broad absorption peaking at 3607 cm<sup>-1</sup> is characteristic for all three compositions. It might also be possible to distinguish absorptions characteristic for P-OH groups near 3670 cm<sup>-1</sup>, but there is too much noise to make disambiguous assignments of these. No previously reported FT-IR spectrum of SAPO<sub>4</sub>-14 exists, so it was compared to other topologies. The broad absorption is somewhat similar to that reported for SAPO<sub>4</sub>-31, where only a very weak absorption at 3622 cm<sup>-1</sup> was observed<sup>96</sup>. The authors proposed from elemental analysis and <sup>29</sup>Si results that Si replaced Al and P according to mechanism SM3. However, their IR results for the sample showed a strong Si-OH absorption at 3742 cm<sup>-1</sup>, which indicates that a SM1 mechanism also contributes.

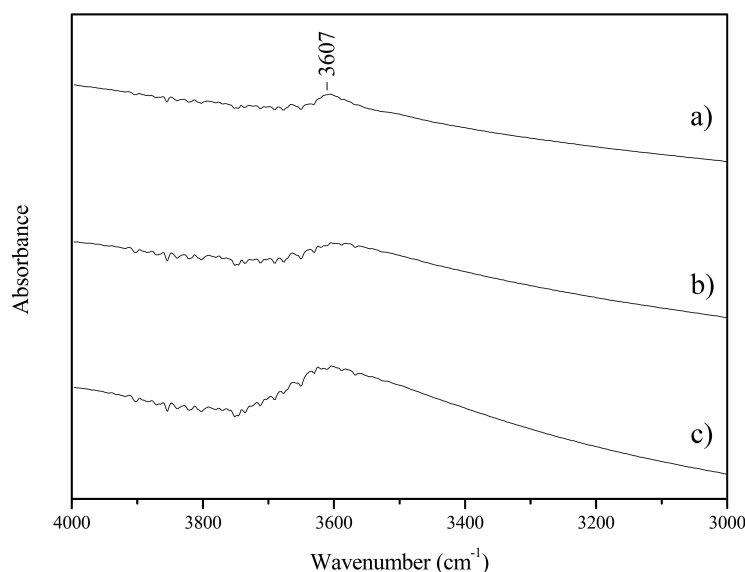


**Figure 4.79:** Background subtracted and normalized FT-IR spectra (in the range: 4000-3000  $\text{cm}^{-1}$ ) of calcined dehydrated samples of tbaSAPO<sub>4</sub>-14F: a) 0.06SAPO<sub>4</sub>-14F; b) 0.08SAPO<sub>4</sub>-14F; c) 0.20SAPO<sub>4</sub>-14F.

The difference between SAPO<sub>4</sub>-31 and the SAPO<sub>4</sub>-14F samples is that no Si-OH absorptions are visible, indicating that the little Si present may be substituted by mechanism SM2. This is consistent with that observed with TGA, where the tba0.06SAPO<sub>4</sub>-14F sample differed greatly compared to tbaAlPO<sub>4</sub>-14F. This also supports the mechanisms of template removal via an acid site. The nature of impure samples makes a distinction between SAPO<sub>4</sub>-14 (Si incorporation in AlPO<sub>4</sub>-14), SAPO<sub>4</sub>-14A (Si incorporation in AlPO<sub>4</sub>-14A), and SAPO<sub>4</sub>-15 (Si incorporation in AlPO<sub>4</sub>-15) highly ambiguous.

As the silicon content of the synthesis gel increases, an increase in the absorption from the observed acid sites would be expected. The ICP-MS results indicate an equal amount of Si in both 0.06SAPO<sub>4</sub>-14F and 0.20SAPO<sub>4</sub>-14F, both having an Si/(Si+Al+P) ratio of 0.019. The normalized FT-IR spectra indicate, however, that the concentration of acid sites increases with increasing Si content in the gels (the samples are named after Si content in the synthesis gel). This indicates that in the absence of seeding the SM3 method contributes to the SM2 mechanism, while in the presence of seed crystals SM2 dominates. This mindset is also supported by the higher Al/P ratio of the 0.20SAPO<sub>4</sub>-14F (Al/P = 0.94) sample compared to the 0.06SAPO<sub>4</sub>-14F sample (0.91), indicating that more phosphorous has been replaced by Si. In the case of the SAPO<sub>4</sub>-14F compositions, seeding seems to have an overall positive effect on the samples.

#### 4.7.2 AlPO<sub>4</sub>-14A

The AlPOs are normally considered neutral sieves, meaning that they have no charge balancing cations resulting from the presence of elements other than Al or P. They may, however, possess

charge balancing cations associated with the Al-OH and P-OH defect sites discussed earlier.  $\text{AlPO}_4\text{-14A}$  is a somewhat unique AlPO, given that it possesses bridging hydroxyls (Al-OH-Al linkages). An illustration of such hydroxyls is given in figure 4.80 a). Even though the material was shown with PXRD to partially collapse upon calcination, it was of interest to try to observe, if any, absorptions of the characteristic Al-OH-Al sites. As can be inferred from the fact that phase-pure  $\text{AlPO}_4\text{-14A}$  has not been obtained prior to this work, this is the first FT-IR spectrum dealing with this particular AlPO.

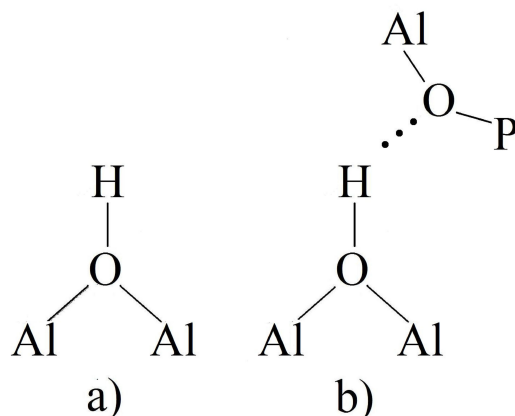


**Figure 4.80:** An illustration of bridging hydroxyls involving only Al, O, and H: undisturbed Al-OH-Al linkage; b) Al-OH-Al linkage forming a hydrogen bond (represented here by three black dots) with the surrounding lattice.

Figure 4.81 shows the FT-IR spectrum for calcined dehydrated  $\text{AlPO}_4\text{-14A}$ . The spectrum is dominated by a broad absorption starting at  $3650\text{ cm}^{-1}$ , peaking at  $3587\text{ cm}^{-1}$ , and continues via a shoulder at  $3391\text{ cm}^{-1}$  down to  $2900\text{ cm}^{-1}$ . Also visible is a weaker and sharper absorption at  $3670\text{ cm}^{-1}$ , and some very weak absorptions at  $3789$ ,  $3761$ , and  $3737\text{ cm}^{-1}$ . The absorption at  $3670\text{ cm}^{-1}$  was attributed to P-OH groups, and the absorptions at  $3789$  and  $3761\text{ cm}^{-1}$  were attributed to Al-OH groups. The absorption at  $3737\text{ cm}^{-1}$  is close to that reported for Si-OH groups, but since there is no Si in the sample such groups are ruled out. Zubkov et al.<sup>151</sup> attributed an absorption at  $3740\text{ cm}^{-1}$  to Al-OH, even though the authors were studying  $\text{SAPO}_4\text{-34}$ . Zibrowius et al.<sup>94</sup> addressed the issue of Al-OH and Si-OH groups both absorbing around  $3745\text{ cm}^{-1}$ , and although the authors ultimately attributed the band to Si-OH groups, they opened for the possibility that they could be a combination of Si-OH and Al-OH. Based on these reports the band at  $3737\text{ cm}^{-1}$  was attributed to Al-OH groups.

The dominating absorption band peaking at  $3587\text{ cm}^{-1}$  is of interesting nature. The wavenumber is similar to that reported<sup>96</sup> for the low frequency Brönsted site absorption in  $\text{SAPO}_4\text{-5}$ , indicating sites perturbed by interactions with the crystal lattice. This is illustrated in figure 4.80 b). Whereas  $\text{SAPO}_4\text{-5}$  also possesses a higher frequency Brönsted site absorption at  $3628\text{ cm}^{-1}$ ,  $\text{AlPO}_4\text{-14A}$  possesses a shoulder at an even lower frequency of  $3391\text{ cm}^{-1}$ . The shoulder might be due to the presence of residual isopropylamine template, more specifically absorptions from either the asymmetric or symmetric  $\text{NH}_2$  stretching vibrations<sup>152</sup>. Based on the unique struc-

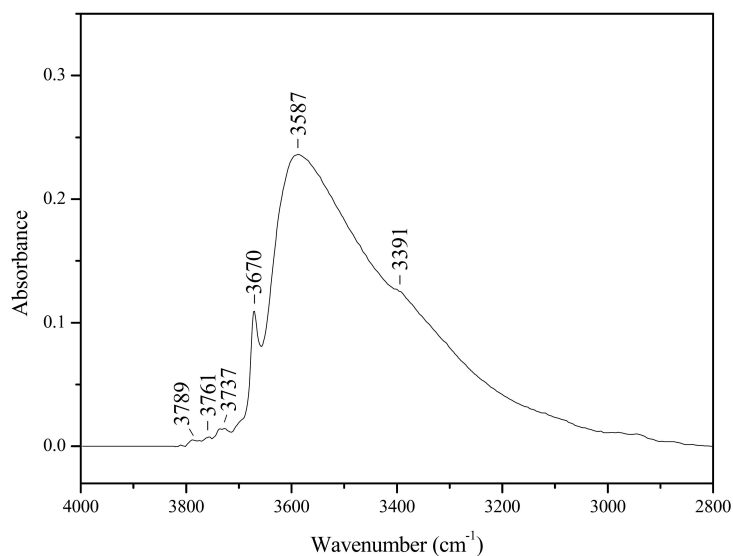


**Figure 4.81:** Background subtracted and baseline corrected FT-IR spectrum (in the range: 4000-2800  $\text{cm}^{-1}$ ) of calcined dehydrated  $\text{AlPO}_4\text{-14A}$ .

ture units of  $\text{AlPO}_4\text{-14A}$ , and the fact that no Si is present, it only seems logical that the broad asymmetric absorption band at  $3587\text{ cm}^{-1}$  is due to the Al-OH-Al sites. This was seen as an indication that, although the PXRD results shows a partial structure collapse, at least some of the characteristics of the framework is preserved. As mentioned, the broad nature of the band may be due to hydrogen bonding between the site and surrounding oxygen atoms, but may also be a result of the destructive calcination. Surface area measurements showed that the material is not very porous after calcination (BET surface area =  $8\text{ m}^2/\text{g}$ ), indicating a structural collapse or densification. This densification may also affect Al-OH-Al sites. There has, however, not been reports (theoretical or experimental) on surface area for  $\text{AlPO}_4\text{-14A}$  prior to this work, making such an assessment difficult. A figure by Brouwer et al.<sup>119</sup> illustrated what appears to be quite large pores surrounding the much smaller isopropylamine molecule, which suggests good theoretical porosity.

### 4.7.3 SAPO<sub>4</sub>-18

SAPO<sub>4</sub>-18 has previously been characterized with FT-IR spectroscopy by Chen et al.<sup>97</sup>. Their sample was synthesized with *N,N*-diisopropylethylamine and a comparison with the sample obtained in this work was of interest. The sample from their work will from hereon be referred to as dipeaSAPO<sub>4</sub>-18. The FT-IR spectrum for dipeaSAPO<sub>4</sub>-18 was reported to consist of a strong absorption band at  $3626\text{ cm}^{-1}$  (high frequency) accompanied by a weaker overlapping band at  $3600\text{ cm}^{-1}$  (low frequency). Both bands were attributed to Brönsted acid sites. In addition, two weak bands were observed at  $3676$  and  $3743\text{ cm}^{-1}$ , attributed respectively to P-OH and Si-OH groups.

Figure 4.82 shows the FT-IR spectrum of a sample of calcined dehydrated SAPO<sub>4</sub>-18 from

this work. The spectrum shows two main absorptions at 3611 and 3587  $\text{cm}^{-1}$ , which was attributed to bridging hydroxyls, Si-OH-Al groups. Also observed in the spectrum are two bands at 3734 and 3676  $\text{cm}^{-1}$ , attributed respectively to Si-OH and P-OH groups. It should be noted, however, that there is a lot of noise, making disambiguated assignments difficult. The dominating presence of the bands associated with Brönsted acidity indicates that Si substitution in the  $\text{AlPO}_4\text{-18}$  framework occurs mainly via the SM2 mechanism.

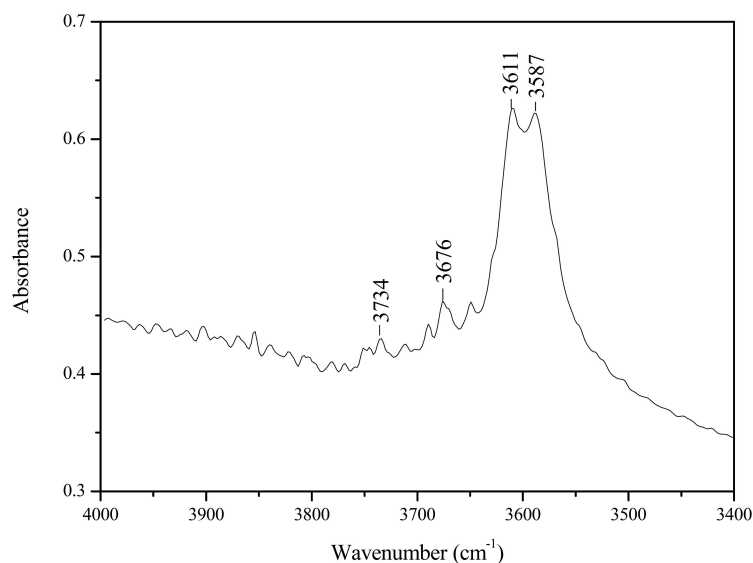


**Figure 4.82:** Background subtracted FT-IR spectrum (in the range: 3900-3400  $\text{cm}^{-1}$ ) of calcined dehydrated  $\text{SAPO}_4\text{-18}$ .

As mentioned previously, the occurrence of two absorptions for Brönsted sites is a result of some sites interacting more with the crystal lattice. In the similar  $\text{SAPO}_4\text{-34}$ , the band at 3626  $\text{cm}^{-1}$  has been attributed<sup>93,98</sup> to bridging hydroxyls residing in the cages, whereas bridging hydroxyls associated with double six-membered rings cause the appearance of the band at 3600  $\text{cm}^{-1}$ . The AEI ( $\text{SAPO}_4\text{-18}$ ) and CHA ( $\text{SAPO}_4\text{-34}$ ) topologies are similar, and seems relevant for an evaluation of these Brönsted sites in  $\text{SAPO}_4\text{-18}$ . Previous FT-IR findings for  $\text{SAPO}_4\text{-18}$  and  $\text{SAPO}_4\text{-34}$  have shown that the high frequency absorption dominates, while the low frequency absorption is about to 50 % lower in intensity. The most distinctive feature observed for the  $\text{SAPO}_4\text{-18}$  sample from this work is that the two absorptions previously addressed have near equal absorption intensities. This would suggest a higher incorporation of Si in the low frequency sites, more specifically the sites involving double six-membered rings. From an FT-IR point of view, this seems to be the critical difference the tea $\text{SAPO}_4\text{-18}$  and the dipea $\text{SAPO}_4\text{-18}$  sample, and may have an impact on catalytic activity. It may also be a result of the different crystallization conditions for the two samples, seeing as the one from this work crystallizes in the presence of excess template and under high pH conditions. The high pH approach then not only allows for fast crystallization of  $\text{SAPO}_4\text{-18}$ , but also alters the way Si is incorporated into the framework.

## 4.8 Catalysis

### 4.8.1 Methanol to Olefins (MTO) reaction

#### Experimental conditions

Selected samples were tested for activity in the Methanol-to-olefins (MTO) reaction. Wafers of appropriate size and weight ( $\approx 20$  mg) were mounted in an *in situ* FT-IR instrument, and subjected to a cooled (ice bath) methanol vapor with He as carrier gas. The volumetric flow rate was adjusted to give a WHSV = 1 in each experiment unless noted. The calculation of volumetric flow rate was done using the Microsoft excel spreadsheet given in appendix B.3.2.

#### SAPO<sub>4</sub>-14F

The chromatograms for the reactor effluents from the MTO reaction over the three SAPO<sub>4</sub>-14F samples are shown in figure 4.83. The chromatogram displays two peaks at the retention times 5.10 and 5.24 min. The first of these peaks was attributed to dimethyl ether formed during the dehydration of methanol<sup>24</sup>:



the latter was attributed to the methanol feed itself. The chromatogram indicates no peaks for olefinic species (C<sub>2</sub>, C<sub>3</sub>, and C<sub>4</sub>) which are the expected products from the MTO reaction. A similar result was obtained for SAPO<sub>4</sub>-46 investigated by Kong et al.<sup>127</sup>. The authors considered the dimethyl ether to be a desirable product, and concluded that their catalyst was highly active in the MTO reaction. The SAPO<sub>4</sub>-14F samples were not considered active in the MTO process.

#### AlPO<sub>4</sub>-14A

Figure 4.84 shows the GC-FID chromatogram of products obtained in the MTO reaction over calcined dehydrated AlPO<sub>4</sub>-14A after various times on stream. It can be seen that the acid sites observed with FT-IR is only capable of converting methanol to dimethyl ether, and no peaks for olefins are observable. This is consistent with that reported<sup>93</sup> earlier for AlPO<sub>4</sub>-18, showing only negligible amounts of hydrocarbons. Even though the material's structure was shown to be thermally unstable with respect to calcination (as shown with PXRD, and inferred from SEM and BET measurements) the remainder still functions as a catalyst, but does not produce the desirable products (olefins). This may be a further indication that the local environment around the Al-OH-Al sites are preserved. It would be interesting to observe (if possible) how the incorporation of Si (SAPO<sub>4</sub>-14A) would affect the conversion of methanol in such a system, and to see if Al-OH-Si sites are equally preserved. However, no reports of such a system exist, with the closest being that of SAPO<sub>4</sub>-15 reported by N. Venkatathri<sup>153</sup>.

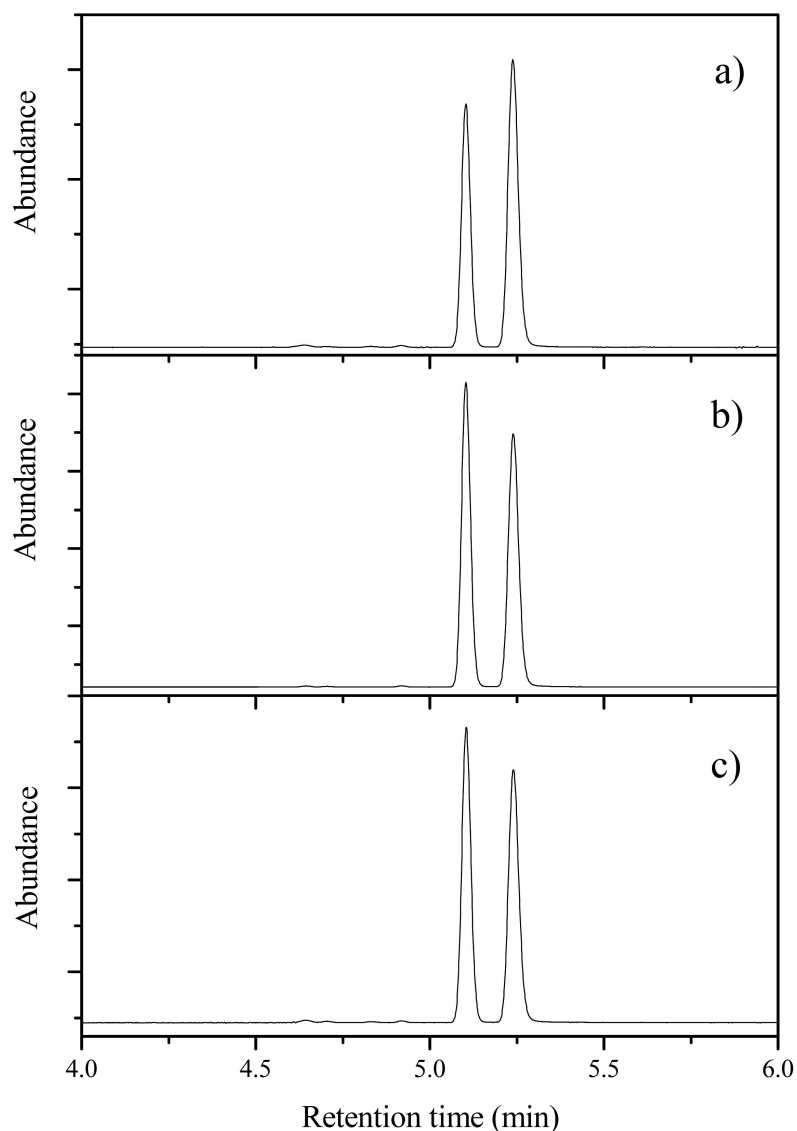


**Figure 4.83:** GC-FID chromatogram of products obtained after 20 min on stream in the MTO reaction over calcined dehydrated: a) 0.06SAPO<sub>4</sub>-14F; b) 0.08SAPO<sub>4</sub>-14F; c) 0.20SAPO<sub>4</sub>-14F. Peaks at 5.10 and 5.24 min were respectively attributed to dimethyl ether and methanol.

### SAPO<sub>4</sub>-18

Figure 4.85 shows the chromatogram of products obtained in the MTO reaction over calcined dehydrated SAPO<sub>4</sub>-18 after various times on stream. In contrast to the SAPO<sub>4</sub>-14F and AlPO<sub>4</sub>-14A samples, the SAPO<sub>4</sub>-18 sample is both able to convert methanol to dimethyl ether, and to convert dimethyl ether further to light olefins. The main products are C<sub>2</sub> and C<sub>3</sub> olefins, with a slightly higher selectivity towards C<sub>3</sub> products. Due to a malfunction of the GC-MS's FID detector, the products had to be analyzed with a TIC detector. Integration and subsequent conversion calculations could therefore not be performed due to differences in sensitivity of the two detectors. The WHSV for this particular experiment was adjusted to 2.5 h<sup>-1</sup> to enable a

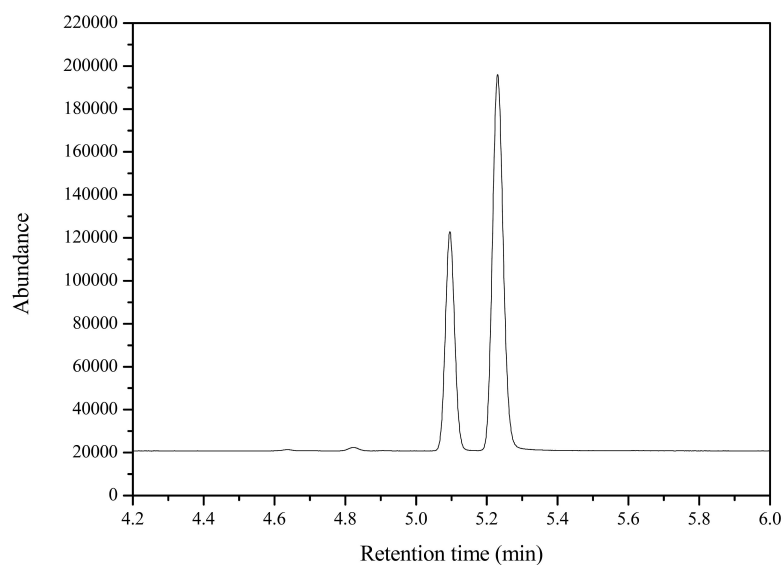


**Figure 4.84:** GC-FID chromatogram of products obtained in the MTO reaction over calcined dehydrated  $\text{AlPO}_4\text{-14A}$  after 20 min on stream. Peaks at 5.10 and 5.24 min were respectively attributed to dimethyl ether and methanol.

comparison with the previous work on  $\text{SAPO}_4\text{-18}$  by Chen et al.<sup>93</sup>. The authors synthesized several samples of  $\text{SAPO}_4\text{-18}$  for comparison, and their sample with an  $\text{Si}/(\text{Si}+\text{Al}+\text{P})$  ratio of 0.028 (labeled by the authors as  $\text{SAPO}_4\text{-18(1)}$ ) was seen as the best compositional match to the sample synthesized in this work ( $\text{Si}/(\text{Si}+\text{Al}+\text{P})$  ratio of 0.031). Even though no calculations for conversion was possible for the sample of this work, a qualitative comparison was performed.

The  $\text{SAPO}_4\text{-18(1)}$  sample was reported to operate at 100% conversion with no observable deactivation for at least 2 h (120 min). The 100% conversion level reported is somewhat misleading since the authors have included dimethylether as a product. The methanol may be completely converted, but the desirable products in the MTO reaction are the olefins. As evident from the methanol peaks in the chromatogram in figure 4.85, 100% conversion levels were not obtained when using the sample from this work. This may be due to the type of reactor used and not a characteristic of the catalyst itself. In the setup used, the methanol is surrounding the catalyst wafer and not directly moving through it. This is a consequence of the dual nature of the FT-IR cell to function both as reactor and as a means for recording *in-situ* spectra. A different result might have been obtained in an idealized reactor. The cell does, however, provide a means of preliminary catalyst testing.

Both samples seem to have a higher selectivity towards  $\text{C}_3$  products than to  $\text{C}_2$  or  $\text{C}_4$  products, and  $\text{SAPO}_4\text{-18(1)}$  has a maximum selectivity for  $\text{C}_3$  of 53% after 10 min on stream. The  $\text{SAPO}_4\text{-18}$  sample from this work seems to deactivate rather quickly, and after 100 min on stream methanol dominates. Accompanying this is the diminished production of  $\text{C}_3$  products. This diminished production which was only slightly observed for the  $\text{SAPO}_4\text{-18(1)}$  sample.

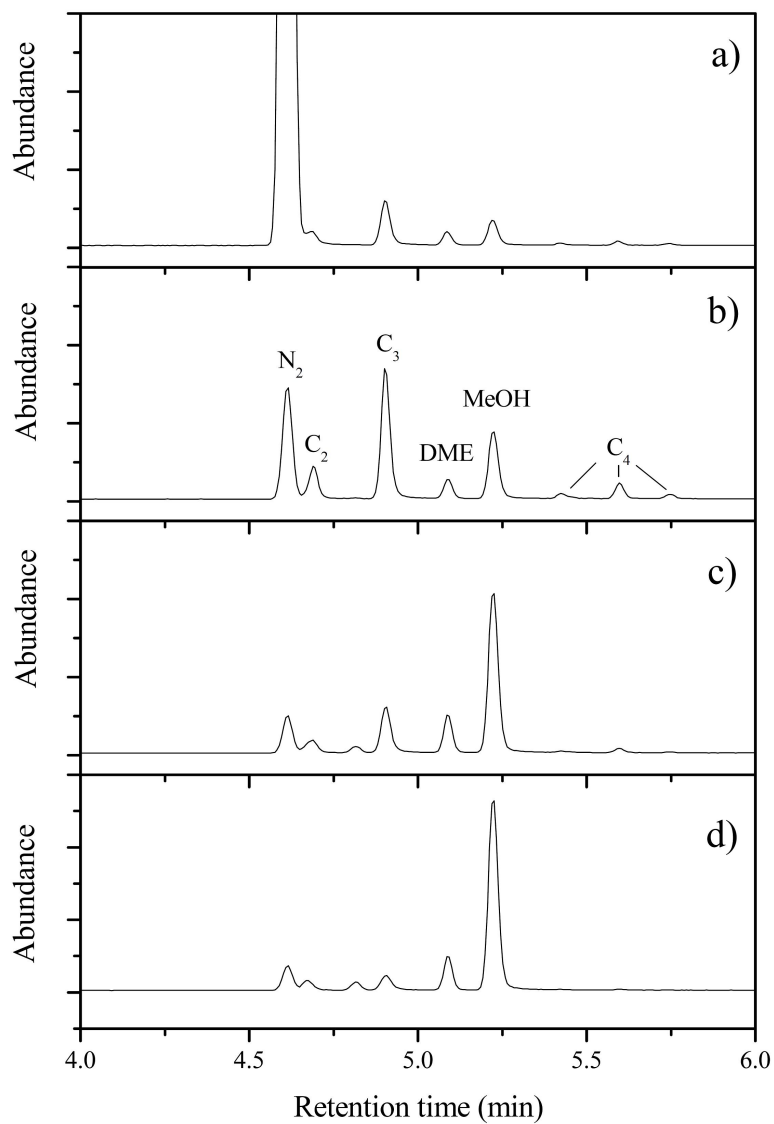


**Figure 4.85:** GC-TIC chromatogram of products obtained in the MTO reaction over calcined dehydrated SAPO<sub>4</sub>-18 after various times on stream: a) 10 min; b) 40 min; c) 70 min; d) 100 min. WHSV = 2.5 h<sup>-1</sup>, T = 400°C.



# Chapter 5

## Conclusions

- The preparations presented in U.S. Patent 4,310,400 by Wilson et al.<sup>6</sup>, yields products in agreement with tabulated  $2\theta$  values for  $\text{AlPO}_4\text{-14F}$ , provided the calcined material is not allowed to rehydrate after heating. The "F" (First generation) was assigned the products obtained, as they were shown<sup>30</sup> to contain the impurities  $\text{AlPO}_4\text{-14A}$  and  $\text{AlPO}_4\text{-15}$ . As shown with an experiment termed pseudo *in-situ* PXRD, the impurities are not visible until the sample has been heated to  $450^\circ\text{C}$ , the point where the final stage of template removal occurs as evident by TGA and DSC. This phenomenon was assigned the large difference in crystallite sizes (SEM) between  $\text{AlPO}_4\text{-14}$  and the impurities, a difference that is removed during the calcination of the material.
- The approach of substituting equimolar amounts of either aluminum with copper, or phosphorous with silicon, provides a way of crystallizing  $\text{CuAPO}_4\text{-14F}$  and  $\text{SAPO}_4\text{-14F}$ . The presence of copper alters the shapes and sizes of the crystallites, preventing them from forming the reported tabular shapes of  $\text{AlPO}_4\text{-14}$ <sup>34</sup>. Increasing copper content leads to agglomeration of the crystallites. Copper favors tetragonally distorted octahedral sites as evident with XAS, but the actual siting of copper is less definable. The  $\text{SAPO}_4\text{-14F}$  samples function poorly as catalysts, producing only dimethyl ether. In both cases, the presence of impurities prevents any disambiguous assignment of observed characteristics or properties to any particular molecular sieve.
- The crystallization of phase-pure  $\text{AlPO}_4\text{-14}$  was not achieved during this thesis work. Several synthesis parameters were tested, where the most of them resulted in the co-crystallization of tridymite or simply  $\text{AlPO}_4\text{-14F}$ . As may be inferred by the previous work done on the AFN topology, the actual catalytic application of these sieves has yet to be reported. The major part of the published articles are concerned with either (presumably) thermally unstable single-crystals or AIPOs. The studies on this topology seems to be concerned with structure more than catalytic applicability, when the ideal case would be a combination of both.

- The “impurity” known as  $\text{AlPO}_4\text{-14A}$ , discovered by Pluth and Smith<sup>30</sup> as single-crystals, was obtained as a pure-phase in this work. The "extra peaks" reported in the calcined powder form by Goepper and Guth<sup>114</sup> have been eliminated, and the results indicate that they were from  $\text{AlPO}_4\text{-14F}$ . The phase is favoured in mixtures of alkaline nature when a surplus of the template isopropylamine is used. The phase is also favoured in acidic medium with an aluminum deficiency in the molar oxide ratio. The template removal destroys most of the material, effectively reducing the composite crystallites' size and shape. In spite of PXRD results, the FT-IR spectrum of calcined dehydrated  $\text{AlPO}_4\text{-14A}$  shows an intense absorption attributed to characteristic Al-OH-Al linkages.
  - $\text{SAPO}_4\text{-43}$  has been successfully synthesized in this thesis work using two templates. Calcination of both materials indicate that the type of template used during synthesis is crucial for thermal stability. In the case of the isopropylamine template, calcination only serves to brutally crack and deform the octahedral crystallites (SEM), whereas in the case of the di-n-propylamine template, calcination is less destructive. Only  $\text{dpaSAPO}_4\text{-43}$  was found to be identifiable after calcination, provided that low heating rates were used. The Si uptake of these two samples seem to vary according to the template used, and the molar oxide ratio itself plays only a minor role.
  - Thermal stability of AlPOs and SAPOs has been shown to directly correlate with the identity of the template used in their synthesis. It is directly evident from the studies of  $\text{SAPO}_4\text{-43}$ , but also indirectly evident from studies of  $\text{AlPO}_4\text{-15}$  as impurity. Calcination of this particular AlPO induces a phase transition to tridymite when synthesized with hexamethylenetetramine as template, but only a partial structure collapse in  $\text{AlPO}_4\text{-14F}$  synthesized with isopropylamine, tert-butylamine, or piperidine.
  - The crystallization of AlPOs and SAPOs in high pH mixtures has been studied in this thesis work. The high pH was obtained by exploiting the alkaline nature of the organic amines used as templates. The dramatic increase in pH during crystallization of acidic gels is effectively eliminated and leads to more phase-pure materials. The templates seem to behave differently in alkaline mixtures, yielding perhaps somewhat unexpected topologies. While the AlPOs show less promise due to competing phases, the presence of silicon in SAPO preparations seem to avoid this problem. The excess of template may also play a role in the fact that topologies can be synthesized in the short time frame of 24 to 72 h, perhaps being linked to the kinetics of the crystallization process. Crystallizing alkaline mixtures generally yields samples composed of rather large crystallites, usually around 20  $\mu\text{m}$  in size.
-

# Chapter 6

## Future work

- As was shown in the previous chapters, dpaSAPO<sub>4</sub>-43 can be obtained in a stable calcined form, provided that the calcination procedure consists of heating samples at a low rate (0.5°C/min). Due to these low rates, TGA experiments would take days, and was not performed during the thesis work. The calcination procedure might be optimized, and perhaps the slow heating isn't necessary until reaching a certain temperature. One could first perform an initial TGA experiment to determine an approximate temperature for the removal of the di-n-propylamine template. The calcination procedure could then be modified to heating the material at a high rate up to 100°C below this temperature, and then utilize slow heating during the actual template removal. If this the works, then various *in-situ* characterization methods (PXRD, FT-IR, TGA) could be used to study the calcination. One could then study the thermal behavior of samples heated slowly and compare them to those heated at higher rates. This would perhaps give more insight into the nature of the template removal, and if significant differences occur, how this behavior relates to the preservation of the material.

The structure of calcined SAPO<sub>4</sub>-43 might be resolved using Rietveld refinement of powder diffraction data, the structure of the as-synthesized material perhaps being a logical starting point. Data collection using synchrotron radiation would probably be preferred. If the structure is solved, one can move on to catalyst testing. The MTO reaction would be an obvious choice, and combined with FT-IR it may give new insight to this process.

The dpaipaSAPO<sub>4</sub>-43 sample was discovered extremely late in the thesis work and needs further characterization. It would be very interesting to study the sample with ICP-MS to see if the presence of isopropylamine also promotes Si uptake in addition to fast crystallization.

- It would be interesting to study the high pH approach to crystallization of AlPOs and SAPOs further, given that the few templates tested in this thesis work showed such promise. The AlPO preparations did show a tendency to form several phases, but this could probably be solved by adjusting the crystallization times. It was found during the

thesis work that SAPO<sub>4</sub>-43 can be preserved during calcination using di-n-propylamine as template, but not using isopropylamine. If other unstable topologies could be synthesized with alternate templates it would perhaps also be possible to preserve their structures during the calcination process. It is perhaps possible to synthesize a more thermally stable AlPO<sub>4</sub>-14A by using a mixture of isopropylamine and triethylamine. This would give further insight into the stability of this material, and enable testing of the hypothesis regarding the relation between thermal stability and the size of the template used in synthesis.

Also, as shown with ICP-MS, the Si uptake varies depending on the template used in syntheses. The high pH approach could be expanded by altering the phosphorous source and using for instance H<sub>3</sub>PO<sub>3</sub> or P<sub>2</sub>O<sub>5</sub> instead of H<sub>3</sub>PO<sub>4</sub>. The material somewhat arbitrarily named Vermiculite may be a SAPO topology not yet characterized, and crystallizing SAPOs in alkaline mixtures with lower crystallization temperatures (150°C) might produce similar results. The lowering of temperature will probably result in the need for longer crystallization times. SAPO<sub>4</sub>-50 may also be obtained from a gel with molar oxide ratio: 4.36R:0.80Al<sub>2</sub>O<sub>3</sub>:1.00P<sub>2</sub>O<sub>5</sub>:0.40SiO<sub>2</sub>:40.00H<sub>2</sub>O using the di-n-propylamine template. One could try a temperature of 150°C and a crystallization time of 7 days. The AFY topology has been shown to be thermally unstable, but similar slow heating procedures may also work for this material.

- With FT-IR studies in mind, the high pH preparations need to be modified to yield smaller crystallites (<5 μm). Large crystallites (>10 μm) tend to absorb too much IR radiation causing noisy spectra. Also, samples with large crystallites require the preparation of extremely thin wafers that are prone to cracks. Possible solutions to this could be the use of seed crystals or stirring during crystallization. The dual template approach tested for dpaipaSAPO<sub>4</sub>-43 showed some promise with reduction of crystallite size, and could be explored further by varying the ratio of R2/R1. It could also be tested in conjunction with factors such as seeding, stirring, and aging, which in turn might decrease the crystallite size even further. It could of course also be expanded to other topologies.
-

# References

1. Dyer, A. *An Introduction to Zeolite Molecular Sieves*, chapter 2, 4. JOHN WILEY & SONS.
2. Dyer, A. *An Introduction to Zeolite Molecular Sieves*, chapter 1, 1. JOHN WILEY & SONS.
3. Baerlocher, C., McCusker, L., Hanson, R., and Treacy, M. World Wide Web electronic publication, (2009).
4. Barrer, R. M. *Proceedings of the Royal Society of London. Series A, Mathematical and Physical Sciences*, 392–420 (1938).
5. Cundy, C. and Cox, P. *Microporous and Mesoporous Materials* **82**, 5 (2005).
6. Wilson, S. T., Lok, B. M., and Flanigen, E. M. United States Patent 4,310,440, January (1982).
7. Wilson, S. T., Lok, B. M., Messina, C. A., Cannan, T. R., and Flanigen, E. M. *J. Am. Chem. Soc.* **104**, 1146–1147 (1982).
8. Dyer, A. *An Introduction to Zeolite Molecular Sieves*, chapter 2, 135. JOHN WILEY & SONS.
9. Lok, B. M., Messina, C. A., Patton, R. L., Gajek, R. T., Cannan, T. R., and Flanigen, E. M. United States Patent 4,440,871, April (1984).
10. Wilson, S. T. and Flanigen, E. M. United States Patent 4,567,029, January (1986).
11. Cundy, C. and Cox, P. *Microporous and Mesoporous Materials* **82**, 65–66 (2005).
12. Atkins, P., Overton, J., Rourke, J., Weller, M., and Armstrong, F. *Inorganic Chemistry*, chapter 25, 681. OXFORD University Press, fourth edition (2006).
13. Holmen, A. *Heterogen katalyse*, 4. Institutt for kjemisk prosess teknologi, NTNU (2008).
14. *Inorganic chemistry*, 683. Oxford University Press, fourth edition (2006).
15. Holmen, A. *Heterogen katalyse*, 13. Institutt for kjemisk prosess teknologi, NTNU (2008).

16. Dyer, A. *An Introduction to Zeolite Molecular Sieves*, chapter 2, 121. JOHN WILEY & SONS.
  17. Holmen, A. *Heterogen katalyse*, 88. Institutt for kjemisk prosesssteknologi, NTNU (2008).
  18. Holmen, A. *Heterogen katalyse*, 183. Institutt for kjemisk prosesssteknologi, NTNU (2008).
  19. Atkins, P., Overton, J., Rourke, J., Weller, M., and Armstrong, F. *Inorganic Chemistry*, chapter 25, 683. OXFORD University Press, fourth edition (2006).
  20. Dyer, A. *An Introduction to Zeolite Molecular Sieves*, chapter 2, 124. JOHN WILEY & SONS.
  21. Dyer, A. *An Introduction to Zeolite Molecular Sieves*, chapter 2, 125. JOHN WILEY & SONS.
  22. Solomons, T. and Fryhle, C. B. *Organic Chemistry*, chapter Chapter 10, 474–476. John Wiley & Sons, Inc.
  23. Solomons, T. and Fryhle, C. B. *Organic Chemistry*, chapter Chapter 11, 497. John Wiley & Sons, Inc.
  24. Stöcker, M. *Microporous and Mesoporous Materials* **29**, 3–48 (1999).
  25. Dahl, I. M. and Kolboe, S. *Catalysis letters* **20**, 329–336 (1993).
  26. Kolboe, S. *Acta Chemica Scandinavica A* **40**, 771–713 (1986).
  27. Mikkelsen, y., Ola, R. P., and Stein, K. *Microporous and Mesoporous materials* **40**, 95–113 (2000).
  28. Hereijgers, B. P., Bleken, F., Nilsen, M. H., Stian, S., Lillerud, K.-P., Bjørgen, M., and Olsbye, U. *Journal of catalysis* **264**, 77–87 (2009).
  29. Broach, R. W., Wilson, S. T., and Kirchner, R. M. *Proceedings of the 12th International Zeolite Conference* , 1715–1722 (1999).
  30. Pluth, J. J. and Smith, J. V. *Acta Crystallographica Section C* **43**, 866–870 (1987).
  31. Helliwell, M., Kaučič, V., Cheetam, G., Harding, M., Kariuki, B., and Rizkallah, P. *Acta Crystallographica Section B* **49**, 413–420 (1993).
  32. Rajić, N. and Kaučič, V. *Zeolites* **Vol 10**, 169–173 March (1990).
  33. Parise, J. B. *Acta Crystallographica Section C* **42**, 670–673 (1986).
-

34. Zibrowius, B., Lohse, U., and Richter-Mendau, R. *J. CHEM. SOC. FARADAY TRANS. Vol 87*, 1433–1437 (1991).
  35. Yang, H., Walton, R. I., Biedasek, S., Antonijevic, S., Wimperis, S., Ramirez-Cuesta, A. J., Li, J., and Kolesnikov, A. I. *J. Phys. Chem. B* **109**, 4464–4469 (2005).
  36. Girnus, I., Löffler, E., Lohse, U., and Neissendorfer, F. .
  37. Weller, M. T. *Inorganic Materials Chemistry*, chapter 1, 1–3. Oxford Science Publications.
  38. Weller, M. T. *Inorganic Materials Chemistry*, chapter 1, 6. Oxford Science Publications.
  39. Atkins, P. and de Paula, J. *Physical chemistry*, chapter 13, 700. OXFORD University Press, eight edition (2006).
  40. Weller, M. T. *Inorganic Materials Chemistry*, chapter 1, 10. Oxford Science Publications.
  41. Atkins, P. and de Paula, J. *Physical chemistry*, chapter 13, 704. OXFORD University Press, eight edition (2006).
  42. Atkins, P., Overton, J., Rourke, J., Weller, M., and Armstrong, F. *Inorganic Chemistry*, chapter 6, 170. OXFORD University Press, fourth edition (2006).
  43. Weller, M. T. *Inorganic Materials Chemistry*, chapter 1, 11. Oxford Science Publications.
  44. Weller, M. T. *Inorganic Materials Chemistry*, chapter 1, 15. Oxford Science Publications.
  45. Thomas, R. *Practical guide to ICP-MS: A tutorial for beginners*, 7. CRC Press Taylor & Francis Group, second edition (2008).
  46. Thomas, R. *Practical guide to ICP-MS: A tutorial for beginners*, 3. CRC Press Taylor & Francis Group, second edition (2008).
  47. Thomas, R. *Practical guide to ICP-MS: A tutorial for beginners*, 27. CRC Press Taylor & Francis Group, second edition (2008).
  48. Thomas, R. *Practical guide to ICP-MS: A tutorial for beginners*, 60. CRC Press Taylor & Francis Group, second edition (2008).
  49. Zhou, W. and Wang, Z. L. *Scanning microscopy for nanotechnology: Techniques and applications*, chapter 1, 9–13. Springer, first edition (2006).
  50. Amelinckx, S., van Dyck, D., van Landuyt, J., and van Tendeloo, G. *Electron microscopy*, chapter 2, 306. VCH A Wiley company.
-

51. Zhou, W. and Wang, Z. L. *Scanning microscopy for nanotechnology: Techniques and applications*, chapter 1, 18. Springer, first edition (2006).
  52. Yao, N. and Wang, Z. L. *Handbook of microscopy for nanotechnology*, chapter 11, 329. Kluwer Academic Publishers.
  53. Zhou, W. and Wang, Z. L. *Scanning microscopy for nanotechnology: Techniques and applications*, chapter 1, 2–3. Springer, first edition (2006).
  54. Amelinckx, S., van Dyck, D., van Landuyt, J., and van Tendeloo, G. *Electron microscopy*, chapter 2, 310. VCH A Wiley company.
  55. Zhou, W. and Wang, Z. L. *Scanning microscopy for nanotechnology: Techniques and applications*, chapter 1, 5. Springer, first edition (2006).
  56. Amelinckx, S., van Dyck, D., van Landuyt, J., and van Tendeloo, G. *Electron microscopy*, chapter 2, 305. VCH A Wiley company.
  57. Brown, M. E. *Introduction to thermal analysis*, chapter 2, 19–20. Kluwer Academic Publishers, second edition (2006).
  58. Brown, M. E. *Introduction to thermal analysis*, chapter 2, 57–58. Kluwer Academic Publishers, second edition (2006).
  59. Karge, H. G. and Weitkamp, J. *Characterization I*, chapter 1, 96. Springer, first edition (1998).
  60. Marchese, L., Frache, A., Gianotti, E., Marta, G., M., C., and S., C. *Microporous and Mesoporous materials* **30**, 145–153 (1999).
  61. Prakash, A., Hartmann, M., and Kevan, L. *J. Phys. Chem. B* **101**, 6819–6826 (1997).
  62. Kornatiwski, J., Finger, G., and Schultze, D. *J. Phys. Chem. A* **106**, 3975–3981 (2002).
  63. Finger, G., Kornatowski, J., Lutz, W., Heidemann, D., and Schultze, D. *Thermochimica acta* **409**, 49–54 (2004).
  64. Choudary, V. and Pataskar, S. *Thermochimica acta* **142**, 1–10 (1986).
  65. Malysheva, L., Paukshtis, E., and Kotsarenko, N. *React. Kinet. Catal. Lett.* **24**, 97–101 (1984).
  66. Hernández-Maldonado, A. J., Yang, R. T., Chinn, D., and Munson, C. L. M. . *Langmuir* **19**, 2193–2200 (2003).
-

67. Rouquerol, F., Rouquerol, L., and Sing, K. *Adsorption by powders and Porous Solids: Principles, Methodology and Applications*, chapter 1, 8. Academic press, first edition (1999).
  68. Do, D. D. *Adsorption analysis: Equilibria and kinetics*, chapter 1, 2. Imperial College Press, first edition (1998).
  69. Gregg, S. and Sing, K. *Adsorption, Surface Area and Porosity*, chapter 1, 4. Academic press, second edition (1982).
  70. Rouquerol, F., Rouquerol, L., and Sing, K. *Adsorption by powders and Porous Solids: Principles, Methodology and Applications*, chapter 1, 7. Academic press, first edition (1999).
  71. Gregg, S. and Sing, K. *Adsorption, Surface Area and Porosity*, chapter 1, 3. Academic press, second edition (1982).
  72. Holmen, A. *Heterogen katalyse*, 31. Institutt for kjemisk prosessteknologi, NTNU (2008).
  73. Gregg, S. and Sing, K. *Adsorption, Surface Area and Porosity*, chapter 1, 25. Academic press, second edition (1982).
  74. Holmen, A. *Heterogen katalyse*, 31–32. Institutt for kjemisk prosessteknologi, NTNU (2008).
  75. Gregg, S. and Sing, K. *Adsorption, Surface Area and Porosity*, chapter 1, 45. Academic press, second edition (1982).
  76. Do, D. D. *Adsorption analysis: Equilibria and kinetics*, chapter 1, 84. Imperial College Press, first edition (1998).
  77. Brunauer, S., Emmet, P., and Teller, E. *Zeolites* **60**, 309–319 (1938).
  78. Do, D. D. *Adsorption analysis: Equilibria and kinetics*, chapter 1, 91–93. Imperial College Press, first edition (1998).
  79. Koningsberger, D. and Prins, R. (1988).
  80. Miller, D. F. *Basics of Radio Astronomy for the Goldstone-Apple Valey Radio Telescope*, chapter 3, 26. California Institute of Technology, (1997).
  81. Miller, J. and Drillon, M. *Magnetism: Molecules to Materials IV*, chapter 8, 283. Wiley (2002).
  82. Fay, M. J., Proctor, A., Hoffman, D. P., and Hercules, D. M. *Anal. Chem.* **60**, 1225 (1988).
  83. Koningsberger, D. and Prins, R. (1988).
-

84. Stuart, B. *Infrared Spectroscopy: Fundamentals and applications*, 21. John Wiley & sons, Ltd, first edition (2004).
  85. Stuart, B. *Infrared Spectroscopy: Fundamentals and applications*, 3. John Wiley & sons, Ltd, first edition (2004).
  86. Stuart, B. *Infrared Spectroscopy: Fundamentals and applications*, 4. John Wiley & sons, Ltd, first edition (2004).
  87. Stuart, B. *Infrared Spectroscopy: Fundamentals and applications*, 46. John Wiley & sons, Ltd, first edition (2004).
  88. Stuart, B. *Infrared Spectroscopy: Fundamentals and applications*, 6. John Wiley & sons, Ltd, first edition (2004).
  89. Stuart, B. *Infrared Spectroscopy: Fundamentals and applications*, 7. John Wiley & sons, Ltd, first edition (2004).
  90. Griffiths, P. R. and de Haseth, J. A. *Fourier Transform Infrared Spectrometry*, 4. John Wiley & sons, Inc, second edition (2007).
  91. Griffiths, P. R. and de Haseth, J. A. *Fourier Transform Infrared Spectrometry*, 3. John Wiley & sons, Inc, second edition (2007).
  92. Lok, B. M., Messina, C. A., Patton, R. L., Gajek, R. T., Cannan, T. R., and Flanigen, E. M. *J. Am. Chem. Soc.* **106**, 6092–6093 (1984).
  93. Chen, J., Wright, P. A., Thomas, J. M., Natarjan, S., Marchese, L., Bradley, S. M., Sankar, G., Catlow, C. R. A., Gai-Boyes, P. L., Townsend, R. P., and Lok, C. M. **98**, 10216–10224 (1994).
  94. Zibrowius, B., Löffler, E., and Hunger, M. *Zeolites* **12**, 167–174 (1992).
  95. Marchese, L., Chen, J., Wright, P. A., and Thomas, J. M. *J. Phys. Chem.*, year = .
  96. Mériaudeau, P., Tuan, V., Nghiem, V., Lai, S., Hung, L., and Naccache, C. *Journal of catalysis* **169**, 55–56 (1997).
  97. Chen, J., Thomas, J. M., Wright, P. A., and Townsend, R. P. **28**, 241–248 (1994).
  98. Smith, L., Cheetham, A., Marchese, L., Thomas, J., Wright, P., Chen, J., and Gianotti, E. *Catalysis letters* **41**, 13–16 (1996).
  99. Bleken, F., Bjørgen, M., Palumbo, L., Bordiga, S., Svelle, S., Lillerud, K.-P., and Olsbye, U. *Top. Catal.* **52**, 218–228 (2009).
-

## References

---

100. McNair, H. M. and Miller, J. M. *Basic gas chromatography*, chapter 1, 4. John Wiley & sons, Inc (1998).
  101. McNair, H. M. and Miller, J. M. *Basic gas chromatography*, chapter 1, 3. John Wiley & sons, Inc (1998).
  102. Grob, R. L. and Barry, E. F. *Modern practice of gas chromatography*, chapter 8, 406. John Wiley & sons, Inc, fourth edition (2004).
  103. McNair, H. M. and Miller, J. M. *Basic gas chromatography*, chapter 1, 112. John Wiley & sons, Inc (1998).
  104. Miller, J. M. *Chromatography: concepts and contrasts*, chapter 10, 309. John Wiley & sons, Inc (2005).
  105. McMaster, M. C. *GC/MS: a practical user's guide*, chapter 1, 4. John Wiley & sons, Inc (2008).
  106. Mathisen, K., Nicholson, D. G., Fitch, A. N., and Stockenhuber, M. *Journal of Materials Chemistry* **15**, 204–217 (2004).
  107. Antonijevic, S., Ashbrook, S. E., Biedasek, S., Walton, R. I., Wimperis, S., and Yang, H. *JACS* , 8054–8062 (2006).
  108. Ashbrook, S. E., Cutajar, M., Pickard, C. J., Walton, R. I., and Wimperis, S. .
  109. Muñoz, T. J., Prakash, A. M., Kevan, L., and Balkus, K. J. J. *J. Phys. Chem. B* **102**, 1379–1386 (1998).
  110. Flanigen, E. M., Lok, B. M., Patton, L. R., and Wilson, S. T. *Pure & Appl. Chem* **58**, 1351–1358 (1986).
  111. Nicholson, D. G. and Nilsen, M. H. *Journal of materials chemistry* **10**, 1965–1971 (2000).
  112. Burton, I. D., Hargreaves, J. S. J., Nicholson, D. G., Nilsen, M. H., and Stockenhuber, M. *Journal of materials chemistry* **11**, 1441–1446 (2001).
  113. Moen, A. and Nicholson, D. G. *J. Chem. Soc. Faraday trans* **91**, 3529–3535 (1995).
  114. Goepper, M. and Guth, J. *Zeolites* **11**, 477–482 (1991).
  115. Rajić, N. and Stojaković, D. Kaučič, V. *Zeolites* **Vol 10**, 802–805 November/December (1990).
  116. Zibrowius, B., Schmidt, W., Weidenthaler, C., and Ruschewitz, U. Scientific poster.
  117. World Wide Web electronic publication.
-

118. Cundy, C. and Cox, P. *Microporous and Mesoporous Materials* **82**, 35–36 (2005).
  119. Brouwer, D. H., Chézeau, J.-M., and Fyfe, C. A. *Microporous and Mesoporous materials* **88**, 163–169 (2006).
  120. Painter, P. C. and Coleman, M. M. *Fundamentals of Polymer Science: An introductory text*, 239. CRC Press, first edition (1997).
  121. Akporiaye, D., Dahl, I., Mostad, H., and Wendelbo, R. *Zeolites* **17**, 517–522 (1996).
  122. Pluth, J. J., Smith, J. V., and Bennet, J. M. *J. Am. Chem. Soc.* **111**, 1692–1698 (1989).
  123. Akolekar, D.B. and Kaliaguine, S. **2**, 137–144 (1994).
  124. Pluth, J., Smith, J., and Richardson Jr., J. *J. Phys. Chem.* **92**, 2734–2738 (1988).
  125. Richardson, Jnr, J. W., Pluth, J. J., and Smith, J. V. *Acta Crystallographica Section B* **44**, 367–373 (1988).
  126. Ma, Y., Li, N., Ren, X., Xiang, S., and Guan, N. *Journal of Molecular Catalysis A: Chemical* **250**, 9–14 (2006).
  127. Kong, W., Dai, W., Li, N., Guan, N., and Xiang, S. *Journal of Molecular Catalysis A: Chemical* **308**, 127–133 (2009).
  128. Ojo, A. F. and McCusker, L. B. *Zeolites* **11**, 460–465 (1991).
  129. Akolekar, D. B. *Zeolites* **15**, 583–590 (1995).
  130. Dai, P.-S. E., Petty, R. H., Ingram, C. W., and Szostak, R. *Applied Catalysis A: Genera* **143**, 101–110 (1996).
  131. Felsche, J., Luger, S., and Baerlocher, C. *Zeolites* **6**, 367–372 (1986).
  132. Dimitriu, E., Azzouz, A., Hulea, V., Lutic, D., and Kessler, H. *Microporous Materials* **10**, 1–12 (1997).
  133. Pluth, J., Smith, J., Bennet, J., and Cohen, J. *Acta cryst. Section C* **40**, 2008–2011 (1984).
  134. Calligaris, M., Nardin, G., and L., R. *Zeolites* **3**, 205–208 (1983).
  135. Qiu, S., Wenqin, P., Kessler, H., and Guth, J.-L. **9**, 440–444 (1989).
  136. Simmen, A., McCusker, L., Baelocher, C., and Meier, W. *Zeolites* **11**, 654–661 (1991).
  137. Colthup, N., Daly, L., and Wiberley, S. *Introduction to Infrared and Raman Spectroscopy*, chapter 11, 100. Academic press, third edition.
-

138. Čejka, J., Bekkum, H. v., Corma, A., and Schüth, F. *Introduction to Zeolite Molecular Sieves (Studies in surface science and catalysis)*, chapter 4, 117–120. Elsevier B.V., first edition.
  139. Wendelbo, R., Akporiaye, D., Andersen, A., Dahl, I. M., and Mosand, H. B. *Applied Catalysis A: General* **142**, 197–207 (1996).
  140. Zhao, X.-X., Xu, X.-L., Sun, L.-B., Zhang, L.-L., and Liu, X.-Q. *Energy and Fuels* **23**, 1534–1528 (2009).
  141. Rungrojchaipon, P., Wang, X., and Jacobson, A. J. *Microporous and Mesoporous materials* **109**, 478–484 (2008).
  142. Brown, M. E. *Introduction to thermal analysis*, chapter 2, 77. Kluwer Academic Publishers, second edition (2006).
  143. Brown, M. E. *Introduction to thermal analysis*, chapter 2, 16. Kluwer Academic Publishers, second edition (2006).
  144. Fernandez, R., Giotto, M. V., Pastore, H. O., and Cardoso, D. *Microporous and Mesoporous Materials* **53**, 135–144 (2002).
  145. Liu, P., Ren, J., and Sun, Y. *Catalysis communications* **9**, 1804–1809 (2008).
  146. Yang, X., Xu, Z., Tian, Z., Ma, H., Xu, Y., Qu, W., and Lin, L. *Catalysis communications* **109**, 139–145 (2006).
  147. Rayner-Canham, G. and Overton, T. *Descriptive inorganic Chemistry*, chapter 20, 554. W.H. Freeman and company, fourth edition (2006).
  148. Åsbrink, S. and Norby, L. *Acta Cryst section B* **26**, 8–15 (1970).
  149. Brown, G. M. and Chidambaram, R. *Acta Cryst section B* **25**, 676–687 (1968).
  150. Stuart, B. *Infrared Spectroscopy: Fundamentals and applications*, 45. John Wiley & sons, Ltd, first edition (2004).
  151. Zubkov, S., Kustov, L. M., Kazansky, V. B., Girnus, I., and Fricke, R. *J. Chem. Soc. Faraday Trans.* **87**, 897–900 (1991).
  152. Colthup, N., Daly, L., and Wiberley, S. *Introduction to Infrared and Raman Spectroscopy*, chapter 11, 339. Academic press, third edition.
  153. Venkatathri, N. *Indian Chemical Society* **2**, 137–144 (1994).
-

# Appendix A

## Additional data

### A.1 Results from ICP-MS analyses

	weight (ug/g):				moles (umol/g)			
	Al	Si	P	Cu	Al	Si	P	Cu
ipaAlPO14F	228 946	-	285 395	-	8485,13	-	9214,03	-
ipaAlPO14A	175 399	-	215 563	-	6500,59	-	6959,47	-
teaAlPO-5	233 438	-	293 937	-	8651,62	-	9489,79	-
ipa001CuAPO-14F	215 187	-	272 730	2 681	7975,20	-	8805,12	42,18437272
ipa003CuAPO-14F	182 705	-	226 344	9 036	6771,35	-	7307,56	142,2025395
ipa008CuAPO-14F	191 769	-	245 173	11 909	7107,31	-	7915,44	187,4129263
tba006SAPO-14F	301 582	12 977	379 003	-	11177,16	462	12236,18	-
tba008SAPO-14F	196 518	5 040	237 951	-	7283,31	179	7682,30	-
tba020SAPO-14F	199 415	8 138	242 376	-	7390,68	290	7825,14	-
dipaSAPO-34	252 516	41 278	282 338	-	9358,69	1 470	9115,32	-
ipaSAPO-20	494 903	60 248	450 723	-	18341,97	2 145	14551,66	-
ipaSAPO-43	225 010	79 290	190 603	-	8339,27	2 823	6153,66	-
teaSAPO-18	347 919	23 279	397 447	-	12894,48	829	12831,64	-
dpaSAPO-43	419 997	79 690	402 768	-	15565,83	2 837	13003,42	-
pipSAPO-20	141 592	25 836	141 324	-	5247,65	920	4562,65	-
	Si/(Si+Al+P)	Cu/(Cu+Al+P)	(Al+P)/Si	(Al+P)/Cu				
ipa001CuAPO-14F	-	0,003	-	-				
ipa003CuAPO-14F	-	0,010	-	-				
ipa008CuAPO-14F	-	0,012	-	-				
tba006SAPO-14F	0,019	-	51	398				
tba008SAPO-14F	0,012	-	83	99				
tba020SAPO-14F	0,019	-	53	80				
dipaSAPO-34	0,074	-	13	-				
ipaSAPO-20	0,061	-	15	-				
ipaSAPO-43	0,163	-	5	-				
teaSAPO-18	0,031	-	31	-				
dpaSAPO-43	0,090	-	10	-				
pipSAPO-20	0,086	-	11	-				

**Figure A.1:** Excel spreadsheet with results from ICP-MS analyses of various samples synthesized in this thesis work.

## A.2 BET isotherm data

BET Isotherm data					
<b>AIPO-14F 600degC</b>		<b>AIPO-14F550g</b>		<b>0.01CuAPO-14F</b>	
(p/p <sup>o</sup> )	Quantity (cm <sup>3</sup> /g STP)	(p/p <sup>o</sup> )	Quantity (cm <sup>3</sup> /g STP)	(p/p <sup>o</sup> )	Quantity(cm <sup>3</sup> /g STP)
0.057682608	91.6022	0.060905573	84.8941	0.061483945	92.8075
0.082227948	92.9196	0.081247315	85.9934	0.079323944	93.8231
0.121327568	94.9110	0.121419557	87.8973	0.121621569	95.9495
0.161973108	96.7061	0.161249805	89.6911	0.165203681	97.6669
0.206287410	98.0903	0.205375059	91.0653	0.210555213	99.0028
<b>0.03CuAPO-14F</b>		<b>0.06SAPO-14F</b>		<b>0.08SAPO-14F</b>	
(p/p <sup>o</sup> )	Quantity (cm <sup>3</sup> /g STP)	(p/p <sup>o</sup> )	Quantity (cm <sup>3</sup> /g STP)	(p/p <sup>o</sup> )	Quantity (cm <sup>3</sup> /g STP)
0.076491228	70.4610	0.061869909	71.67807273	0.064527848	63.61956818
0.077451259	70.5465	0.078466728	72.47537273	0.077287098	64.27363636
0.132906212	71.4978	0.127797270	73.81691364	0.122909414	65.79616364
0.163616638	72.0648	0.170106158	74.59300455	0.163914291	67.01833182
0.204164745	72.5386	0.214602076	75.12889091	0.208170952	67.94195909
<b>0.20SAPO-14F</b>		<b>AIPO-14A</b>		<b>AIPO-5</b>	
(p/p <sup>o</sup> )	Quantity (cm <sup>3</sup> /g STP)	(p/p <sup>o</sup> )	Quantity (cm <sup>3</sup> /g STP)	(p/p <sup>o</sup> )	Quantity (cm <sup>3</sup> /g STP)
0.065179039	90.54556364	0.060833919	1.7269	0.065425083	51.0562
0.078440962	91.30655	0.078221097	1.8257	0.080844547	51.3080
0.122586946	93.10664545	0.119383124	1.9986	0.126295024	51.7866
0.164029303	94.37212273	0.159532661	2.1459	0.163416541	52.0607
0.206791218	95.31840909	0.199602692	2.2709	0.203822882	52.2855
<b>SAPO-18</b>		<b>SAPO-34</b>		<b>SAPO-43</b>	
(p/p <sup>o</sup> )	Quantity (cm <sup>3</sup> /g STP)	(p/p <sup>o</sup> )	Quantity (cm <sup>3</sup> /g STP)	(p/p <sup>o</sup> )	Quantity (cm <sup>3</sup> /g STP)
0.068270492	175.5167	0.063695397	179.1756	0.062105917	90.3409
0.087184346	175.7500	0.118251962	179.1423	0.073911492	91.7301
0.133161994	176.1602	0.119325864	179.1431	0.125925524	94.8278
0.162451894	176.3489	0.161628205	179.0549	0.169424875	96.2568
0.202101920	176.5430	0.200847057	178.9524	0.217853609	97.2661

Figure A.2: Excel spreadsheet with BET isotherm data for samples synthesized in this thesis work.

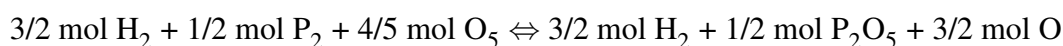
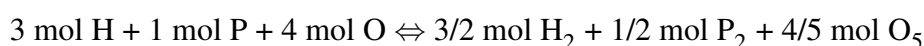
# Appendix B

## Resources

### B.1 Conversions

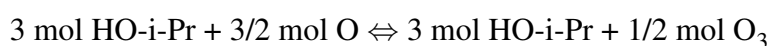
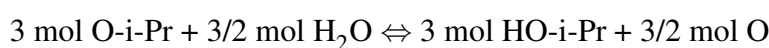
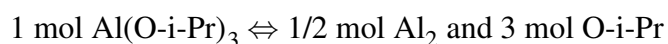
#### B.1.1 Conversion from phosphoric acid to phosphorous pentoxide

The common phosphorous source for AlPO related syntheses is phosphoric acid ( $\text{H}_3\text{PO}_4$ ), but is usually written in molar oxide ratios as phosphorous pentoxide ( $\text{P}_2\text{O}_5$ ). The following conversion was used to obtain moles of phosphoric acid expressed as moles of phosphorous pentoxide:



#### B.1.2 Conversion from aluminum isopropoxide to alumina

When working with preparations where aluminum isopropoxide ( $\text{Al}(\text{O-i-Pr})_3$ , where i-Pr =  $(\text{OCH}(\text{CH}_3))$ ) is the source of aluminum, the resulting molar oxide ratio is often stated with respect to alumina ( $\text{Al}_2\text{O}_3$ ). To convert the number of moles aluminum isopropoxide to number of moles alumina, the following conversion was used:



## B.2 Crystallographic Information Files (CIF)

### B.2.1 AlPO<sub>4</sub>-14A

```
#####
# Crystallographic Information File (CIF) for AlPO-14A #
# #
# By: I dar Hoftani ska #
# #
# Reference: Pluth, J. J. & Smith, J. V. (1987). Acta Cryst. C43, 866-870. #
# #
#####

data_AlPO-14A
_chemical_name_systematic
'AlPO-14A'

_cell_length_a 24.085
_cell_length_b 14.393
_cell_length_c 8.7122
_cell_angle_alpha 90
_cell_angle_beta 94.260
_cell_angle_gamma 90
_cell_formula_units_Z 1
_symmetry_space_group_name_H-M 'C2/c'

loop_
_atom_site_label
_atom_site_type_symbol
_atom_site_fract_x
_atom_site_fract_y
_atom_site_fract_z
_atom_site_B_iso_or_equiv
_atom_site_occupancy
P1 P 0.33817 0.73198 0.42986 0.0082 1.0
P2 P 0.17397 0.53087 0.06070 0.0078 1.0
P3 P 0.5 0.49464 0.75 0.0104 1.0
P4 P 0.00842 0.32112 0.47374 0.0093 1.0
Al 1 Al 0.00 0.55471 0.25 0.0107 1.0
Al 2 Al 0.22189 0.62359 0.37596 0.0088 1.0
Al 3 Al 0.45019 0.62979 0.50032 0.0112 1.0
Al 4 Al 0.09788 0.38885 0.25913 0.0082 1.0
O1 O 0.17511 0.7082 0.4315 0.0154 1.0
O2 O 0.14182 0.2882 0.1995 0.0137 1.0
O3 O 0.38148 0.6611 0.4929 0.0175 1.0
O4 O 0.28631 0.6761 0.3749 0.0170 1.0
O5 O 0.15011 0.5921 -0.0688 0.0134 1.0
O6 O 0.13047 0.4706 0.1253 0.0148 1.0
O7 O 0.22085 0.4696 0.0019 0.0139 1.0
O8 O 0.20189 0.5950 0.1865 0.0137 1.0
O9 O 0.46013 0.5554 0.6546 0.0374 1.0
O10 O 0.46549 0.4347 0.8443 0.0505 1.0
O11 O 0.05565 0.4905 0.3356 0.0116 1.0
O12 O 0.03037 0.3742 0.6178 0.0135 1.0
O13 O 0.00697 0.77674 0.4709 0.0193 1.0
O14 O 0.05694 0.3061 0.3740 0.0114 1.0
O15 O 0.04188 0.3716 0.0979 0.0151 1.0
N1 N 0.3680 0.2717 0.3968 0.062 1.0
C1 C 0.3305 0.3466 0.4384 0.1405 1.0
C2 C 0.2887 0.3702 0.3146 0.1074 1.0
C3 C 0.1455 0.0844 0.4596 0.085 1.0
H1 H 0.066 0.501 0.398 0.0051 1.0

#End of data for AlPO-14A
```

**Figure B.1:** CIF file made in this thesis work for the generation of a simulated x-ray diffraction pattern for AlPO<sub>4</sub>-14A.

B.2.2 AIPO<sub>4</sub>-15

```
#####
# Crystallographic Information File (CIF) for AIPO-15 #
# #
# By: Idar Hofnani ska #
# #
# Reference: J. J. Pluth, J. V. Smith, Acta Crystallogr. Sec. C 40 (1984) 2008 #
# #
#####

data_AIPO-15
_chemical_name_systematic
'AIPO-15'

_cell_length_a 9.6167
_cell_length_b 9.5720
_cell_length_c 9.5563
_cell_angle_alpha 90
_cell_angle_beta 103.589
_cell_angle_gamma 90
_cell_formula_units_Z 1
_symmetry_space_group_name_H-M 'P21/n'

loop_
_atom_site_label
_atom_site_type_symbol
_atom_site_fract_x
_atom_site_fract_y
_atom_site_fract_z
_atom_site_B_iso_or_equiv
_atom_site_occupancy
P1 P 0.34830 0.53183 0.69853 529 1.0
P2 P 0.13673 0.30797 0.29463 506 1.0
Al 1 Al 0.37209 0.53719 0.38618 573 1.0
Al 2 Al 0.31503 0.22896 0.60731 597 1.0
O1 O 0.29674 0.58593 0.54344 784 1.0
O2 O 0.19438 0.12742 0.69302 913 1.0
O3 O 0.48683 0.48033 0.26314 786 1.0
O4 O 0.28440 0.38569 0.70988 802 1.0
O5 O 0.16583 0.26782 0.45379 912 1.0
O6 O 0.20999 0.44859 0.27945 774 1.0
O7 O 0.30331 0.69867 0.29189 908 1.0
O8 O 0.47629 0.17560 0.73909 884 1.0
O9 O 0.44566 0.36468 0.50306 788 1.0
O10 O 0.35324 0.06688 0.49997 1402 1.0
O11 O 0.53720 0.14339 0.31701 1943 1.0
N N 0.10388 0.80953 0.48671 1579 1.0
H1 H 0.4748 0.3109 0.4499 27 1.0
H2 H 0.3938 0.9970 0.5477 25 1.0
H3 H 0.3202 0.0438 0.4218 27 1.0
H4 H 0.6000 0.1442 0.2698 46 1.0
H5 H 0.4675 0.0928 0.2750 48 1.0
H6 H 0.0240 0.7849 0.4936 51 1.0
H7 H 0.0928 0.8565 0.4179 36 1.0
H8 H 0.1581 0.7310 0.4901 45 1.0
H9 H 0.1445 0.8500 0.5601 30 1.0

#End of data for AIPO-15
```

**Figure B.2:** CIF file made in this thesis work for the generation of a simulated x-ray diffraction pattern for AIPO<sub>4</sub>-15.

## B.3 Calculations

### B.3.1 Calculation of theoretical % mass loss for TGA analysis

Calculation of theoretical %mass loss for TGA analysis		
1 mol tbaAlPO-14:	2 mol [C <sub>4</sub> H <sub>12</sub> N] <sup>+</sup>	148 g/mol
	2 mol OH <sup>-</sup>	34 g/mol
	2 mol H <sub>2</sub> O	36 g/mol
	Al <sub>8</sub> P <sub>8</sub> O <sub>32</sub>	976 g/mol
	<b>Total:</b>	<b>1192 g/mol</b>
percent template, [C <sub>4</sub> H <sub>12</sub> N]		12,25
percent water H <sub>2</sub> O		3,02
percent water H <sup>+</sup> and OH <sup>-</sup>		3,02
Percent template, water, and hydroxide ions		18,29
1 mol ipaAlPO-14:	2 mol [C <sub>3</sub> H <sub>10</sub> N] <sup>+</sup>	120 g/mol
	2 mol OH <sup>-</sup>	34 g/mol
	2 mol H <sub>2</sub> O	36 g/mol
	Al <sub>8</sub> P <sub>8</sub> O <sub>32</sub>	976 g/mol
	<b>Total:</b>	<b>1164 g/mol</b>
percent template, [C <sub>3</sub> H <sub>9</sub> N]		10,14
percent water H <sub>2</sub> O		3,09
percent water H <sup>+</sup> and OH <sup>-</sup>		3,09
Percent template, water, and hydroxide ions		16,32

**Figure B.3:** Excel spreadsheet showing the calculated theoretical % mass loss possible in tbaAlPO<sub>4</sub>-14F and ipaAlPO<sub>4</sub>-14F.

### B.3.2 Calculation of carrier gas flow

Calculation of N2 flow based on predetermined T, WHSV and catalyst mass							
Date:	17.02.2010						
				<b>Calibration constants</b>			
Ambient T / °C	Ambient T / K	MeOHtemp / C	MeOHtemp / K	Cat / mg	A	B	C
23	296,15	0	273,15	18	0,703	0,854	0,174
WHSV/h-1	pMeOH / hPa	pAtm / hPa	R / J/Kmol	n' / mol/h	V'N2 / m3/h	V'N2 / ml/min	h / cm
1	40,4	1013,25	8,3145	0,0005618	0,0003286	5,47640	<b>3,3</b>
<b>Read off N2 flow :</b>				<b>3,3</b>			
				$Y = A + BX + CX^2$ Y designates flow in cm, X is the flow in ml/min $p(\text{MeOH}) = 40,41808 + 2,59623T + 0,0647T^2 + 0,00156T^3$ T/C			

**Figure B.4:** Excel spreadsheet for calculating carrier gas flow for a target WHSV and known catalyst weight. By courtesy of Morten Bjørgen.